

# Durham E-Theses

---

## *Synthetic and computational studies of conjugated acetylenic systems*

Koentjoro, Olivia Fatma

### How to cite:

---

Koentjoro, Olivia Fatma (2003) *Synthetic and computational studies of conjugated acetylenic systems*, Durham theses, Durham University. Available at Durham E-Theses Online:  
<http://etheses.dur.ac.uk/3653/>

### Use policy

---

The full-text may be used and/or reproduced, and given to third parties in any format or medium, without prior permission or charge, for personal research or study, educational, or not-for-profit purposes provided that:

- a full bibliographic reference is made to the original source
- a [link](#) is made to the metadata record in Durham E-Theses
- the full-text is not changed in any way

The full-text must not be sold in any format or medium without the formal permission of the copyright holders.

Please consult the [full Durham E-Theses policy](#) for further details.

University of Durham



A Thesis Entitled

**Synthetic and Computational Studies of  
Conjugated Acetylenic Systems**

Submitted by

**Olivia Fatma Koentjoro BSc. Honours**

(Graduate Society)

Department of Chemistry  
University of Durham  
South Road Laboratories  
Durham DH1 3LE UK

A copyright of this thesis rests with the author. No quotation from it should be published without his prior written consent and information derived from it should be acknowledged.



A Candidate for the Degree of Doctor of Philosophy  
2003

1 2 MAR 2004

*'There are no such things as electron deficient compounds,  
only theory deficient chemist'.*

*R.E. Rundle*

## Acknowledgements

First of all I would like to thank Dr. Paul Low for his supervision, help, and support during the course of my Ph.D. I would also like to thank Dr. Roger Rousseau for his guidance and encouragement with the theoretical side of my Ph.D. Special thanks are given to Michael Paterson and Rachel Roberts for friendship, support, help, patience, and understanding. Many thanks are given to my parents for all their help, encouragement and support.

I would also like to thank the past, present, and honorary members of Lab 100 first of all for their friendship along then for the chance to learn whether it be in chemistry or everyday life. Thanks go out to the other Ph.D. students and honorary members of Lab 100, namely: Philipp Zuber, Mark Allen, Richard Cordiner, and Rachel Roberts; the project students, namely: Hanilore Lonsdale, Gavin Forest, Katie Gatenby, Carl Barker, Deborah Corcoran, and Tim Hayes.

This research would not have been possible without the aid and enthusiasm of the department technical staff, namely: Dr. Alan Kenwright, Mrs. Catherine Heffernan and Mr. Ian McKeag (NMR); Dr. Mike Jones and Miss Lara Turner (Mass Spectrometry); Mrs. Jaraka Dostal (Elemental analysis); Dr. Horst Puschmann, Dr. Dimitri S. Yufit and Dr. Andres Goeta (X-ray crystallography); Dr. Mark Garner, Mr. Colin Greenhalgh, Mr. Alan Harland (Computing); Dr. Tony Royston (Mac. Computing); Mr. Lenny Lauchlan (Chromatography); Mr. Peter Coyne and Mr. Malcolm Richardson (Glassblowing); Mr. Barry Barker, Mr. George Rowe, Mr. Kelvin Appleby (Electrical Technicians); Mr. David Hunter (High Pressure Operations); Mr. Jimmy Lincoln, Mrs. Elizabeth Wood, Mr. Anthony Baxter, and Mr. Joe Peel (Stores) and Dr. Euan Ross and Dr. Hillary Hull (Administration). I also thank all the other people who worked and studied in the chemistry department who have not been mentioned.



Thanks are also extended to the people with whom collaboration of this research was carried out with, namely: Dr. Roger Rousseau (computational studies), Dr. Carlo Nervi (spectroelectrochemical studies), Dr. Andrew Beeby, as well as members of the Beeby group, Karen Findlay and Simon Rutter (spectroscopic studies). The financial support from Isobelle Fleck Scholarship (University of Durham) and Overseas Research Award are gratefully acknowledged.

Last but not least I would like to thank Dr. Darren Holling for editorial discussion, and also a calming influence during writing of this thesis, and just for being there.

## Memorandum

The work present within this thesis was carried out at the University of Durham between October 2000 and September 2003. This thesis is the work of the author, except where acknowledged by reference and has not been submitted for any other degree. The copyright of this thesis lies solely with the author and no quotation from it should be published without prior written consent and information derived from it should be acknowledged.

Part of this work has been the subject of the following:

- Koentjoro, O. F., Zuber, P., Goeta, A.E., Puschmann, H., Howard, J.A.K., Low, P.J., *J. Organomet. Chem.*, **670**, 178, 2003.
- Koentjoro, O.F., Rousseau, R., Low, P.J, *Organometallics*, **20**(22), 4502, 2001.

and has been presented at:

- 37<sup>th</sup> Universities of Scotland Inorganic Conference (USIC), Edinburgh, 2003.
- 39<sup>th</sup> IUPAC Congress and the 86<sup>th</sup> Conference of the Canadian Society for Chemistry, Ottawa, 2003.
- RSC Coordination Chemistry Discussion Group Meeting, Manchester, 2003.
- Durham University Chemistry Department Final Year Postgraduate Symposium, 2003.
- Laboratoire de Chimie du Solide et Inorganique Molaiculaire, UMR. 6511 CNRS-Universite de Rennes 1, France, 2002.
- 36<sup>th</sup> Universities of Scotland Inorganic Conference (USIC), Edinburgh, 2002.
- 2<sup>nd</sup> Chianti Electrochemistry Meeting, Sienna, 2002.
- 5<sup>th</sup> International Symposium of Functional  $\pi$ -Materials, Ulm, 2002.
- 84<sup>th</sup> Conference of the Canadian Society for Chemistry, Montreal, 2000.

## Abbreviations

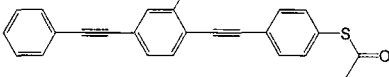
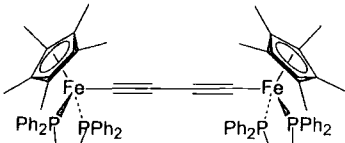
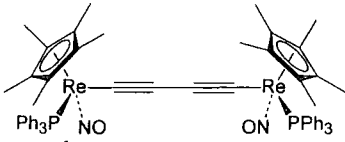
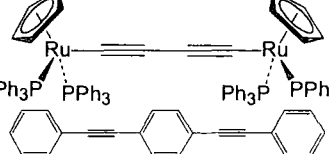
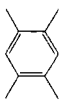
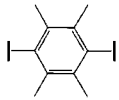
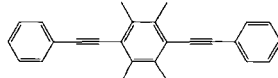
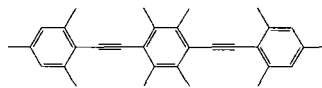
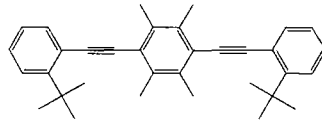
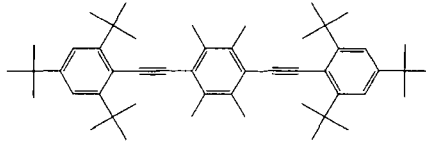
A	acceptor
1-Ad	1-adamantyl
ADF	Amsterdam Density Functional Program
B	Becke
bipy	bipyridinium
BO	bond order
BuLi	butyl lithium
CBPQT4+	cyclobis(paraquat-p-phenylene)
Cp	cyclopentadienyl
CPU	Computer Processing Unit
CSA	camphorsulphonic acid
CV	Cyclic Voltametry
CVE	Cluster Valence Electron
D	donor
dba	dibenzylideneacetone
DFT	Density Functional Theory
DIBAL-H	diisobutyl aluminium hydride
1/5DN	1,5-dioxynaphthalene
dppm	bis(diphenylphosphino)methane
dppf	1,1'-bis(diphenylphosphino)ferrocene
dppp	1,3-bis(diphenylphosphino)propane
$\epsilon$	extinction coefficient
EAN	effective atomic number
EI-MS	Electron Ionization-Mass Spectrometry
EPA	ethyl pentane alcohol
FAB-MS	Fast Atom Bombardment- Mass Spectrometry
GC-MS	Gas Chromatography-Mass Spectrometry
HF	Hartree-Fock
HMPA	hexamethylphosphorus triamide
HOMO	highest occupied molecular orbital
ICT	intervalence charge transfer
IR	infrared
Kc	comproportionation constant
LDA	lithium di(isopropyl)amine
LiHDMS	lithium hexamethyldisilazide
LP	lone pair
LUMO	lowest unoccupied molecular orbital
LYP	Lee-Yang-Parr
MCH/IP	4:1 methyl cyclohexane : 2-methyl butane
mDRAM	molecular dynamic random access memory
NBO	Natural Bond Order
NDR	negative differential resistance
NIR	near infrared
NLO	nonlinear optic

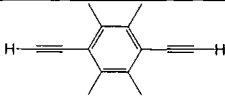
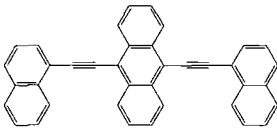
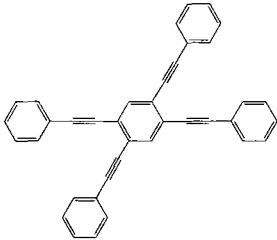
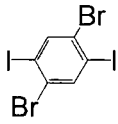
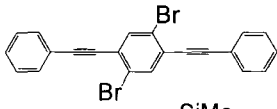
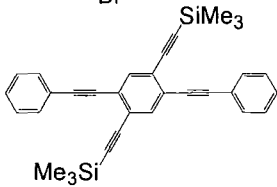
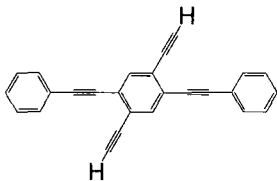
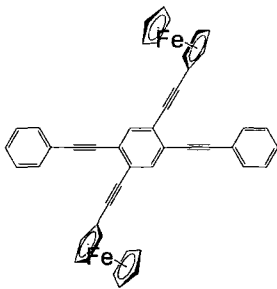
NMR.	Nuclear Magnetic Resonance
OPE	oligo(phenylene ethynylene)
OTTLE	optically transparent thin-layer electrochemical
PA	trans – poly(acetylene)
PCC	pyridinium chlorochromate
PCy3	tricyclohexylphosphine
PDA	trans – poly(diacetylene)
PES	photoelectron spectroscopy
Ph	C <sub>6</sub> H <sub>5</sub>
PPE	poly-(phenylene) ethynylene
PPV	poly-(phenylene)vinylene
PSEP	polyhedral skeletal electron pair
PTA	trans – poly(triacetylenes)
S	Slater
SAM	self assembled monolayer
SCF	self-consistent field
SEP	skeletal electron pairs
SOMO	singly occupied molecular orbital
STM	scanning tunneling microscopy
STO	Slater-type orbital
TCNQ	tetracyanoquinodimethane
THF	tetrahydrofuran
TLC	thin layer chromatography
TMNO	trimethyl N-oxide (Me <sub>3</sub> NO)
TR3	time-resolved resonance Raman
TTF	tetrathiafulvalene
UV/Vis	Ultra Violet/Visible Light


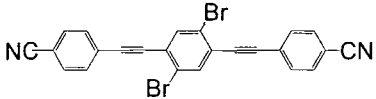
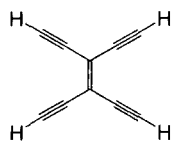
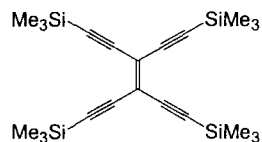
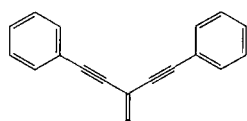
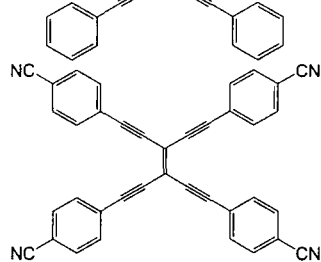
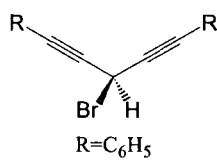
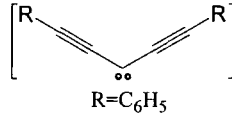
## Statement of Copyright

No part of this thesis may be reproduced by any means, nor transmitted, nor translated into any machine or language without the written permission of the author.

## Compound Numbering

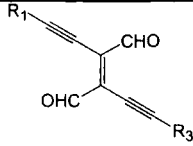
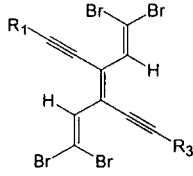
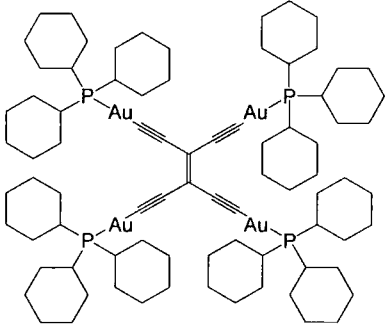
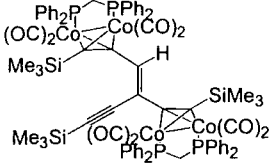
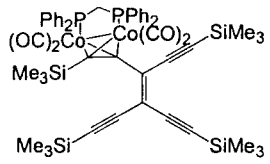
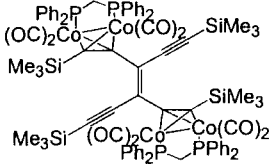
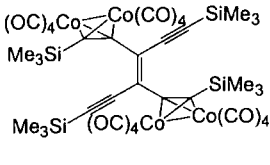
Name	Structure	No
Ethyl substituted 4,4'-di(phenyleneethynylene)-benzothioacetate [ $\{\text{Fe}(\text{dppe})_2\text{Cp}^*\}_2(\mu\text{-C}\equiv\text{C-C}\equiv\text{C})$ ]		1
[ $\{\text{Re}(\text{PPh}_3)\text{NOCp}^*\}_2(\mu\text{-C}\equiv\text{C-C}\equiv\text{C})$ ]		2
[ $\{\text{Ru}(\text{PPh}_3)_2\text{Cp}\}_2(\mu\text{-C}\equiv\text{C-C}\equiv\text{C})$ ]		3
1,4-bis(phenylethynyl)benzene		4
tetramethylbenzene		5
1,4-diiodo-2,3,5,6-tetramethylbenzene		6
1,4-bis(phenylethynyl)-2,3,5,6-tetramethylbenzene		7
1,4-bis(2',4',6'-tri(methyl)phenylethynyl)-2,3,5,6-tetra(methyl)benzene		8
1,4-bis(2'-t-butylphenylethynyl)-2,3,5,6-tetra(methyl)benzene		9
1,4-bis(2',4',6'-tri('butyl)phenylethynyl)-2,3,5,6-tetra(methyl)benzene		10
		11

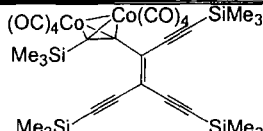
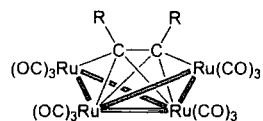
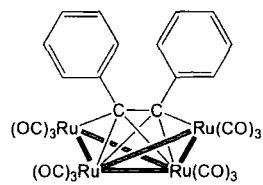
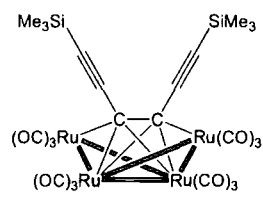
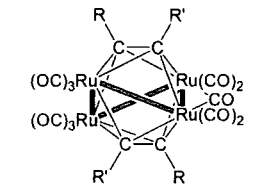
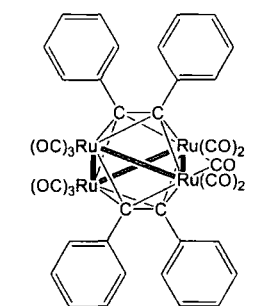
1,4-ethynyl-2,3,5,6-tetra(methyl)benzene		12
9,10-di(1-ethynylnaphthalene)anthracene		13
1,2,4,5-tetra(phenylethynyl)benzene		14
1,4-dibromo-2,5-diiodo-benzene		15
1,4-dibromo-2,5-bis(phenylethynyl)benzene		16
1,4-bis(phenylethynyl)-2,5-bis(trimethylsilylethynyl)benzene		17
1,4-diethynyl-2,5-bis(phenylethynyl)benzene		18
1,4-phenylethynyl-2,5-bis(ferrocenylethynyl)benzene		19

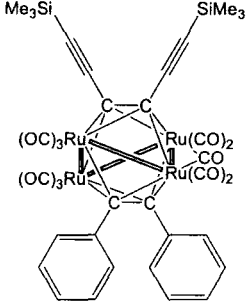
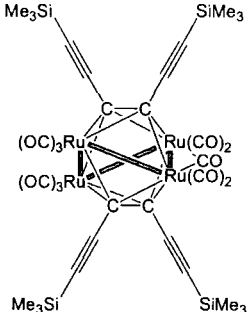
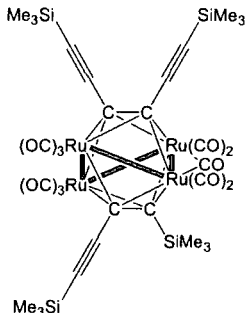
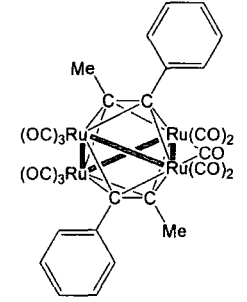
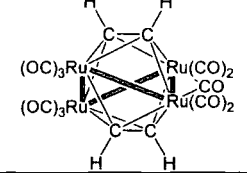
1,4- <i>bis</i> (4'-ethynylbenzonitrile)- 2,5- <i>bis</i> (4''-ethynyl-N,N- dimethylaniline)benzene		20
1,4- <i>bis</i> (ethynylbenzonitrile)-2,5- dibromobenzene		21
3,4-diethynylhex-3-ene-1,5-diyne		22a
1,6- <i>bis</i> (trimethylsilyl)-3-4- <i>bis</i> ((trimethylsilyl)ethynyl)hex-3- ene-1,5-diyne		22b
1,6- <i>bis</i> (phenyl)-3,4- <i>bis</i> (phenylethynyl)-hex-3-ene- 1,5-diyne		22c
1,6- <i>bis</i> (cyanophenyl)-3-4- <i>bis</i> ((4- cyanophenyl)ethynyl)hex-3-ene- 1,5-diyne		22e
		23
		24

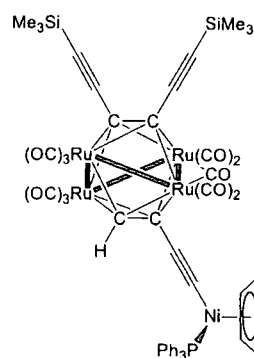
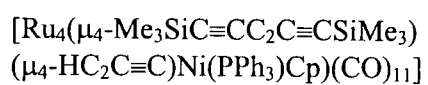
$  \begin{array}{c}  \text{R} \quad \text{R} \\  \diagdown \quad \diagup \\  \text{C} \\  \diagup \quad \diagdown \\  \text{N} \text{---} \text{N} \text{Li} \\    \\  \text{Tos}  \end{array}  $	25
R=Me <sub>3</sub> C, Me <sub>3</sub> Si	
$  \begin{array}{c}  \text{R} \quad \text{H} \quad \text{R} \\  \diagdown \quad   \quad \diagup \\  \text{C} \\    \\  \text{C} \\  \diagup \quad   \quad \diagdown \\  \text{R} \quad \text{H} \quad \text{R}  \end{array}  $	26
R=Ph, Me, Me <sub>3</sub> C, Me <sub>3</sub> Si	
$  \begin{array}{c}  \text{Pr}_3^i\text{Si} \quad \text{SiPr}_3^i \\  \diagdown \quad \diagup \\  \text{C} \text{---} \text{C} \\    \quad   \\  \text{OH} \quad \text{OH} \\  \diagup \quad \diagdown \\  \text{Pr}_3^i\text{Si} \quad \text{SiPr}_3^i  \end{array}  $	27
$  \begin{array}{c}  \text{Pr}_3^i\text{Si} \quad \text{SiPr}_3^i \\  \diagdown \quad \diagup \\  \text{C} \text{---} \text{C} \\    \quad   \\  \text{O} \quad \text{O} \text{---} \text{OEt} \\  \diagup \quad \diagdown \\  \text{Pr}_3^i\text{Si} \quad \text{SiPr}_3^i  \end{array}  $	28
R <sub>1</sub> —C≡C—H	
29	
$  \begin{array}{c}  \text{HO} \quad \text{H} \\  \diagdown \quad \diagup \\  \text{C} \text{---} \text{C} \\  \diagup \quad \diagdown \\  \text{R}_1 \quad \text{R}_2  \end{array}  $	30
$  \begin{array}{c}  \text{O} \\     \\  \text{R}_1 \text{---} \text{C} \text{---} \text{C} \text{---} \text{R}_2  \end{array}  $	31
$  \begin{array}{c}  \text{Br} \quad \text{Br} \\  \diagdown \quad \diagup \\  \text{C} \text{---} \text{C} \\  \diagup \quad \diagdown \\  \text{R}_1 \quad \text{R}_2  \end{array}  $	32
$  \begin{array}{c}  \text{O} \\     \\  \text{Br} \text{---} \text{C} \text{---} \text{C} \text{---} \text{OMe} \\    \quad   \\  \text{MeO} \text{---} \text{C} \quad \text{C} \text{---} \text{Br} \\     \\  \text{O}  \end{array}  $	33
$  \begin{array}{c}  \text{O} \\     \\  \text{R}_1 \text{---} \text{C} \text{---} \text{C} \text{---} \text{OMe} \\    \quad   \\  \text{MeO} \text{---} \text{C} \quad \text{C} \text{---} \text{R}_3 \\     \\  \text{O}  \end{array}  $	34



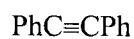
		35
		36
1,1,2,2-[Au(PCy <sub>3</sub> )] <sub>4</sub> -tetraethynylethanes		37
[{Co <sub>2</sub> (CO) <sub>4</sub> (μ-dppm)} <sub>2</sub> {μ,η <sup>2</sup> :μ,η <sup>2</sup> -(Me <sub>3</sub> SiC <sub>2</sub> C(H)=C(C <sub>2</sub> SiMe <sub>3</sub> )C≡CSiMe <sub>3</sub> )}]		38
[Co <sub>2</sub> (CO) <sub>4</sub> (μ-dppm){μ,η <sup>7</sup> -Me <sub>3</sub> SiC <sub>2</sub> C(C≡CSiMe <sub>3</sub> )=C(C≡CSiMe <sub>3</sub> ) <sub>2</sub> }]		39
[{Co <sub>2</sub> (CO) <sub>4</sub> (dppm)} <sub>2</sub> {μ-η <sup>2</sup> :η <sup>2</sup> -Me <sub>3</sub> SiC <sub>2</sub> C(C≡CSiMe <sub>3</sub> )C(C≡CSiMe <sub>3</sub> )C <sub>2</sub> SiMe <sub>3</sub> }]		40
[{Co <sub>2</sub> (CO) <sub>6</sub> } <sub>2</sub> {μ,η <sup>2</sup> -Me <sub>3</sub> SiC <sub>2</sub> C(C≡CSiMe <sub>3</sub> )=C(C≡CSiMe <sub>3</sub> )C <sub>2</sub> SiMe <sub>3</sub> }]		41

$[\text{Co}_2(\text{CO})_6\{\mu, \eta^2\text{-Me}_3\text{SiC}_2\text{C}(\text{C}\equiv\text{CSiMe}_3)=\text{C}(\text{C}\equiv\text{CSiMe}_3)_2\}]$		42
$[\text{Ru}_4(\mu\text{-RC}_2\text{R})(\text{CO})_{12}]$		43
$[\text{Ru}_4(\mu\text{-PhC}_2\text{Ph})(\text{CO})_{12}]$		43a
$[\text{Ru}_4(\mu\text{-SiMe}_3\text{C}\equiv\text{CC}_2\text{C}\equiv\text{CSiMe}_3)(\text{CO})_{12}]$		43b
$[\text{Ru}_4(\mu_4\text{-RC}_2\text{R}')_2(\text{CO})_{11}]$		44
$[\text{Ru}_4(\mu_4\text{-PhC}_2\text{Ph})_2(\text{CO})_{11}]$		44a

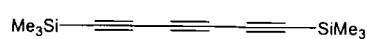
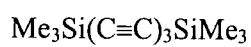
$[\text{Ru}_4(\mu_4\text{-PhC}_2\text{Ph})(\mu_4\text{-Me}_3\text{SiC}\equiv\text{CC}_2\text{C}\equiv\text{CSiMe}_3)(\text{CO})_{11}]$		44b
$[\text{Ru}_4(\mu_4\text{-Me}_3\text{SiC}\equiv\text{CC}_2\text{C}\equiv\text{CSiMe}_3)_2(\text{CO})_{11}]$		44c
$[\text{Ru}_4(\mu_4\text{-Me}_3\text{SiC}\equiv\text{CC}_2\text{C}\equiv\text{CSiMe}_3)(\mu_4\text{-Me}_3\text{SiC}_2\text{C}\equiv\text{CSiMe}_3)(\text{CO})_{11}]$		44d
$[\text{Ru}_4(\mu_4\text{-MeC}_2\text{Ph})_2(\text{CO})_{11}]$		44e
$[\text{Ru}_4(\mu_4\text{-HC}_2\text{H})_2(\text{CO})_{11}]$		44f



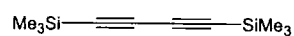
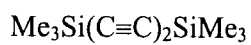
44g



45a



45b



45c

## Abstract

Conjugated molecular materials offer a range of useful physical properties from highly efficient luminescent behaviour to wire like conduction. This thesis describes the synthesis, molecular and electronic structures of a range of unusually conjugated organic and organometallic compounds.

A combination of synthetic and absorption spectroscopic studies, as well as calculations (DFT) were used to probe the electronic structure of the 1,4-*bis*(phenylethynyl)benzene and 1,2,4,5-tetraethynyl benzene framework. These revealed that the ground state of 1,4-*bis*(phenylethynyl)benzene type molecules can be described as thermally populated distributions of conformers, while the excited state is best described in terms of planar conformations with considerable acetylenic character.

A novel synthesis of 1,1,2,2-tetraethynylethenes has been discovered involving cross-coupling reactions of tetrachloroethene with terminal acetylenes. Reactions of these tetraethynylethenes with  $[\text{Co}_2(\text{CO})_6(\text{L}_2)][\text{L}_2 = (\text{CO})_2, \text{dppm}]$  give complexes with one or two (*trans*) cobalt fragment coordinated to the acetylenic moieties.

A theoretical study of the electronic structure of  $[\text{Ru}\{(\text{C}\equiv\text{C})_n\text{R}\}(\text{L})_2\text{Cp}]$  ( $n = 1-6$ ;  $\text{L} = \text{CO}, \text{PH}_3$ ;  $\text{R} = \text{CH}_3, \text{H}, \text{C}_6\text{H}_4\text{NH}_2\text{-}p, \text{C}_6\text{H}_5, \text{C}_6\text{H}_4\text{NO}_2\text{-}p, \text{CN}$ ) has been carried out. The redox potentials of these species may be tuned by the length of the polyyne ligand, the nature of the supporting ligands, as well the electronic properties of the non-metal end-cap.

Electrochemical and spectroelectrochemical analysis of  $[\text{Ru}_4(\text{CO})_{11}(\mu_4\text{-}(\text{RC}_2\text{C}\equiv\text{CR})_2)]^{0/2-}$  have revealed an unusual reversible conversion of 62/64 CVE cluster frameworks. This switching behaviour has been modelled using  $[\text{Ru}_4(\text{CO})_{11}(\mu_4\text{-HC}_2\text{H})_2]^{0/2-}$  via DFT methods.

# Table of Contents

Contents	Page Number
Acknowledgment	i
Memorandum	iii
Abbreviation	iv
Statement of Copyright	v
Compound Numbering	vi
Abstract	xiv
Table of Contents	xv

## Chapter 1. Introduction

1.1. Strategies for Molecular Electronics	1
1.2. Historical Perspective	2
1.3. Molecular Wires	5
1.3.1. Poly(phenylene ethynylene)	6
1.3.2. Poly(triacetylene)	11
1.3.3. Carbon Nanotubes	14
1.3.4. Metal Capped Carbyne	15
1.4. Molecular Junctions	24
1.4.1. Substituted 1,3,5-Triethynylbenzene	26
1.4.2. Substituted 1,2,4,5-Tetraethynylbenzene	28
1.4.3. 1,1,2,2-Tetraethynylethene	30
1.5. Molecular Switches	31
1.5.1. Photoresponse Based Switch	31
1.5.2. Topological Rearrangement Based Switch	33
1.5.3. Redox Based Switch	34
1.6. Molecular Logic Devices	36
1.7. Memory Devices/Data Storage	38

1.8. Future challenges	39
------------------------	----

## Chapter 2. Synthesis and Photophysics of Ethynylated Aromatic Systems

2.1. Ethynylated Aromatic Systems as Potential Molecular Wires	40
2.2. Synthesis and Photophysics of Linear Ethynylated Aromatic Systems	42
2.2.1. 1,4- <i>bis</i> (Phenylethynyl)benzene	42
2.2.2. 1,4- <i>bis</i> (Phenylethynyl)-2,3,5,6-tetra(methyl)benzene	51
2.2.3. 1,4- <i>bis</i> (2',4',6'-tri(Methyl)phenylethynyl)-2,3,5,6-tetra(methyl)benzene	56
2.2.4. Photophysics of Linear Ethynylated Aromatic Systems	62
2.2.5. 9,10-di(1-Ethynyl)naphthalene)anthracene	64
2.3. Synthesis and Photophysics of 1,2,4,5-Tetraethynyl Substituted Benzenes	70
2.3.1. 1,2,4,5-tetra(Phenylethynyl)benzene	70
2.3.2. 1,4- <i>bis</i> (Phenylethynyl)-2,5- <i>bis</i> (ethynyl)benzene	78
2.3.3. 1,4- <i>bis</i> (Phenylethynyl)-2,5- <i>bis</i> (ethynylferrocene)benzene	82
2.3.4. 1,4- <i>bis</i> (4'-Ethynylbenzonitrile)-2,5- <i>bis</i> (4''-ethynyl-N,N-dimethylaniline)benzene	84
2.4. Conclusion	86
2.5. General Experimental	87
2.5.1. Reagent, Materials, and Solvent	87
2.5.2. NMR, Mass, FTIR and UV-Vis Spectroscopy	87
2.5.3. Gas Liquid Chromatography, Elemental and X-Ray Analysis	88
2.5.4. CV Analysis	88
2.6. Experimental	89
2.6.1. 1,4-ethynyl-2,3,5,6-tetra(methyl)benzene (1,4-ethynyldurene) ( <b>12</b> )	89
2.6.2. 1,4- <i>bis</i> (phenylethynyl)-2,3,5,6-tetramethylbenzene (1,4- <i>bis</i> (phenylethynyl)-durene) ( <b>8</b> )	90
2.6.3. 1,4- <i>bis</i> (2',4',6'-tri(methyl) phenylethynyl)-2,3,5,6- tetra	

(methyl)benzene (1,4-(mesitylethynyl)durene) ( <b>9</b> )	91
2.6.4. 9,10-di(1-ethynynaphthalene)anthracene ( <b>13</b> )	91
2.6.5. 1,2,4,5-tetra(phenylethynyl)benzene ( <b>14</b> )	92
2.6.6. 1, 4-dibromo-2,5- <i>bis</i> (phenylethynyl)benzene ( <b>16</b> )	93
2.6.7. 1,4- <i>bis</i> (phenylethynyl)-2,5- <i>bis</i> (trimethylsilylethynyl)benzene ( <b>17</b> )	94
2.6.8. 1,4- <i>bis</i> (phenylethynyl)-2,5- <i>bis</i> (ethynyl)benzene ( <b>18</b> )	95
2.6.9. 1,4-phenylethynyl-2,5- <i>bis</i> (ferrocenylethynyl)benzene ( <b>19</b> )	95
2.6.10. 1,4- <i>bis</i> (ethynylbenzonitrile)-2,5-dibromobenzene ( <b>21</b> )	96
2.6.11. 1,4- <i>bis</i> (4'-ethynylbenzonitrile)-2,5- <i>bis</i> (4''-ethynyl-N,N- dimethylaniline)benzene ( <b>20</b> )	97

### Chapter 3. 1,1,2,2-Tetraethynylethenes as Potential Molecular Junctions

3.1. Synthetic Routes to the Formation of 1,1,2,2-Tetraethynylethenes	98
3.2. New Synthetic Method for the Formation of Functionalised 1,1,2,2-Tetraethynylethenes	109
3.3. Reaction of Dicobalt Hexacarbonyl <i>bis</i> (diphenylphosphino)methane with 1,6- <i>bis</i> (Trimethylsilyl)-3,4- <i>bis</i> ((trimethylsilyl)ethynyl) hex-3-ene-1,5-diyne	116
3.4. Reaction of Dicobalt Octacarbonyl with 1,6- <i>bis</i> (Trimethylsilyl) -3,4- <i>bis</i> ((trimethylsilyl)ethynyl)hex-3-ene-1,5-diyne	125
3.5. Conclusion	126
3.6. Experimental	126
3.6.1. 1,6- <i>bis</i> (trimethylsilyl)-3-4- <i>bis</i> ((trimethylsilyl)ethynyl) hex-3-ene-1,5-diyne ( <b>22b</b> )	126
3.6.2. 1,6- <i>bis</i> (cyanophenyl)-3-4- <i>bis</i> ((benzonitrile)ethynyl) hex-3-ene-1,5-diyne ( <b>22e</b> )	127
3.6.3. $[\text{Co}_2(\text{CO})_4(\text{dppm})\{\mu, \eta^2\text{-Me}_3\text{SiC}_2\text{C}(\text{C}\equiv\text{CSiMe}_3)=\text{C}(\text{C}\equiv\text{CSiMe}_3)_2\}]$ ( <b>39</b> )	128
3.6.4. $[\{\text{Co}_2(\text{CO})_4(\text{dppm})\}_2\{\mu\text{-}\eta^2\text{:}\eta^2\text{-Me}_3\text{SiC}_2\text{C}(\text{C}\equiv\text{CSiMe}_3)\text{C}(\text{C}\equiv\text{CSiMe}_3)\text{C}_2\text{SiMe}_3\}]$ ( <b>40</b> )	129
3.6.5. Reaction of crude 1,6- <i>bis</i> (trimethylsilyl)-3-4- <i>bis</i> ((trimethylsilyl)ethynyl)hex-3-ene-1,5-diyne with $[\text{Co}_2(\text{CO})_6(\text{dppm})]$	130



3.6.5.1. $\text{Co}_2(\text{CO})_4(\text{dppm})(\mu, \eta^2\text{-Me}_3\text{SiC}_2\text{C}\equiv\text{CSiMe}_3)$	130
3.6.5.2. $[\text{Co}_2(\text{CO})_4(\text{dppm})\{\mu, \eta^2\text{-Me}_3\text{SiC}_2\text{C}(\text{C}\equiv\text{CSiMe}_3)=\text{C}(\text{C}\equiv\text{CSiMe}_3)_2\}]$ (39)	131
3.6.5.3. $[\{\text{Co}_2(\text{CO})_4(\text{dppm})\}_2\{\mu, \eta^2\text{-(Me}_3\text{SiC}_2\text{C}(\text{H})=\text{C}(\text{C}\equiv\text{CSiMe}_3)_2)\}]$ (38)	131
3.6.6. Reaction of 1,6-bis(trimethylsilyl)-3-4-bis(((trimethylsilyl)ethynyl)hex-3-ene-1,5-diyne with $[\text{Co}_2(\text{CO})_8]$	132
3.6.6.1 $[\{\text{Co}_2(\text{CO})_6\}_2\{\mu\text{-}\eta^2\text{:}\eta^2\text{-Me}_3\text{SiC}_2\text{C}(\text{C}\equiv\text{CSiMe}_3)\text{C}(\text{C}\equiv\text{CSiMe}_3)\text{C}_2\text{SiMe}_3\}]$ (41)	132
3.6.6.2. $[\text{Co}_2(\text{CO})_6\{\mu, \eta^2\text{-Me}_3\text{SiC}_2\text{C}(\text{C}\equiv\text{CSiMe}_3)=\text{C}(\text{C}\equiv\text{CSiMe}_3)_2\}]$ (42)	133

## Chapter 4. Studies Utilising Density Functional Theory

4.1. The Relationship between Molecular Modelling and Chemistry	134
4.2. Electronic Structure Calculation Methods	135
4.2.1. Density Functional Theory	137
4.2.2. Applicability of Density Functional Theory to Transition Metal Systems	139
4.3. Geometry Optimisation	139
4.4. Polyynyl Complexes as Potential Molecular Wires	143
4.5. Electronic Structure of Polyynyl Complexes	146
4.5.1. Geometry Optimisation	150
4.5.2. Electronic Structure and Bonding	149
4.5.3. Charge Distribution	159
4.5.4. C-C Bond Order	164
4.5.5. Variation of the Supporting Ligand on the Metal	166
4.5.6. Effects of Oxidation	171
4.6. Conclusion	178
4.7. Experimental	179
4.7.1. Computational Method	179

## Chapter 5. Synthetic and Computational Study of Ru<sub>4</sub>C<sub>4</sub> Clusters

5.1. Transition Metal Cluster as Potential Molecular Switches	180
5.2. Theoretical and Structural Analysis	185
5.3. Synthesis and Characterisation of Ru <sub>4</sub> C <sub>4</sub> Clusters	193
5.4. Molecular Structures	200
5.5. Electrochemistry and IR Spectroelectrochemistry	206
5.6. Computational Analysis	210
5.7. Molecular Switching Behaviour	221
5.8. Experimental	222
5.8.1. Spectroelectrochemistry	222
5.8.2. Computational Method	223
5.8.3. Experimental	224
5.8.3.1. [Ru <sub>4</sub> (μ <sub>4</sub> -η <sup>2</sup> -Me <sub>3</sub> SiC≡CC <sub>2</sub> C≡CSiMe <sub>3</sub> ) <sub>2</sub> (CO) <sub>11</sub> ] ( <b>44c</b> )	224
5.8.3.2. [Ru <sub>4</sub> (μ <sub>4</sub> -η <sup>2</sup> -PhC <sub>2</sub> Ph) <sub>2</sub> (CO) <sub>11</sub> ] ( <b>44a</b> )	225
5.8.3.3. [Ru <sub>4</sub> (μ <sub>4</sub> -η <sup>2</sup> -Me <sub>3</sub> SiC≡CC <sub>2</sub> C≡CSiMe <sub>3</sub> )(μ <sub>4</sub> -η <sup>2</sup> -PhC <sub>2</sub> Ph)(CO) <sub>11</sub> ] ( <b>44b</b> )	226
5.8.3.4. [Ru <sub>4</sub> (μ <sub>4</sub> -Me <sub>3</sub> SiC≡CC <sub>2</sub> C≡CSiMe <sub>3</sub> )(μ <sub>4</sub> -Me <sub>3</sub> SiC <sub>2</sub> C≡CSiMe <sub>3</sub> )(CO) <sub>11</sub> ] ( <b>44d</b> )	227
5.8.3.5. [Ru <sub>4</sub> (μ <sub>4</sub> -η <sup>2</sup> -Me <sub>3</sub> SiC≡CC <sub>2</sub> C≡CSiMe <sub>3</sub> )(μ <sub>4</sub> -η <sup>2</sup> -(HC <sub>2</sub> C≡C)Ni(PPh <sub>3</sub> )Cp)(CO) <sub>11</sub> ] ( <b>44g</b> )	228
5.8.3.6. [Ru <sub>4</sub> (μ <sub>4</sub> -η <sup>2</sup> -(Me <sub>3</sub> SiC≡CC <sub>2</sub> C≡CSiMe <sub>3</sub> )(CO) <sub>10</sub> (PPh <sub>3</sub> ) <sub>2</sub> ]	229
<b>Bibliography</b>	230

### Accompanying Compact Disk

Associated .cif files for the crystal structures, extra experimental data not discussed in the thesis, .log files for molecular structure calculations used to generate molecular structure and orbital pictures.

# Chapter 1. Introduction

## 1.1. Strategies for Molecular Electronics

Miniaturisation of components for the construction of useful devices and machines is currently pursued by the so called “top down” approach in which known architectures and structures are reduced in physical size and critical dimension as advances are made in both lithographic methods and as new materials become available. It has been observed by Moore that for integrated circuits the device speed thus the chip density doubles approximately every 24-18 months.<sup>1</sup> Currently photolithographic techniques can produce microchips with a size of approximately  $0.1\mu\text{m}$ . Further decreases following this method are likely, through advances in both photolithographic techniques and new materials for use in critical areas, such as the construction of the vital gate insulator in metal oxide field effect transistors.<sup>2-4</sup> However, when the critical dimensions on integrated circuits becomes less than  $0.01\mu\text{m}$ , quantum mechanical tunneling will lead to significant current leakage through insulating materials, which can detrimentally affects the devices performance.<sup>5</sup>

An alternative strategy towards technology at the nanometer scale is the so called “bottom-up” approach, which utilises atoms or molecules to build up nanometer-sized functional structures. Often the rate determining step in existing computational architectures is the time it takes for an electron to travel between two points. By employing molecular scale dimensions the transmit time would be minimised thus increasing computational operating speed. Present computational systems utilise approximately  $10^{10}$  silicon based devices.<sup>6</sup> In order to manufacture true nanoscale molecular electronic circuits, new fabrication methods along with new input-output strategies and software-hardware integration routines will need to be devised. Before these issues can be satisfactorily addressed, a considerable body of work aimed at understanding the way in which single molecules can be



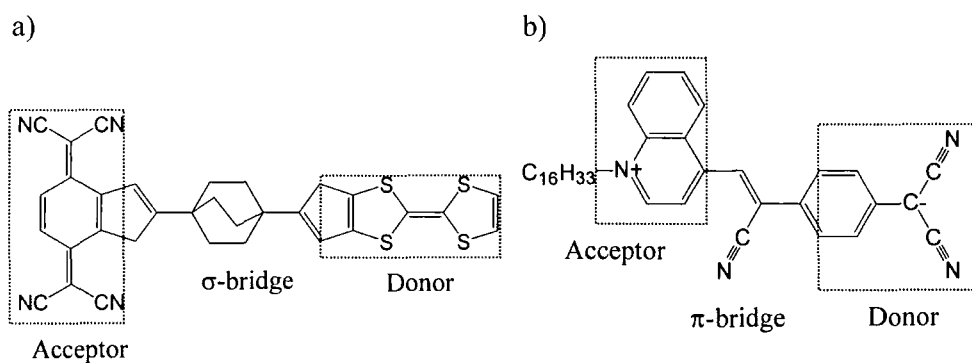
tailored to act as wires, switches, junctions and transistor-like devices manner needs to be carried out along with a method of how these systems can be assembled to interact with each other in a controlled and rational in a manner.

At present the design of electronic digital devices is governed by the need to optimise the component size and speed, the latter being limited by the natural temporal response time. The two components are conflicting design goals; therefore, several compromises need to be made in terms of the hardware-software duality. This materialises as programmed logic (memory or software dominant) versus wired logic (CPU or hardware dominant).<sup>5</sup> The hardware-software duality can be utilised in the design of a multiple architecture computer which is defect tolerant.<sup>7</sup> A molecular machine would contain numerous types of wires and switches that are laid out according to certain wiring conventions which results in multiple hardware defects due to incompatibilities in assembling different types of components. The hardware defects are paid for in the software programming effort, which needs to configure routines that can route around the defects as well as to configure logically the intact resources into the machine.

## 1.2. Historical Perspective

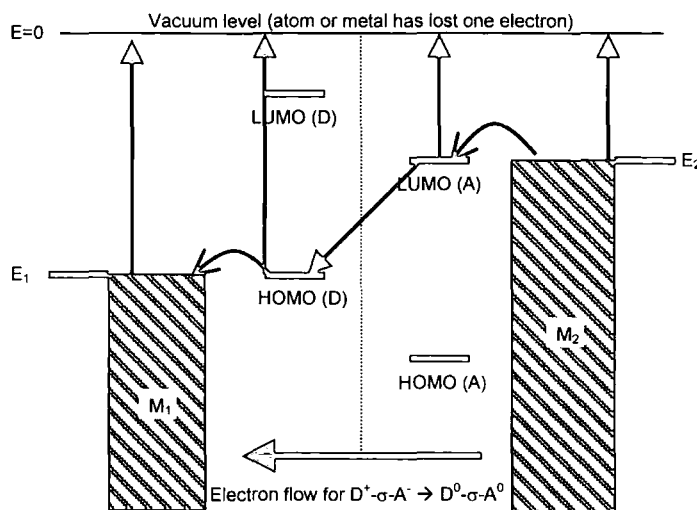
The idea of molecular electronics was launched when it was proposed that a system comprising of a donor  $\pi$ -system (D) linked by a  $\sigma$ -bonded tunneling bridge to an acceptor  $\pi$ -system (A) (**Figure 1a**) had the potential to act as a unimolecular rectifier.<sup>8</sup> The D terminus is a tetrathiafulvalene (TTF) unit which is a good organic one-electron donor, while the A terminus is a tetracyanoquinodimethane (TCNQ) unit which is a good one-electron acceptor. The purpose of the  $\sigma$  bridge is to decouple the molecular orbitals of the donor moiety D from the molecular orbitals of the acceptor moiety A. If the decoupling between D and A is complete, then intramolecular electron transfer becomes impossible leading to rectification behaviour through tunneling. When this D- $\sigma$ -A

arrangement is placed between two metal electrodes, it should form the working rectifier. In practical terms the proposed rectifier had several problems, among them the fact that the HOMO and LUMO levels of the organic donor and acceptor do not match the Fermi levels of metals; it is difficult to assemble defect-free monolayers of molecules; and reliable electrical contacts must be made with macroscopic metal electrodes.



**Figure 1.** Models for a) D-σ-A and b) D-π-A molecular rectifiers.

Electron transfer in the rectifier is facilitated by an inelastic tunneling through the molecule from the electronically excited state  $D^+-\sigma-A^-$  to the ground state  $D^0-\sigma-A^0$  (**Figure 2**). Current movement starts with a charge transfer from the cathode to the acceptor. The mechanism consist of two resonant electron transfers across metal-organic interfaces, followed by (or simultaneous with) an inelastic downhill intramolecular electron transfer, which achieves, overall, the migration of one electron from  $M_2$  to  $M_1$ . However, charge cannot flow between acceptor and donor until the energy levels of the anode are lowered enough to allow a transfer of charge from the HOMO (D) to the metal anode. The tunneling process from LUMO (A) to HOMO (D) is irreversible, and the overall electron transfer is from acceptor to donor.<sup>8</sup>



**Figure 2.** The proposed working rectifier  $M_1|D-\sigma-A|M_2$ .<sup>9</sup>

Advances in scanning tunneling microscopy (STM) technology have given researchers tools to probe and manipulate individual molecules which has led to conductivity testing of several potential rectifiers as well as molecular wires. Strong rectification behaviour has also been observed in Langmuir-Blodgett films of  $\gamma$ -(n-hexadecyl)quinolinium tricyanoquinodimethanide (**Figure 1b**) placed between two metal electrodes.<sup>10</sup> The donor (quinolinium) and acceptor (tricyanoquinodimethanide) moieties in this system are connected by a  $\pi$  bridge instead of a  $\sigma$  bridge, and both the donor and acceptor moieties are redox active, in contrast to the earlier example described above. The HOMO of the molecule shows a delocalised charge density, spread on both the  $D^+$  part and the bridge, while the LUMO is localised on the  $A^-$  part. The shortness of the  $\pi$ -bridge allows for a strong intervalence transfer between the D and A ends of the molecule. This system exists in a zwitterionic ground state  $D^+-\pi-A^-$ , while the first excited state is the undissociated form  $D^0-\pi-A^0$ . Electron transfer from metal electrodes to a neutral ground-state molecule creates a zwitterionic excited state form that by intervalence transfer can regenerate the neutral form. The rectification arises due to the allowed intramolecular intervalence transfer transition.

There are three principle research domains of molecular electronics, which comprise molecular magnets and actuators, molecular conductance junctions encompassing for example: wires, diodes, and switches, and, finally, molecular optoelectronics which include displays, data processing and optical memory.<sup>11</sup> The discussion below is limited to areas of intramolecular charge transport and the implications of this work on the design and synthesis of molecular wires, junction and switches. This discussion is not intended to be comprehensive, but rather a snapshot of the current research ongoing in this area. For a more complete discussion of molecular electronics in a broader context the reader is directed to the literature and reference cites therein.<sup>2, 12-18</sup> However, despite a few remarkable experiments, very few potential molecular components have been experimentally tested and evaluated for their capacity to conduct electrons (or holes) along a molecular axis to date. Many wire-like molecules have been designed by drawing analogies with compounds that have been assessed and from theoretically derived models. Where possible the examples used to illustrate the different research areas discussed will be taken from molecules which have been evaluated for electron conduction.

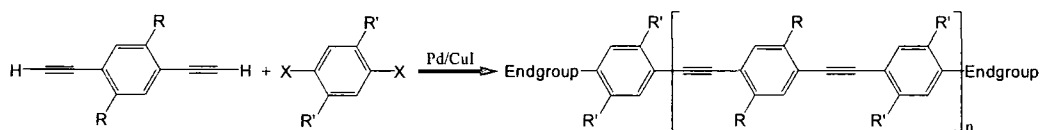
### **1.3. Molecular Wires**

The description of a wire is that it must provide a pathway for the transport of charge from one terminus to another which is more efficient than transport through space. From a design perspective the wire must also be linear and of a fixed length in order to span the gap between two components in the circuit. Regardless of the mechanism of action perceived, it should be apparent that the successful molecular wires candidate structures will offer rigid, linear,  $\pi$ -conjugated frameworks in which the delocalised network of  $\pi$ -symmetry orbitals provide a pathway for electron movement.<sup>15</sup> A major consideration in molecular devices is consumption/dissipation of energy, since transfer of large numbers of electrons would lead to excessive heat problems. One proposed solution to this problem relies upon a fundamental change in the perceived mechanism of

operation of molecular devices. These devices would not function *via* electron transfer but rather *via* electrostatic interaction produced by small reshapes of the electron density due to the input signals which would be responsible for the transmission of information throughout the system.<sup>5</sup>

### 1.3.1. Poly(phenylene ethynylene)

Conjugated molecules comprising of alternating single and double or triple carbon-carbon bonds can conduct electrons through their  $\pi$ -system and consequently many molecular wires are based on this phenomenon.<sup>5</sup> One class of molecules, namely poly(phenylene ethynylene) (PPE) has been synthesised (**Scheme 1**), *via* Pd-Cu catalysed coupling, with highly controlled lengths for use as molecular wires in bridging nanogaps.



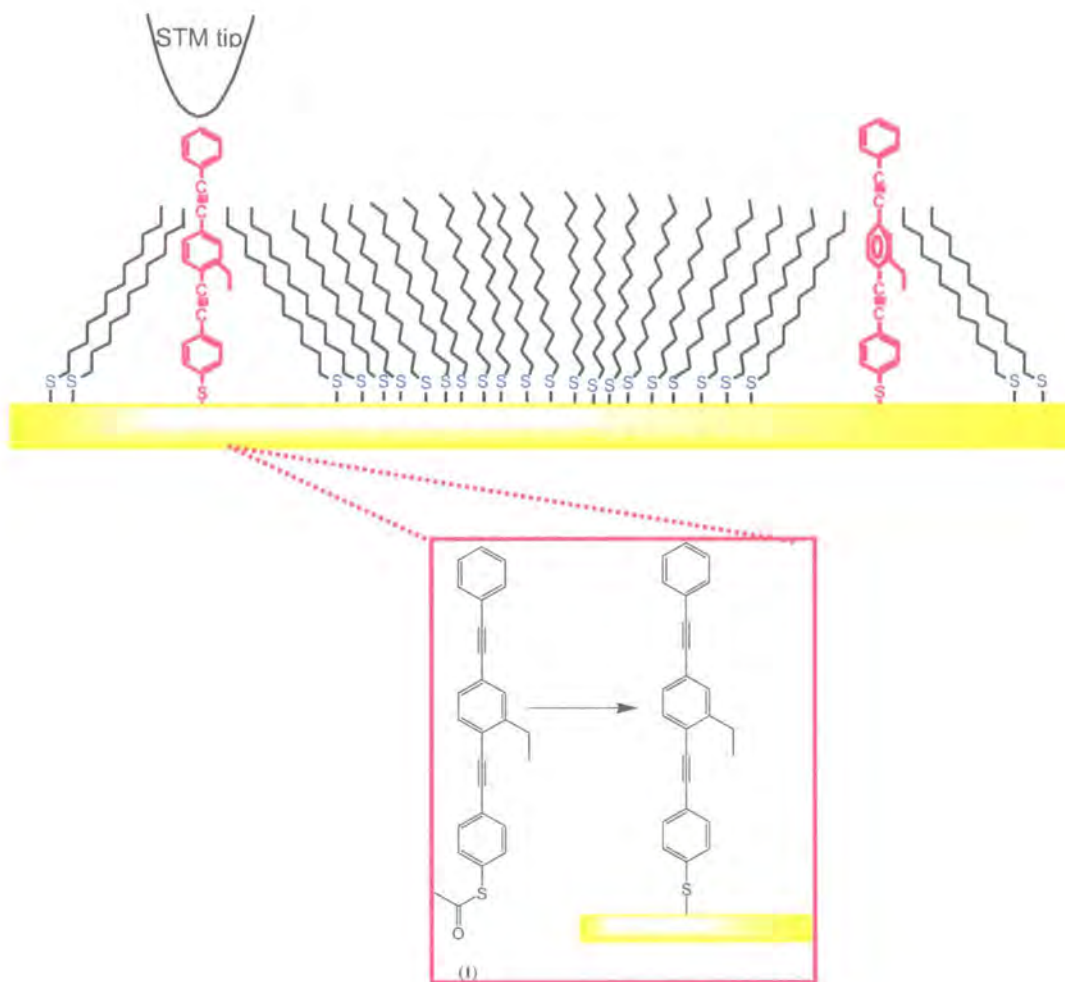
**Scheme 1.** Synthesis of PPE.

One of the PPEs that have been successfully tested for conductance is the ethyl substituted 4,4'-di(phenyleneethynylene)-benzothioacetate (**1**) which can self assemble on gold when converted to the thiolate (**Figure 3**).<sup>19</sup> STM imaging showed bright, stable, isolated spots at domain boundaries and defect sites in the self assembled monolayer (SAM) of the support composed of dodecanethiolate. An apparent tunneling barrier height measurement showed that the relative measure of conductivity of **1** was approximately twice that of the dodecanethiolate support material.<sup>19</sup> The oligomer showed conductance bistability, with the environmental matrix determined to be a critical factor for switching. A well ordered matrix reduces the rate of switching, while a poorly ordered one yields an increase in the switching frequency. The stochastic on-off



switching of the current observed in the STM images has been explained in terms of changes in ring conformation and thus electron localisation. When all the phenyl rings in phenylene ethynylene oligomers are planar, the  $\pi$ -orbital overlap of the molecule is continuous. Thus, the electrons flow between the two metal termini, i.e. conductivity, is maximised. However, if the phenyl rings are perpendicular with respect to each other there is a discontinuity in the  $\pi$ -orbital network and this minimises the free flow of electrons across the molecule, hence decreasing conductivity.<sup>5, 20, 21</sup> It has been hypothesised that the conductivity of these phenylene ethynylene oligomers arises from transfer of electrons (holes) through the  $\pi$ -orbital backbone that extends over the entire molecule. An alternate explanation for the stochastic on-off switching for molecules such as **1** in terms of fluctuation of the thiol-gold contact leading to mobility of the molecules tethered to the gold surface *via* a thiol linkage has also been proposed.<sup>22</sup>

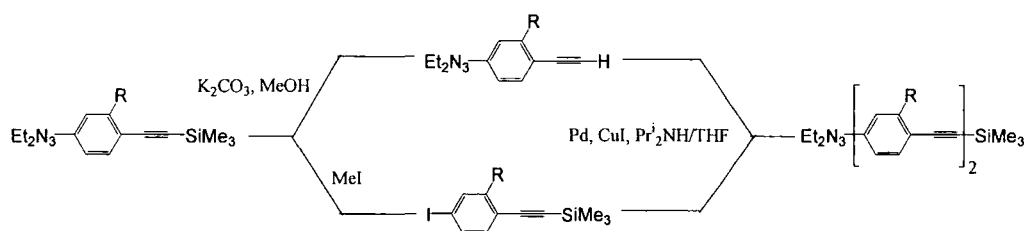
Theoretical results show that in solution state the barrier to rotation about alkynyl-aryl single bond is very low, less than 1 kcal/mol.<sup>20</sup> Accordingly, in solution 1,4-phenylene ethynylene does not have a preference for either planar or perpendicular orientation and all possible conformers are present in dilute solutions at room temperature. The switching frequency for an isolated molecule has been calculated to be 390.6 GHz, corresponding to a switching cycle of 2.56 ps. The rotational barrier increases to 38 kcal/mol for a molecule in an ordered SAM of supporting substrate due to steric effects from neighboring molecules, which translates to a very large time for the switching cycle.<sup>23</sup>



**Figure 3.** Schematic representation of **1** and its self assembly on gold.

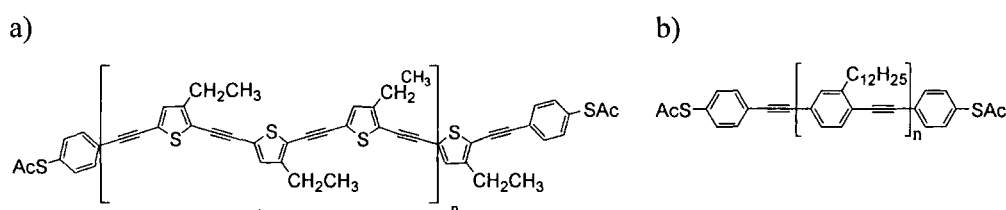
A range of PPEs of similar type to **1** have been synthesised using a divergent-convergent method as a way to double molecular length at each iteration (**Scheme 2**), thereby avoiding tedious linear assembly.<sup>24</sup> A further advantage of this method is that an incomplete reaction produces a product that is half the length of the target molecules, and thus easy to separate. There are three reaction steps involved in the divergent-convergent synthesis: an iodination, a protodesilylation and a Pd/CuI catalysed cross-coupling. One half of the starting material is treated with MeI and a protodesilylation is carried out on the second half. The two portions are then combined under Pd/Cu cross-coupling conditions generating a dimer of the starting material. The dimer has the same endgroups as

generating a dimer of the starting material. The dimer has the same endgroups as the monomer, so the entire process can be repeated until the desired length of the molecule is obtained.<sup>24</sup> Once the PPE has been synthesised then the thiol end groups can be attached, protected as the thioacetyl moieties, which will serve as binding sites for adhesion to gold surfaces.<sup>24</sup>



**Scheme 2.** Synthesis of oligo(1,4-phenyleneethynylene) using the iterative divergent-convergent method.

The compounds that have been synthesised using the method described above include oligo(2,5-thiophene ethynylene),<sup>25</sup> and oligo(1,4-phenylene ethynylene) (**Figure 4**).<sup>24</sup> The 1,4-phenylene ethynylene compounds exhibit improved rigidity over the 2,5-thiophene ethynylenes. This is important in increasing the planarity of the PPEs which has been postulated as an important factor to improve conductivity due the continuous  $\pi$ -overlap of the backbone.



**Figure 4.** Illustration of a) oligo(2,5-thiophene ethynylene),  
b) oligo(1,4-phenylene ethynylene).

A fairly common phenomenon in nanometer-scale devices is negative differential resistance (NDR). This behaviour occurs in the region of negative slope on an I-V curve mapping resistance, where  $R = V/I$ , the differential resistance is less than zero. The differential or dynamic resistance is defined by

$$R_d = \frac{dV}{dI}$$

For negative differential resistance, the resistance itself will always be positive, but the differential resistance does not necessarily have to be. This means that the current goes down when the voltage is increased.

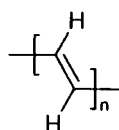
A specific type of oligo(1,4-phenylene ethynylene) containing active amino or nitro redox centers and terminated with thioacetyl alligator clips have been shown to have NDR which is manifested as an interband tunneling between the valence band and the conduction band.<sup>26</sup> NDR is characterised as a plateau or decrease in current with increasing voltage before there is an increase in current. This behaviour has been linked to multi-state memory and logic devices. The presence of either the amino or nitro redox centers is crucial for the observance of NDR behaviour.<sup>27</sup>

A possible mechanism for NDR is a two step reduction process that modifies charge transport through the molecule.<sup>27</sup> As the voltage increases the molecule initially undergoes a one-electron reduction, turning so as to align the phenyl rings on the conduction channel, a further voltage increase causes a second-electron reduction with subsequent blocking of the current. It is postulated that the planarity of the PPEs leads to better packing in the self assembly of the layer and the alkynes permit significant overlap of the  $\pi$ -orbital system even with small distortions from planarity, increasing the delocalisation of the molecular orbitals.<sup>26</sup>

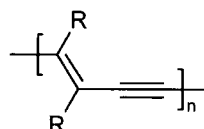
### 1.3.2. Poly(triacetylene)

The chemical and physical properties of various polyacetylenes<sup>28, 29</sup> and poly(diacetylenes)<sup>30</sup> have been extensively studied,<sup>31</sup> whereas much less is known about poly(triacetylenes) (PTA) (**Figure 5**). Peralknylated building blocks containing the 3,4-diethynylhex-3-ene-1,5-diyne (1,1,2,2-tetraethynylethene) moiety can be used as a building block to afford oligomers and polymers with PTA backbone.<sup>32</sup>

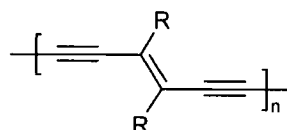
*Trans* – Polyacetylene (PA)



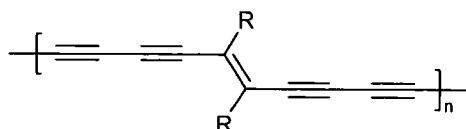
*Trans* – Poly(diacetylene) (PDA)



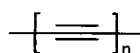
*Trans* – Poly(triacetylene) (PTA)



*Trans* – Poly(pentaacetylene) (PPA)



Carbyne

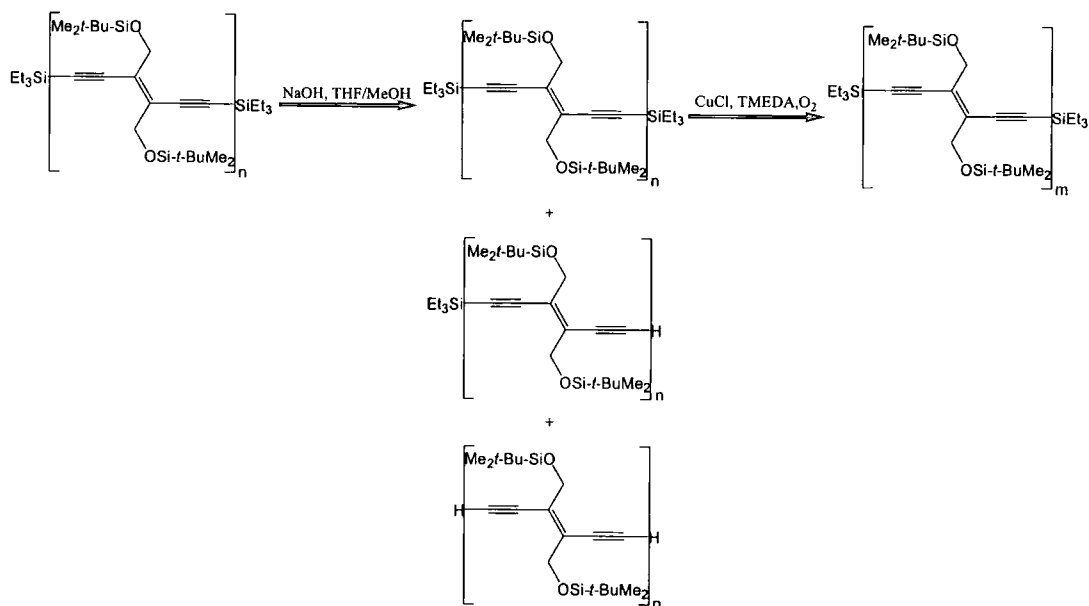


**Figure 5.** Progression of linear  $\pi$  – conjugated all – carbon backbones from *trans*-polyacetylene to carbyne.

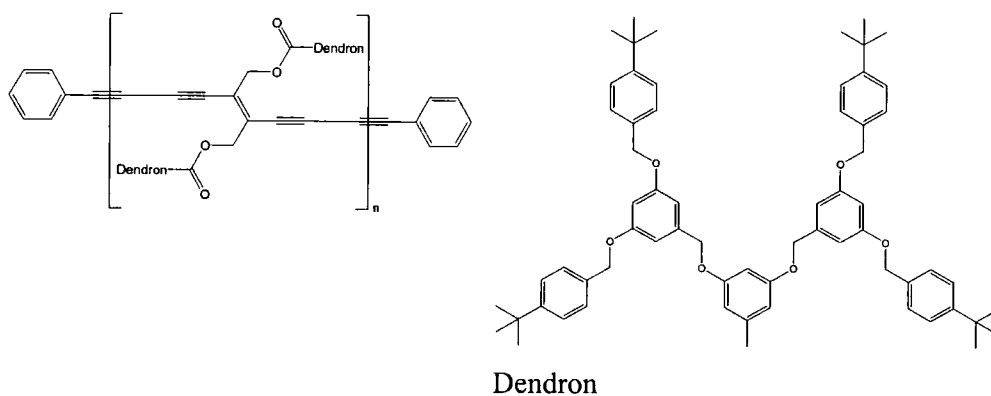
The additional acetylenic moiety in each repeat unit of polytriacetylene increases the spacing between latterly appended side chains thus reducing its ability to undergo intramolecular steric repulsions that cause distortions from planarity of the linear  $\pi$ -conjugated backbone.<sup>33</sup> The PTA molecule has been viewed as multianometer long  $\pi$ -conjugated rod like oligomers which have the potential to act as molecular wires spanning nanogaps.

The general strategy of the PTA oligomers synthesis (**Scheme 3**) relies on statistical deprotection of terminal triethylsilyl groups of suitable oligo(*trans*-enediyne) monomers. The deprotection step generates a mixture of mono and di-deprotected oligomers which then can be further oligomerised under oxidative Hay conditions.<sup>34</sup> Different end-caps can be introduced into the molecule during the Hay polymerisation step.<sup>34, 35</sup> Crystal structures of PTA type oligomers show preference of the planar backbones for the *s-trans* conformation with respect to the buta-1,3-diyndiyl moieties since this geometry accommodates the bulky lateral silyl groups. The  $\pi$ -conjugated system is perfectly planar, with only minimal squared sum deviations of the backbone C-atoms from the best plane.<sup>36</sup>

Lateral attachment of dendrons along the conjugated backbone of PTA oligomers, affords cylindrically shaped dendrimers which can be viewed as insulated molecular wires (**Figure 6**).<sup>37</sup> The insulating layer created by the dendrons protects and stabilises the central conjugated backbone, but does not result in a loss of  $\pi$ -conjugation despite the distortion from planarity as a consequence of steric compression of the bulky dendritic side chains.<sup>37</sup> Electron conjugation of the backbone is not the result of orbital overlap within a specific plane but rather from cylindrical orbitals. Overlap is therefore maintained upon rotation about  $C_{sp}$ - $C_{sp}$  and  $C_{sp}$ - $C_{sp^2}$  single bonds which has a very small rotation barrier.<sup>36</sup> It was determined that for this type of linearly conjugated polymer the effective conjugation length was 7-10 monomeric units. However, a 24 unit long oligomer (17.8 nm) has been synthesised which is the longest known molecular rod comprised of fully conjugated non-aromatic carbon backbone.<sup>36, 38</sup>



**Scheme 3.** Synthesis of PTA oligomers by statistical deprotection-oligomerisation sequence.



**Figure 6.** Molecular oligodiyne wires with lateral second generation dendritic side chains.

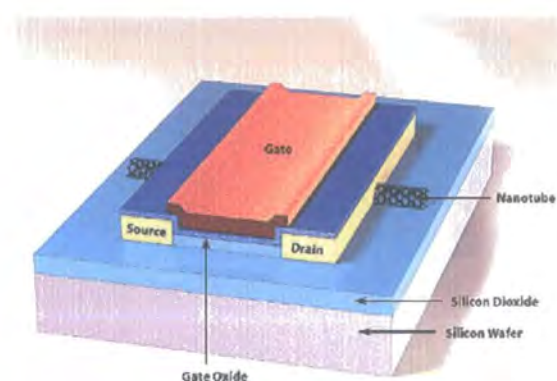
Another example of an insulated molecular wire involves a double helical insulated complex  $(C_6F_5)((CH_2)_6CH=CH_2)Ph_2Pt-(C\equiv C)_4-Pt((CH_2)_6CH=CH_2)Ph_2(C_6F_5)$  which will be discussed in section 1.3.4.

### 1.3.3. Carbon Nanotubes

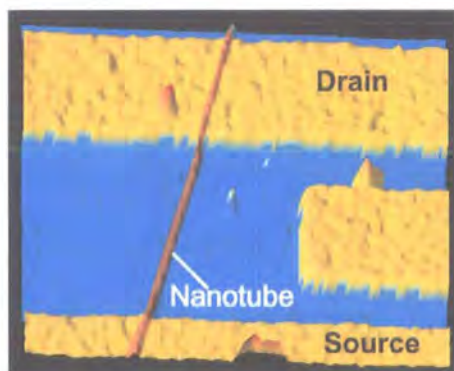
Ever since their discovery, carbon nanotubes have been regarded as possible candidates for potential micro electronic components due to their electrical properties and mechanical stiffness. A carbon nanotube can be thought of as a graphitic sheet rolled to create a seamless cylinder.<sup>39</sup> The majority of work on carbon nanotubes has been performed on single walled nanotubes which display simpler relationships between their electronic properties and structure than multi walled nanotubes. Conducting carbon nanotubes have the advantage of having minimal resistance and the possibility of tuning their conductance by changing their diameter, wrapping angle and the mechanical stress applied to them. The disadvantages of these materials as components in electronic devices lie in the inability to selectively prepare nanotubes of defined length, as well as the presence of impurities from most preparations which leads to conduction problems.<sup>40</sup> Electrical measurements carbon nanotube transistors indicate that it behaves as a traditional semiconductor device.<sup>41</sup>

A basic structure of a field effect transistor involves two metal electrodes designated as source and drain, connected by a semiconducting channel. In conventional devices, the channel is made of silicon, but can be replaced by carbon nanotubes. A third electrode, the gate, is separated from the channel by a thin insulating film. Normally, if no charge is placed on the gate, then no charge will flow into the channel. Application of potential to the gate causes a charge flow in the channel, resulting in a change from an insulating to conducting state allowing current to pass between the source and the drain. Similar devices have also been constructed using a “top gated” architecture (**Figure 7**). Carbon nanotubes can behave as a field effect transistor when they are positioned so as to bridge two noble metal electrodes which act as source and drain. The electrodes were fabricated on top of a SiO<sub>2</sub> film grown on a silicon wafer and the wafer itself used as the gate electrode (**Figure 8**).<sup>42</sup>





**Figure 7.** Schematic of a top gated carbon nanotube field effect transistor.<sup>39</sup>



**Figure 8.** Carbon nanotube on top to bridge two noble metal electrodes.<sup>39</sup>

Carbon nanotubes field effect transistors have excellent operating characteristics that are as good as or better than state of the art silicon devices. However, there are still problems that need to be addressed, such as electron conduction that occurs when defects are present within the nanotubes.

#### 1.3.4. Metal Capped Carbyne

Elemental carbon chains constitute the simplest molecular wire,<sup>43</sup> and have been utilised as a building block for use in the assembly of polymetallic structures. Polycarbon moieties based on a carbon spacer  $-(C\equiv C)_n-$  have the

ability to coordinate to metals *via* a  $\sigma$  or  $\pi$  manner, and to mediate electron flow between the two redox centres. When termini possessing different redox states are present at both ends of the spacer, an odd electron-containing species or mixed-valence compound can be generated electrochemically, allowing the efficiency of the wires to be tested without the need to tether the molecule to an electrode.<sup>44</sup>

Mixed valence compounds are commonly dinuclear transition metal complexes, whose absorbance spectra are characterised by the presence of a weak intervalence charge transfer (ICT) band. The ICT band is characteristic of the optically induced intramolecular electron transfer in the NIR spectral domain which is absent in the spectra of the reduced and oxidised states.<sup>45</sup> Depending on the degree of delocalisation of the unpaired electron over both capping redox sites, a classification has been proposed by Robin and Day.<sup>46</sup> Materials are allocated into Class I, II or III depending on the strength of the electronic interaction between the sites of differing oxidation states, ranging from no interaction (Class I) through modest interaction (Class II) to very strong electronic coupling (Class III).<sup>47, 48</sup>

A mixed valence compound belonging to Class I is totally localised, has no through bridge interaction between the two redox termini, and no ICT band can be observed. Class II mixed valence compounds show interaction between the two redox termini, giving rise to an ICT band, but the interaction is sufficiently weak so as to localise the charge. For Class II molecules often the ICT band is solvent dependent. A complex is classified as Class III if the electron is fully delocalised and the system possesses its own unique properties. Generally the ICT band shows limited solvatochromism, and the difference in redox couple potentials ( $\Delta E$ ), where  $\Delta E = E_{M2} - E_{M1}$ , is larger than 200 mV as observed in the cyclic voltammetry trace. These materials generally possess novel optical and electronic properties in addition to those of the separate sites. Solvatochromism of the ICT band depends on the localisation of the orbitals involved in the transition in much

the same way as any electronic absorption may be affected by solvent environment.<sup>49</sup>

An evaluation of the strength of electronic interaction through a given bridge can be made using the free energy of comproportionation,  $\Delta G_c$ , according to the comproportionation equilibrium, which also defines the comproportionation constant  $K_c$  from the reaction:<sup>50</sup>



$\Delta G_c$  can be determined experimentally by cyclic voltammetry and relating  $\Delta E$  to  $\Delta G_c$  via the Nernst equation,  $\Delta G_c = -nF\Delta E$ . The magnitude of  $K_c$  is determined by the sum of all energy factors such as through bridge and through space electronic interaction, solvation, steric interaction or structural distortions, relating to the stability of the reactant and product complexes and is given by the expression:<sup>50</sup>

$$K_c = \exp \left( \frac{nF\Delta E}{RT} \right)$$

Consequently the  $K_c$  value indicates the thermodynamic stability of the mixed valence species, but cannot solely be attributed to the through bridge interaction, which is a value that is described by  $H_{ab}$ .

$H_{ab}$  is a very informative parameter with regard to charge delocalisation in the molecule which allows comparison between similar sets of compounds to be made. From the spectral characteristics of the ICT band in the UV absorption, the calculation of  $H_{ab}$  can be performed depending on the class of the mixed valence compound in the Robin and Day classification.<sup>46</sup> Only the calculation of  $H_{ab}$  for a Class III compounds will be described due to the interest in these compounds in molecular electronics. The value of  $H_{ab}$  for Class III compounds, where electronic delocalisation is optimal, can be approximated according to the equation:<sup>51</sup>

$$H_{ab} = \bar{\nu}_{\max}/2$$

In the ideal case of a Class III complex, the electron is delocalised in one molecular orbital that spreads over the whole molecule. The observed ICT does not involve directional charge transfer (unless the molecule is non-symmetrical) but corresponds to a low-energy molecular transition between delocalised levels.<sup>52</sup> The bandwidths of Class III complexes at half height ( $\Delta\bar{\nu}_{1/2}$ ) are much narrower than predicted based on the equation

$$\Delta\bar{\nu}_{1/2} = [2310\bar{\nu}_{\max}]^{1/2}$$

which has been derived for Class II complexes. The Class III case is characterised by a distinct asymmetry in the band shape, a consequence of the so-called band “cut-off” at  $h\bar{\nu}_{\max} = 2H_{ab}$ .<sup>48</sup>

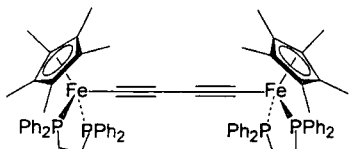
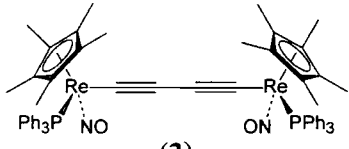
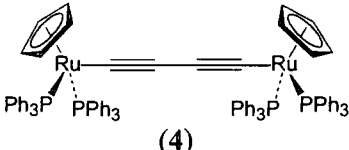
Symmetrical bimetallic complexes linked by a sp carbon chain leading to compounds with a general formula of  $L_nM-C_x-ML_n$  have the possibility to exist in a various numbers of redox states which differ by one electron increments in the case of even carbon chains. The example of  $[\{Fe(dppe)_2Cp^*\}_2(\mu-C\equiv C-C\equiv C)]$  (**2**),  $[\{Re(PPh_3)NOCp^*\}_2(\mu-C\equiv C-C\equiv C)]$  (**3**), and  $[\{Ru(PPh_3)_2Cp\}_2(\mu-C\equiv C-C\equiv C)]$  (**4**) half sandwich complexes (**Table 1**) linked by a four carbon spacer will be discussed as their properties are representative of the group and there is an abundance of data in the literature. For a more comprehensive review of the area the reader is directed to the literature and references cited therein.<sup>44, 53, 54</sup>

The efficiency of bimetallic conjugated carbon complexes in transferring electrons from one metal terminus to another can be inferred from their electrochemical and spectroscopic properties (**Table 1**). The compounds **2**, **3**, and **4** all exhibit values large for  $K_c$  within approximately three order of magnitude.

The relatively large values for  $K_c$  observed for all three species indicate the presence of a strong exchange interaction between the two metal centres propagated through the  $-C\equiv C-C\equiv C-$  bridge. This reflects the extent of delocalisation between the metal centres in the ground state. The one dimensional alkyne chain acts as a molecular wire to convey the odd electron from one metal centre to the other.<sup>55</sup> Although **2** has the highest  $K_c$  value, this can be attributed to the fact that the iron end groups are more electron donating, which is also manifested in the fact that the diiron complexes are much easier to oxidise thermodynamically.<sup>55</sup>

Spectroscopic and theoretical studies have shown that the radical cations of the half sandwich bimetallic complexes have delocalised ground state electronic structures. The dicationic species of **2**, **3**, and **4** were synthesised *via* a chemical oxidation process. IR spectroscopy performed on the dication species of **2** indicated that the alkyne bridge remained in a single bond-triple bond form by the presence of a stretching frequency in the region  $1950-2160\text{ cm}^{-1}$ .<sup>55</sup> In contrast the doubly oxidised species of **3**<sup>63</sup> and **4**<sup>58, 61</sup> contains a cumulenenic structure. The IR active band for  $\nu(C=C)$  of  $[\{Ru(PPh_3)_2Cp\}_2(\mu-C=C=C=C)]^{2+}$  is observed near  $1740\text{ cm}^{-1}$ ,<sup>58</sup> while a Raman active band at  $1883\text{ cm}^{-1}$  was attributed to the carbon fragment of  $[\{Re(NO)(PPh_3)Cp^*\}_2(\mu-C=C=C=C)]^{2+}$ . The alkyne chain of the dication species of **2** has a higher triple bond character compared to the neutral species,<sup>55</sup> while the carbon chain for the dication of **3** and **4** shows full cumulenenic behaviour.<sup>58,61,63</sup>

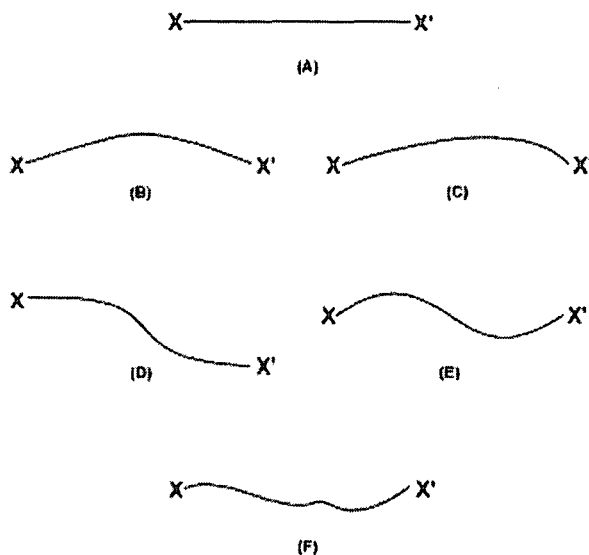
**Table 1.** Representative  $L_nM-C_x-M'L'_n$  complexes along with their electrochemical and spectroscopic properties. <sup>a</sup>All processes are one electron processes. ( $\Delta\nu_{1/2} = [2310 \bar{\nu}_{\max}]^{1/2}$ ;  $H_{AB} = \bar{\nu}_{\max}/2$ )

	Couple <sup>a</sup>	$\Delta E$ (V)	$K_c$	NIR $\lambda_{\max}$ (nm)	NIR $\epsilon$ (M <sup>-1</sup> cm <sup>-1</sup> )	$\Delta_{1/2}$ (observed) (cm <sup>-1</sup> )	$\Delta_{1/2}$ (calculated) (cm <sup>-1</sup> )	$H_{AB}$ (eV)
 (2)	Fe <sup>II</sup> -Fe <sup>III</sup> <sup>55</sup>	0.72	$1.6 \times 10^{12}$	1326	11700	3250	4220	0.47
	Fe <sup>III</sup> -Fe <sup>IV</sup> <sup>56</sup>	0.99	$5.9 \times 10^{16}$					
 (3)	Re <sup>I</sup> -Re <sup>II</sup> <sup>57</sup>	0.53	$1.1 \times 10^9$	883 1000 1200	15000 9400 3200	1500 1200 1800	4166 5000 5663	0.516 0.620 0.702
 (4)	Ru <sup>II</sup> -Ru <sup>III</sup> <sup>58</sup>	0.64	$1.5 \times 10^{11}$	877	8000	3600	5131	0.71
	Ru <sup>III</sup> -Ru <sup>IV</sup>	0.65	$1.5 \times 10^{11}$	819	900	3400	5308	0.76

Polyynes molecules can adopt linear, symmetric bow, unsymmetric bow, kinked, S-shaped, and random carbon chain conformations (**Figure 9**). Interestingly, bond angles do not provide a direct measure or a reliable qualitative indicator of carbon chain conformations. If the bending in a molecule always has the same directional sense, even when every bond angle is only slightly less than  $180^\circ$ , a distinctly curved system results. If the directional sense of the bending changes from bond to bond, giving a zigzag pattern, a much more linear system results.<sup>59</sup> The crystal structures obtained for the neutral bimetallic complexes **2**,<sup>55</sup> **3**,<sup>57</sup> and **4**<sup>60, 61</sup> show a carbon spacer comprising of alternating single bonds-triple bonds similar to those of butadiyne. There is no real appreciable bending of the carbon chains with all M-C<sub>4</sub>-M moieties having only a  $2^\circ$  to  $11^\circ$  deviation from linearity. In general a more pronounced curvature of the (C $\equiv$ C)<sub>n</sub> chain is observed as the carbon chain length increases. The exception to this is found for compounds carrying a (C<sub>6</sub>F<sub>5</sub>)(p-tol<sub>3</sub>P)<sub>2</sub>Pt end cap (**Scheme 4**), where the curvature for its C<sub>12</sub> compound is larger than that for its C<sub>16</sub> compound.<sup>62</sup> The carbon chains in the C<sub>12</sub> compound almost form a semicircle, while the carbon chains in the C<sub>16</sub> compound forms a slight S-shape.

In an effort to increase the lengths of alkyne spacers, fully characterised rhenium analogues of **3** have been made with C<sub>6</sub>, C<sub>8</sub>, C<sub>12</sub> and C<sub>16</sub> carbon spacers. In general the synthesis proceeds *via* a step-growth approach by employing acetylenic homo and cross-coupling procedures depending on the desired spacer length.<sup>64</sup> The methodology used to synthesise the aforementioned chain lengths failed to synthesise pure complexes containing chain lengths of C<sub>20</sub>.<sup>65</sup> The C<sub>8</sub> homologue of the half sandwich diiron complex,<sup>66</sup> and the C<sub>6</sub> homologue of the diruthenium complex have also been synthesised.<sup>60</sup> The curvature often associated with these longer chain species has been attributed to crystal packing effects.<sup>62, 67, 68</sup> An increase in the spacer chain length leads to a much more exposed carbon chain making it susceptible to intermolecular reactions, thus decreasing the stability of the molecule especially for compounds with electron rich termini.<sup>65, 69,</sup>

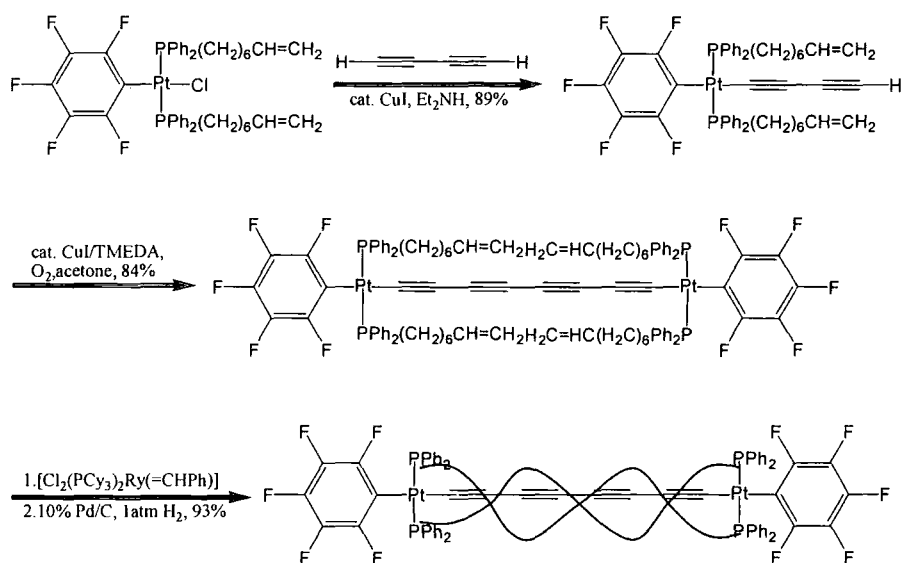
70



**Figure 9.** Types of carbon chain conformations: (A) linear, (B) symmetric bow, (C) unsymmetric bow, (D) kinked, (E) S-shaped, (F) random.<sup>59</sup>

In order to stabilise higher redox states of  $\text{M}-(\text{C}\equiv\text{C})_n-\text{M}$ , insulation of the exposed longer carbon chains was investigated. The metal end cap used was  $(\text{C}_6\text{F}_5)\text{Pt}$  since  $\text{C}_6\text{F}_5$  has been shown to increase Lewis acidity of the platinum and retard phosphine dissociation which is thought to cause oligomerisation. The two phosphane ligands on the platinum each contain hexamethylenevinyl  $((\text{CH}_2)_6\text{CH}=\text{CH}_2)$  groups.<sup>71, 72</sup> The complex was subjected to a copper catalysed reaction with a 1,3-butadiynyl complex, followed by a Hay coupling, and then a reaction with Grubbs ruthenium metathesis catalyst, and finally hydrogenation to give a double helical complex (**Scheme 4**). The resulting double helical structure can be viewed as a  $\text{sp}^3$  carbon chain which three dimensionally shields a  $\text{sp}$  carbon chain analogous to insulating a conventional wire. The  $\text{sp}^3$  chain has a barrier of rotation of 12 kcal/mol representing the measure of  $\text{sp}$  carbon chain protection.<sup>71</sup>





**Scheme 4.** Synthesis of a double helical complex  $[(\text{C}_6\text{F}_5)\text{Pt}(\text{PPh}_2)_2\text{C}\equiv\text{C}-\text{C}\equiv\text{C})_2((\text{CH}_2)_6\text{CH}=\text{CH})_2]$ .<sup>71</sup>

Attempts have been made to tune the level of electronic coupling of metal polynyl complexes by varying the endcaps of the molecule, and by inserting various spacers into the carbon chain. The different endcaps that have been used range from metal centres having electron donating character to those having electron withdrawing character, to changing one of the endcaps for an organic molecule containing donating/accepting properties. Metal centres that have been used include  $\text{Cp}(\text{PPh}_3)(\text{PMe}_3)\text{Ru}$ ,<sup>58</sup>  $\text{Ru}(\text{dppm})\text{Cp}^*$ ,  $\text{Ru}(\text{dppe})\text{Cp}^*$ ,<sup>61</sup>  $\text{Cp}^*(\text{NO})(\text{P}(p\text{-C}_6\text{H}_4\text{Me})_3)\text{Re}$ ,  $\text{Cp}^*(\text{NO})(\text{P}(p\text{-C}_6\text{H}_4'\text{Bu})_3)\text{Re}$ ,<sup>64</sup>  $\text{Cp}^*(\text{dppe})\text{Fe}$ <sup>56</sup> and  $\text{Cp}^*(\text{CO})_2\text{Fe}$ .<sup>73</sup> One of the most common organic endcap used is  $\text{C}_6\text{H}_4\text{-X}$ , where X is varied from electron withdrawing to electron donating moieties. These endcaps are used to illustrate preferential one way electron transfer which causes the molecule to act as a rectifying component, or as a polarised molecular wire.<sup>73</sup> In general an increase in electron donation properties of the ligands surrounding the metal results in a larger interaction of the end cap with the acetylene chain, giving these compounds stabilised oxidation states and defined spectroscopic signals.

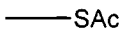
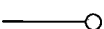
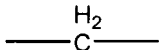

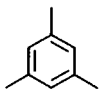
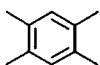
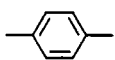
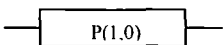
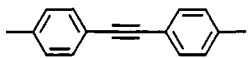
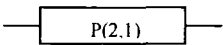
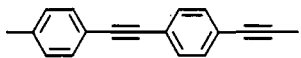
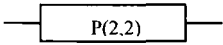
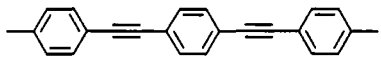
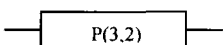
As the length of the carbon chain increases, there is a need to incorporate linkers to maintain the rigidity of the carbon chain, facilitate the synthetic process, increase the chemical stability of the compound, and increase the high level of electronic coupling. Popular spacers include 2,5-thiophene,<sup>69</sup> and 1,4-benzene.<sup>55</sup> <sup>60</sup> Insertion of a spacer does not always prove beneficial, and care must be taken to choose a spacer that is not detrimental to the strength of electronic coupling. An example of is shown by insertion of the 1,4-benzene spacer between the alkyne moieties of a diiron compound. This was found to reduce the electronic interactions between termini compared to the compound with no spacer as shown by the lowering of the  $K_c$  value.<sup>55</sup>

## 1.4. Molecular Junctions

At present, the conceivable implementations of molecular electronic technology will require a critical interface between the active molecular components and a solid (surface) electrode interface.<sup>74</sup> The construction of these molecule-surface interfaces and the issues of molecule-surface interactions are amongst the bigger obstacles to the realisation of molecular electronics technology. In order to maximise these molecule-macroscopic connections a reasonable level of integration within each functional molecular unit is desirable. It follows that in addition to molecular components such as wires and rectifiers, it will be necessary to develop molecular “junctions” capable of interconnecting these molecular components to permit the construction of more complicated devices such as molecular adders and other logic circuits.<sup>75</sup>

It has been proposed that different chemical combinations of oligo(phenylene ethynylene) (OPE), methylene and thioacetyl alligator clips can correspond to different functions in circuitry (**Table 2**).<sup>5</sup> Although transport through linear molecules has been tested, there are still problems involving testing of devices involving more than two termini.<sup>6</sup>

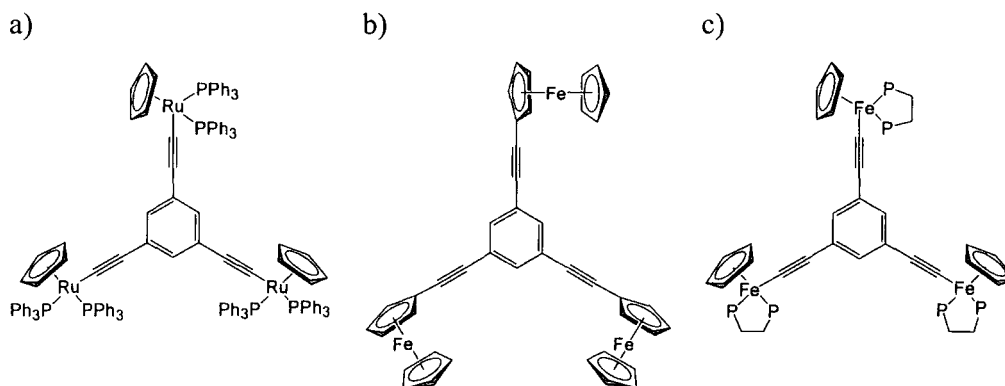
**Table 2.** Chemical symbols and their corresponding molecular circuit symbols.

Chemical Symbol	Molecular Circuit Symbol	Description
 SAc		Contact to input or output
		Transport barrier
	T-Junction	1,3,5-Trisubstituted benzene
	Q-Junction	1,2,4,5-Tetrasubstituted benzene
		1,4-Disubstituted benzene
		1,4-(Phenyl ethynylene)-1,4-phenylene
		1,4-(Phenyl ethynylene)-1,4-(phenylene ethynylene)
		1,4-(Phenyl ethynylene)-1,4-(phenylene ethynylene)-1,4-phenylene

Compounds carrying central ethynyl substituted benzene cores are of interest due to their geometry and active coordination sites. These cores enable simple reactions to be used in order to extend the molecule in several directions forming star shaped molecules as potential molecular junctions. In terms of molecular circuit symbols, 1,3,5-triethynyl substituted benzene can be considered as a T-junction, while 1,2,4,5-tetraethynyl substituted benzene can be considered as a Q-junction.

### 1.4.1. Substituted 1,3,5-triethynylbenzene

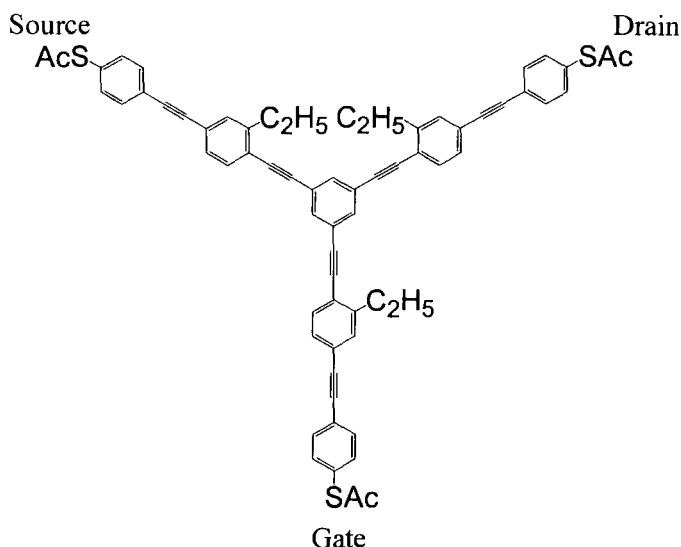
There have been numerous studies on compounds containing 1,3,5-triethynyl substituted benzene cores linked to metal endcaps. It was thought that metal acetylide complexes would possess delocalised  $\pi$ -systems which allow communication between coordinated metal centres.<sup>76, 77</sup> Various metal moieties such as  $\text{Cp}(\text{PPh}_3)_2\text{RuC}\equiv\text{C}-$  and  $\text{CpFeC}_5\text{H}_4\text{C}\equiv\text{C}-$  have been attached to a central 1,3,5-triethynyl benzene core (**Figure 10**).<sup>76</sup> The symmetrical compound  $[\{\text{Cp}(\text{PPh}_3)_2\text{RuC}\equiv\text{C}\}_3(1,3,5\text{-C}_6\text{H}_3)]$  (**Figure 10a**) undergoes three successive one electron oxidations which are reversible on a cyclic voltammetry time scale, but it decomposes at longer time scales resulting in relatively small comproportion constants for the first two oxidations.<sup>76</sup> In contrast, the compound  $[\{\text{CpFeC}_5\text{H}_4\text{C}\equiv\text{C}\}_3(1,3,5\text{-C}_6\text{H}_3)]$  (**Figure 10b**) gives no indication of communication between the  $\text{Fe(II)}$  metal centres.<sup>78, 79</sup> Despite the fact that  $[\{\text{CpFeC}_5\text{H}_4\text{C}\equiv\text{C}\}_3(1,3,5\text{-C}_6\text{H}_3)]$  contains multiple ferrocenyl subunits, the cyclic voltammetry displays only a single reversible anodic process. This implies that the central aryl nucleus does not allow the peripheral ferrocenyl subunits to communicate electronically with one another.<sup>79, 80</sup>



**Figure 10.** Depiction of a)  $[\{\text{Cp}(\text{PPh}_3)_2\text{RuC}\equiv\text{C}\}_3(1,3,5\text{-C}_6\text{H}_3)]$ ,  
 b)  $[\{\text{CpFeC}_5\text{H}_4\text{C}\equiv\text{C}\}_3(1,3,5\text{-C}_6\text{H}_3)]$ , and  
 c)  $[\{\text{Cp}^*(\text{dppe})\text{Fe}(\text{C}\equiv\text{C})\}_3(1,3,5\text{-C}_6\text{H}_3)][\text{PF}_6]_2$ .

The complex  $[\{\text{Cp}^*(\text{dppe})\text{Fe}(\text{C}\equiv\text{C})\}_3(1,3,5\text{-C}_6\text{H}_3)][\text{PF}_6]_2$  (**Figure 10c**) has been shown to have two distinct intervalence charge transfer bands which are attributed to two independent pathways of electron transfer *via* the singlet and triplet state of the mixed valence compound.<sup>80</sup> This phenomenon has been explained as the quantum interference effect,<sup>81, 82</sup> which is a cancellation effect that occurs due to contributions from two electron transfer paths. Each path implies a mixing of the metal orbitals with different ligand orbitals thus resulting in molecular orbitals exhibiting different symmetry. This effect has been observed in compounds with interactions in the *meta* position. Perhaps this is why it is still possible for complexes of *meta* substituted triethynyl benzene to have a small  $K_c$  value.<sup>81</sup> Related work in this area<sup>83-85</sup> have shown that all similar compounds suffer from the same problems of weak electronic communication between the metal centres making them unsatisfactory as a potential molecular wires or switches.

A purely organic potential molecular three terminal junction reminiscent of a molecular sized field effect transistor in which there is a source, drain, and gate with thioacetyl alligator clips has also been synthesised (**Figure 11**).<sup>86</sup> However, conduction studies have yet to be carried out, due to the need of a six probe testing array.<sup>87</sup>



**Figure 11.** 1,3,5-Triethynyl substituted benzene proposed to act as a molecular switch.

#### 1.4.2. Substituted 1,2,4,5-tetraethynylbenzene

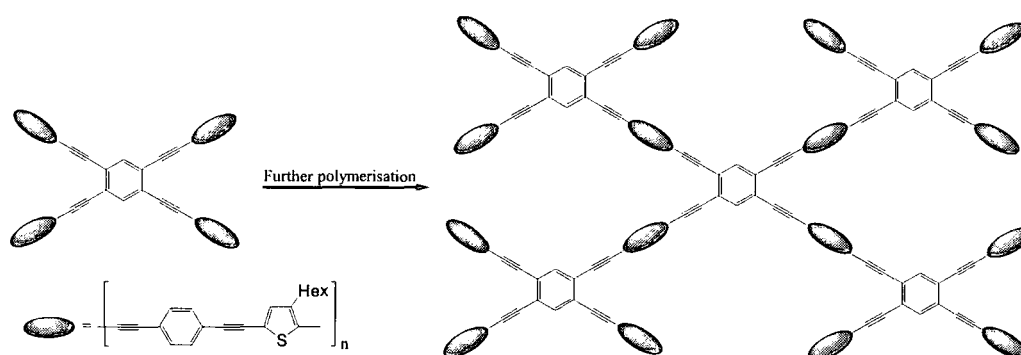
Because of the quantum interference effect observed for 1,3,5-trisubstituted benzene type compounds, the search for communication through an aromatic core turned to those involving a 1,2,4,5-tetrasubstituted benzene core which do not have the destructive *meta* effect. In studies to date, the 1,2,4,5-tetrasubstituted benzene compounds have usually been synthesised as a precursor to extended fused ring structures *via* electrophile induced cyclisation reactions<sup>88-90</sup> or as precursors to star shaped polymers.<sup>91, 92, 93</sup>

Fused polycyclic aromatics were synthesised by subjecting *p*-alkoxyphenylethynyl substituted aromatics to an electrophilic induced cyclisation reaction.<sup>89, 90</sup> The reaction may be affected by electrophiles such as trifluoroacetic acid or iodonium trifluoroacetate. The general requirement for fused polycyclic aromatics precursor systems, in addition to the carbocation directing group, is that the alkynyl group and the aromatic ring undergoing electrophilic substitution must

be *ortho*-substituted. The systems of particular interest are those containing *p*-alkoxyphenylethynyl-substituted aromatic pairs which are configured *para* to each other. The synthesis of this precursor commences at 1,4-dibromo-2,5-diiodobenzene, which was chosen due to the chemoselectivity of the iodide position to Pd-catalysed cross coupling reaction.<sup>89</sup>

Polycondensation between 1,4-diethynylbenzene and 2,5-diiodo-3-hexylthiophene under mild conditions results in the corresponding poly(arylene ethynylene) oligomer. This oligomer can be further reacted with 1,2,4,5-tetrahalobenzene to yield a new type of star-type branched polymer (**Figure 12**).<sup>91</sup> Other star-type compounds such as 1,4-diphenylethynylene-2,5-bis(*n*-hexyloxy)benzene and 1,4-diphenylethynylene-2,5-bis(*n*-dodecyloxy)benzene have also been synthesised for photoluminescent and electroluminescent applications.<sup>92</sup>

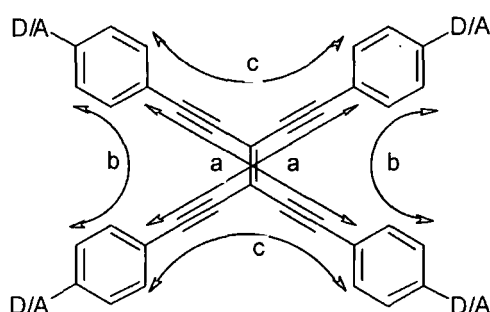
Only recently has there been interest in the utilising these types of compounds as molecular wires.<sup>75</sup> There has been very little work in the area of understanding the properties of 1,2,4,5-tetrasubstituted aryl compounds, especially for utilisation as a working model of molecular junctions and switches.



**Figure 12.** Model for star shaped polymers.

### 1.4.3. 1,1,2,2-Tetraethynylethene

A peralkynylated 1,1,2,2-tetraethynylethene allows a total of six conjugation pathways in two dimensions, which consist of two linear *cis*- and two linear *trans*-conjugation as well as two *geminal* cross-conjugation pathways (Figure 13). Both the *trans* and *cis* orientation provide one dimensional conjugation pathways, while the *geminal* orientation gives a two dimensional conjugation through a combination of four linear and two cross-conjugated paths.



**Figure 13.** The six possible conjugation pathways in 1,1,2,2-tetraethynylethene derivatives, a and b are *trans*- and *cis*- linear conjugation while c is a *geminal* conjugated pathway.

Intramolecular donor-acceptor interaction are more effective with *cis*- and *trans*-linearly conjugated electronic pathways rather than the *geminal* pathway.<sup>94</sup> This property was determined by observing the magnitude of donor-acceptor conjugation *via* UV-Vis spectroscopy where all donor-acceptor substituted 1,1,2,2-tetraethynylethenes display broad absorption bands at lower energies than those expected for intramolecular charge transition. The result of this study shows the *trans/cis* substituted donor acceptor 1,1,2,2-tetraethynylethenes have larger bathochromic shift for their charge transfer band compared to the *geminal* isomer indicating a more efficient conjugation pathway.<sup>95</sup>



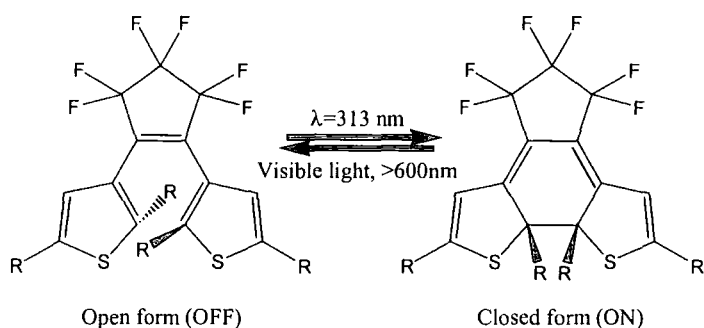
## 1.5. Molecular Switches

Molecular switches are systems that possess two or more reversible bistable states. A wide variety of molecular properties can be utilised to effect switching, including structural, electronic, optical absorption, luminescent and magnetic changes, while the different switching conditions include chemical, thermal, optical and electrochemical stimuli.<sup>15</sup>

### 1.5.1. Photoresponse Based Switch

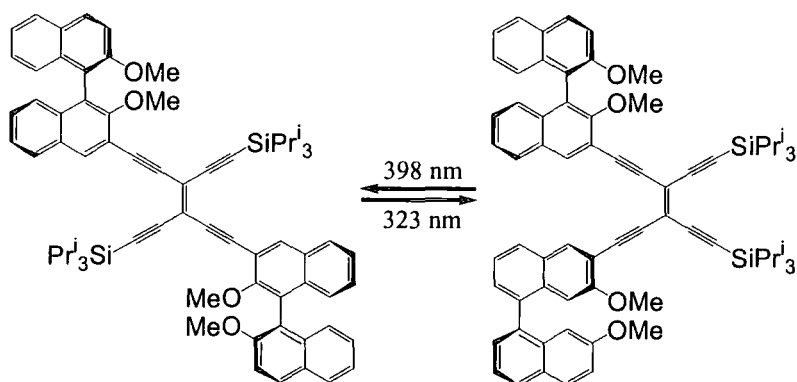
Since conductivity of a molecular wire relies on the conjugated  $\pi$ -system within the molecular candidate, any change in the system that interrupts the  $\pi$ -system and reduces conductivity can be considered a switching mechanism. Switching based on photoresponsivity of the molecule are particularly attractive since light allows for a fast and clean interconversion process in the absence of thermal back reactions.<sup>96</sup>

One popular switch that has been utilised is based on the reversible isomerisation of 1,2-bis-(3-thienyl)ethene derivatives (**Figure 14**).<sup>97-101</sup> This core unit has been shown to have good quantum yield as well as remarkable fatigue resistance. The initial open form, where the conjugation pathway is interrupted can be converted to the closed form by irradiation with UV light at 313 nm resulting in a planar conjugated wire which is the ON position (**Figure 14**). This process can be reversed on irradiation of visible light having a wavelength larger than 600 nm, as seen by the recovery of the original UV absorption spectra.



**Figure 14.** Light induced photoisomerism of 1,2-bis-(3-thiyl)ethane core.

One of the most interesting properties of arylated 1,1,2,2-tetraethynylethenes is their ability to undergo reversible photochemical *cis-trans* and *trans-cis* isomerisation.<sup>96</sup> Since both isomer forms benefit from strain free planarity, the process is not accompanied by undesirable thermal isomerisation. One example of a fully reversible molecular photoswitch is based on a 1,1,2,2-tetraethynylethene core containing (R)-1,1'-binaphthalene functionalisation (**Figure 15**). The two states can be interconverted in  $\text{CH}_2\text{Cl}_2$  solutions with light having a wavelength 323 or 398 nm.<sup>96</sup>

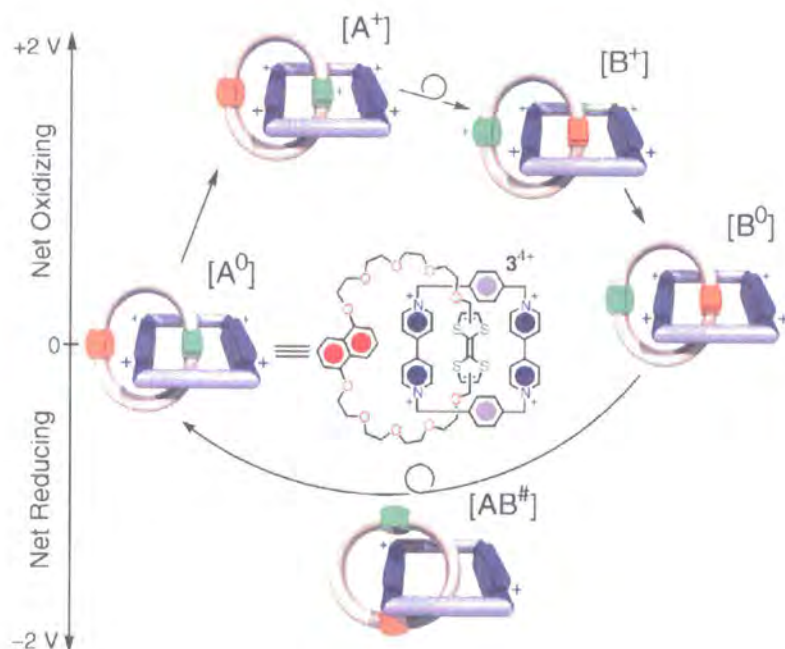


**Figure 15.** A novel fully light driven molecular switch based on a 1,1,2,2-tetraethynylethene core.<sup>96</sup>

### 1.5.2. Topological Rearrangement Based Switch

A different class of molecular switch involves compounds whose component parts can undergo spatial reorganisation with respect to one another without cleavage of bonds. An attractive class of molecule to study for this type of switching are rotaxanes<sup>102, 103</sup> and catenates<sup>7</sup> in which one part of the complex can move with respect to the other part of the complex due to an alteration in redox potential or pH.<sup>104</sup>

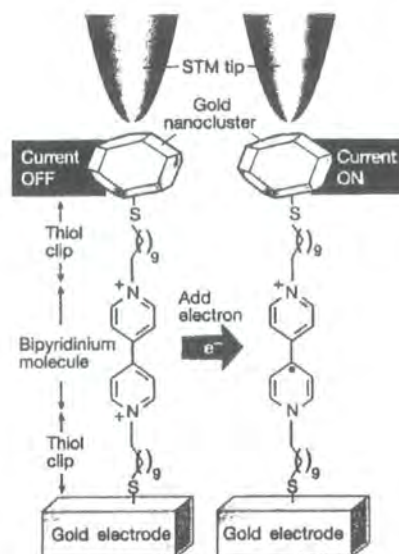
To illustrate the behaviour of these type of compounds the example of a catenate that undergoes conformational change due to an alternation in redox potential is taken (**Figure 16**). The catenate contains a TTF unit and a 1,5-dioxynaphthalene (1/5DN) ring system interlocked with another ring system containing cyclobis(paraquat-*p*-phenylene) (CBPQT<sup>4+</sup>). The design of the catenate is based on the fact that in solution, polyether chains carrying TTF derivatives exhibit extremely strong binding towards CBPQT<sup>4+</sup>, while systems containing 1/5DN are more weakly bound. The TTF units are readily oxidisable, while in contrast the 1/5DN units are quite difficult to oxidise. In solutions the CBPQT<sup>4+</sup> component resides preferentially around the TTF, and upon oxidation the polyether component circumrotates with respect to the CBPQT<sup>4+</sup> component so that the 1/5DN ring system occupies this cavity.



**Figure 16.** Proposed mechanochemical mechanism of the device fabrication from a bistable [2]catenate.

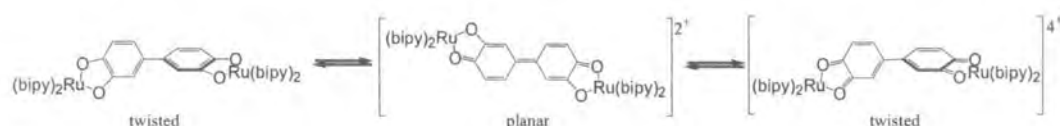
### 1.5.3. Redox Based Switch

Molecules containing redox centers whose oxidation number and hence electronic structure can be changed reversibly have considerable potential as switches. It has been demonstrated that in a complex containing a functionalised polymethylene chain with a central reversibly reducible bipyridinium (bipy) sandwiched between a gold nanocluster and a gold electrode, control of electron transport between gold contacts can be achieved by changing the redox state of the bipy moiety (**Figure 17**).<sup>105, 106</sup> When the bipy molecule is in its oxidised  $\text{bipy}^{2+}$  state no current can flow, however, when voltage is applied, the  $\text{bipy}^{2+}$  is reduced to  $\text{bipy}^+$ , and a large current flows as measured by STM.



**Figure 17.** A switch that works by changing a chemical state of a molecule.<sup>106</sup>

An example of a switch that utilises both conformational control as well as electrochemical means involves a complex containing 3,3',4,4'-tetrahydroxybiphenyl as a bridging ligand. The bridging ligand can change conformation from planar (conducting form) to non-planar (insulating form) (**Figure 18**) depending on its oxidation state. In the neutral and +4 state the molecule adopts a twisted form but in the +2 state the double bond between the rings confers a planarity to the system.<sup>107</sup>

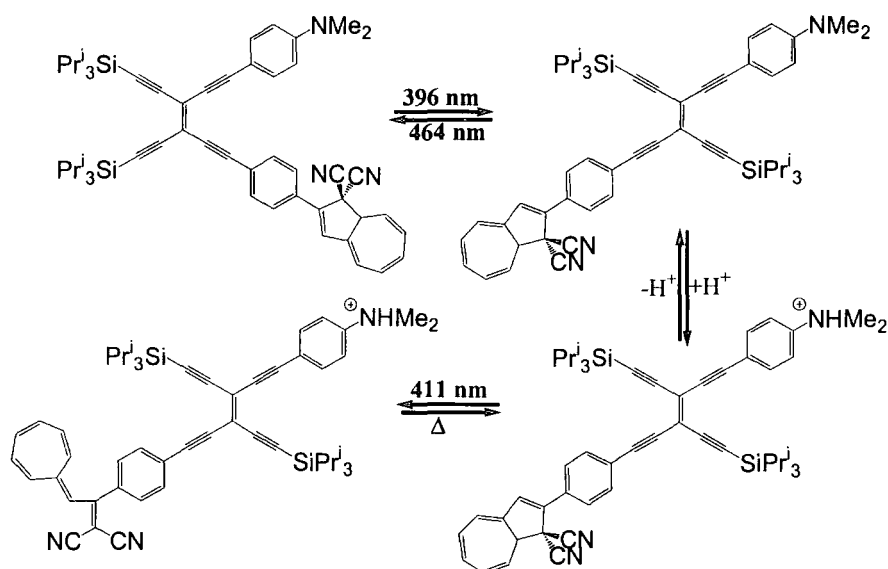


**Figure 18.** A redox switch based on changes in the conjugated pathway.

## 1.6. Molecular Logic Devices

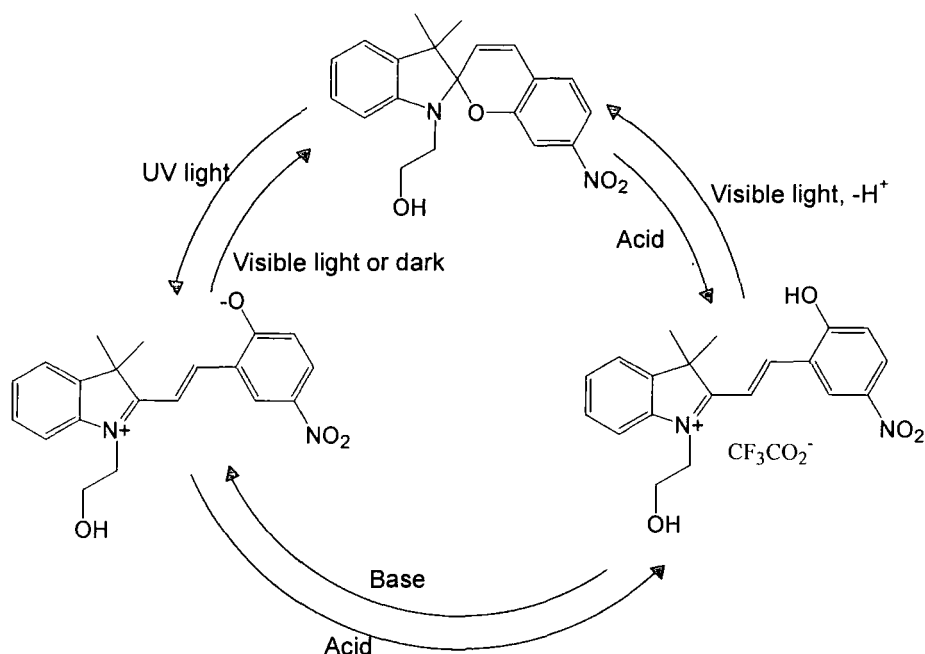
If the definition of switching is extended from controlling electron flow in a circuit to a more general one of bistable molecules that can be interconverted between two states then the area of logic gates is reached. The binary logic of computing is based on bits that can be written and read as 0 or 1. In positive logic, 0 represents a signal that is below a defined threshold, while 1 represents signal above the threshold.<sup>108</sup> A possible area in which such bistable molecule could be used is optical data storage, where each molecule would store one bit of information. This requires the molecule to be able to form uniform arrays and be individually addressable. When two or more logical functions (independently switchable 0/1 processes) are combined in a single molecule, sophisticated behaviour reminiscent of the logic gates used as electronic components start to emerge.<sup>15</sup>

One such example of a logic gate, which is also a three way chromophoric switch, possesses a 1,1,2,2-tetraethynylethene core, with a variety of peripheral subunits (**Figure 19**).<sup>109</sup> This switch contains three addressable subunits: a central bond that can undergo *cis-trans* isomerisation (logical 0 to logical 1), a dihydroazulene unit (0) that can convert to a vinylheptafulvalene (1) upon irradiation, and a proton sensitive N,N-dimethylanilino group (0=deprotonated, 1=protonated). The presence of three switchable units means that the molecule can exist in eight principal different states. It has also been demonstrated that the photoreversible switching between the dihydroazulene and vinylheptafulvalene can occur on the femtosecond time scale leading to potential ultrafast logic functions.<sup>110</sup>



**Figure 19.** Three way chromophoric molecular switch.<sup>109</sup>

Another three state molecular switch based on spiropyran has been developed to respond to two optical inputs and one chemical input producing two possible optical outputs (**Figure 20**).<sup>111</sup> The colourless spiropyran switches to merocyanine upon irradiation with UV light, which upon treatment of acid protonates, then converts back to the spiropyran upon irradiation with visible light. In the alternative cycle, the starting spiropyran is treated with acid to form the protonated merocyanine, is deprotonated with base, and converted back to the spiropyran by irradiation of visible light.<sup>112</sup>



**Figure 20.** Three state molecular switch.<sup>112</sup>

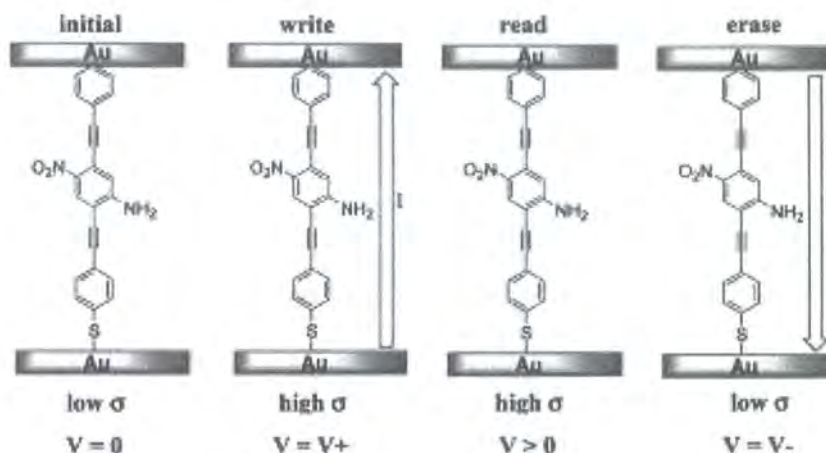
## 1.7. Memory Devices/Data Storage

A redox active OPE in a self assembled nanoscale molecular device has been demonstrated to have charge storage capabilities and hence the potential to operate as a molecular dynamic random access memory (mDRAM).<sup>113</sup> This memory device operates by storage of a high or low conductivity state. Electronic measurements were performed in a nanostructure that had a metal top contact, a SAM active region and a metal bottom contact.<sup>114</sup>

The read, write and erase sequence for the redox active OPE (**Figure 21**) illustrates an initially low-conductivity (low  $\sigma$ ) state which is charged (written) into a high conductivity (high  $\sigma$ ) state upon application of a voltage pulse. The high conductivity state persists as a stored bit which is read in the low voltage region, and is unaffected by subsequent read pulses.<sup>113</sup> The negative pulse erases the bit, resetting the cell. This ability to program, read and refresh the state of the



molecular device accomplish the functionality of a RAM. This effect was only observed for nitro containing oligo(1,4-phenylene ethynylene), and can persisted up to a temperature of 260 K.<sup>113</sup>



**Figure 21.** Write, read, and erase sequence of a redox active oligo(1,4-phenylene ethynylene) and its use as a one-bit RAM. The arrows indicate the direction of current that flows during the write pulse.

## 1.8. Future challenges

Bottom-up design of electronic circuitry using molecular functional units is still in its infancy. While some dramatic results have been achieved, many challenges remain. Although single devices have been shown to function, connecting large numbers of devices to make a useful circuit has yet to be realised. Moreover, there needs to be a better understanding in the principles involved in self assembly of molecules to form a uniform layer, the manner in which single molecules can be addressed, as well as the surface chemistry for attachment of molecules in a controlled, and directional manner.

## Chapter 2. Synthesis and Photophysics of Ethynylated Aromatic Systems

### 2.1. Ethynylated Aromatic Systems as Potential Molecular Wires

The construction of large molecular structures and connectors from smaller components has been compared to assembling devices with a molecular construction set, and many types of molecular rods and connectors have been synthesised for this purpose.<sup>75, 115</sup> Many of these molecular assemblies have served as model systems with which to study fundamental issues such as electron transfer, donor-acceptor conjugation circuitry, nonlinear optic (NLO) behaviour and liquid crystallinity, and play an important role in establishing design roles for molecular electronics and nanotechnology.<sup>116</sup> The rational design of these molecular building blocks therefore plays a crucial role in the construction of molecular architectures. The acetylene moiety is a useful connecting unit since its structural linearity does not suffer fluctuation due to *cis-trans* isomerisation processes found in alkene based systems, it has a small steric demand, and there are numerous synthetic methods already in place to connect the  $sp^2$  or  $sp$  carbon to an  $sp^2$  or  $sp$  carbon centre.<sup>117-121</sup> Also due to the isotropic distribution of the  $\pi$ -electrons along the C-C axis,<sup>122</sup> acetylenic linkages are capable of transmitting electronic perturbation efficiently making it a good molecular wire.<sup>38, 123, 124</sup> These linkages also provide space between adjacent aromatic rings so that they do not sterically interact, as in biphenyl.<sup>125</sup>

Consequently, many ethynylated aromatic systems, such as 1,4-bis(phenylethynyl)benzenes, 9,10-bis(phenylethynyl)anthracenes, 2,5-bis(phenylethynyl)thiophenes, and 2,5-bis(phenylethynyl) metallacylopentadienes, have been studied and found to display interesting structural, electronic, nonlinear optical, and luminescent properties. The stiff, linear nature of these compounds often results in liquid-crystalline behavior,<sup>124</sup> and it is interesting to note that

many of the models used to rationalise the phase behavior assume cylindrical symmetry along the ethynyl axis. The fluorescent and electroluminescent properties of both molecular and polymeric systems based upon these motifs have prompted speculation about the suitability of these compounds for alternatives to poly-(phenylene)vinylene (PPV) as emitting layers in electroluminescent devices.<sup>124</sup> In addition the conjugated  $\pi$ -system has led to the development of molecular wire-like architectures,<sup>86</sup> for which remarkably low resistivities have been measured.<sup>20, 126</sup> The origin of many of these fascinating properties may be directly attributed to the extended, linear  $\pi$ -conjugation that runs along the principal molecular axis which, at any point in time, is dependent upon the relative orientation of the planar aromatic moieties. Conductivity of molecular scale wires is thought to arise from intramolecular electron transfer processes facilitated by the delocalised  $\pi$ -backbone that extends over the entire molecule.

An ethynylated aromatic systems that has been tested for conductance is the thiolate form of **1** which can self assemble on gold (**Figure 3**) as has been discussed in section 1.3.1.<sup>19</sup> The stochastic on-off switching of the current observed in the STM images has been explained in terms of changes in ring conformation. Indeed, it has recently been claimed that conformational changes may be used to modify the conductive properties of a 1,4-bis(phenylethynyl)benzene derivative, giving rise to a molecular switch.<sup>127, 128</sup> Through a series of reports, the wire-like conduction, conformational dependent switching and negative differential resistance properties of this general class of material have been described.<sup>126</sup>

The HOMO-LUMO gap in these materials, and hence their emissive properties, will vary with the effective conjugation length, which in turn will alter their photo- and electroluminescence characteristics. While it is true that the barrier to rotation around the  $sp^2$ - $sp$  single bond is small for a single molecule that does not mean that the orbital arrangements are rotationally invariant. This is supported by semiempirical calculations which state that planarisation leads to a

minimisation of the HOMO-LUMO band gap thus leading to a red shift of the  $\lambda_{\text{max}}$  seen in the UV-vis spectra of oligo(phenylene ethynylenes).<sup>129</sup> To engineer molecular devices based upon conjugated frameworks, a firm grasp of the factors that control the geometry of the compound, and hence the  $\pi$ -conjugation pathway, in both the ground and excited states is required.

This chapter describes the synthetic organic phase of a long term project directed towards the construction of molecular scale electronic devices. The specific goals of this portion of the project were:

- a) to investigate synthetic methodologies for the preparation of 1,4-bis(arylethynyl)benzene derivatives in which relative rotation of the aromatic groups is sterically restricted, and examine the role of relative intra-ring orientation on the electronic structure of this “wire-like” motif,
- b) to investigate synthetic methodologies for preparation of 1,2,4,5-tetraethynyl substituted benzene derivatives, and assess the suitability of this motif as a four-way molecular junction.

## 2.2. Synthesis and Photophysics of Linear Ethynylated Aromatic Systems

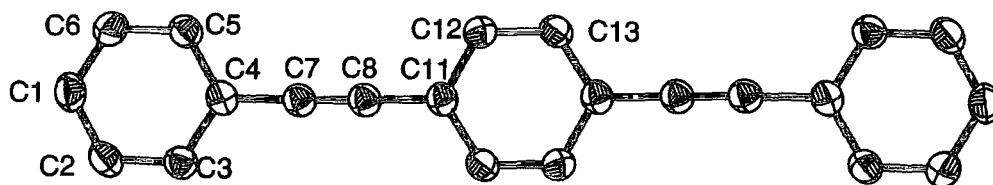
### 2.2.1. 1,4-*bis*(Phenylethynyl)benzene

The molecular structure of 1,4-*bis*(phenylethynyl)benzene (**5**) was confirmed by X-ray crystallography using single crystals grown from  $\text{CH}_2\text{Cl}_2:\text{MeOH}$  and one of the two molecules in the unit cell is shown in **Figure 22**.<sup>i</sup> The three aromatic rings are approximately co-planar, with the outer rings C(1)-C(6) and C(1')-C(6') rotated 5.36° and 0.41° with respect to the inner

---

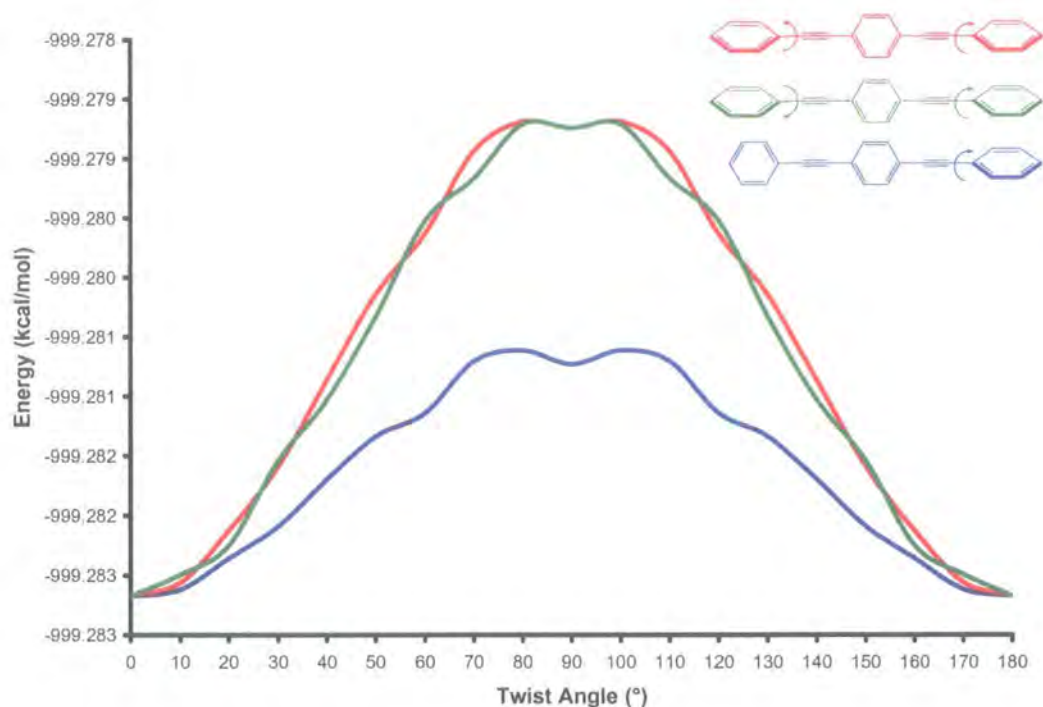
<sup>i</sup> Solid state molecular structure courtesy of T.B. Marder.

aromatic ring. The alkyne moieties connecting the outer and inner rings has a definite single-triple-single bond alteration with C(4)-C(7) 1.431(2) Å, C(7)-C(8) 1.205(2) Å, C(8)-C(11) 1.428(2) Å. The alkyne moieties connecting the rings are almost linear with a C(4)-C(7)-C(8) angle of 176.9(2)°, and a C(7)-C(8)-C(11) angle of 178.7(2)°. The molecule packs in a planar-perpendicular alternating motif.



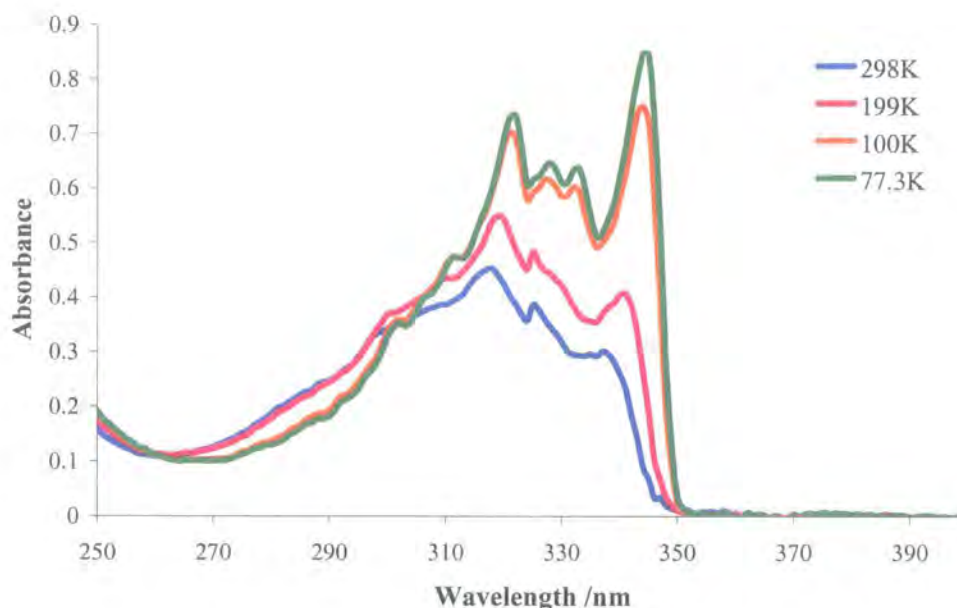
**Figure 22.** Molecular structure of **5** depicted with a 50% ellipsoid probability.  
Hydrogen atoms have been omitted for clarity.

The barrier to rotation about the alkyne-arene single bond in the ground state is low, allowing relatively free rotation about this bond unless the molecular motion is restricted by the environment, for example, as in an ordered monolayer or polymer matrix.<sup>130-132</sup> The calculated change in energy for **5** with varied rotation (0-90°) of either one or both of the outer aromatic rings with respect to a fixed orientation of the inner aromatic ring was performed using Gaussian98 at a B3LYP/6-31G\*\* level, and shows almost no change in energy with rotation, ca. 0.005 kcal/mol (**Figure 23**). The energy of the molecule at different rotations was taken after a single point energy calculation, starting from the planar geometry optimised structure of **5**. Thus, engineering control over the molecular conformation in materials derived from **5** for potential applications is a formidable challenge. Photo-excitation may offer one avenue for transient control over the conformation of the molecular skeleton although there is little information available regarding the nature of the molecular and electronic structure of the excited states of these materials.<sup>133, 134</sup>



**Figure 23.** Calculated change in energy for **5** with rotation.

Despite earlier reports claiming the existence of meta stable rotational conformers in dilute solution,<sup>133</sup> photophysical measurements of **5**, recorded in aerated cyclohexane at 283 K, indicate that **5** behaves in a conventional manner, with no evidence for aggregation, undergoing emission from the lowest vibrational level of the first excited singlet state.<sup>134</sup> In cyclohexane solution, the UV-vis spectrum of **5** features a series of partially resolved absorption bands between 250 and 350 nm, with a sharp band-edge at the red end of the absorption profile.<sup>135</sup> Upon lowering the temperature, the UV-Vis spectrum of **5** in ethyl pentane alcohol (EPA) shows a sharpening of the absorption profile with a significant increase in absorption at the red edge (**Figure 24**). It has been proposed that in the low-temperature glass there is a more limited range of conformations, with a greater bias toward the planar form. However, since the rotational barrier in the ground state is low, cooling to 77 K does not adequately reduce  $kT$  to limit the material to only the planar form.<sup>134</sup>

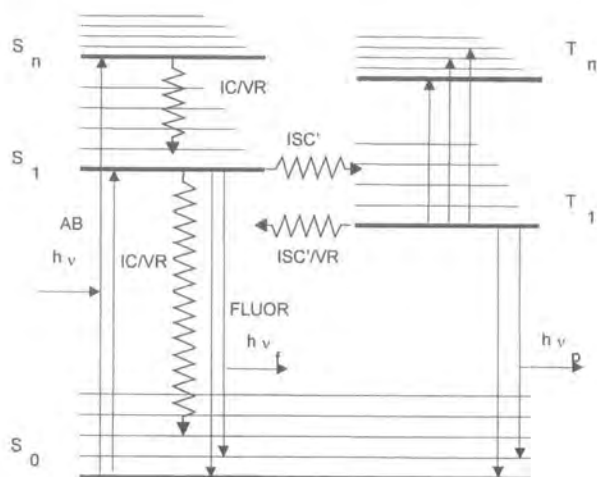


**Figure 24.** Variation temperature absorption spectra of **5**.<sup>ii</sup>

The electronic states of a molecule can be conveniently described in terms of a Jablonski diagram (**Figure 25**), and probed using a combination of absorption, emission and excitation spectroscopies. A simple absorption spectrum arises from transitions from the  $S_0$  ( $v = 0$ ) state to higher lying states. The emission spectrum is obtained by exciting the sample at a fixed wavelength ( $\lambda_{\text{ex}}$ ) and recording the intensity of emission as a function of wavelength,  $\lambda_{\text{em}}$ . It should be noted that Kasha's Rule states that the emission normally originates from the  $S_1(v = 0)$  state due to the rapid non-radiative relaxation of the higher lying  $S_n(v = m)$  states. Assuming a similar structure in the ground and  $S_1$  states, the similar vibrational structure of the  $S_0$  and  $S_1$  states leads to a mirror image relationship between the absorption and emission spectral profiles.

<sup>ii</sup> Absorption spectra courtesy of K. Findlay.





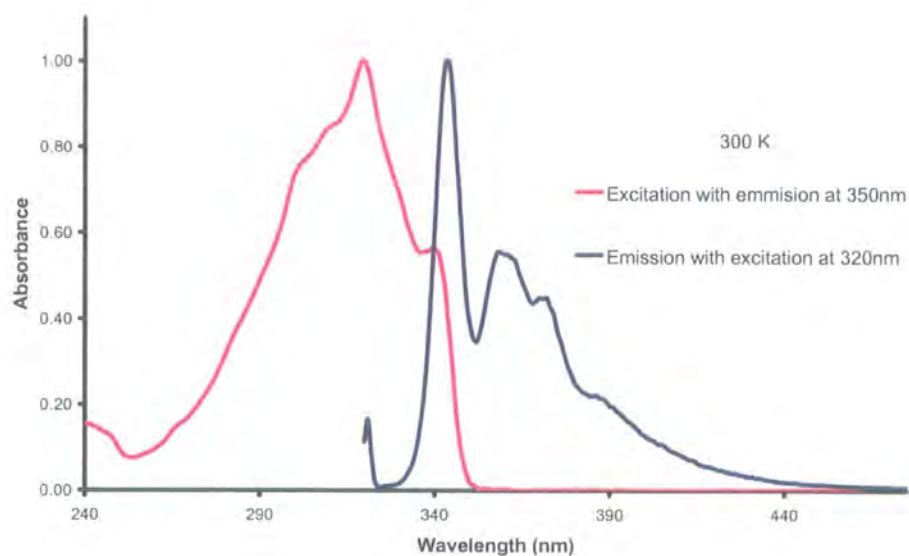
**Figure 25.** Jablonski diagram describing the electronic states of a molecule.

At 300 K, the absorption and excitation profiles of **5** in EPA are fairly featureless, and the emission spectrum is not a good approximation of the mirror image of either, indicating a different distribution of conformers in the ground and excited states (**Figure 26a**).<sup>134</sup> Upon lowering the temperature, there should be a limited range of conformations available in the ground state, with a greater bias toward the lowest energy (i.e. planar) form. At 77 K, the absorption and excitation spectrum of **5** are considerably sharper, and more closely form a mirror image of the emission spectrum, indicating similar distribution of conformers in the ground and excited states (**Figure 26b**).<sup>134</sup> In turn, this suggests that the lowest energy vibrational state of the S<sub>1</sub> state is planar.<sup>134</sup> These conclusions are in agreement with those found in the investigation of dynamics of the fluorescence of a substituted oligo(phenylene ethynylene).<sup>136</sup> The study indicated that rotational relaxation occurred very rapidly in the excited state, with a recorded time constant of 60 ps, interpreted in terms of a quadratic coupling model. Fast time-resolved emission spectroscopy was used to demonstrate that the blue edge of the emission shifted in a subtle fashion at early times after excitation, which lends to the evidence for the rapid planarisation of the excited state. There is a suggestion that the oligo(phenylene ethynylene) behaves as though the potential well is very

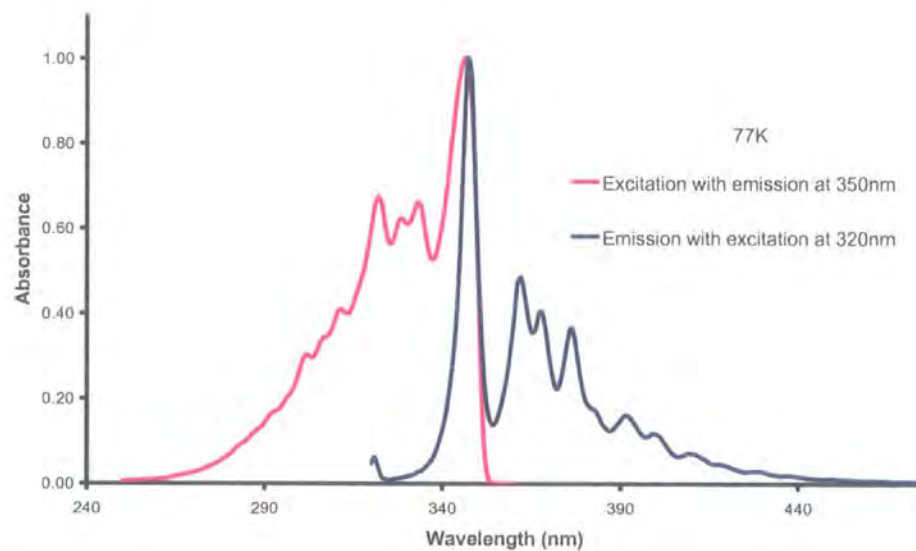


small in the ground electronic state but that in the first excited state the planar form is considerably more stable than the nonplanar conformers.<sup>136</sup>

a)



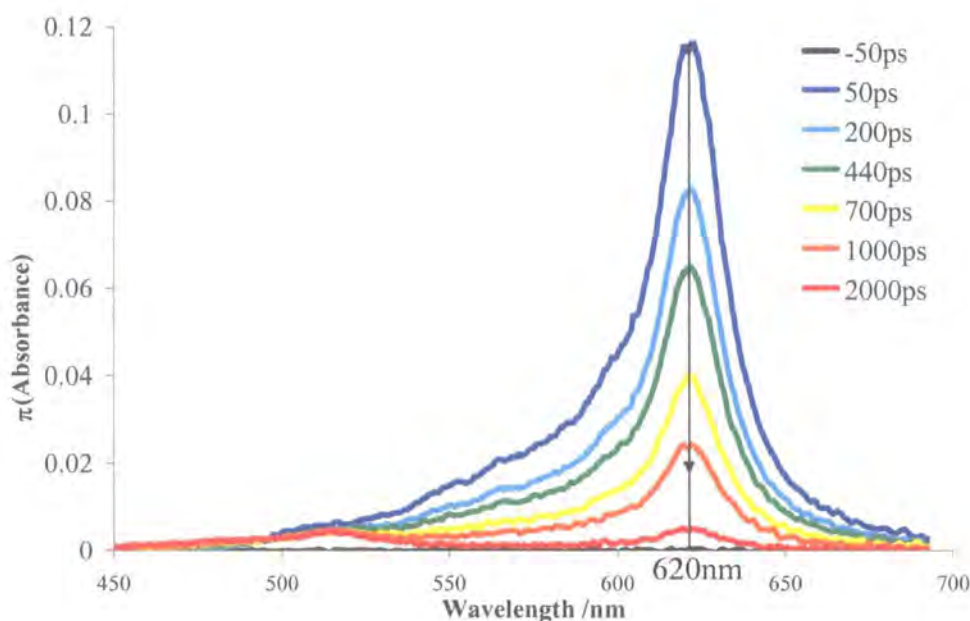
b)



**Figure 26.** Excitation and emission spectra of **5** at a) 300K and b) 77K.<sup>iii</sup>

<sup>iii</sup> Excitation and emission spectra courtesy of K. Findlay.

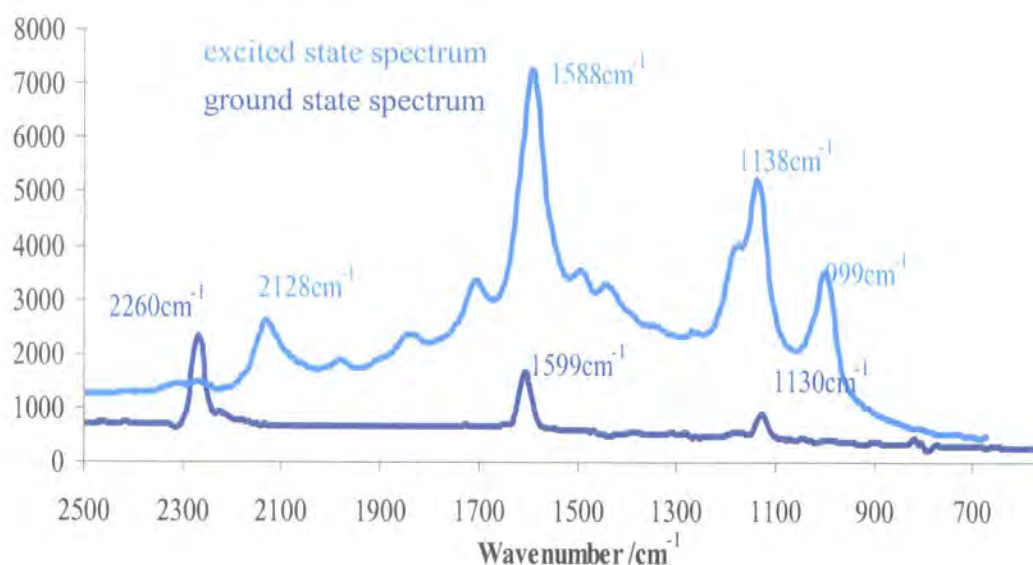
In order to establish the optimum wavelength for time-resolved resonance Raman spectra, the  $S_n \leftarrow S_1$  transient absorption spectra of **5** in cyclohexane solution were recorded by ultra-fast pump-probe spectroscopy. The spectra were collected from samples excited at 267 nm and probed in the range 450-700 nm. At early time intervals after excitation the transient absorption shows a strong band centred at 625 nm, which increased in intensity by ca. 20% and shifted to 620 nm over a 50 ps period, after which the absorption band decayed with a lifetime similar to the fluorescence lifetime (**Figure 27**).<sup>137</sup>



**Figure 27.** Transient absorbance spectra of **5**.<sup>iv</sup>

The non-resonance Raman spectrum of the ground electronic state of **5** as a dilute cyclohexane solution was obtained using 532 nm excitation (**Figure 28**) and shows the presence of three major bands centred at 2260, 1599 and 1130  $\text{cm}^{-1}$ .<sup>137</sup> The highest wavenumber band is associated with the localised vibrational motion of the acetylene groups, whilst that at ca. 1600  $\text{cm}^{-1}$  is assigned to the symmetric stretch of all three aromatic rings along the molecule's long axis.<sup>138</sup>

<sup>iv</sup> Transient absorbance spectra courtesy of A. Beeby.



**Figure 28.** The non-resonance Raman spectrum of the electronic ground state and the ps time-resolved resonance Raman spectra of the  $S_1$  state of **5**.<sup>v</sup>

The ps time-resolved resonance Raman (TR<sup>3</sup>) spectra of the  $S_1$  state of **5** were obtained by pumping at 267 nm and probing at 588 nm, to the blue of the transient absorption band. The TR<sup>3</sup> spectra also showed subtle, but distinct, changes during the first 50 ps following excitation. The spectrum of the  $S_1$  state of **5** shows bands at 2128, 1588, 1138 and 999  $\text{cm}^{-1}$  (**Figure 28**). The intensity of all of the bands increased by ca. 20-25% over the first 50 ps. This observation may be due to reorientation within the excited state changing the electronic structure and Raman excitation profiles. Hence, the Raman cross-sections may be dynamic shortly after excitation. After this initial rapid change the TR<sup>3</sup> signal decayed with a lifetime matching that of the singlet excited state.<sup>137</sup>

The profiles of the ground and  $S_1$  excited state Raman spectra are similar, indicating that there is little change in the bonding and electronic structure upon excitation. The decrease in the frequency of the (C≡C) band to 2128  $\text{cm}^{-1}$  is indicative of a small reduction in the bond strength of the acetylene moiety in the

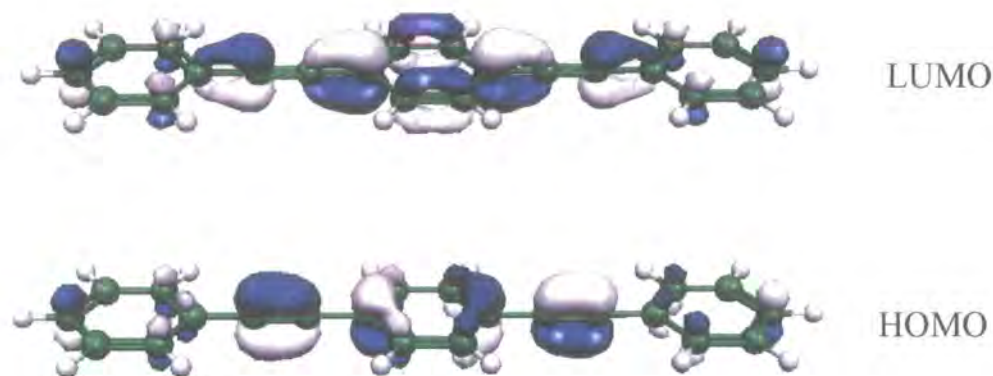
<sup>v</sup> Pico-second TR<sup>3</sup> courtesy of A. Beeby.

excited state.<sup>137</sup> The shift of the acetylene band by ca. 90  $\text{cm}^{-1}$  upon excitation is consistent with shifts in the Raman bands for the ground and  $S_2$  excited states of diphenylacetylene to be 2217 and 2099  $\text{cm}^{-1}$  respectively.<sup>139</sup> Whilst this 118  $\text{cm}^{-1}$  shift to lower wavenumber represents a weakening of the  $\text{C}\equiv\text{C}$  central bond in the  $S_2$  state, it was concluded that the bond order was still “triple” and that the excited molecule is linear. Significantly, the spectrum of the  $S_1$  state of **5** does not indicate the presence of a cumulenyl/quinoidal structure, which would be expected to show a strong band near 2000  $\text{cm}^{-1}$ . Butatriene derivatives exhibit intense Raman bands at ca. 2040  $\text{cm}^{-1}$  assigned to the symmetrical stretching vibration of the ( $\text{C}=\text{C}=\text{C}=\text{C}$ ) linkage.<sup>140</sup> Furthermore, it was found that extended conjugation leads to a further lowering of the vibration frequency of ( $\text{C}=\text{C}=\text{C}=\text{C}$ ) in the Raman spectrum.

The HOMO of **5**, whilst sensitive to the precise molecular geometry, was calculated using Gaussian98 at a B3LYP/6-31G\*\* level, to be essentially delocalised over the molecule (**Figure 29**), with bonding character between the carbon atoms of the acetylenes, and anti-bonding with respect to the  $\text{C}_{\text{sp}}\text{-C}_{\text{sp}^2}$  bonds, whilst the reverse is true of the LUMO (**Figure 29**). Given the large number of lower lying occupied orbitals which contribute to the acetylenic and aromatic sub-structure of the molecule, it is perhaps not surprising that promotion of a single electron from the HOMO to LUMO does not bring about a significant change in the bond order of the acetylene.

Photo-excitation may offer a degree of transient control over the conformation of the molecular skeleton. However, steric restriction to rotation of the aromatic rings can also be used to engineering control over the molecular conformation in materials derived from **5** for potential applications.

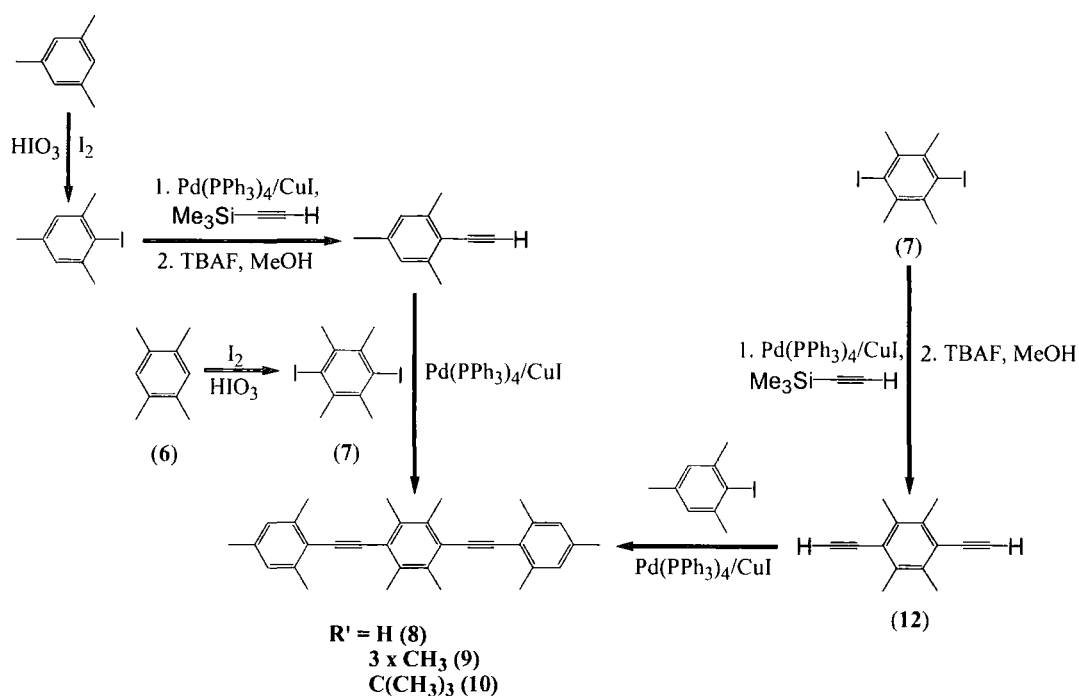




**Figure 29.** HOMO and LUMO of **5** calculated using Gaussian98 at a B3LYP/6-31G\*\* level.

### 2.2.2. 1,4-*bis*(Phenylethynyl)-2,3,5,6-tetra(methyl)benzene

In order to impose steric restriction to rotation of the outer aromatic rings in a three ring system linked by acetylenic moieties, a synthetic protocol was established. The central aromatic core chosen was 1,2,4,5-tetra(methyl)benzene (durene, **6**) to introduce a degree of steric bulk around the central core from the methyl groups, and allowing for variations of the outer aromatic rings. The synthesis of the sterically congested bis(arylethynyl)benzene skeleton can be envisioned using a number of synthetic pathways, two of which are illustrated in **Scheme 5**. The first pathway proceeds *via* a halide functionalisation of an outer aromatic ring, which was then ethynylated, and subsequently coupled to a halide functionalised inner aromatic ring, such as **7**. The second pathway approaches the problem from the opposite direction, where initially the inner aromatic ring is halide functionalised to produce compounds such as **7**. This functionalised inner aromatic ring was then ethynylated to give **12**, and subsequent Sonagashira coupling to a halide functionalised outer aromatic ring produces the desired compound. The ability of the second synthetic pathway to easily substitute the outer aromatic rings containing a variety of strictly bulky ligands was a factor in the decision to employ this particular synthetic method.



**Scheme 5.** Two different synthetic pathways for the synthesis of a three ring system.

Iodination of **6** was performed to produce the aryl dihalide as a precursor to subsequent Sonagashira coupling reactions. The synthesis of 1,4-diiodo-2,3,5,6-tetra(methyl)benzene (**7**) proceeded according to a procedure by Suzuki,<sup>141</sup> involving durene, iodine and periodic acid as the oxidising agent, which were dissolved in a slurry of sulphuric acid, water and glacial acetic acid and heated over a period of time (3h). The crude product obtained after solvent removal was purified by washing with acetone to remove the excess iodine and recrystallisation from hot acetone to give the desired product as a white powder. A higher yield (96%) for the reaction can be obtained compared to those quoted in the literature (80-87%,<sup>141</sup> 52%<sup>142</sup>) by periodically returning the sublimed iodine to the reaction mixture.

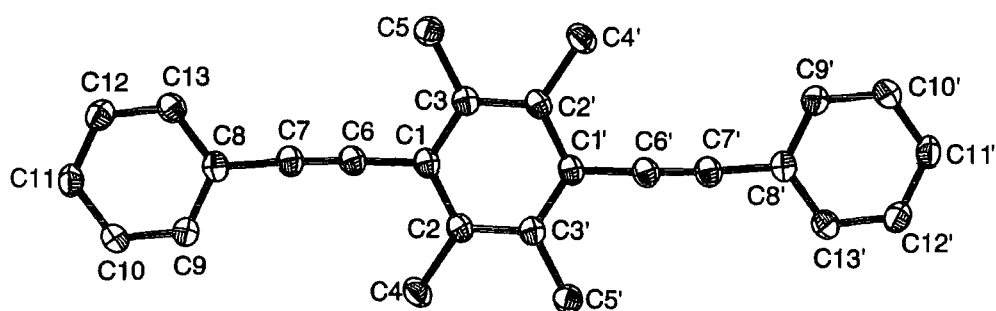
Access to the reactive C-I bonds in **7** is restricted by the methyl groups, and there was the need to ensure that subsequent Sonagashira coupling would

proceed using the chosen catalyst and base. A test reaction was performed between **7** and the unencumbered phenyl acetylene to ensure that the active form of the Pd catalyst can insert into the C-I bonds of **7** performing the oxidative addition portion of the catalytic cycle. The direct reaction between **7** and phenyl acetylene was performed instead of ethynylating **7** due to the commercial availability of phenyl acetylene. The Pd(PPh<sub>3</sub>)<sub>4</sub> (2.5%)-CuI (2.5%) catalysed coupling reaction between **7** and phenyl acetylene was carried out at room temperature in NEt<sub>3</sub> (72 h) to afford the desired 1,4-*bis*(phenylethynyl)-2,3,5,6-tetra(methyl)benzene (**8**) as thick white needles. The reaction was performed at ambient temperature which is known to minimise side reactions, in reactions involving a reactive halide.

The aromatic region of the <sup>1</sup>H NMR spectrum of **8** showed a multiplet ranging from δ 7.34-7.40 ppm due to the *meta* and *para* protons of the outer phenyl rings. The doublet at δ 7.57 ppm is due to the *ortho* protons of the outer aromatic ring. All four methyl groups of **8** are magnetically equivalent and gave a singlet at δ 2.52 ppm. The <sup>13</sup>C NMR spectrum shows two resonances at δ 88.88 ppm and 98.32 ppm from the acetylenic carbons, a resonance at δ 18.68 due to the methyl groups, while the remaining six resonances were assigned to the magnetically distinct aromatic carbon centres. The IR spectrum of **8** displayed a weak ν(C≡C) band at 2208 cm<sup>-1</sup>, while in the EI-MS spectrum the molecular ion was observed at *m/z* 334 together with fragment ions at *m/z* 319-304 arising from sequential loss of methyl groups.

The molecular structure of **8** was confirmed by X-ray crystallography using single crystals grown from CH<sub>2</sub>Cl<sub>2</sub>:MeOH and is shown in **Figure 30**, with crystallographic data given in **Table 3**. The three aromatic rings are approximately co-planar, with the outer phenyl rings C(8)-C(13) and C(8')-C(13') rotated 1.51° with respect to the inner ring. The torsion angle measured to determine the ring rotation with respect to each other is C(13)-C(8)-C(3)-C(1). The alkyne connecting the outer C(8)-C(13) and inner C(1)-C(3) rings has a

definite single-triple-single bond alternation with C(8)-C(7) 1.440(2) Å, C(7)-C(6) 1.198(2) Å, C(6)-C(1) 1.436(2) Å. The alkyne moieties connecting the rings are almost linear with a C(8)-C(7)-C(6) angle of 176.2(11)°, and a C(7)-C(6)-C(1) angle of 177.4(1)°. The molecule packs in a zigzag fashion with the hydrogens of the molecule connecting head to tail. The molecular structure of this model material clearly demonstrates that in order to engineer the relative rotation of the C(8)-C(13) and C(1)-C(3) aryl rings about the C(6)-C(7) ethynyl axis increased steric bulk needs to be introduced to the *ortho* position C(9) and C(13) of the outer aromatic ring.



**Figure 30.** Molecular structure of **8** depicted with a 50% ellipsoid probability.  
Hydrogen atoms have been omitted for clarity.



**Table 3.** Crystal data and structure refinement for **8** and **9**.

	<b>8</b>	<b>9</b>
Empirical formula	C <sub>26</sub> H <sub>22</sub>	C <sub>32</sub> H <sub>34</sub>
Formula weight	334.44	418.59
Temperature	120(2) K	120(2) K
Wavelength	0.71073 Å	0.71073 Å
Crystal system	Monoclinic	Triclinic
Space group	P 2 <sub>1</sub> /c	P -1
Unit cell dimensions	a = 7.6382(3) Å α = 90° b = 5.5306(2) Å β = 90.18(1)° c = 22.4684(8) Å γ = 90°	a = 5.8283(1) Å α = 92.26(1)° b = 6.3713(2) Å β = 99.59(1)° c = 16.2212(4) Å γ = 90.90(1)°
Volume	949.2(1) Å <sup>3</sup>	593.32(3) Å <sup>3</sup>
Z	2	1
Density (calculated)	1.170 Mg/m <sup>3</sup>	1.172 Mg/m <sup>3</sup>
Absorption coefficient	0.066 mm <sup>-1</sup>	0.066 mm <sup>-1</sup>
F(000)	356	226
Crystal size	0.50 x 0.14 x 0.02 mm <sup>3</sup>	0.30 x 0.30 x 0.10 mm <sup>3</sup>
Theta range for data collection	1.81 to 27.50°	2.55 to 29.00°
Index ranges	-9 ≤ h ≤ 9, -6 ≤ k ≤ 7, -29 ≤ l ≤ 29	-7 ≤ h ≤ 7, -8 ≤ k ≤ 8, -22 ≤ l ≤ 22
Reflections collected	8848	5059
Independent reflections	2172 [R(int) = 0.0499]	3093 [R(int) = 0.0404]
Completeness to theta	100.0 %	98.3 %
Absorption correction	None	None
Max. and min. transmission	-	-
Refinement method	Full-matrix least-squares on F <sup>2</sup>	Full-matrix least-squares on F <sup>2</sup>
Data / restraints / parameters	2172 / 0 / 168	3093 / 0 / 213
Goodness-of-fit on F <sup>2</sup>	0.928	1.025
Final R indices [I > 2σ(I)]	R1 = 0.0406, wR2 = 0.0945	R1 = 0.0476, wR2 = 0.1364
R indices (all data)	R1 = 0.0692, wR2 = 0.1062	R1 = 0.0610, wR2 = 0.1470
Largest diff. peak and hole	0.148 and -0.240 e.Å <sup>-3</sup>	0.398 and -0.216 e.Å <sup>-3</sup>

### 2.2.3. 1,4-*bis*(2',4',6'-tri(Methyl)phenylethynyl)-2,3,5,6-tetra(methyl)benzene

A similar protocol to that described for **8** was employed in the synthesis of 1,4-*bis*(2',4',6'-tri(methyl)phenylethynyl)-2,3,5,6-tetra(methyl)benzene (**9**) (Scheme 5), which has an increased steric bulk at the *ortho* position of the outer aromatic ring. The compound 1-ethynyl-2,4,6-trimethylbenzene was prepared *via* Pd(PPh<sub>3</sub>)<sub>4</sub>/CuI catalysed coupling reaction between 1-iodo-2,4,6-trimethylbenzene and trimethylsilylacetylene followed by a desilylation to produce the terminal acetylene. However, isolation of the product proved to be a problem, and a pure product could not be obtained. Thus the route of coupling **7** with 1-ethynyl-2,4,6-trimethylbenzene was abandoned. An alternate route, involving the initial preparation of 1,4-diethynyl-2,3,5,6-tetra(methyl)benzene (**12**), followed by cross-coupling with 1-iodo-2,4,5-trimethyl benzene was therefore explored.

Alkynyl zinc reagents have been shown to couple with 1-iodo-2,4,6-trimethylbenzene.<sup>143</sup> Successful reactions involve coupling of ethynylzincbromide, generated *in situ* from HC≡CMgBr and dry ZnBr<sub>2</sub>, with 1-iodo-2,4,6-trimethylbenzene. However, attempts to couple 1-iodo-2,4,6-trimethylbenzene with other metal acetylides such as those containing MgBr and SnBu<sub>3</sub> were not successful, or gave only poor yields of the ethynyl products.<sup>143</sup> Perhaps this type of reaction could facilitate the isolation of 1-ethynyl-2,4,6-trimethylbenzene.

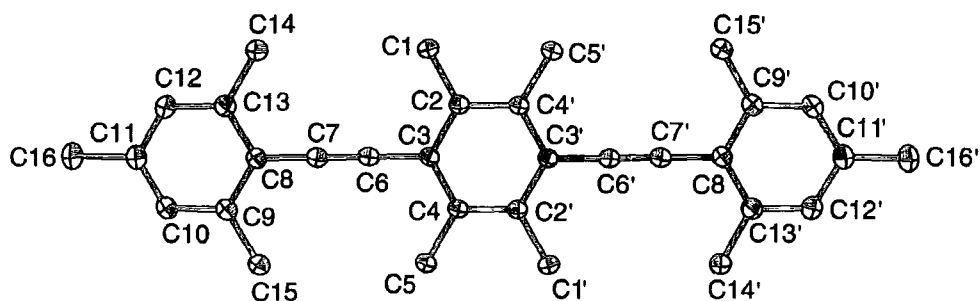
The palladium/copper catalysed (Pd(PPh<sub>3</sub>)<sub>4</sub>/CuI) coupling reaction between **7** and trimethylsilylacetylene was found to proceed at ambient temperature followed by extraction of the alkylammonium salt by-product into an aqueous layer. The crude acetylenic product was isolated and desilylated (NBu<sub>4</sub>F/H<sub>2</sub>O) without further purification. The desired terminal di(acetylene), **12**, was obtained as a pure yellow-coloured solid from the reaction mixture by Soxhlet extraction (hexane).

The IR spectrum of **12** showed a weak absorption band for  $\nu(\text{C}\equiv\text{C})$  at 2097  $\text{cm}^{-1}$  and the EI-MS spectrum exhibited a molecular ion at  $m/z$  182. The  $^1\text{H}$  NMR spectrum showed two singlets at  $\delta$  2.34 ppm and 3.46 ppm with a ratio of 1:6 representing the terminal alkyne proton and the protons of the methyl groups on the aromatic ring, respectively. The  $^{13}\text{C}$  NMR spectrum shows two resonances at  $\delta$  82.24 ppm and 85.73 ppm that are due to the acetylenic carbons, while the peak at  $\delta$  18.25 ppm was attributed to the methyl groups on the aromatic ring. The last two remaining resonances at  $\delta$  122.61 ppm and 136.32 ppm are due to the carbons of the aromatic ring.

Given the success of the Pd/Cu cross-coupling protocols utilised in the synthesis of **12**, similar conditions were investigated to promote the cross coupling of **12** with 1-iodo-2,4,6-trimethylbenzene. It is known that Sonagashira type coupling reactions are sensitive to the source of catalytically active Pd species, and the base used in the reaction. A variety of reaction conditions were explored using a combinatorial array in which solvent ( $\text{NEt}_3$ ,  $\text{NHet}_2$ ,  $\text{NH}^i\text{Pr}_2$ ,  $\text{Bu}^n\text{NH}_2$ ) and source of the palladium catalyst ( $\text{Pd}(\text{PPh}_3)_4$ ,  $\text{PdCl}_2(\text{PPh}_3)_2$ ,  $\text{PdCl}_2(\text{dppf})$ ,  $\text{Pd}_2(\text{dba})_3(\text{dppf})$ ,  $\text{Pd}_2(\text{dba})_3/\text{P}^n\text{Bu}_3$ ) was systematically varied. Analysis of the various reactions (GC-MS) revealed a similar distribution of products in all cases, with mono-, di-, and tri- ethynyldurene substituted mesitylenes being observed in all cases possibly due to impure starting materials or as a consequence of *trans*-halogenation of the aryl starting material. The sluggish nature of the reaction even at elevated temperatures can be attributed to the sterically crowded reaction sites, with **9** being observed in the crude reaction mixtures by GC-MS. On preparative scale, Pd/Cu catalysed cross coupling of **12** with 1-iodo-2,4,6-trimethylbenzene in  $\text{NEt}_3$  at ambient temperature gave **9** in moderate yield (27%).

The  $^1\text{H}$  NMR spectrum of **9** showed three singlets at  $\delta$  2.32, 2.53, and 2.56 ppm which represents the protons of the methyl groups of both the mesitylene and durene groups. The singlet at  $\delta$  6.93 ppm is due to the protons at C(10) and C(12) (**Figure 31**). The  $^{13}\text{C}$  NMR spectrum shows three resonances at  $\delta$  21.03, 21.27, and 26.61 ppm that are due to the C(1), C(14), C(16) methyl carbons. The two acetylenic carbons have very similar chemical shift at  $\delta$  96.04 and 96.07 ppm due to the similarity of their environment, being surrounded by *ortho* methyls of the aromatic rings. The symmetry of the molecule gives rise to six aromatic carbons between  $\delta$  120.39 and 139.75 ppm. The IR spectrum displayed a very weak absorption band for  $\nu(\text{C}\equiv\text{C})$  at  $2128\text{ cm}^{-1}$  while the EI-MS spectrum exhibited a molecular ion at  $m/z$  418 with a fragmentation pattern indicating methyl loss.

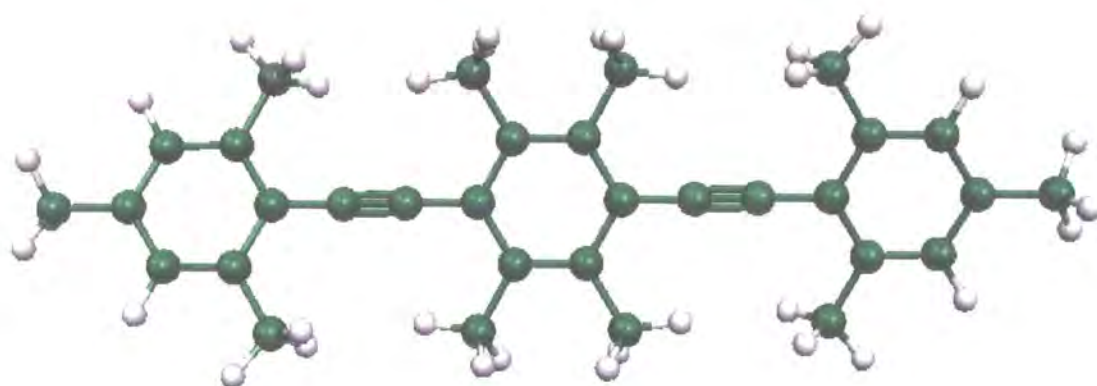
The molecular structure of **9** was confirmed by X-ray crystallography using single crystals grown from  $\text{CH}_2\text{Cl}_2$  and is shown in **Figure 31**, with crystallographic data given in **Table 3**. The molecular structure shows a planar geometry, with the acetylene moieties linking the aromatic rings providing enough space between C(1) and C(14) thus negating the need to adopt a twisted confirmation. The three aromatic rings are approximately co-planar, with the outer mesitylene rings C(8)-C(13) and C(8')-C(13') are rotated  $2.56^\circ$  with respect to the inner ring C(2)-C(4). The alkyne moieties C(6)-C(7) connecting the outer and inner rings has a definite single-triple-single bond alteration with C(8)-C(7)  $1.443(1)\text{ \AA}$ , C(7)-C(6)  $1.200(1)\text{ \AA}$ , C(6)-C(3)  $1.437(1)\text{ \AA}$ . The alkyne moieties connecting the rings are almost linear with a C(8)-C(7)-C(6) angle of  $178.81(9)^\circ$ , and a C(7)-C(6)-C(3) angle of  $178.34(10)^\circ$ . It appears that crystal packing forces has imposed a planar packing motif for the molecule.



**Figure 31.** Molecular structure of **9** depicted with a 50% ellipsoid probability.

Hydrogen atoms have been omitted for clarity.

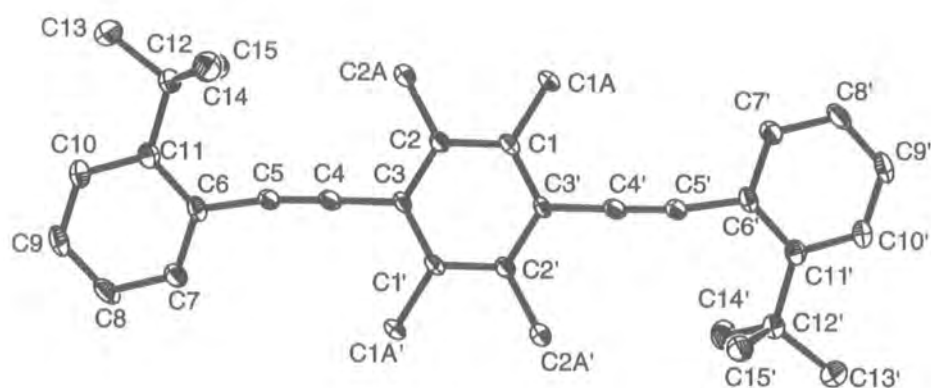
In order to probe the potential role of crystal packing forces on the observed solid state molecular structure, a computational study of the molecular geometry of **9** in the gas phase was performed. Results obtained for the geometry optimisation of **9** calculated using Gaussian98 at a B3LYP/6-31G\*\* level indicated that the outer mesitylene rings have a rotation of  $0.54^\circ$  and  $0.61^\circ$  with respect to the inner ring and is in accordance with the solid state molecular structure of the molecule (**Figure 32**). The ring rotations were calculated by taking the equivalent of C(8)-C(13)-C(3)-C(2) torsion angle (**Figure 31**). The calculated change in energy for **9** with varied ( $0$ - $90^\circ$ ) rotation of outer mesitylene rings with respect to a fixed orientation of the inner aromatic ring indicated that the most stable energy was obtained when the outer mesitylene rings are rotated by about  $10^\circ$ . However, the extent of the stabilisation energy of the molecule is only about 1 kcal/mol. In light of this, it is slightly surprising that both the solid state molecular structure and the geometry optimised structure only have an outer mesitylene ring rotation of less than  $3^\circ$ . It seems that the planar structure obtained in both the solid state molecular structure and the gas phase calculation (**Figure 31** and **32**) has fallen into a shallow local minimum, with the global minimum for the molecule having an outer mesitylene ring rotation of  $10^\circ$ .



**Figure 32.** Geometry optimised structure of **9** calculated using Gaussian98 at a B3LYP/6-31G\*\* level.

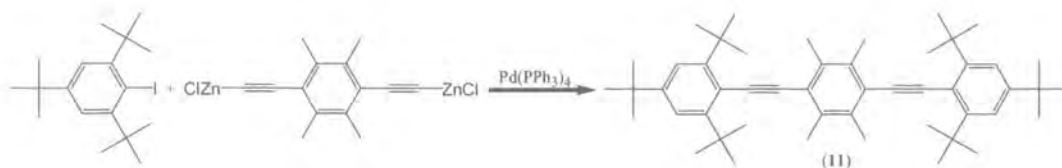
Both **Figure 31** and **32** indicate the need to introduce ligands with even greater steric bulk on the outer aromatic rings. The synthesis of such a molecule was carried out *via* a Sonagashira coupling between 1-ethynyl-2-*t*-butylbenzene and **7** to form 1,4-*bis*(2'-*t*-butyl ethnylbenzene)-2,3,5,6-tetra(methyl)benzene (**10**).<sup>144</sup> The molecular structure of **10**<sup>iv</sup> shows a molecule that is still fairly planar with the outer aromatic rings C(6)-C(11) and C(6')-C(11') rotated by 13.49° with respect to the inner ring C(1)-C(3) defined by taking the C(6)-C(5)-C(4)-C(3) torsion angle. However, the alkyne moieties C(5)-C(6) connecting the rings are no longer linear with a C(6)-C(5)-C(4) angle of 171.7(3)°, and a C(5)-C(4)-C(3) angle of 178.4(3)° (**Figure 33**).<sup>144</sup> This is consistent with the low bending force constants for acetylenes accommodating the presence of the bulky *t*-butyl groups on the outer aromatic rings.<sup>59</sup>

<sup>iv</sup> Solid state molecular structure courtesy of S. Rutter.



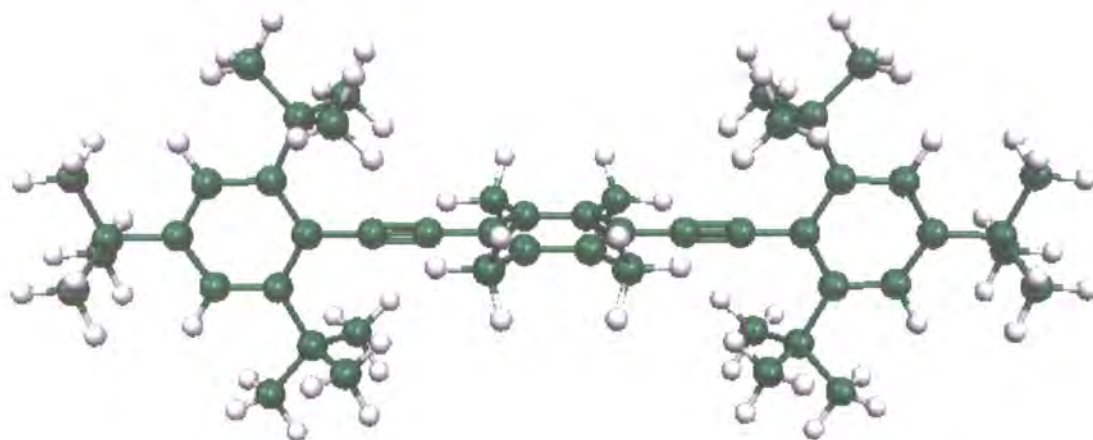
**Figure 33.** Molecular structure of **10** depicted with a 50% ellipsoid probability.<sup>144</sup> Hydrogen atoms have been omitted for clarity.

Attempts to couple 1,4-ethynyl-2,3,5,6-tetra(methyl)benzene and 1-iodo-2,4,6-tri(*t*-butyl)benzene to produce 1,4-*bis*(2',4',5'-*t*-butylethynylbenzene)-2,3,5,6-tetra(methyl)benzene (**11**) were unsuccessful. It was intended that **11** would have an increased steric bulk of the ligands of the outer aromatic rings over **10**. In reactions performed at room and elevated temperatures using Pd(PPh<sub>3</sub>)<sub>4</sub> and PdCl<sub>2</sub>(PPh<sub>3</sub>)<sub>2</sub>, 1-iodo-2,4,6-tri(*t*-butyl)benzene was recovered exclusively. Recrystallisation of the palladium residue gave PdI<sub>2</sub>(PPh<sub>3</sub>)<sub>2</sub>, which has been obtained previously as a by-product from reactions of an alkylhalide with Pd(PPh<sub>3</sub>)<sub>4</sub>.<sup>145, 146</sup> The presence of PdI<sub>2</sub>(PPh<sub>3</sub>)<sub>2</sub> indicates a halide exchange with CuI, since the 1-iodo-2,4,6-tri(*t*-butyl)benzene was recovered without any change in halide. If the active species Pd(PPh<sub>3</sub>)<sub>2</sub> cannot oxidatively add to 1-iodo-2,4,6-tri(*t*-butyl)benzene, then Pd(PPh<sub>3</sub>)<sub>2</sub> will exit the catalytic cycle by obtaining two iodides, most likely from HNR<sub>3</sub>I produced when the copper-alkyne is formed. It is known that Sonagashira reactions are hampered by problems stemming from steric hindrance, especially those arising from the *ortho* position. A possible solution to this is the application of the Negishi protocol using ethynyl metals, especially those containing Zn (**Scheme 6**).<sup>143, 147</sup>



**Scheme 6.** Possible synthetic route to the formation of **11**.

Gas phase computational study of the molecular geometry can reproduce solid state molecular structures with reasonable accuracy. For this reason the geometry optimisation of **11** calculated using Gaussian98 at a B3LYP/6-31G\*\* level was performed to see what the possible solid state molecular structures of **11** would be. Geometry optimisation of **11** revealed a structure that is completely twisted with outer aromatic ring rotations of  $89.8^\circ$  with respect to the inner ring (**Figure 34**).



**Figure 34.** Geometry optimised structure of **11** calculated using Gaussian98 at a B3LYP/6-31G\*\* level.

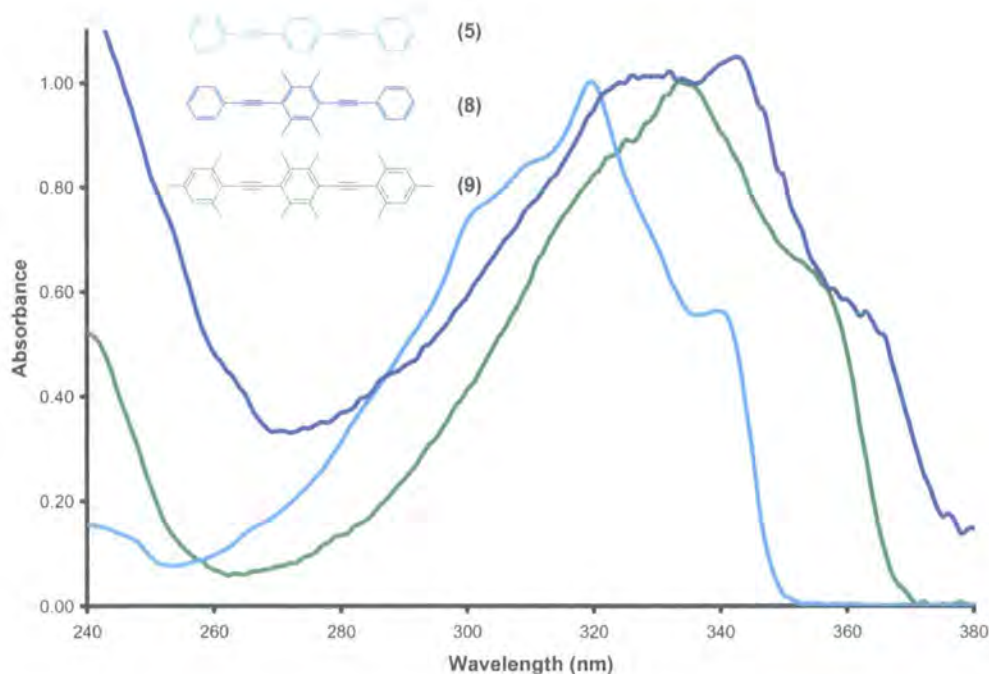
#### 2.2.4. Photophysics of Linear Ethynylated Aromatic Systems<sup>vii</sup>

Solid state molecular structures indicate that the molecules **8**, **9**, **10** are fairly planar, with similarities in rotation of the outer aromatic rings with respect

<sup>vii</sup> All spectroscopic data courtesy of K. Findlay.



to the inner rings, deviation of linearity for the alkyne moieties, as well as the single/triple bond variation in the molecules. The solid state molecular structures of the molecules stated above are similar to that of **5** (Table 4). Solution state photophysical measurements can give insights into the behaviour of these molecules with respect to the planar **5**, since solid state data obtained for these molecules are not directly comparable with the solution-based studies described earlier, and packing effects may be responsible for enforcing planar geometries in the solid state. Room temperature absorbance spectra of the three compounds in cyclohexane indicated that they behave in a similar manner with the  $\lambda_{\text{max}}$  for durene derivatives red shifted due to the higher HOMO energy caused by an increased number of donating methyl groups in the molecule (Figure 35). The absorbance spectra of **8** displayed a broad  $\lambda_{\text{max}}$  at 315 nm with an extinction coefficient ( $\epsilon$ ) of 47800 M<sup>-1</sup>cm<sup>-1</sup>. This  $\lambda_{\text{max}}$  is slightly shifted with respect to that of **5** which demonstrates a  $\lambda_{\text{max}}$  at 320 nm with  $\epsilon$  of 58000 M<sup>-1</sup>cm<sup>-1</sup>.

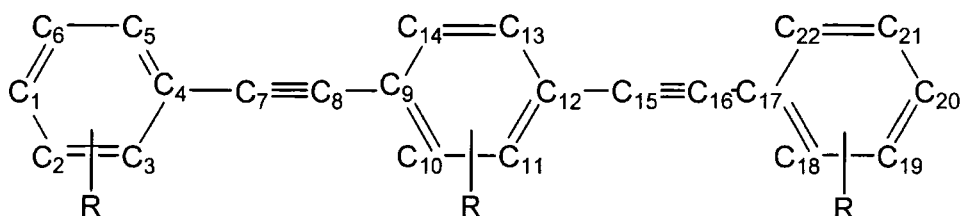


**Figure 35.** Absorbance spectra for **5**, **8**, and **9** in cyclohexane at 298K.

**Table 4.** Selected bond length and angles for **5**, **8**, **9**, and **10**.

	<b>5</b>	<b>8</b>	<b>9</b>	<b>10</b>
C(4)-C(7)	1.431(2) Å	1.440(2) Å	1.443(1) Å	1.441(3) Å
C(7)-C(8)	1.205(2) Å	1.198(2) Å	1.200(1) Å	1.202(3) Å
C(8)-C(9)	1.428(2) Å	1.436(2) Å	1.437(1) Å	1.436(3) Å
C(4)-C(7)-C(8)	176.9(2)°	176.2(11)°	178.81(9)°	171.7(3)°
C(7)-C(8)-C(9)	178.7(2)°	177.4(1)°	178.34(10)°	178.4(3)°
C(3)-C(4)-C(9)-C(10)	5.36°	1.51°	2.56°	13.49°

Numbering system for **Table 4**:

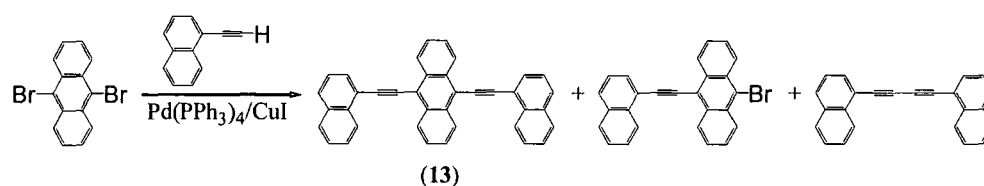


### 2.2.5. 9,10-di(1-Ethynynaphthalene)anthracene

Other than photo-excitation and the presence of highly sterically congested aromatic moieties on materials, perihydrogen interactions are alternate steric constraints that can be utilised to engineer control over the molecular conformation. Given the difficulty in preparing **11**, the possibility of using alternate steric constraints was investigated which utilises molecules such as 9,10-di(1-ethynynaphthalene)anthracene (**13**), which has perihydrogen interactions between the naphthalene and anthracene rings in the molecule.

The synthesis of **13** proceeded *via* Pd(PPh<sub>3</sub>)<sub>4</sub>/CuI coupling between 1-ethynynaphthalene and 9,10-dibromoanthracene (**Scheme 7**). The reaction was

carried out in refluxing diethylamine, and afforded the desired product in good yield (92%) as a poorly soluble orange powder. The EI-MS spectrum was obtained using a solid sample of **13** due to the insolubility of the compound in suitable solvents. The spectrum exhibited a molecular ion at  $m/z$  478, and a fragment ions at 350 and 326 representing the loss of naphthalene and ethynylnaphthalene respectively. The IR spectrum contained a weak absorption band for  $\nu(\text{C}\equiv\text{C})$  at  $2192\text{ cm}^{-1}$ . The  $^1\text{H}$  NMR spectrum showed resonances only in the aromatic region which consisted of two multiplets at  $\delta$  7.61, and 7.73, three doublets at  $\delta$  7.95, 8.05 and 8.71, and a multiplet at 8.87 ppm. The  $^{13}\text{C}$  NMR spectrum shows two resonances at  $\delta$  90.98 and 100.41 ppm due to the acetylenic carbons and fourteen resonances in the aromatic region of the spectrum arising from the non-equivalent aromatic carbons of the molecule.



**Scheme 7.** Reaction scheme for the synthesis of **13** along with its by-products.

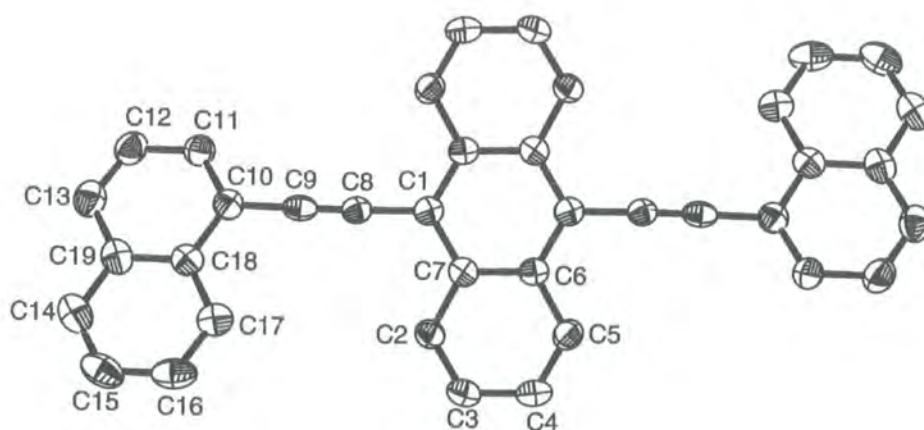
Square orange crystals of good quality were produced upon recrystallisation from hot  $\text{CH}_2\text{Cl}_2$ , and the molecular structure of **13** was confirmed by X-ray crystallography as shown in **Figure 36**, with crystallographic data given in **Table 5**. The two naphthalene rings lie in the same plane, rotated  $21.66^\circ$  and  $23.67^\circ$  with respect to the anthracene ring, defined by the C(10)-C(11)-C(1)-C(7') and C(6)-C(1')-C(18')-C(10') torsion angle, respectively, while the distance between the perihydrogens, H(2) and H(17) is  $2.54\text{ \AA}$ . The alkynes moieties connecting the outer and inner rings have a definite single-triple-single bond alteration with C(10)-C(9)  $1.446(3)\text{ \AA}$ , C(9)-C(8)  $1.139(3)\text{ \AA}$ , C(8)-C(1)  $1.461(3)\text{ \AA}$ . The  $\text{C}\equiv\text{C}$  bond length of  $1.139\text{ \AA}$  is approximately  $0.07\text{ \AA}$  shorter than for the  $\text{C}\equiv\text{C}$  in molecular structures of molecules containing three aromatic rings

connected by acetylenic moieties. The alkyne moieties connecting the ring systems *via* C(1) and C(10) are almost linear with a C(10)-C(9)-C(8) angle of 179.0(3)°, and a C(9)-C(8)-C(1) angle of 178.2(3)°.

**Table 5.** Crystal data and structure refinement for **13**, 9-bromo-10-(1-ethynynaphthalene)anthracene and 1,4-dinaphthylbuta-1,3-diyne.

	<b>13</b>	9-bromo-10-(1-ethynynaphthalene)anthracene	1,4-dinaphthylbuta-1,3-diyne
Empirical formula	C <sub>38</sub> H <sub>22</sub>	C <sub>26</sub> H <sub>15</sub> Br	C <sub>24</sub> H <sub>14</sub>
Formula weight	478.56	407.29	302.35
Temperature	120(2) K	120.0(1) K	120(2) K
Wavelength	0.71073 Å	0.71073 Å	0.71073 Å
Crystal system	Monoclinic	Orthorhombic	Monoclinic
Space group	C2/c	P 2 <sub>1</sub> 2 <sub>1</sub> 2 <sub>1</sub>	P 2 <sub>1</sub> /n
Unit cell dimensions	a = 21.761(1) Å α = 90° b = 9.3983(4) Å β = 122.16(1)° c = 14.3421(6) Å γ = 90°	a = 5.0917(3) Å α = 90° b = 14.9671(8) Å β = 90° c = 22.7608(11) Å γ = 90°	a = 8.2091(3) Å α = 90° b = 12.6627(5) Å β = 100.40(2)° c = 15.2126(6) Å γ = 90°
Volume	2483.25(19) Å <sup>3</sup>	1734.55(16) Å <sup>3</sup>	1555.4(1) Å <sup>3</sup>
Z	4	4	4
Density (calculated)	1.280 Mg/m <sup>3</sup>	1.560 Mg/m <sup>3</sup>	1.291 Mg/m <sup>3</sup>
Absorption coefficient	0.073 mm <sup>-1</sup>	2.377 mm <sup>-1</sup>	0.073 mm <sup>-1</sup>
F(000)	1000	824	632
Crystal size	0.20 x 0.14 x 0.02 mm <sup>3</sup>	0.58 x 0.08 x 0.04 mm <sup>3</sup>	0.30 x 0.15 x 0.15 mm <sup>3</sup>
Theta range for data collection	2.21 to 26.50°	1.63 to 28.99°	2.11 to 27.50°
Index ranges	-27 ≤ h ≤ 27, -11 ≤ k ≤ 11, -18 ≤ l ≤ 18	-6 ≤ h ≤ 6, -19 ≤ k ≤ 20, -31 ≤ l ≤ 31	-10 ≤ h ≤ 10, -16 ≤ k ≤ 16, -19 ≤ l ≤ 19
Reflections collected	11740	16356	8754
Independent reflections	2581 [R(int) = 0.0882]	4595 [R(int) = 0.0322]	3580 [R(int) = 0.0532]
Completeness to	100.0 %	100.0 %	99.9 %

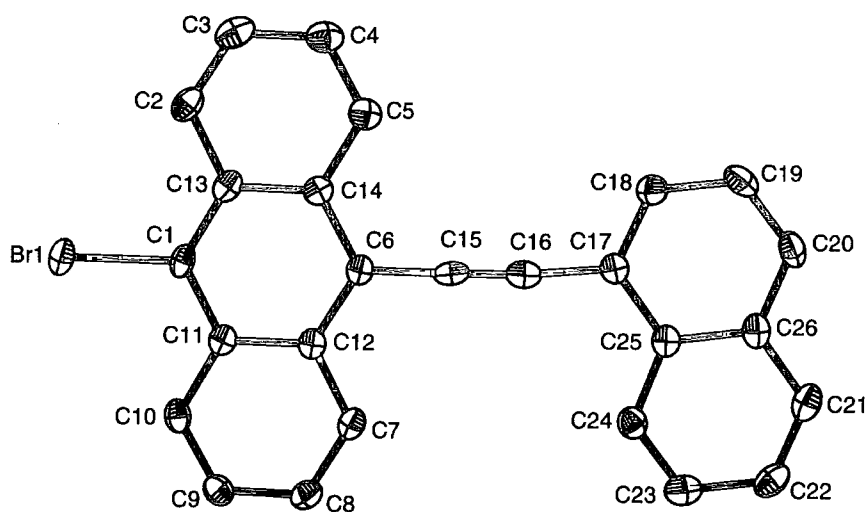
theta			
Absorption correction	None	Semi-empirical from equivalents	None
Max. and min. transmission	-	0.9109 and 0.3393	0.9891 and 0.9784
Refinement method	Full-matrix least-squares on F <sup>2</sup>	Full-matrix least-squares on F <sup>2</sup>	Full-matrix least-squares on F <sup>2</sup>
Data / restraints / parameters	2581 / 0 / 217	4595 / 0 / 304	3580 / 0 / 273
Goodness-of-fit on F <sup>2</sup>	0.975	1.075	0.869
Final R indices [I > 2sigma(I)]	R1 = 0.0506, wR2 = 0.0910	R1 = 0.0278, wR2 = 0.0656	R1 = 0.0444, wR2 = 0.0927
R indices (all data)	R1 = 0.1377, wR2 = 0.1079	R1 = 0.0324, wR2 = 0.0674	R1 = 0.0907, wR2 = 0.1058
Extinction coefficient	0.0011(3)	-0.002(7)	
Largest diff. peak and hole	0.297 and -0.218 e.Å <sup>-3</sup>	0.427 and -0.263 e.Å <sup>-3</sup>	0.212 and -0.228 e.Å <sup>-3</sup>



**Figure 36.** Molecular structure of **13** depicted with a 50% ellipsoid probability. Hydrogen atoms have been omitted for clarity.

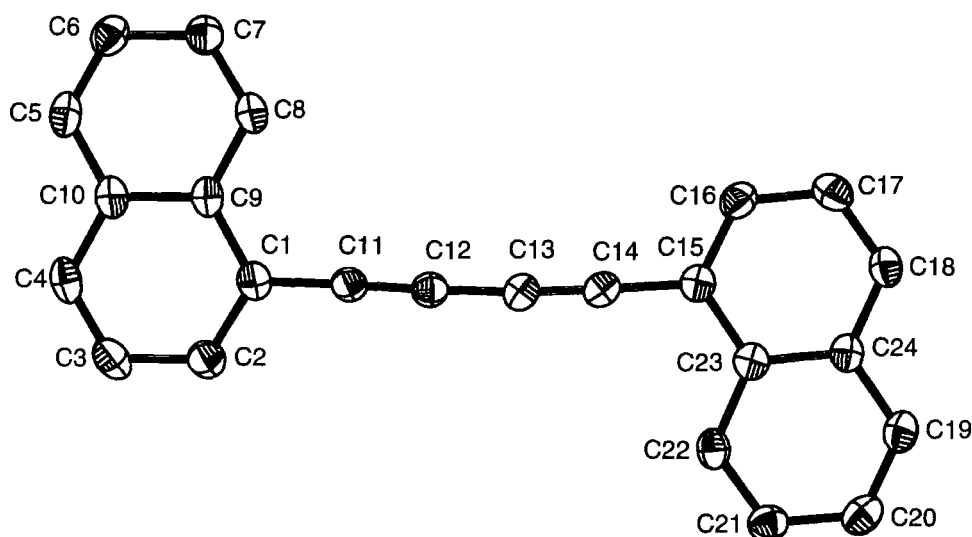
Preliminary room temperature photophysical studies including absorption, excitation and emission spectra indicated that **13** behaves in a similar manner to **5**, undergoing relaxation in the  $S_1$  state to a presumably more planar conformation. However, remaining photophysical measurements, such as variational temperature absorbance spectra, remains to be done.

Crystals of 9-bromo-10-(1-ethynynaphthalene)anthracene (**Scheme 7**) and 1,4-dinaphthylbuta-1,3-diyne (**Scheme 7**) were also isolated as by-products from the reaction between 1-ethynynaphthalene and 9,10-dibromoanthracene and were separated by hand. The compound 9-bromo-10-(1-ethynynaphthalene)anthracene resulted from the partial coupling of 9-bromo-10-(1-ethynynaphthalene)anthracene to 9,10-dibromoanthracene, while 1,4-dinaphthylbuta-1,3-diyne was produced as a result of homocoupling of 1-ethynynaphthalene due to the presence of oxygen in the reaction. The molecular structure of 9-bromo-10-(1-ethynynaphthalene)anthracene was confirmed by X-ray crystallography as shown in **Figure 37**, with crystallographic data given in **Table 5**. The bond lengths along the C(6)-C(15)-C(16)-C(17) chain connecting the naphthalene and anthracene rings show a definite single-triple-single bond alternation with C(6)-C(15) 1.461(3) Å, C(15)-C(16) 1.150(3) Å, C(16)-C(17) 1.445(3) Å. The aromatic moieties in the molecule are coplanar with a torsion angle of 0.65° between the naphthalene and anthracene moieties defined by the C(6)-C(14)-C(17)-C(18) torsion angle. The alkyne moiety connecting the rings is slightly bent with a C(6)-C(15)-C(16) angle of 178.6(2)°, and a C(15)-C(16)-C(17) angle of 175.5(2)°.



**Figure 37.** Molecular structure of 9-bromo-10-(1-ethynynaphthalene)anthracene depicted with a 50% ellipsoid probability. Hydrogen atoms have been omitted for clarity.

The molecular structure of 1,4-dinaphthylbuta-1,3-diyne was confirmed by X-ray crystallography as shown in **Figure 38**, with crystallographic data given in **Table 5**. The two naphthalene rings lie in approximately the same plane, rotated  $2.76^\circ$  with respect to each other. The carbon chain connecting the outer and inner rings has a definite single-triple-single bond alternation with C(1)-C(11) 1.429(2) Å, C(11)-C(12) 1.203(2) Å, C(12)-C(13) 1.376(2) Å, C(13)-C(14) 1.209(2) Å, C(14)-C(15) 1.435(2) Å. This butadiyne moiety connecting the rings is almost linear with a C(1)-C(11)-C(12) angle of  $178.34(17)^\circ$ , and a C(13)-C(14)-C(15) angle of  $178.04(16)^\circ$ . The C≡C bond length and linearity of the diyne moiety are in accordance to other molecular structures containing two aromatic rings connected by buta-1,3-diyne moieties.<sup>148-150</sup>



**Figure 38.** Molecular structure of 1,4-dinaphthylbuta-1,3-diyne depicted with a 50% ellipsoid probability. Hydrogen atoms have been omitted for clarity.

## 2.3. Synthesis and Photophysics of 1,2,4,5-Tetraethynyl Substituted Benzenes

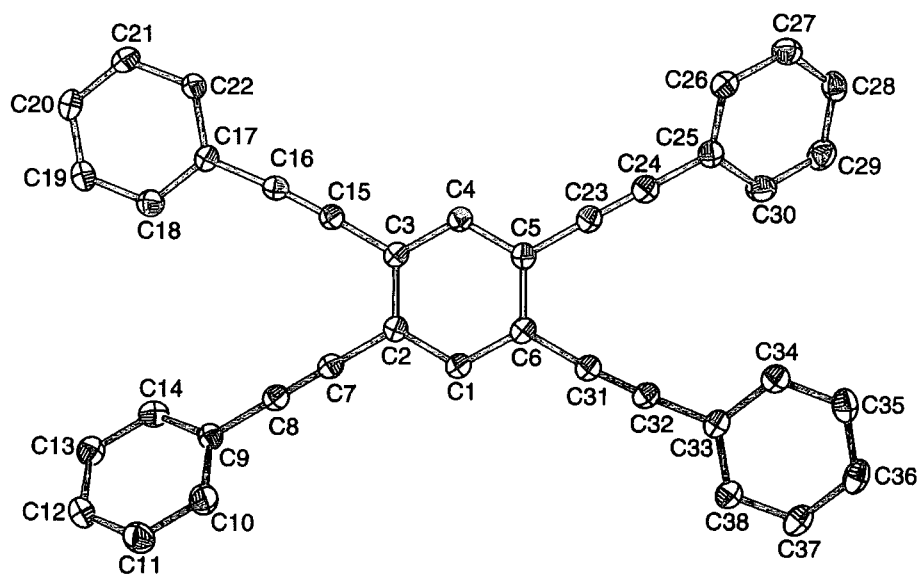
### 2.3.1. 1,2,4,5-tetra(Phenylethynyl)benzene

The remarkable electronic properties of systems based upon **5** prompts consideration of materials such as 1,2,4,5-tetra(phenylethynyl)benzene (**14**), which may be considered as two fused 1,4-bis(phenylethynyl)benzene wires, as potential multi-functional junctions. The simplest model of this, **14**, has been synthesised by the Pd-catalysed coupling of phenylacetylene with the commercially available 1,2,4,5-tetrabromobenzene.<sup>93, 151</sup> The crystal structure for this molecule, solved in the  $C_{2/c}$  space group, has been claimed;<sup>151</sup> however, data has not been deposited for reference by others. Compound **14** was re-prepared and the crystal structure re-determined from single yellow spar-like crystals grown from  $CH_2Cl_2$ :hexane.

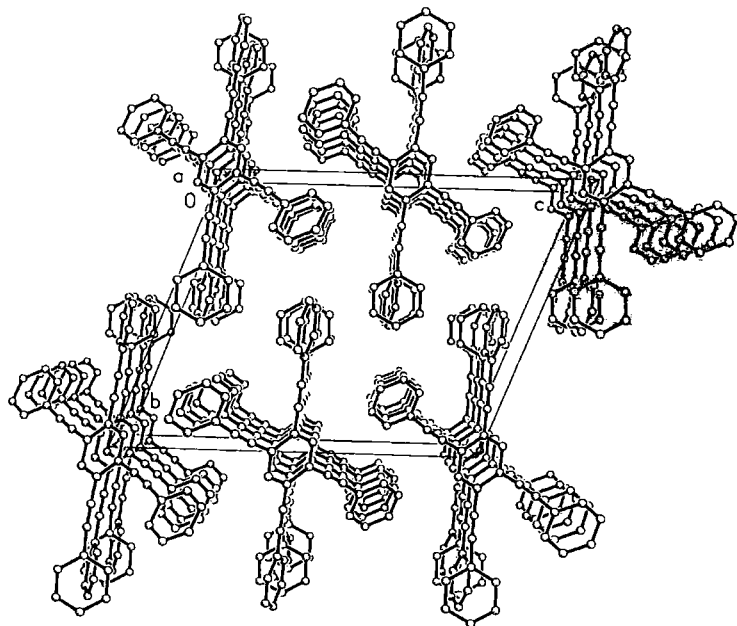


One of the three distinct molecules in the extended lattice is illustrated in **Figure 39**, with the crystallographic data given in **Table 6**. The parameters quoted below are representative of the other independent molecules in the unit cell.

The outer aromatic rings of C(17)-C(22), C(25)-C(30), C(33)-C(38), C(9)-C(14) possessed a rotation of 9.28°, 27.81°, 12.62° and 32.39°, respectively, with respect to the inner aromatic ring (**Figure 39**). The rotation of the aromatic rings are for example, defined by a torsion angle of C(17)-C(22)-C(3)-C(4). The alkyne moieties connecting the outer and inner rings have a definite single-triple-single bond alteration, taking the example of C(3)-C(15) 1.431(2) Å, C(15)-C(16) 1.203(2) Å, C(16)-C(17) 1.431(2) Å and C(5)-C(23) 1.430(2) Å, C(23)-C(24) 1.2053(2) Å, C(24)-C(25) 1.437(2) Å. The alkyne moieties connecting the rings are almost linear with a C(3)-C(15)-C(16) angle of 176.75(15)°, and a C(15)-C(16)-C(17) angle of 175.88(15)°. The remaining alkyne bonds and angles are very similar to those already stated. The molecule packs with the three coplanar rings packing in a planar motif, while the remaining rings are orientated in an almost perpendicular fashion (**Figure 40**).



**Figure 39.** Molecular structure of **14** depicted with a 50% ellipsoid probability.  
Hydrogen atoms have been omitted for clarity.

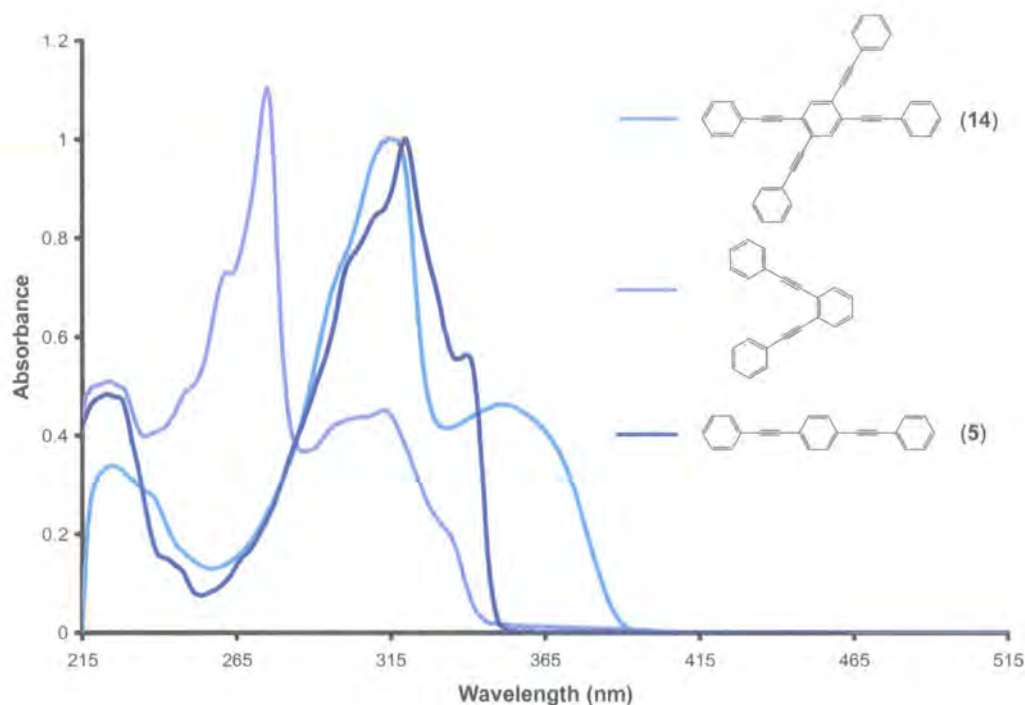


**Figure 40.** Packing diagram associated with solid state structure of **14**.

**Table 6.** Crystal data and structure refinement for **14** and **16**.

	<b>14</b>	<b>16</b>
Empirical formula	C <sub>38</sub> H <sub>22</sub>	C <sub>11</sub> H <sub>6</sub> Br
Formula weight	478.56	218.07
Temperature	120(2) K	100(2) K
Wavelength	0.71073 Å	0.71073 Å
Crystal system	Triclinic	Monoclinic
Space group	P-1	P2(1)/c
Unit cell dimensions	a = 9.7428(3) Å α = 110.96(1)° b = 15.4742(5) Å β = 90.00(2)° c = 18.7050(6) Å γ = 99.01(2)°	a = 18.364(6) Å α = 90° b = 3.903(1) Å β = 104.579(4)° c = 11.884(4) Å γ = 90°
Volume	2596.0(1) Å <sup>3</sup>	824.4(4) Å <sup>3</sup>
Z	4	4
Density (calculated)	1.224 Mg/m <sup>3</sup>	1.757 Mg/m <sup>3</sup>
Absorption coefficient	0.069 mm <sup>-1</sup>	4.915 mm <sup>-1</sup>
F(000)	1000	428
Crystal size	0.48 x 0.14 x 0.08 mm <sup>3</sup>	0.42 x 0.32 x 0.02 mm <sup>3</sup>
Theta range for data collection	1.17 to 27.00°	2.29 to 28.28°
Index ranges	-12 ≤ h ≤ 12, -9 ≤ k ≤ 19, -23 ≤ l ≤ 23	-24 ≤ h ≤ 24, -5 ≤ k ≤ 5, -15 ≤ l ≤ 15
Reflections collected	24640	8778
Independent reflections	11218 [R(int) = 0.0361]	2037 [R(int) = 0.0568]
Completeness to theta	98.9 %	99.9 %
Absorption correction	Semi-empirical from equivalents	Integration
Max. and min. transmission	0.9945 and 0.9674	0.905 and 0.215
Refinement method	Full-matrix least-squares on F <sup>2</sup>	Full-matrix least-squares on F <sup>2</sup>
Data / restraints / parameters	11218 / 0 / 861	2037 / 0 / 109
Goodness-of-fit on F <sup>2</sup>	0.966	1.080
Final R indices [I > 2σ(I)]	R1 = 0.0476, wR2 = 0.1255	R1 = 0.0368, wR2 = 0.0951
R indices (all data)	R1 = 0.0844, wR2 = 0.1477	R1 = 0.0456, wR2 = 0.1033
Largest diff. peak and hole	0.313 and -0.209 e.Å <sup>-3</sup>	1.800 and -1.210 e.Å <sup>-3</sup>

An attempt was made to correlate room temperature absorbance spectra of **14** with simpler fragments of the molecule such as **5**, and 1,2-*bis*(phenylethynyl)benzene (**Figure 41**) since solution state photophysical measurements can give insights into the behaviour of these molecules.

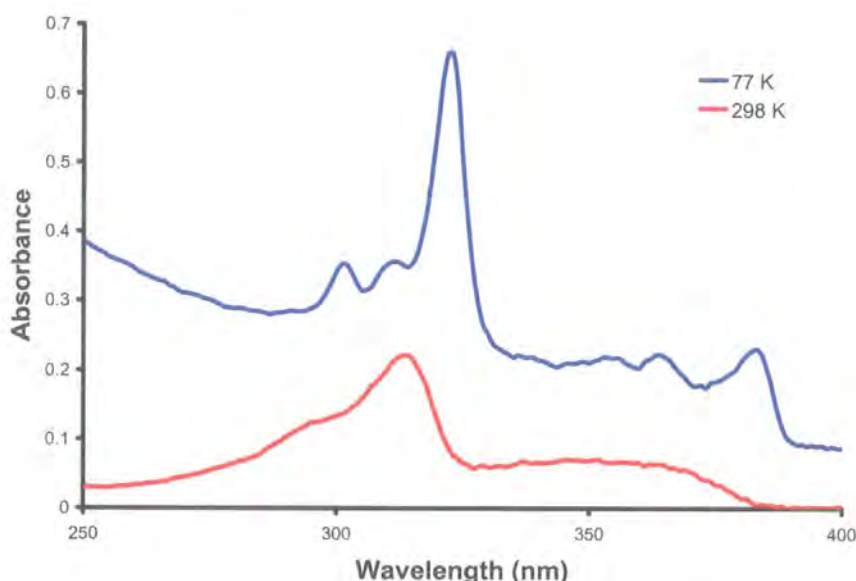


**Figure 41.** Room temperature absorbance spectra of **14**, **5**, and 1,2-*bis*(phenylethynyl)benzene.

The absorbance spectrum of **14** had  $\lambda_{\text{max}}$  at 315 nm with  $\epsilon$  of 25900 M<sup>-1</sup>cm<sup>-1</sup>; the profile also revealed a broad shoulder around 350 nm. One of the fragments of **14** was 1,2-*bis*(phenylethynyl)benzene with an *ortho* interaction between the phenyl acetylene moieties through the aromatic core. The absorbance spectrum of 1,2-*bis*(phenylethynyl)benzene had  $\lambda_{\text{max}}$  at 275 nm with  $\epsilon$  of 741300 M<sup>-1</sup>cm<sup>-1</sup>, the profile also revealed a broad shoulder band around 310 nm. In contrast, **5** demonstrates a  $\lambda_{\text{max}}$  at 320 nm with  $\epsilon$  of 58000 M<sup>-1</sup>cm<sup>-1</sup>. There is a small shoulder at 340 nm, which is different in profile from the broad shoulders exhibited by the spectrum of **14** and 1,2-*bis*(phenylethynyl)benzene. The

absorbance spectra indicate that there is little correlation between **14** and the simpler fragments of **14**, i.e. **5** and 1,2-*bis*(phenylethynyl)benzene, with none of the absorbance profiles matching. This is in accordance with the presence of a different chromophore in **14**, than those in **5** and 1,2-*bis*(phenylethynyl)benzene.

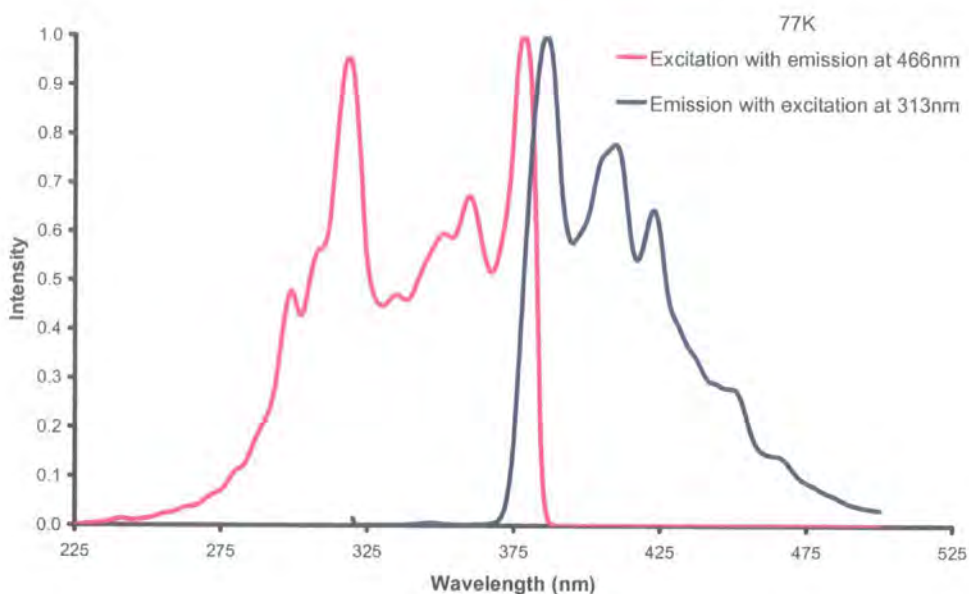
Room temperature absorbance spectra of **14** in methyl cyclohexane and 2-methyl butane (isopentane) with a 4:1 ratio (MCH/IP) shows a featureless profile reminiscent of that for **5**, which sharpens as the temperature is lowered (**42**).<sup>viii</sup> This observation is consistent with the idea of increased planarity of the molecule at lower temperatures.



**Figure 42.** Absorbance spectra for **14** in MCH/IP at 298K and 77K.<sup>viii</sup>

At 77K, the excitation-emission spectrum collected is again reminiscent of that for **5**. The excitation spectrum is approximately the mirror image of the emission spectrum, indicating similar distribution of conformers in the ground and excited state (**Figure 43**).<sup>viii</sup> This again indicates that the distribution of conformers in the excited state is planar in agreement with the planar distribution of conformers of **14** in a low temperature solvent.

<sup>viii</sup> Absorbance spectra courtesy of K. Findlay.



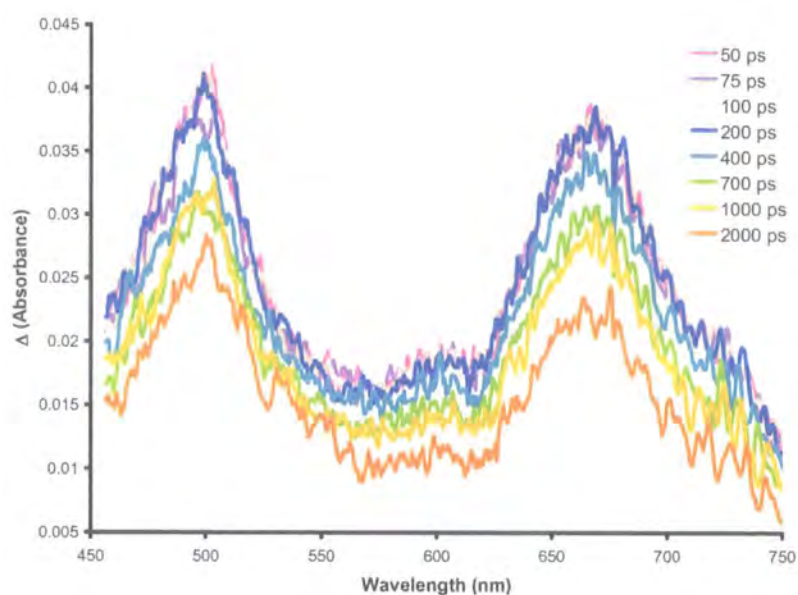
**Figure 43.** Excitation and emission spectra of **14** in MCH/IP at 77K.<sup>viii</sup>

Transient absorbance spectra collected for **5** (**Figure 27**) showed a strong band centred at 620 nm.<sup>137</sup> In contrast, the transient absorbance spectra for **14** collected under similar conditions demonstrate two strong bands, centred at 500 nm and 670 nm (**Figure 44**). These two absorbance bands increased and decayed simultaneously over the observed period. This indicates that the chromophore in **14** is distinct to that of **5**, and not simply that of **5** with substitutions at the two and five positions.<sup>ix</sup>

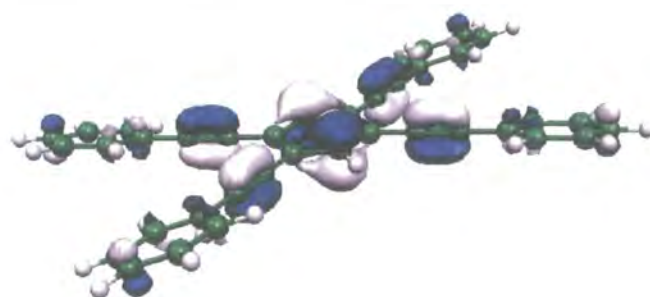
Though **14** may be considered as two fused **5** wires, a molecular orbital calculation performed on this molecule using Gaussian98 at the B3LYP/6-31G\*\* level indicates that orbital interaction through the aromatic core is not merely the sum of two fused **5** wires. The two highest occupied orbitals of the molecule show both *ortho* and *meta* interaction through the aromatic core (**Figure 45**). Geometry optimisation of **14** gave a structure in which the outer aromatic rings were twisted by 14.4-17.9° with respect to the inner aromatic rings, which is similar to the rotation of the outer aromatic rings found in the solid state molecular structure.

<sup>ix</sup> Transient absorbance spectra courtesy of S. Rutter.

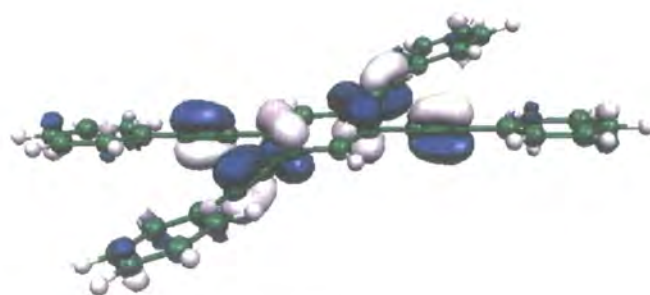




**Figure 44.** Transient absorbance spectra of **14**.<sup>ix</sup>



HOMO<sub>-1</sub>



HOMO

**Figure 45.** HOMO and HOMO<sub>-1</sub> orbitals of **14** calculated using Gaussian98 at a B3LYP/6-31G\*\* level.

While 1,2,4,5-tetraethynyl benzenes of  $D_{2h}$  symmetry are known (e.g. **14**), having been prepared in one-pot fashion by coupling of terminal alkynes with 1,2,4,5-tetrahalobenzenes under Sonogashira cross-coupling conditions, quite remarkably, tetraethynyl benzenes with  $C_{2h}$  symmetry (e.g. 1,4-*bis*(phenylethynyl)-2,5-*bis*(trimethylsilylethynyl)benzene) are rare. The desire to engineer different functionality around the central core of these tetraethynyl junctions, together with the well-known chemoselectivity of aryl iodides over aryl bromides under Sonogashira conditions, suggested the use of 1,4-dibromo-2,5-diiodo-benzene (**15**)<sup>152</sup> as a key building block.

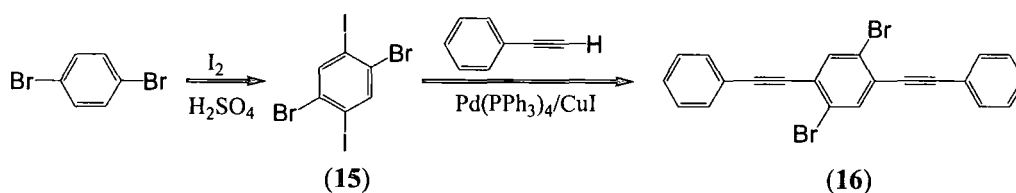
### 2.3.2. 1,4-*bis*(Phenylethynyl)-2,5-*bis*(ethynyl)benzene

Aromatic iodides have long been recognised as a valuable synthetic tool in carbon-carbon bond formation, thus, methods which allow regioselective introduction of an iodine atom into an organic molecule have attracted great interest.<sup>141, 142, 152, 153</sup> The intermediate **15** is a versatile building block as the Sonogashira coupling at the iodine positions which proceeds under mild conditions can be effected with complete chemoselectivity using Pd-catalysed cross-coupling reactions, leaving the bromine positions intact for further cross-coupling under more aggressive conditions. This reaction was performed following the procedure outlined by Hart,<sup>154</sup> and forms the aryl core for the subsequent compounds (**Scheme 8**). The iodination of 1,4-dibromobenzene requires the harsh conditions employed by this method, namely refluxing for a long periods of time in  $H_2SO_{4(conc)}$ . When the Suzuki protocol<sup>141</sup> was employed, the resulting yield was very low.

The compound **15** can then be subsequently reacted with phenyl acetylene to produce 1,4-dibromo-2,5-*bis*(phenylethynyl)benzene (**16**) which is a useful precursor for subsequent Sonogashira reactions on route to form tetraethynyl benzenes with  $C_{2h}$  symmetry. The compound **16** has previously been prepared *via*



reaction of 2,5-dibromo-terephthalaldehyde with diphenyl( $\alpha$ -chlorobenzyl)phosphate in the presence of NaH.<sup>155</sup> However, this reaction gave a moderate yield (48%) so instead a simple palladium catalysed coupling between **15** and phenylacetylene under mild conditions was employed, which gave the precursor for star type tetraethynyl benzene complexes in 70% yield (**Scheme 8**). A more vigorous cross-coupling reaction under elevated temperatures does not give an increased yield of the desired **16**, but rather results in the formation of a low solubility material,<sup>156</sup> which was not characterised.



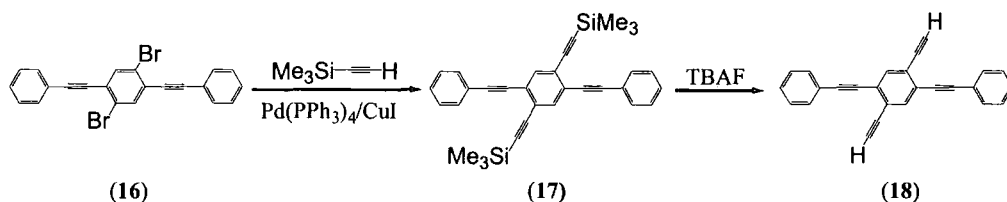
**Scheme 8.** Synthetic route to the formation of **16**.

The EI-MS spectrum of **16** exhibited a molecular ion at  $m/z$  436, while the IR spectrum had a weak absorption band for  $\nu(\text{C}\equiv\text{C})$  at  $2221\text{ cm}^{-1}$ . The  $^1\text{H}$  NMR spectrum showed only peaks in the aromatic region which consisted of a doublet at  $\delta$  7.38 ppm, a multiplet at  $\delta$  7.58 ppm, and a singlet at  $\delta$  7.79 ppm from the uncoupled proton on the inner aromatic ring. The  $^{13}\text{C}$  NMR spectrum shows two resonances at  $\delta$  86.79 and 96.64 ppm due to the acetylenic carbons, with all seven non equivalent aromatic carbon resonances observed.

The molecular structure of **16** was confirmed by X-ray crystallography using single crystals grown from  $\text{CH}_2\text{Cl}_2:\text{MeOH}$  (**Figure 46**), with crystallographic data given in **Table 6**. One of the interesting features of the structure is that the two outer aromatic rings are rotated by  $40.2^\circ$  with respect to the plane of the inner rings, which is one of the largest rotation observed for a three ring phenyl system linked by alkyne moieties (**Table 4**). The acetylene moieties connecting the outer and inner rings has a definite single-triple-single

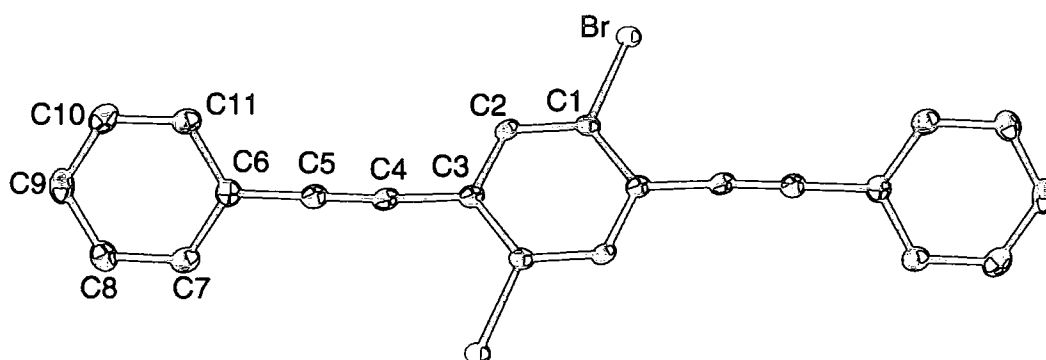
bond alteration with C(6)-C(5) 1.442(4) Å, C(5)-C(4) 1.203(4) Å, C(4)-C(3) 1.434(4) Å, with the alkyne moieties being nearly linear with a C(6)-C(5)-C(4) angle of 178.8(3)°, and a C(5)-C(4)-C(3) angle of 174.2(3)°. The molecule packs in a herringbone fashion with approximately 6 Å between the bromine atoms (**Figure 47**).

Wire-like sub-structures were assembled from a cross-coupling reaction of **16** with two equivalents of the appropriate aryl acetylene. One such compound was 1,4-diethynyl-2,5-*bis*(phenylethynyl)benzene (**18**), which was synthesised *via* a palladium catalysed coupling between **16** and trimethylsilylacetylene to give 1,4-*bis*(phenylethynyl)-2,5-*bis*(trimethylsilylethynyl)benzene (**17**) as a tan solid after the removal of the alkylammonium salt and chromatography. The silyl group was readily removed (NBu<sub>4</sub>F/H<sub>2</sub>O) (**Scheme 9**) to afford the terminal di(alkyne) product, **18**, with an overall yield of ca. 80%. Further functionalisation of the reactive C≡CH moieties makes compounds such as **18** an ideal entry point into larger systems, although these reactions were not investigated in this study.

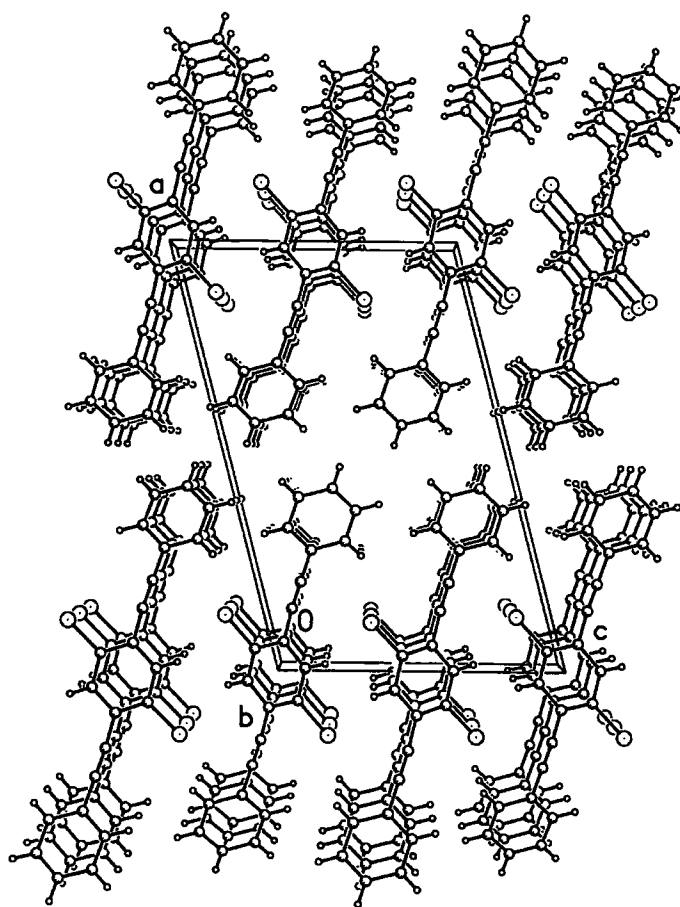


**Scheme 9.** Reaction scheme for the synthesis of **18**.

The same synthesis was also attempted utilising a palladium catalysed coupling between **16** and 2-methyl-3-butyne-2-ol as the initial protecting group. However, the yield obtained for 1,4-*bis*(phenylethynyl)-2,5-*bis*(2-methyl-3-butyne-2-ol)benzene was considerably lower than that for **17**. Attempts to deprotect this material under the standard conditions (KOH/toluene/110°C) resulted in extensive decomposition of the protected material and only minimal amounts of **18** could be obtained in this manner.



**Figure 46.** Molecular structure of **16** depicted with a 50% ellipsoid probability. Hydrogen atoms have been omitted for clarity.



**Figure 47.** Packing diagram associated with solid state structure of **16**.

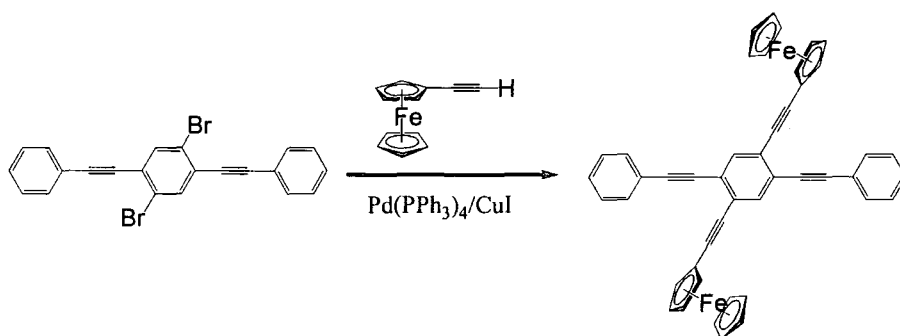
The IR spectrum of **17** showed two medium to weak absorption bands for  $\nu(\text{C}\equiv\text{C})$  at 2220 and at 2159  $\text{cm}^{-1}$  and the EI-MS spectrum exhibited a molecular ion at  $m/z$  470 with fragment peaks at  $m/z$  455-380 indicating subsequent loss of up to six methyl groups. The  $^1\text{H}$  NMR spectrum displayed a singlet at  $\delta$  -0.12 attributed to the protons of the  $\text{SiMe}_3$  groups. The aromatic region displays two multiplets at  $\delta$  7.35 ppm and 7.53 ppm and a singlet at  $\delta$  7.66 ppm. The  $^{13}\text{C}$  NMR spectra of these types of star molecules are characterised by four acetylenic carbons, a cluster of three closely spaced resonances at approximately 120 ppm which are due to the quaternary carbons of the aromatic rings, and four remaining peaks due to the remaining carbons of the aromatic rings. The  $^{13}\text{C}$  NMR spectrum shows a resonance at  $\delta$  0.0 due to the  $\text{SiMe}_3$  groups, four resonances between  $\delta$  87.28 ppm and 102.28 ppm that are due to the acetylenic carbons, with all seven non-equivalent aromatic carbon resonances observed.

The  $^1\text{H}$  NMR spectrum of **18** showed a singlet at  $\delta$  3.47 ppm with an integration of two protons attributed to the acetylenic protons of the molecule. The aromatic region consisted of two multiplets at  $\delta$  7.38 and 7.57 ppm and a singlet at  $\delta$  7.71 ppm. The  $^{13}\text{C}$  NMR spectrum displayed four resonances between  $\delta$  81.01 and 98.65 ppm attributed to the acetylenic carbons, with all seven non equivalent aromatic carbon resonances observed. The IR spectrum of **18** showed two weak absorption bands for  $\nu(\text{C}\equiv\text{C})$  at 2223 and 2105  $\text{cm}^{-1}$  and the EI-MS spectrum exhibited a molecular ion at  $m/z$  326.

### 2.3.3. 1,4-*bis*(Phenylethynyl)-2,5-*bis*(ferrocenylethynyl)benzene

Due to the versatility of precursor **16**, redox active groups can be attached directly using Sonagashira coupling reactions. Similar coupling protocols to those described above were used to synthesise the redox active ferrocene derivative, where ethynyl ferrocene was found to couple well with **16** to afford 1,4-

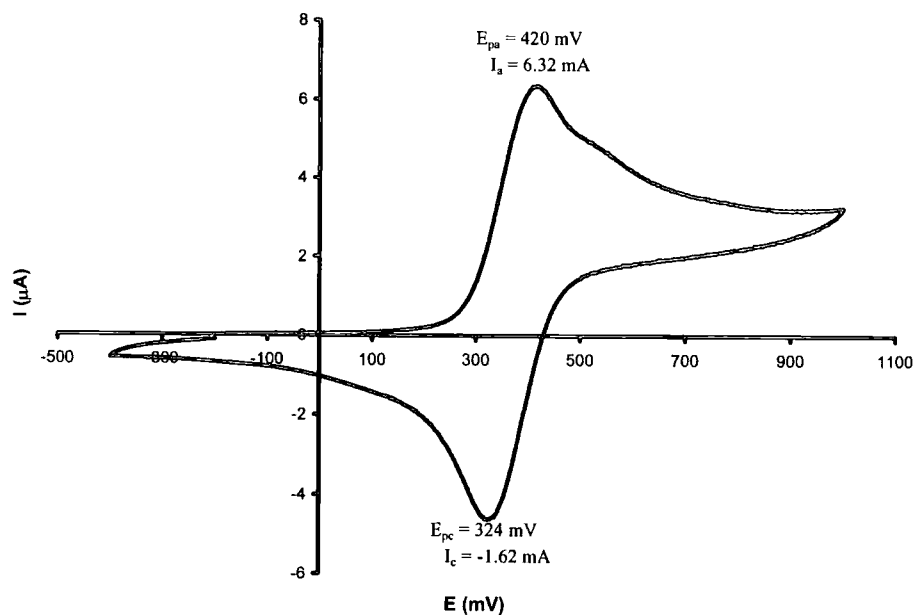
*bis(phenylethynyl)-2,5-bis(ethynylferrocene)benzene* (**19**) (**Scheme 10**) as a bright red powder after washing to remove the alkyl ammonium salts, and recrystallisation from hot benzene.



**Scheme 10.** Reaction scheme for the synthesis of **19**.

The FAB-MS spectrum of **19** exhibited a molecular ion at  $m/z$  694, and a fragment ions at  $m/z$  629 and  $m/z$  564 representing the subsequent loss of two cyclopentadiynyl (Cp) moieties. The IR spectrum contained a weak absorption band for  $\nu(\text{C}\equiv\text{C})$  at  $2204\text{ cm}^{-1}$ . The  $^1\text{H}$  NMR spectrum showed three resonances at  $\delta$  4.21, 4.28, and 4.54 ppm in a 5:2:2 ratio representing the protons of the Cp ring, while the aromatic region showed a multiplet at  $\delta$  7.40, a doublet at  $\delta$  7.63, and a singlet at  $\delta$  7.70 ppm. The  $^{13}\text{C}$  NMR spectrum showed four resonances between  $\delta$  64.69 and 71.60 ppm attributed to the carbons of the Cp rings, four resonances between  $\delta$  79.01 and 94.84 ppm due to the acetylenic carbons, with all seven non-equivalent aromatic carbon resonances observed.

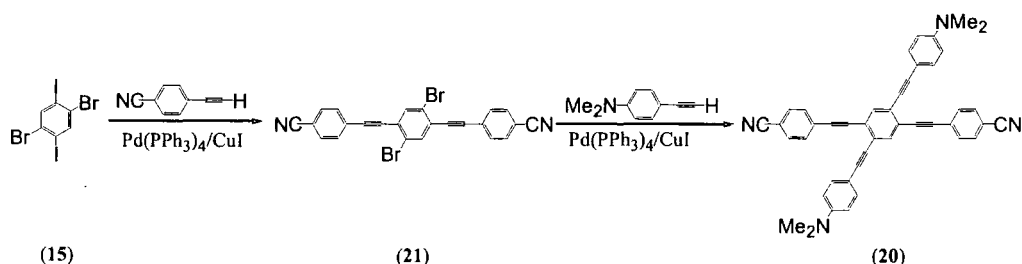
The cyclic voltammetric (CV) trace of **19** (**Figure 48**) was performed at a 100mV/s scan rate in  $\text{CH}_2\text{Cl}_2$  and showed a single quasi-reversible wave at 3.2 V. The quasi reversible nature of the redox event was established by comparing  $i_{\text{pa}}/i_{\text{pc}}$  values at different scan rates, and it was found that these values increased with  $v^{1/2}$  but were not proportional to it. The quasi reversible nature is attributed to the fact that energy matching, and hence orbital overlap between the ferrocene centres and the aromatic core is quite poor.



**Figure 48.** The CV trace of **19** at a scan rate of 100mV/s.

#### 2.3.4. 1,4-*bis*(4'-Ethynylbenzonitrile)-2,5-*bis*(4''-ethynyl-N,N-dimethylaniline)benzene

The synthesis of 1,4-*bis*(4'-ethynylbenzonitrile)-2,5-*bis*(4''-ethynyl-N,N-dimethylaniline)benzene (**20**) was carried out in a similar manner to that described for **18** via a two step Sonagashira coupling, starting from **15** core, and first coupling with ethynylbenzonitrile to give 1,4-*bis*(ethynylbenzonitrile)-2,5-dibromobenzene (**21**) followed by a second coupling with 4-ethynyl-N,N-dimethylaniline (**Scheme 11**).



**Scheme 11.** Reaction scheme for the synthesis of **20**.

The coupling of **15** with ethynylbenzonitrile proceeds at ambient temperature, to produce an off-white sparingly soluble material. The impurities were extracted into cold  $\text{CH}_2\text{Cl}_2$ , since **21** is only sparingly soluble in this solvent as well as in all other common solvents. The low solubility of this material hampered efforts to obtain a meaningful NMR spectrum. However, this intermediate could be readily characterised from the nujol mull IR spectrum, and the EI-MS spectrum. The IR spectrum showed a weak absorption band which was tentatively assigned as  $\nu(\text{C}\equiv\text{C})$  at  $1936\text{ cm}^{-1}$ , and a strong absorption band again tentatively assigned as  $\nu(\text{C}\equiv\text{N})$  at  $2236\text{ cm}^{-1}$ . It is acknowledged that in some donor-acceptor type compounds the assignment is reversed. The EI-MS spectrum exhibited a molecular ion at  $m/z$  486 and a fragment peak at 326 corresponding to loss of bromine.

The second step was the coupling of **21** with 4-ethynyl-N,N-dimethylaniline ( $\text{Pd}(\text{PPh}_3)_4/\text{CuI}/\text{NEt}_3$ ) to produce **20**. The reaction was performed at elevated temperatures producing an insoluble orange powder which was washed with water to remove any alkylammonium salts, then washed with MeOH, EtOH and finally diethyl ether to remove the water. The desired compound was obtained after recrystallisation from hot  $\text{CH}_2\text{Cl}_2$ . The low solubility of **20** again hampered efforts to obtain a meaningful NMR spectrum. The IR spectrum showed a weak absorption band which was tentatively assigned as  $\nu(\text{C}\equiv\text{C})$  at  $1936\text{ cm}^{-1}$ , and a strong absorption band again tentatively assigned

as  $\nu(\text{C}\equiv\text{N})$  at  $2236\text{ cm}^{-1}$ , and the EI-MS spectrum exhibited a molecular ion at  $m/z$  614 and a fragment peak at 478 indicating a loss of ethynylbenzonitrile.

A small amount of product could be dissolved in  $\text{CDCl}_3$  at  $50\text{ }^\circ\text{C}$ , to obtain an NMR spectrum. However the signals obtained were not consistent with the desired product but were consistent with that of 1,4-*bis*(4'-ethynylbenzonitrile)-2-(4''-ethynyl-N,N-dimethylaniline)-3-(bromo)benzene. It is believed that a small amount of 1,4-*bis*(4'-ethynylbenzonitrile)-2-(4''-ethynyl-N,N-dimethylaniline)-3-(bromo)benzene is present in the sample of **20** and has a better solubility in the NMR solvent, thus giving the observed spectrum. It has also been observed that **20** was not stable in solution indicated by a bleaching of the sample when left in either  $\text{CH}_2\text{Cl}_2$  or THF.

## 2.4. Conclusion

Variable temperature fluorescence experiments suggest that for 1,4-bis(phenylethynyl)benzene type molecules, the ground state is well described in terms of a thermally populated distribution of conformers, while the excited state in these materials is best described in terms of a planar conformation with considerable acetylenic character. Despite the low barrier to rotation about the aryl-ethynyl single bond photoexcitation may offer a mechanism by which to transiently impose a planar geometry upon the molecular framework. Further studies in this area are now being directed toward utilising a combination of steric constraints and photochemical response to engineer molecular conformation. A combination of DFT-based calculations and transient absorption spectroscopy were used to probe the electronic structure of the 1,2,4,5-tetraethynyl benzene framework. Results indicate that the dominant chromophore in this motif is distinctive, and the material is not well described in terms of two crossed bis(phenyl)ethynyl moieties.



## 2.5. General Experimental

### 2.5.1. Reagents, Materials, and Solvents

All manipulations involving air sensitive reagents were performed under an atmosphere of purified nitrogen using standard Schlenk techniques. All solvents used in reactions were dried and distilled prior to use using standard methods,<sup>157</sup> with the exception of AnalR hexane and methanol. Preparative TLC was performed on 20 x 20 cm glass plates coated with silica gel (Merck GF254, 0.5 mm thick). Unless otherwise noted, all chemicals were purchased from commercial sources and used without further purification. Literature methods were used to prepare trimethylsilylacetylene,<sup>158</sup> 4-ethynyl-N,N-dimethylaniline, 4-ethynylbenzonitrile,<sup>159</sup>  $\text{Pd}(\text{PPh}_3)_4$ ,<sup>160</sup>  $\text{Pd}(\text{PPh}_3)_2\text{Cl}_2$ ,<sup>161</sup>  $[\text{Co}_2(\text{CO})_6(m\text{-dppm})]$ ,<sup>162</sup> ethynylferrocene,<sup>163</sup> 1,3-butadiyne,<sup>164</sup>  $\text{Ni}(\text{C}\equiv\text{CC}\equiv\text{CH})(\text{PPh}_3)\text{Cp}$ ,<sup>165</sup> 1,6-bis(trimethylsilyl)-1,3,5-hexatriyne,<sup>166</sup>  $\text{RuCl}(\text{PPh}_3)_2\text{Cp}$ ,<sup>167</sup> 1,4-dibromo-2,5-diiodobenzene,<sup>154</sup> 1,2,4,5-tetrakis(phenylethynyl)benzene,<sup>93</sup>  $[\text{Ru}_4(\mu_4\text{-}\eta^2\text{-Me}_3\text{SiC}\equiv\text{CC}_2\text{C}\equiv\text{CSiMe}_3)(\text{CO})_{12}]$ ,<sup>168</sup>  $[\text{Ru}_4(\mu_4\text{-}\eta^2\text{-PhC}_2\text{Ph})(\text{CO})_{12}]$ ,<sup>169, 170</sup> 1,4-diiodo-2,3,5,6-tetra(methyl)benzene.<sup>152</sup>

### 2.5.2. NMR, Mass, FTIR and UV-vis Spectroscopy

$^1\text{H}$  and  $^{13}\text{C}$  NMR spectra were obtained using the following spectrometers: Varian Mercury at 200 MHz, Bruker AM-250 at 250 MHz, Varian Unity ASM – 100 at 300 MHz, Varian VXR400, Varian Mercury at 400 MHz, and Varian Unity Inova at 500 MHz. All spectra were obtained using either  $\text{CDCl}_3$ ,  $(\text{CH}_3)_4\text{Si}$ ,  $\text{C}_6\text{DH}_5$ , and/or  $(\text{CH}_3)(\text{CH}_2\text{D})\text{SO}$  as internal references.

GC – MS analyses were performed on a Hewlett – Packard 5890 Series II chromatograph equipped with a 5971A mass selective detector and a fused silica column. EI mass spectra were obtained using Micromass Autospec or a Finigan

Trace MS mass spectrometer. All low resolution Fast Atom Bombardments were performed at the EPSRC National Mass Spectrometry Service Centre.

Infrared spectra were recorded from samples in Nujol mounted between NaCl disks or in solutions (0.1 mm  $\text{CaF}_2$  cell) as indicated using a Nicolet Avatar FT-IR spectrometer. UV – vis spectra were obtained in a 1 mm path length quartz cell with a Varian Cary 5 UV – Vis – NIR spectrophotometer.

### **2.5.3. Gas Liquid Chromatography, Elemental and X-Ray Analysis**

Chromatographic analyses were performed on a Hewlett Packard 5890 Series II gas liquid chromatograph equipped with a 25 m cross-linked methyl silicone capillary column with a flame ionisation detector.

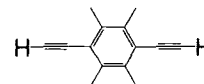
Carbon, hydrogen and nitrogen analysis were obtained using an Exeter Analytical CE-440 Elemental Analyser. Crystal structures were obtained from a Bruker Smart 1K CCD diffractometer or a Bruker Smart 6K CCD diffractometer.

### **2.5.4. CV Analysis**

Cyclic voltametry experiments were recorded between ambient and  $-40^\circ\text{C}$  using an EG & G Verastat II potentiometer. The CV was performed in either dry  $\text{CH}_2\text{Cl}_2$  or THF containing 0.1 M  $[\text{NBu}_4]\text{PF}_6$ . Solutions were purged with nitrogen prior to measurements using a Pt working electrode with Pt wire as a pseudo reference and counter electrode. The scans were referenced against internal ferrocene/ferrocinium redox couples at 0.39 V.

## 2.6. Experimental

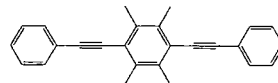
### 2.6.1. 1,4-ethynyl-2,3,5,6-tetra(methyl)benzene (1,4-ethynyldurene) (12)



Dry  $\text{NH}_4\text{Et}_2$  (50 ml) was introduced to an oven-dried Schlenk flask and rigorously degassed by three freeze-pump-thaw sequences. The compound 1,4-diiodo-2,3,5,6-tetra(methyl)benzene (9.95 g, 0.026 mol) was added followed by trimethylsilyl acetylene (20 ml, 0.14 mol),  $\text{Pd}(\text{PPh}_3)_4$  (0.78 g, 0.06 mmol) and  $\text{CuI}$  (0.12 g, 0.065 mmol). The solution was stirred overnight, and the solvent removed *in vacuo*. The residue was extracted into  $\text{CH}_2\text{Cl}_2$  then washed with a saturated aqueous solution of sodium bicarbonate, dried over  $\text{MgSO}_4$ , and the solvent removed. The solid was dissolved in THF (100 ml) and MeOH (20 ml). To the solution TBAF (20 ml, 1 M sol in THF) was added and the solution stirred for 3h. The solvent was removed and the crude product was purified by overnight Soxhlet extraction using hexane as the extraction solvent. Evaporation of the extract gave the desired product as a yellow solid (3.58 g, 0.019 mol, 73 %).

IR (nujol):  $\nu(\text{C}\equiv\text{C})$  2097  $\text{w cm}^{-1}$ .  $^1\text{H}$  NMR (399 MHz,  $\text{CDCl}_3$ ):  $\delta$  2.34 (s, 12H,  $\text{CH}_3$ ), 3.46 (s, 2H, H).  $^{13}\text{C}$  NMR (100 MHz,  $\text{CDCl}_3$ ):  $\delta$  18.25 ( $\text{CH}_3$ ), 82.24, 85.73 (2 x  $\text{C}\equiv\text{C}$ ), 122.61, 136.32 (2 x Ar). EI - MS ( $m/z$ ): 182  $[\text{M}]^+$ , 167  $[\text{M}-\text{Me}]^+$  Anal. Calc'd for  $\text{C}_{14}\text{H}_{14}$ .1/4 $\text{CH}_2\text{Cl}_2$ : C 84.13, H 7.13%. Found: C 86.91, H 7.49%.

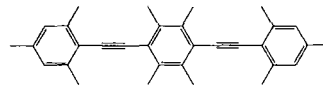
**2.6.2. 1,4-bis(phenylethynyl)-2,3,5,6-tetra(methyl)benzene**  
**(1,4-bis(phenylethynyl)-durene) (8)**



Dry  $\text{NEt}_3$  (50 ml) was introduced to an oven-dried Schlenk flask and rigorously degassed by three freeze-pump-thaw sequences. The compound 1,4-diiododurene (2.08 g, 5.38 mmol) was added followed by phenyl acetylene (2.5 ml, 17.69 mmol),  $\text{Pd}(\text{PPh}_3)_4$  (0.18 g, 0.15 mmol) and  $\text{CuI}$  (0.03 g, 0.15 mmol). The solution was stirred overnight. The solvent was removed from the resulting brown solution *in vacuo* and the residue extracted into hot  $\text{CH}_2\text{Cl}_2$  then washed with a saturated aqueous solution of sodium bicarbonate, dried over  $\text{MgSO}_4$ , and the solvent removed. The crude product was purified by column chromatography (silica, hexane) and the product (yellow band) was eluted with hexane. The product was recrystallised from  $\text{CH}_2\text{Cl}_2$ :MeOH (1.02 g, 2.55 mol, 57%).

IR (nujol):  $\nu(\text{C}\equiv\text{C})$  2208 w  $\text{cm}^{-1}$ .  $^1\text{H}$  NMR (499 MHz,  $\text{CDCl}_3$ ):  $\delta$  2.52 (s, 12H,  $\text{CH}_3$ ), 7.34-7.40 (m, 6H, Ar), 7.57 (d, 4H, Ar,  $J_{\text{HH}}=8$  Hz).  $^{13}\text{C}$  NMR (125 MHz,  $\text{CDCl}_3$ ):  $\delta$  18.68 ( $\text{CH}_3$ ), 88.88, 98.32 (2 x  $\text{C}\equiv\text{C}$ ), 123.54, 127.10, 128.37, 128.64, 131.62, 135.93 (6 x Ar). EI - MS ( $m/z$ ): 334  $[\text{M}]^+$ , 319-304  $[\text{M}-n\text{CH}_3]^+$  ( $n=1-2$ ). Anal. Calc'd for  $\text{C}_{26}\text{H}_{22}$ : C 93.41, H 6.58%. Found: C 92.36, H 7.02%.

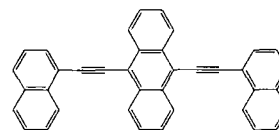
**2.6.3. 1,4-bis(2',4',6'-tri(methyl))-2,3,5,6-tetra(methyl)benzene  
(1,4-(ethynylmesitylene)durene) (9)**



Dry  $\text{NEt}_3$  (50 ml) was introduced to an oven-dried Schlenk flask and rigorously degassed by three freeze-pump-thaw sequences. The compound 1,4-ethynyl-2,3,5,6-tetra(methyl)benzene (1 g, 5.49 mmol) was added followed by iodomesitylene (2.7 g, 10.97 mmol),  $\text{Pd(PPh}_3)_4$  (0.3 g, 0.26 mmol) and  $\text{CuI}$  (0.1 g, 0.52 mmol). The solution was stirred for two days, and the solvent removed *in vacuo*. The residue was extracted into  $\text{CH}_2\text{Cl}_2$  then washed with a saturated aqueous solution of sodium bicarbonate, dried over  $\text{MgSO}_4$ , and the solvent removed. The impurities were extracted into hexane, leaving behind the desired product as a yellow solid (0.61 g, 1.46 mmol, 27 %).

IR (nujol):  $\nu(\text{C}\equiv\text{C})$  2128 vw  $\text{cm}^{-1}$ .  $^1\text{H}$  NMR (499 MHz,  $\text{CDCl}_3$ ):  $\delta$  2.32 (s, 6H,  $\text{CH}_3$ ), 2.53 (s, 12H,  $\text{CH}_3$ ), 2.56 (s, 12H,  $\text{CH}_3$ ), 6.93 (s, 4H, Ar).  $^{13}\text{C}$  NMR (105 MHz,  $\text{CDCl}_3$ ):  $\delta$  21.03, 21.27, 26.61 (3 x  $\text{CH}_3$ ), 96.04, 96.07 (2x  $\text{C}\equiv\text{C}$ ), 120.39, 123.57, 127.44, 135.05, 137.37, 139.75 (6 x Ar). EI - MS ( $m/z$ ): 418  $[\text{M}]^+$ , 388  $[\text{M}-2\text{CH}_3]^+$  Anal. Calc'd for  $\text{C}_{32}\text{H}_{34}$ : C 91.86, H 8.13%. Found: C 90.77, H 8.12%.

**2.6.4. 9,10-di(1-ethynylnaphthalene)anthracene (13)**

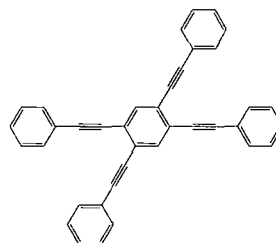


Dry  $\text{NHet}_2$  (30 ml) was introduced to an oven-dried Schlenk flask and rigorously degassed by three freeze-pump-thaw sequences. The compound 1-ethynylnaphthalene (1.07 g, 7.04 mmol) was added followed by 9,10-dibromoanthracene (1.15 g, 3.42 mmol),  $\text{Pd(PPh}_3)_4$  (0.51 g, 0.04 mmol) and  $\text{CuI}$

(0.06 g, 0.03 mmol). The solution was heated at reflux overnight, cooled and the solvent removed *in vacuo*. The crude product was washed with water, MeOH, EtOH and diethyl ether. The orange solid remaining contained the desired product and was recrystallised from hot CH<sub>2</sub>Cl<sub>2</sub> (1.5 g, 3.13 mmol, 92%).

IR (nujol):  $\nu(\text{C}\equiv\text{C})$  2192 w cm<sup>-1</sup>. <sup>1</sup>H NMR (499 MHz, CDCl<sub>3</sub>):  $\delta$  7.73 (m, 8H, Ar), 7.95 (d, 4H, Ar,  $J_{\text{HH}}=7.99$ ), 8.05 (d, 3H, Ar,  $J_{\text{HH}}=6.99$ ), 8.71 (d, 3H, Ar,  $J_{\text{HH}}=8.49$ ), 8.87 (m, 4H, Ar). <sup>13</sup>C NMR (125 MHz, CDCl<sub>3</sub>):  $\delta$  90.98, 100.41 (2x C $\equiv$ C), 125.72, 126.62, 126.88, 127.28, 127.44, 127.67, 128.79, 129.79, 131.18, 132.54, 133.13, 133.50, 133.65, 136.63 (14 x Ar). EI - MS ( $m/z$ ): 478 [M]<sup>+</sup>, 350 [M-C<sub>10</sub>H<sub>7</sub>+H]<sup>+</sup>, 326 [M-C<sub>12</sub>H<sub>8</sub>]<sup>+</sup>. Anal. Calc'd for C<sub>38</sub>H<sub>22</sub>: C 95.39, H 4.60 %. Found: C 94.78, H 4.51%.

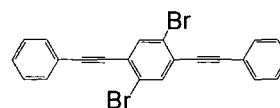
#### 2.6.5. 1,2,4,5-tetra(phenylethynyl)benzene (14)



Dry NEt<sub>3</sub> (70 ml) was introduced to an oven-dried Schlenk flask and rigorously degassed by three freeze-pump-thaw sequences. The compound 1,2,4,5-tetrabromobenzene (2 g, 5.08 mmol) was added followed by phenyl acetylene (3 ml, 21.23 mmol), Pd(PPh<sub>3</sub>)<sub>4</sub> (0.15 g, 0.12 mmol) and CuI (0.03 g, 0.15 mmol). The solution was heated at reflux overnight forming a dark red solution containing a white precipitate. The precipitate was collected by filtration, extracted into CH<sub>2</sub>Cl<sub>2</sub> then washed with a saturated aqueous solution of sodium bicarbonate, dried over MgSO<sub>4</sub>, and the solvent removed. The crude product was purified by column chromatography (silica, hexane) and the product (yellow band) was eluted with hexane. The product was recrystallised from CH<sub>2</sub>Cl<sub>2</sub>:hexane to give pale yellow spars (1.22 g, 2.55 mmol, 50%).

IR (nujol):  $\nu(\text{C}\equiv\text{C})$  2223 vw, 2202 vw  $\text{cm}^{-1}$ .  $^1\text{H}$  NMR (499 MHz,  $\text{CDCl}_3$ ):  $\delta$  7.36-7.40 (m, 11H, Ar), 7.59-7.62 (m, 7H, Ar), 7.79 (s, 22H, Ar).  $^{13}\text{C}$  NMR (125 MHz,  $\text{CDCl}_3$ ):  $\delta$  87.79, 95.73 (2 x  $\text{C}\equiv\text{C}$ ), 123.22, 125.59, 128.72, 129.01, 132.00, 135.16 (6 x Ar). EI - MS ( $m/z$ ): 478  $[\text{M}]^+$ , 400  $[\text{M}-\text{Ar}]^+$ . Anal. Calc'd for  $\text{C}_{38}\text{H}_{22}$ : C 95.39, H 4.60%. Found: C 95.09, H 4.57%.

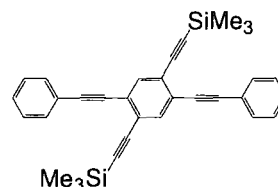
#### 2.6.6. 1, 4-Dibromo-2,5-bis(phenylethynyl)benzene (16)



Dry  $\text{NHPr}^i_2$  (30 ml) was introduced to an oven-dried Schlenk flask and rigorously degassed by three freeze-pump-thaw sequences. The compound 1,4-dibromo-2,5-diiodo-benzene (2.03 g, 4.15 mmol) was added followed by phenyl acetylene (1.0 ml, 9.12 mmol),  $\text{Pd}(\text{PPh}_3)_4$  (0.46 g, 0.43 mmol) and  $\text{CuI}$  (0.05 g, 0.26 mmol). The solution was heated at reflux overnight forming a yellow solution with white precipitate which was presumed to be the alkylammonium salt  $[\text{NHPr}^i_2]\text{I}$ . The solution was cooled and the solvent removed *in vacuo*. The residue was extracted into  $\text{CH}_2\text{Cl}_2$ , washed with a saturated aqueous solution of sodium bicarbonate, dried over  $\text{MgSO}_4$ , and the solvent removed. The impurities were extracted into MeOH and the product recrystallised from  $\text{CH}_2\text{Cl}_2$ :MeOH giving white needle-like crystals (1.27 g, 2.9 mmol, 70%).

IR (nujol):  $\nu(\text{C}\equiv\text{C})$  2221 w  $\text{cm}^{-1}$ .  $^1\text{H}$  NMR (499 MHz,  $\text{CDCl}_3$ ):  $\delta$  7.38 (m, 6H, Ar), 7.58 (m, 4H, Ar), 7.79 (s, 2H, Ar).  $^{13}\text{C}$  NMR (125 MHz,  $\text{CDCl}_3$ ):  $\delta$  86.79, 96.64 (2 x  $\text{C}\equiv\text{C}$ ), 122.28, 123.71, 126.38, 128.48, 129.13, 131.79, 136.01 (7 x Ar). EI<sup>+</sup> - MS ( $m/z$ ): 436  $[\text{M}]^+$ . Anal. Calc'd for  $\text{C}_{22}\text{H}_{12}\text{Br}_2$ : C 60.55, H 2.75%. Found: C 60.34, H 2.61%.

#### 2.6.7. 1,4-*bis*(phenylethynyl)-2,5-*bis*(trimethylsilylethynyl)benzene (17)

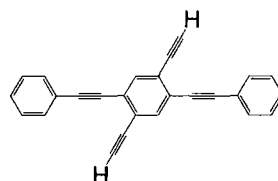


Dry NEt<sub>3</sub> (50 ml) was introduced to an oven-dried Schlenk flask and was rigorously degassed by three freeze-pump-thaw sequences. The compound 1,4-dibromo-2,5-*bis*(phenylethynyl)benzene (2.1 g, 4.8 mmol) was added followed by trimethylsilyl acetylene (5.5 ml, 3.82 g, 39 mmol), Pd(PPh<sub>3</sub>)<sub>4</sub> (0.34 g, 0.03 mmol) and CuI (0.04 g, 0.21 mmol). The solution was heated at reflux overnight, cooled, and the solvent removed *in vacuo*. The residue was extracted into CH<sub>2</sub>Cl<sub>2</sub>, washed with a saturated aqueous solution of sodium bicarbonate, dried over MgSO<sub>4</sub>, and the solvent removed. The product was purified by column chromatography (silica, hexane) and eluted with a CH<sub>2</sub>Cl<sub>2</sub>:hexane gradient. The product was a yellow solid (2.03g, 89%).

IR (nujol):  $\nu(\text{C}\equiv\text{C})$  2220 w, 2159 m cm<sup>-1</sup>. <sup>1</sup>H NMR (250 MHz, CDCl<sub>3</sub>):  $\delta$  0.26 (s, 18H, SiMe<sub>3</sub>), 7.35 (m, 6H, Ar), 7.53 (m, 4H, Ar), 7.66 (s, 2H, Ar). <sup>13</sup>C NMR (63 MHz, CDCl<sub>3</sub>):  $\delta$  -0.12 (SiMe<sub>3</sub>), 87.28, 95.32, 100.91, 102.28 (4 x C $\equiv$ C), 122.91, 125.25, 125.38, 128.33, 128.67, 131.73, 135.35 (7 x Ar). EI<sup>+</sup> - MS (*m/z*): 470 [M]<sup>+</sup>, 455-380 [M-*n*CH<sub>3</sub>]<sup>+</sup> *n*=1-6. Anal. Calc'd for C<sub>32</sub>H<sub>30</sub>Si<sub>2</sub>.1/2CH<sub>2</sub>Cl<sub>2</sub>: C 76.09, H 6.05 %. Found: C 74.70, H 6.49%.



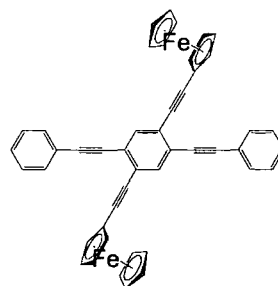
### 2.6.8. 1,4-bis(phenylethynyl)-2,5-bis(ethynyl)benzene (18)



A flask was charged with 1,4-bis(phenylethynyl)-2,5-bis(trimethylsilylethynyl)benzene (0.31 g, 0.65 mmol) which was dissolved in wet THF (10 ml; containing 0.1 ml MeOH). To this solution, TBAF (1 M sol in water, 0.1 ml) was added and the reaction stirred for 1h then the solvent removed *in vacuo*. The product was purified by preparative TLC (CH<sub>2</sub>Cl<sub>2</sub>) resulting in a tan solid (0.19 g, 0.58, 89%).

IR (nujol):  $\nu(\text{C}\equiv\text{C})$  2223 w, 2105 vw cm<sup>-1</sup>. <sup>1</sup>H NMR (499 MHz, CDCl<sub>3</sub>):  $\delta$  3.47 (s, 2H, C $\equiv$ CH), 7.38 (m, 5H, Ar), 7.57 (m, 5H, Ar), 7.71 (s, 2H, Ar). <sup>13</sup>C NMR (125 MHz, CDCl<sub>3</sub>):  $\delta$  81.01, 83.08, 86.85, 98.65 (4 x C $\equiv$ C), 122.67, 124.74, 125.73, 128.39, 128.86, 131.82, 135.60 (7 x Ar). EI - MS (*m/z*): 326 [M]<sup>+</sup>. Anal. Calc'd for C<sub>26</sub>H<sub>14</sub>.1/2CH<sub>2</sub>Cl<sub>2</sub>: C 86.29, H 4.07 %. Found: C 85.20, H 4.20%.

### 2.6.9. 1,4-phenylethynyl-2,5-bis(ethynylferrocene)benzene (19)

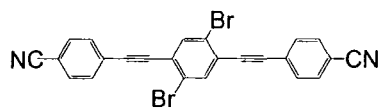


Dry NHPr<sup>i</sup><sub>2</sub> (35 ml) was introduced to an oven-dried Schlenk flask and rigorously degassed by three freeze-pump-thaw sequences. The compound 1,4-dibromo-2,5-bis(phenylethynyl)benzene (0.4 g, 0.94 mmol) was added followed by ethynylferrocene (0.36 g, 1.71 mmol), Pd(PPh<sub>3</sub>)<sub>4</sub> (0.18 g, 0.16 mmol) and CuI

(0.03 g, 0.15 mmol). The solution was heated at reflux for 6 h resulting in a red solution. The solution was cooled and the solvent removed *in vacuo*. The solid residue extracted into CH<sub>2</sub>Cl<sub>2</sub>, washed with a saturated aqueous solution of sodium bicarbonate, dried over MgSO<sub>4</sub>, and the solvent removed. The product was recrystallised from hot benzene to give a bright red powder (0.5 g, 0.73 mmol, 77%).

IR (nujol):  $\nu(\text{C}\equiv\text{C})$ : 2204 w cm<sup>-1</sup>. <sup>1</sup>H NMR (399 MHz, CDCl<sub>3</sub>):  $\delta$  4.21 (s, 10H, Cp), 4.28 (s, 4H, Cp), 4.54 (s, 4H, Cp), 7.40 (m, 6H, Ar), 7.63 (d, 4H, Ar,  $J_{\text{HH}}=9.19$ ), 7.70 (s, 2H, Ar). <sup>13</sup>C NMR (100 MHz, CDCl<sub>3</sub>):  $\delta$  64.68, 69.17, 70.12, 71.60 (4 x Cp), 79.01, 84.04, 87.88, 94.84 (4 x C $\equiv$ C), 123.12, 124.81, 125.33, 128.43, 128.65, 131.75, 134.64 (7 x Ar). FAB - MS ( $m/z$ ): 694 [M]<sup>+</sup>, 629-564 [M-nC<sub>5</sub>H<sub>5</sub>]<sup>+</sup>(n=1-2). Anal. Calc'd for Fe<sub>2</sub>C<sub>46</sub>H<sub>30</sub>.CH<sub>2</sub>Cl<sub>2</sub>: C 72.49, H 4.13%. Found: C 72.52, H 4.20%.

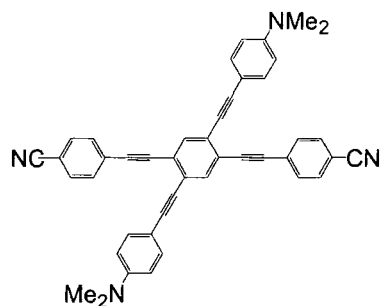
#### 2.6.10. 1,4-bis(ethynylbenzonitrile)-2,5-dibromobenzene (21)



Dry NHEt<sub>2</sub> (30 ml) was introduced to an oven-dried Schlenk flask and rigorously degassed by three freeze-pump-thaw sequences. The compound 1,4-dibromo-2,5-diiodobenzene (1.87 g, 3.83 mmol) was added followed by ethynylbenzonitrile (0.97 g, 7.64 mmol), Pd(PPh<sub>3</sub>)<sub>4</sub> (0.25 g, 0.22 mmol) and CuI (0.05 g, 0.26 mmol). The solution was stirred overnight forming a brown solution with resin-like precipitate. The solvent was removed *in vacuo*. The residue was washed with water, MeOH, EtOH, diethyl ether, and CH<sub>2</sub>Cl<sub>2</sub>, leaving behind white solid which was the desired product. (0.86 g, 1.77 mmol, 46%).

IR (nujol):  $\nu(\text{C}\equiv\text{N})$  2236 s,  $\nu(\text{C}\equiv\text{C})$  1936 w  $\text{cm}^{-1}$ . EI - MS ( $m/z$ ): 486  $[\text{M}]^+$ , 326  $[\text{M}-2\text{Br}]^+$  Anal. Calc'd for  $\text{C}_{24}\text{H}_{10}\text{N}_2\text{Br}_2 \cdot 1/3\text{CH}_2\text{Cl}_2$ : C 56.81, H 2.07, N 5.45%. Found: C 56.27, H 2.02, N 5.49%.

**2.6.11. 1,4-bis(4'-ethynylbenzonitrile)-2,5-bis(4''-ethynyl-N,N-dimethylaniline)benzene (20)**



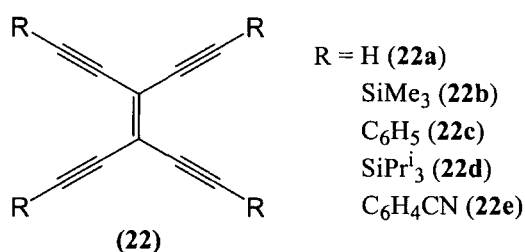
Dry  $\text{NEt}_3$  (50 ml) was introduced to an oven-dried Schlenk flask and rigorously degassed by three freeze-pump-thaw sequences. The compound 1,4-bis(ethynylbenzonitrile)-2,5-dibromobenzene (1.0 g, 2.06 mmol) was added followed by 4-ethynyl-N,N-dimethylaniline (0.59 g, 4.07 mmol),  $\text{Pd}(\text{PPh}_3)_4$  (0.15 g, 0.01 mmol) and  $\text{CuI}$  (0.02 g, 0.01 mmol). The solution was heated at reflux overnight, cooled and the yellow precipitate filtered off. The precipitate was washed with water, MeOH, EtOH, and diethyl ether. The solid was recrystallised from hot  $\text{CH}_2\text{Cl}_2$  to give a yellow powder (0.78 g, 1.27 mmol, 62%).

IR (nujol):  $\nu(\text{C}\equiv\text{N})$  2227 m,  $\nu(\text{C}\equiv\text{C})$  2199 m  $\text{cm}^{-1}$ . EI - MS ( $m/z$ ): 614  $[\text{M}]^+$ , 498  $[\text{M}-\text{CH}_3]^+$ , 478  $[\text{M}-\text{C}_9\text{H}_5\text{N}+\text{H}]^+$  Anal. Calc'd for  $\text{C}_{44}\text{H}_{30}\text{N}_4 \cdot \text{CH}_2\text{Cl}_2$ : C 77.25, H 4.57, N 8.01%. Found: C 76.72, H 3.94, N 8.07%.

## Chapter 3. 1,1,2,2-Tetraethynylethenes as Potential Molecular Junctions

### 3.1. Synthetic Routes to the Formation of 1,1,2,2-Tetraethynylethenes

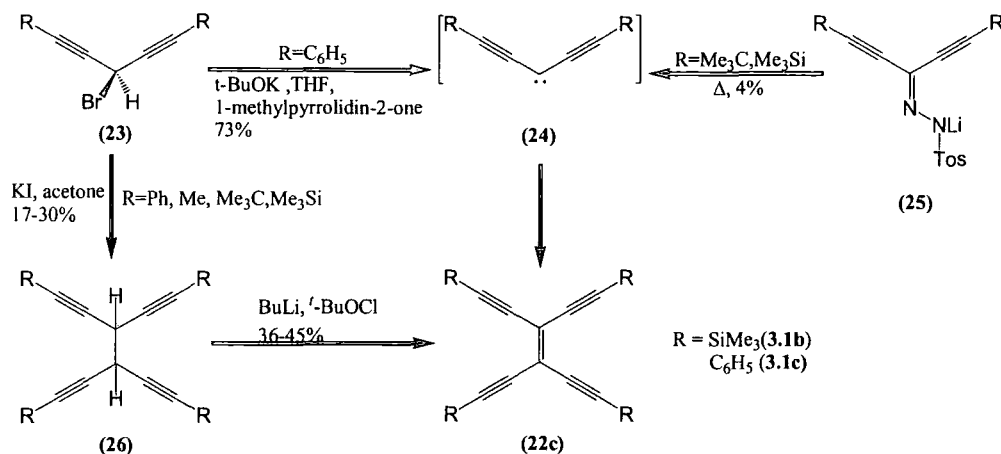
A number of  $\pi$ -conjugated oligomers of defined length and constitution have been investigated for their potential to act as a molecular wire in molecular scale electronics and nanotechnological devices.<sup>15, 171</sup> In the construction of larger, non-linear conjugated systems and carbon-rich networks,<sup>172, 173</sup> the rich variety of peralkynylated building blocks containing 1,1,2,2-tetraethynylethene (3,4-diethynylhex-3-ene-1,5-diyne) (**Figure 49**) available are particularly useful. The development of simple, efficient acetylenic coupling protocols has accelerated progress in this area,<sup>31, 121</sup> and synthetic routes to a large variety of cross-conjugated building blocks with an equally wide variety of functionalised terminal groups are now available.<sup>172, 174, 175</sup>



**Figure 49.** Structure of **22** and its derivatives.

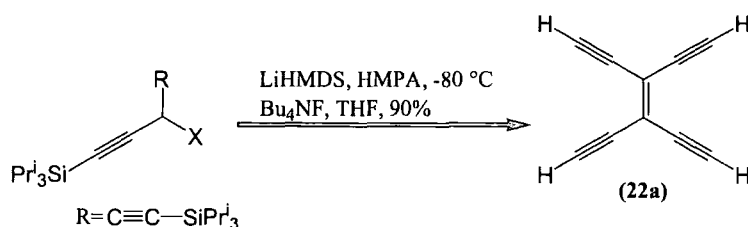
A number of synthetic routes have been employed in the preparation of the 1,1,2,2-tetraethynylethene framework (**22**). For example, treatment of 3-bromo-1,5-diphenylpenta-1,4-diyne (**23**) with potassium tert-butoxide followed by dimerisation of the formed *bis*(phenylethynyl)methylene carbene (**24**) gave **22c** (**Scheme 12**).<sup>176</sup> The reaction between **23** and potassium iodide under Finkelstein

conditions in acetone produced tetrakis(phenylethynyl)ethane (**26**) which can then be dehydrogenated to form **22b** or **22c** depending on the substituents employed in the reaction (**Scheme 12**).<sup>177, 178</sup>

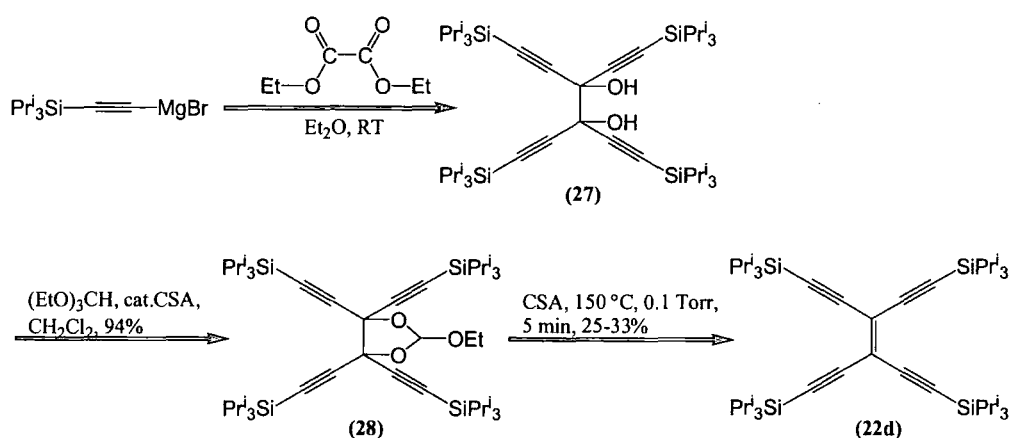


**Scheme 12.** Early synthetic routes to 1,1,2,2-tetraethynylethenes.<sup>33</sup>

A carbenoid coupling-elimination strategy (**Scheme 13**) has also been utilised for the synthesis of **22a**, which involves the slow addition of a mixture of lithium hexamethyldisilazide (LiHMDS) (or alternatively lithium diisopropylamine (LDA)) and hexamethylphosphorous triamide (HMPA) to a THF solution of an alkyne bearing the desired capping groups at low temperature. This reaction is tolerant to a wide range of functional groups and can be applied to the synthesis of both linear and cyclic enediynes.<sup>179, 180</sup> Several 1,1,2,2-tetraethynylethene type molecules have also been synthesised *via* a method involving acid catalysed thermal elimination of an orthoester moiety from the pre-formed carbon framework (**Scheme 14**).<sup>181</sup> The diol precursors (**27**) can be obtained by reaction of the alkynyl Grignard reagent with diethyloxalate. Reaction of the diol with triethyl orthoformate in the presence of catalytic amounts of camphorsulphonic acid (CSA) afforded the corresponding orthoesters (**28**). The elimination of the orthoester moieties by heating with CSA under vacuum and high temperatures produces the desired **22d**.<sup>181</sup>



**Scheme 13.** Carbenoid coupling-elimination as a 1,1,2,2-tetraethynylethene synthetic strategy.

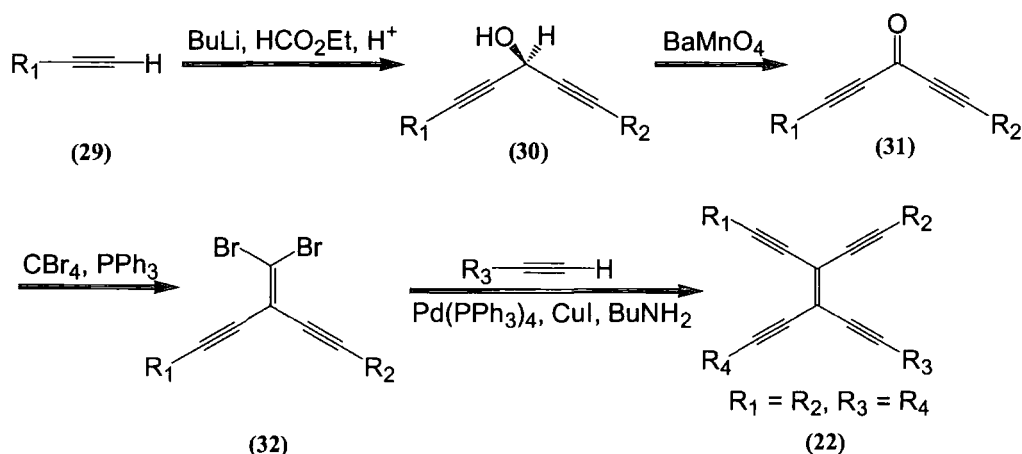


**Scheme 14.** Acid catalysed orthoester thermolysis as a 1,1,2,2-tetraethynylethene synthetic strategy.

Arguably, the most flexible strategies that provide an access to a variety of different functionalisation of the 1,1,2,2-tetraethynylethene framework are those devised by the Diederich *et al.* (Scheme 15 and 16).<sup>33, 182</sup> These methods have been comprehensively reviewed,<sup>33, 183</sup> and only the synthetic methods relevant to the work presented in this thesis will be discussed below.

The *gem*- substituted 1,1,2,2-tetraethynylethene derivatives were synthesised starting from the reaction of butyl lithium (BuLi) with a terminal acetylene (29) to form the lithium acetylides. These were subsequently allowed to react with ethylformate to form the corresponding penta-1,4-diyne-3-ol (30)

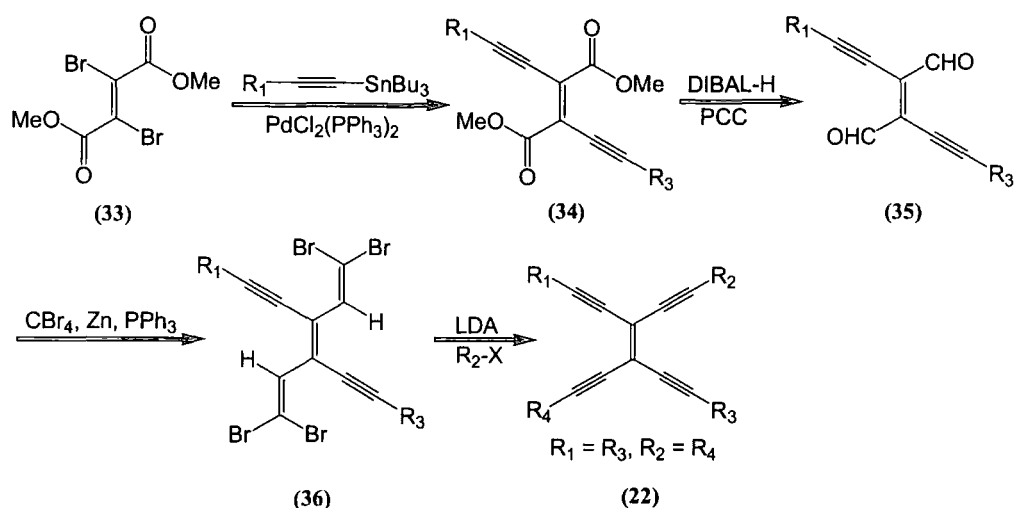
(Scheme 15). Oxidation of **30** using either barium permanganate or pyridinium chlorochromate (PCC) afforded the 1,5-disubstituted penta-1,4-diyn-3-ones (**31**). This oxidation has also been accomplished using  $K_2Cr_2O_7$  in strong acid.<sup>184</sup> The ketone was then converted to the corresponding 3-(dibromomethylidene)penta-1,4-diyne (**32**) according to the Corey and Fuchs dibromoolefination method. A palladium catalysed cross-coupling of the dibromomethylidene with a terminal acetylene yielded the desired *gem* substituted 1,1,2,2-tetraethynylethene (Scheme 15).<sup>33</sup>



**Scheme 15.** Synthesis of *gem*-tetraethynylethenes.

The preparation of *trans*-substituted 1,1,2,2-tetraethynylethenes utilised a palladium catalysed cross-coupling of a stannylated acetylene derivative with dimethyl 2,3-dibromofumarate (**33**) in THF (Scheme 16). Reduction of the resulting diester (**34**) with diisobutyl aluminium hydride (DIBAL-H) followed by PCC oxidation afforded the dialdehyde derivative (**35**), which was subjected to an analogous Corey-Fuchs (dibromoolefination) reaction, as in the synthesis of *gem*-substituted 1,1,2,2-tetraethynylethanes, utilising zinc as a reducing agent to form **36**. Elimination of hydrogen bromide, followed by metallation and subsequent quenching of the resultant dianion can be achieved with a alkyl halide to form the desired *trans*-substituted 1,1,2,2-tetraethynylethenes (Scheme 16).<sup>33</sup>





**Scheme 16.** Synthesis of *trans*-tetraethynylethenes.

The stability of 1,1,2,2-tetraethynylethane compounds largely depends on the steric protection afforded to the carbon skeleton by the substituents. If all the ethynyl moieties carry relatively bulky substituents then the compounds are very kinetically stable and can have a very high melting/decomposition point.<sup>185</sup> In general aryl-substituted 1,1,2,2-tetraethynylethenes are more stable than 1,1,2,2-tetraethynylethenes bearing one or more terminal ethynyl moieties, although bulky  $(\text{Pr}^i)_3\text{Si}$  and  $\text{SiMe}_3$  groups are also very efficient in stabilising the 1,1,2,2-tetraethynylethanes core framework. The stability of the molecule decreases with an increasing number of unsubstituted ethynyl termini and explosive decomposition of **22a** can occur at room temperature.<sup>33</sup> Despite this obvious thermal reactivity, a characteristic of 1,1,2,2-tetraethynylethane compounds **22** is the lack of chemical reactivity associated with the central olefinic bond, and attempts to add electrophiles, carbenes, 1,3-dienes, as well as oxidation and epoxidation of this bond have been all unsuccessful.<sup>186, 187</sup>

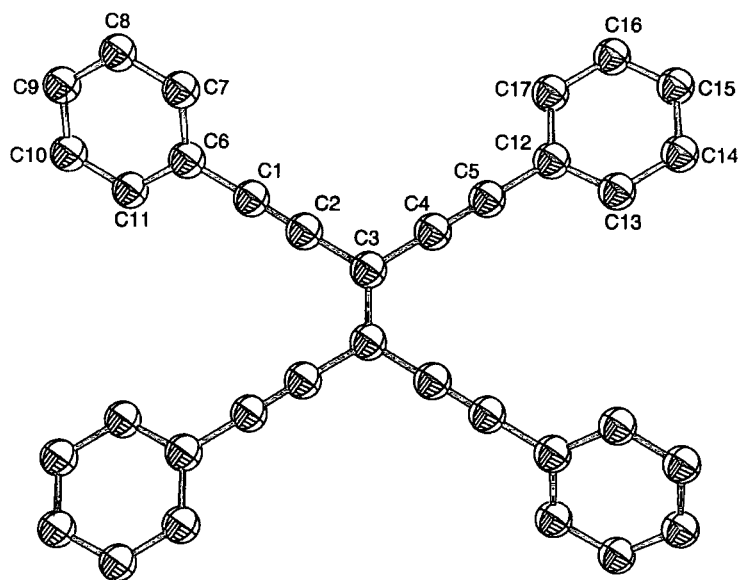
A property that exclusively belongs to aryl-substituted 1,1,2,2-tetraethynylethenes is the ability to undergo reversible, photochemical *trans*→*cis*



and *cis*→*trans* isomerisation.<sup>188</sup> Computational studies have shown that the central olefinic bond displays significant  $\pi^*$ -antibonding character facilitating facile photoisomerism, which lends itself to the construction of molecular switching components. Both *cis* and *trans* forms of aryl 1,1,2,2-tetraethynylethene derivatives are essentially strain free despite the planar geometry of the carbon core, and as a consequence of this almost non-existent thermal activation barrier, the photochemical processes are free from back reactions involving thermal isomerism.<sup>188</sup> In the case of donor/acceptor substituted 1,1,2,2-tetraethynylethanes, the photochemical isomerisation is strongly dependent on the pattern and degree of functionalisation, solvent polarity, and excitation wavelength.<sup>188</sup> This characteristic photochemical isomerisation is utilised in the construction of a light driven molecular switch,<sup>96</sup> and a three way chromophoric molecular switch,<sup>109</sup> which were described in section 1.5.1. and 1.6., respectively.

Numerous crystal structures of 1,1,2,2-tetraethynylethene derivatives have been solved,<sup>33 109, 189</sup> and the X-ray structures have characteristic bond lengths for the central C=C bond between 1.32-1.38 Å, C≡C bonds between 1.16-1.21 Å and C–C bonds between 1.42-1.48 Å.<sup>182, 190</sup> As implied above, in most cases 1,1,2,2-tetraethynylethene compounds display fully or nearly planar  $\pi$ -conjugated carbon cores which in the case of arylated 1,1,2,2-tetraethynylethenes often also include the terminal aryl rings.<sup>172</sup> For the exceptional cases where the terminal aryl rings are not in the plane of the central carbon core, they adopt an orthogonal orientation, thus maintaining conjugation by interaction with the second set of  $\pi$ -orbitals in the adjacent C≡C bond.<sup>95</sup> In the case of 1,6-*bis*(phenyl)-3-4-*bis*((phenyl)ethynyl)hex-3-ene-1,5-diyne (**22c**) (**Figure 50**), the molecules are packed in such a way that the aryl ring of one molecule lies in the cavity between the two aryl rings of the another molecule in an orthogonal position. One of the molecules is nearly planar with the aryl rings sitting at a 1.05-8.29° angle with respect to the central C=C core. In the second molecule, the aryl rings that sit *trans* to each other have approximately the same rotation with respect to the

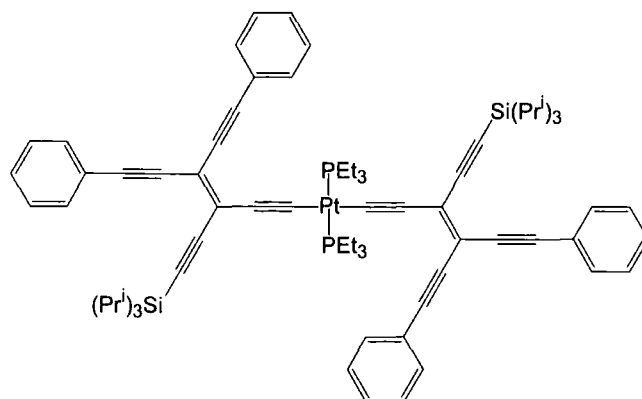
central C=C core. One set of aryl rings have a deviation of 11.62-12.64° with respect to the C=C core, while the other set of *trans* aryl rings are rotated 34.62° with respect to the C=C core.<sup>191</sup>



**Figure 50.** Molecular structure of **22c** depicted with a 50% ellipsoid probability. Hydrogen atoms have been omitted for clarity.<sup>191</sup>

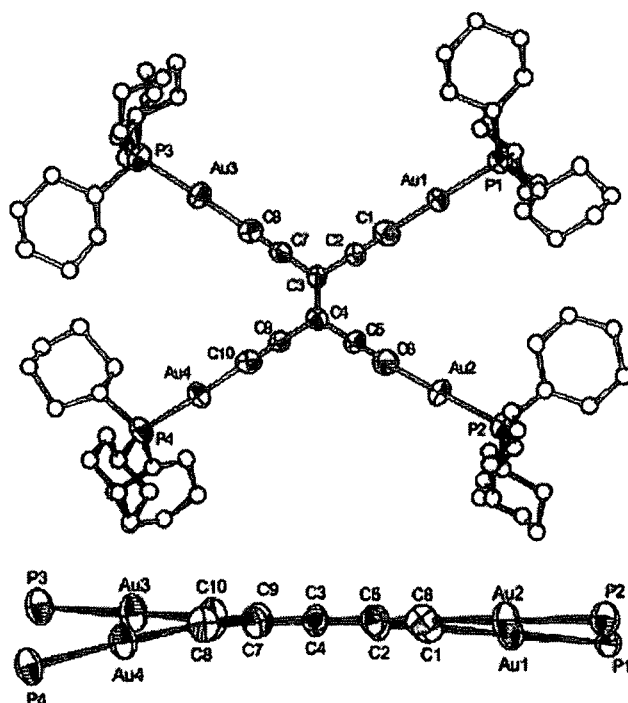
Attempts to synthesise organometallic derivatives of 1,1,2,2-tetraethynylethanes have not been widely pursued. The platinum  $\sigma$ -acetylide complex (**Figure 51**) has been synthesised for its potential as a material for non-linear optics,<sup>192</sup> and as a building block for larger monodispersed oligomers which display remarkable stability and substantial solubility.<sup>121</sup> Structural analysis of a *trans*  $\sigma$ -bis(acetylide) derivative reveals a planar structure in the solid state.<sup>193</sup> Measurements of the second hyperpolarisability constant, by third harmonic generation revealed a nearly complete lack of  $\pi$ -electron delocalisation along the oligomeric backbone.<sup>194</sup> The Pt atoms act as true insulating centres and the Pt-C(sp) bonds hardly possess any  $\pi$  character.<sup>194</sup> This is in contrast to the observation

of interaction that have been made for linearly conjugated platinum ethynyl oligomers and polymers.<sup>195-197</sup>



**Figure 51.** Structure of a platinum  $\sigma$ -acetylide oligomer bound to a 1,1,2,2-tetraethynylethene framework.

Attachment of four  $[\text{Au}(\text{PCy}_3)]_4$  ( $\text{PCy}_3$  = tricyclohexylphosphine) moieties through a  $\text{Au}-\text{C}\equiv\text{C}$   $\sigma$ -bond to the 1,1,2,2-tetraethynylethene framework has resulted in a compound with unique luminescent properties. The synthetic methodology involved a reaction of **22a** with  $\text{AuCl}(\text{PCy}_3)$  in a solution of methanol/methoxide, which afforded  $[\text{Au}(\text{PCy}_3)]_4\{\mu-\text{C}(\text{C}\equiv\text{C})_2=\text{C}(\text{C}\equiv\text{C})_2\}$  (**27**). The tetragold complex (**37**) exhibits a rich photochemical response, with triplet character in the radiative excited states through Au induced spin-orbital coupling. The crystal structure of **37** (**Figure 52**) showed that all bond angles, with acetylenic carbon and gold atoms as vertices, deviate only slightly from linearity ( $171(1)$ - $179(4)^\circ$ ). Most of the core 1,1,2,2-tetraethynylethene framework parameters are slightly elongated from a purely organic 1,1,2,2-tetraethynylethene with the central  $\text{C}=\text{C}$  being  $1.37(2)$  Å, while the  $\text{C}\equiv\text{C}$  bonds are  $1.24(2)$  and  $1.22(2)$  Å and the  $\text{C}-\text{C}$  bonds are  $1.45(2)$  and  $1.44(2)$  Å.

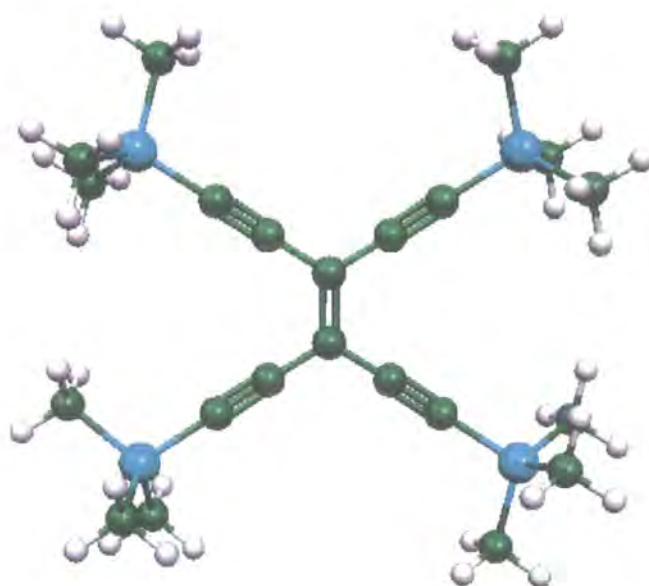


**Figure 52.** Molecular structure of **37** depicted with a 50% ellipsoid probability. Hydrogen atoms have been omitted for clarity.<sup>198</sup>

The cross-conjugated ene{tetra(yne)} framework in **22** contains a total of six conjugation pathways in two dimensions, with the linear *cis*- and *trans*-conjugation being a more effective electronic pathways than the *geminal* cross-conjugation pathway, which has been introduced in section 1.4.3.<sup>94</sup> A theoretical study has been performed to rationalise the impact of different delocalisation pathways of the *trans* versus *geminal* isomers.<sup>199</sup> The molecules studied were tetraethynylethene, as well as the *trans* and *geminal* isomers of diethynylethene. Geometry optimisation and orbital calculations were performed using the B3LYP functional<sup>200</sup> as implemented within the Gaussian 98 software package<sup>201</sup> at a B3LYP/6-31G\*\* level, since this gave the best agreement with experimental results.<sup>188</sup>

The geometry optimised molecular structure of 1,6-*bis*(trimethylsilyl)-3-4-*bis*((trimethylsilyl)ethynyl)hex-3-ene-1,5-diyne (**22b**) has a calculated  $C_{4v}$

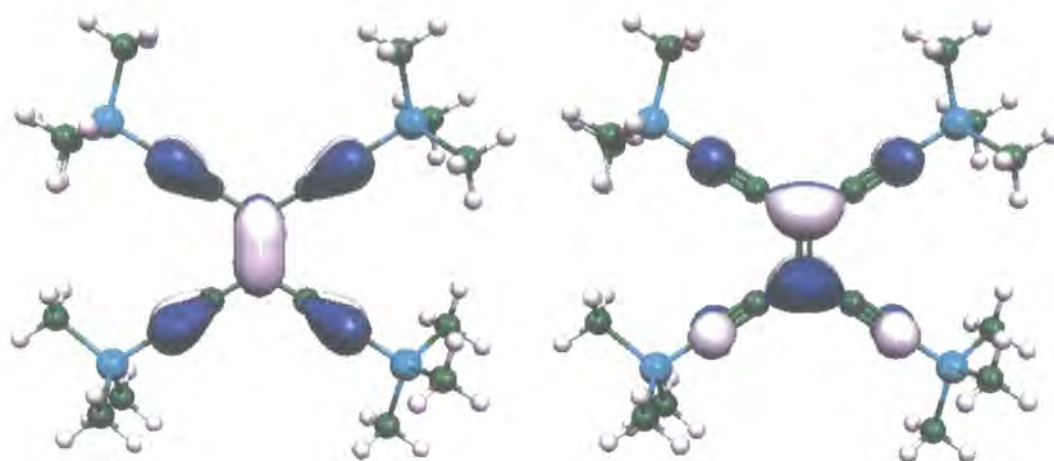
symmetry and contains a central C=C bond length of 1.39 Å, C≡C bond of 1.22 Å and C–C bond of 1.42 Å (**Figure 53**). There is strong delocalisation of the HOMO throughout the whole  $\pi$ -system, while the LUMO shows a strong  $\pi^*$ -antibonding character on the central olefinic bond (**Figure 54**). Since the frontier molecular orbitals are concentrated around the central olefinic bond, promotion of an electron from the HOMO into the LUMO will result in an elongation of this bond, reducing the barrier to rotation and enabling facile isomerisation,<sup>188</sup> which is in agreement with the photochemical isomerisation observed experimentally.



**Figure 53.** Geometry optimised structure of **22b** calculated using Gaussian98 at a B3LYP/6-31G\*\* level.

HOMO

LUMO



**Figure 54.** HOMO and LUMO orbitals of **22b** calculated using Gaussian98 at a B3LYP/6-31G\*\* level.

The natural bond analysis method was used to correlate the changes in molecular and electronic character, such as bond length or absorption frequency, with the electronic structure of the compounds.<sup>199</sup> The study showed that the delocalisation energy favours the *trans* over the *geminal* isomer due to the orientation of the  $\pi^*$  C=C orbital. The difference in stability between the cross and through conjugation in 1,1,2,2-tetraethynylethene is controlled by  $\pi$  delocalisation with minor contribution from  $\sigma$  delocalisation. The four acetylenic arms in 1,1,2,2-tetraethynylethene have a strong additive effect in promoting  $\pi$  delocalisation, causing a significant increase in the central C=C bond length.<sup>199</sup> The findings of this theoretical study correspond to the results of the UV-Vis spectroscopy study on donor-acceptor interaction, which indicate that the larger bathochromic shift, as well as the magnitude of the extinction coefficient value for *trans/cis* substituted donor acceptor 1,1,2,2-tetraethynylethene, leading to a more efficient charge delocalisation along the conjugation pathway.<sup>95</sup>

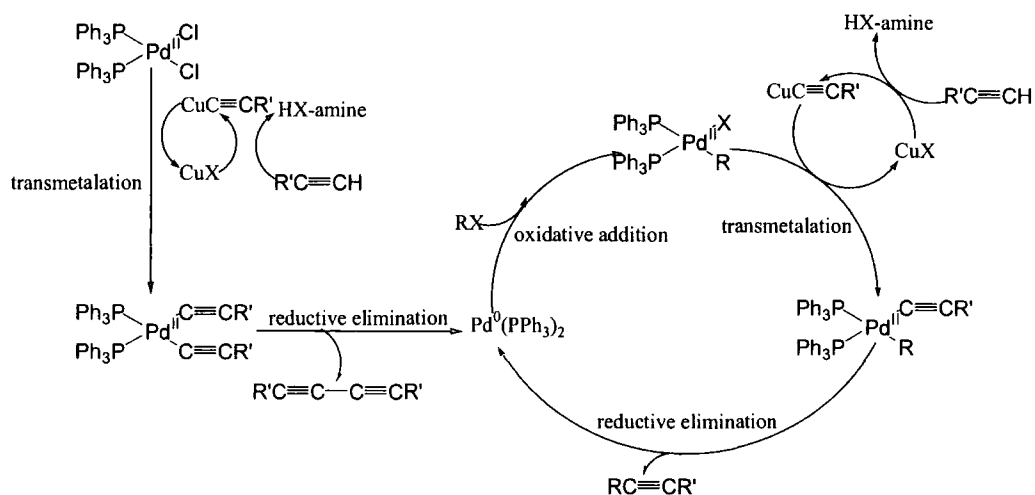
Though the various synthetic method described above are flexible, providing access to a variety of different functionalisation of the 1,1,2,2-tetraethynylethene framework, they are somewhat tedious. The  $\sigma$  attachment of organometallic moieties to the 1,1,2,2-tetraethynylethanes framework has been investigated, however, no attempt has been made to investigate  $\pi$  attachment of organometallic moieties to the same framework. The discussion below will describe a one-pot procedure to synthesise tetra-functionalised 1,1,2,2-tetraethynylethene framework, on route to the investigation of  $\pi$ -interactions of organometallic moieties to the 1,1,2,2-tetraethynylethane framework.

### 3.2. Synthesis and Characterisation of Functionalised

#### 1,1,2,2-Tetraethynylethenes

Conjugated acetylenic compounds are valuable intermediates in organic synthesis for natural products, pharmaceutical, dendrimers and organic molecular materials such as liquid crystal material and molecular wires for use in molecular electronics. Palladium catalysed cross coupling reactions between aryl and alkenyl halides with a variety of acidic or otherwise activated hydrocarbons have emerged as powerful synthetic methodologies for C-C bond formation in a wide variety of systems.<sup>31, 147, 202</sup> While in general terms iodides and bromides react much more readily than chlorides, reflecting the ease of oxidative addition of the C-X bond to the palladium(0) centre, considerable effort is being directed at the development of catalyst systems capable of coupling aryl chlorides under mild conditions, some examples being:  $\text{Na}_2[\text{PdCl}_4]/(1\text{-Ad})_2\text{Pbn}$ ,  $\text{P}^t\text{Bu}_3/\text{CuI}$ ,<sup>203</sup>  $\text{Pd}_2(\text{dba})_3/\text{P}^t(\text{Bu})_3/\text{Cs}_2\text{CO}_3/\text{dioxane}$ ,<sup>204</sup>  $[\text{PdCl}\{\text{C}_6\text{H}_3(\text{OPPr}^i)_2\text{-2,6}\}]$ .<sup>205</sup> However, in the context of the preparation of ene{poly(yne)} systems, it is important to note the facile coupling of 1,2-dichloroethenes with terminal acetylenes to give 1-chloroeneynes or hexa-3-ene-1,4-diynes.<sup>206</sup> It is therefore curious, that tri and tetra chloroethenes have not been examined as reagents for the assembly of larger conjugated systems using palladium based coupling protocols.

The reaction mechanism common to Pd catalysed C-C bond forming reactions follows that of oxidative addition; transmetalation; reductive elimination process. The precise mechanism remains a topic of debate,<sup>202, 207</sup> and probably varies with respect to the particular conditions employed. In the most general of terms, the mechanism of the cross-coupling reaction can be summarised by **Scheme 17**.



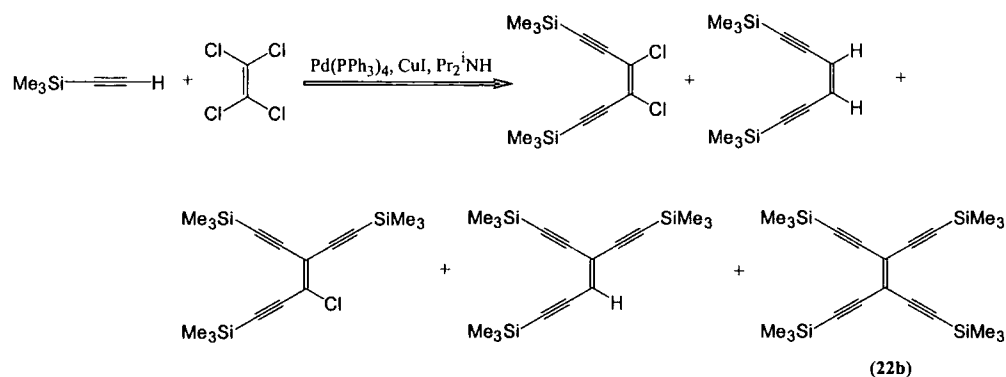
**Scheme 17.** Pd-catalysed cross-coupling reaction of terminal acetylenes with  $sp^2$  halides.<sup>31</sup>

An attempt to obtain 1,6-*bis*(trimethylsilyl)-3,4-*bis*((trimethylsilyl)ethynyl)hex-3-ene-1,5-diyne (**22b**) was performed *via* a  $Pd(PPh_3)_4$  (2.5%)/ $CuI$  (2.5%) catalysed cross-coupling reaction of tetrachloroethene with an excess of  $Me_3SiC\equiv CH$  in refluxing  $Pr_2NH$ . This afforded a mixture of products which were identified by GC-MS as the desired **22b** (ca. 30%), dichloro-*bis*(trimethylsilyl)-hexenediyne (three isomers, ca. 23%), chloro-*bis*(trimethylsilyl)-hexenediyne (one isomer, ca. 6%), 1,6-*bis*(trimethylsilyl)-3-(trimethylsilylethynyl)-hex-3-ene-1,5-diyne (ca. 11%) and the diyne  $Me_3SiC\equiv CC\equiv CSiMe_3$  (ca. 14%), with yields estimated from the



integrated area of each peak in the GC trace (**Scheme 18**). However, extensive extraction and chromatography procedures failed to adequately separate the partially coupled and hydrodehalogenated compounds from the desired product.

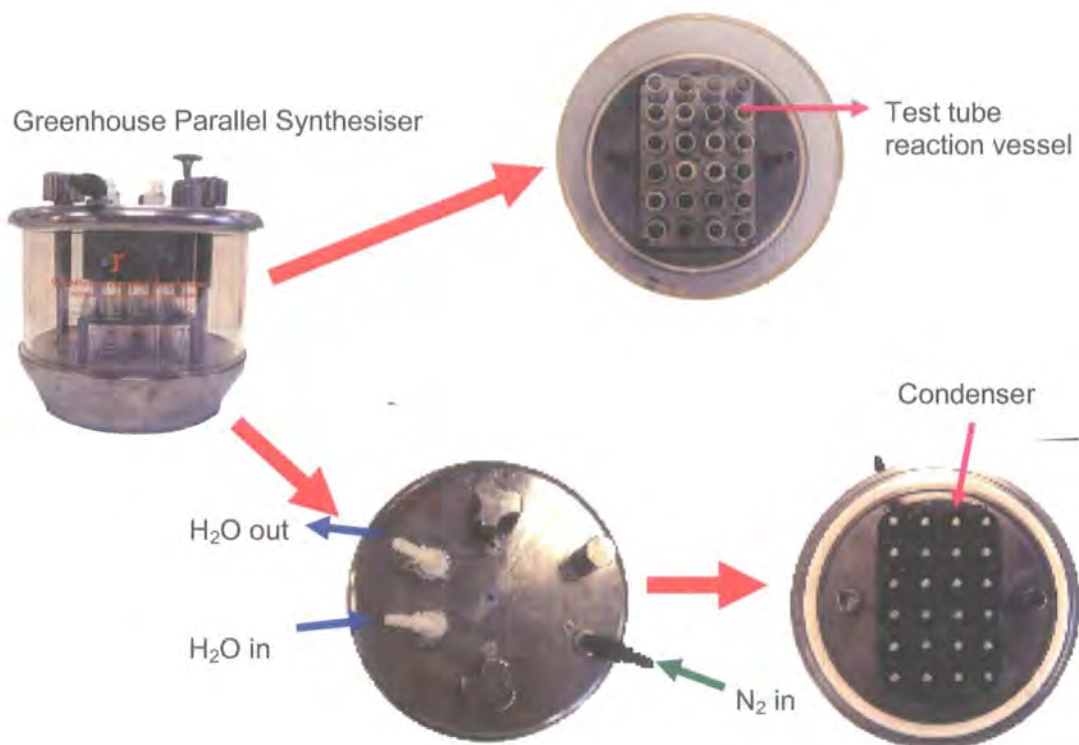
In order to minimise the formation of side products (**Scheme 18**) the reaction was repeated at room temperature. The reaction was monitored by GC-MS at regular time intervals. Initially only the presence of homocoupling products and  $\text{PPh}_3$  were observed. After 6 h the presence of one isomer of dichloro-*bis*(trimethylsilyl)-hexenediyne was observed exclusively which continued to increase in quantity up to 24 h. At longer times both 1,6-*bis*(trimethylsilyl)-3-(trimethylsilylethynyl)-hex-3-ene-1,5-diyne and **22b** were observed in approximately equal proportions. These products persisted in the reaction mixture for approximately 2 h, while the major product, dichloro-*bis*(trimethylsilyl)-hexenediyne, continued to increase in quantity until approximately 50 h. The product distribution at 50 h persisted until the reaction was terminated after 96h. While the dichloroenediyne was not isolated, these observations provide encouraging evidence for the possible preparation of a potentially useful synthetic intermediate.



**Scheme 18.** Cross coupling reaction between  $\text{Me}_3\text{SiC}\equiv\text{CH}$  and tetrachloroethene performed at room temperature.

The cross-coupling reaction described above was also performed with strictly two equivalents of  $\text{Me}_3\text{SiC}\equiv\text{CH}$  at elevated temperature for only 4h, the reaction again monitored by GC. After 2h, the major product was chloro-tris(trimethylsilyl)-hexenediyne, with **22b** and three isomers of dichloro-bis(trimethylsilyl)-hexenediyne present in comparable amounts. After 4h, a similar mixture of products to those described in **Scheme 18** began to form.

It is known that palladium/copper catalysed cross coupling reactions are sensitive to both the phosphine ligands supporting the catalytically active palladium catalyst and the base used in the reaction. In an effort to identify conditions appropriate to maximise the yield of **22b**, a series of different reactions were explored utilising a combinatorial array in which solvent ( $\text{Et}_3\text{N}$ ,  $\text{Et}_2\text{NH}$ ,  $\text{Pr}_2^i\text{NH}$ ) and source of the palladium catalyst [ $\text{Pd}(\text{PPh}_3)_4$ ,  $\text{PdCl}_2(\text{PPh}_3)_2$ ,  $\text{Pd}_2(\text{dba})_3/\text{dppf}$ ,  $\text{Pd}_2(\text{dba})_3/\text{P}^t\text{Bu}_3$ ] were varied whilst keeping the ratio of trimethylsilylacetylene and reaction temperature constant. The apparatus is depicted in **Figure 55**, where each test tube reaction vessel was charged with a 0.01 M solution of the various catalysts in THF, followed by the amine, CuI, tetrachloroethylene, and finally trimethylsilylacetylene. The greenhouse parallel synthesiser was placed on a stirrer hotplate, and the reactions were stirred at reflux under  $\text{N}_2$  overnight. The crude reaction products were analysed by GC-MS. For all reactions a certain degree of homocoupling product,  $\text{Me}_3\text{SiC}\equiv\text{CC}\equiv\text{CSiMe}_3$ , was present since the assembly of the reactor precludes the establishment of a strictly oxygen free environment.



**Figure 55.** Parallel synthesiser array used for cross coupling test reactions.

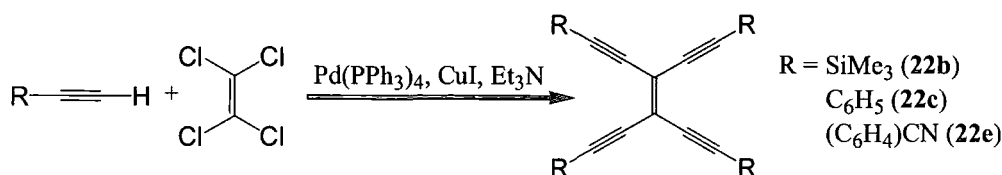
The results indicated the choice of amine to be quite crucial to the success of the reaction. The use of  $\text{Pr}_2^i\text{NH}$  as a solvent for the cross-coupling of tetrachloroethene and trimethylsilylacetylene gave a mixture of various isomers of di-, tri- and tetra-trimethylsilylacetylene substituted ethene, with the products present in similar amounts to each other. Using  $\text{Et}_2\text{NH}$  as the solvent gave a mixture of mainly tris- trimethylsilylacetylene substituted ethene along with a number of unidentifiable products. The reaction using  $\text{Pd}_2(\text{dba})_3(\text{P-}^t\text{Bu}_3)/\text{CuI}/\text{Et}_2\text{NH}$  gave **22b** as the major product, with other small amounts of products which were unidentified. When  $\text{Et}_3\text{N}$  was used as a solvent as opposed to  $\text{Pr}_2^i\text{NH}$ , a greater relative amount of the **22b** was formed together with a mixture of di-, tri- and tetra-trimethylsilylacetylene substituted ethenes. In each solvent, the product distribution was similar, regardless of the nature of the pre-catalyst employed.

From the combinatorial array results it was possible to identify the use of Et<sub>3</sub>N as solvent as the most critical factor in maximising the yield of **22b**. The pre-catalyst Pd(PPh<sub>3</sub>)<sub>4</sub> was chosen, as in addition to being readily available the presence of the additional free phosphine in the reaction mixture was thought to help stabilise the resting state of the catalyst. The cross-coupling reaction between 1,1,2,2-tetrachloroethene and trimethylsilylacetylene was carried out on a preparative scale using Pd(PPh<sub>3</sub>)<sub>4</sub>/CuI/Et<sub>3</sub>N. The product **22b** was readily isolated by filtration of the reaction mixture, to remove the precipitated trialkylammonium salts, followed by precipitation of the product in acidified MeOH and recrystallisation. Care was taken during the precipitation step, as in the presence of trace amount of the amine reaction solvent, sufficient methoxide is generated to desilylate the highly ethynylated reaction products, which upon concentration on one occasion spontaneously detonated. It was therefore essential that the MeOH used to precipitate the product was acidified by addition of several drops of HCl prior to use.

In this manner, **22b** was isolated in moderate but comparable yield to that obtained by the four-step method detailed by Rubin *et al.*<sup>182</sup> The EI-MS spectrum of **22b** exhibited a molecular ion at *m/z* 412, while the IR spectrum had an absorption band for  $\nu(\text{C}\equiv\text{C})$  at 2166 and 2147 cm<sup>-1</sup>, and a band for  $\nu(\text{C}=\text{C})$  at 1612 cm<sup>-1</sup>. The <sup>1</sup>H NMR spectrum showed only a singlet at  $\delta$  0.00 ppm attributed to the SiMe<sub>3</sub> groups. The <sup>13</sup>C NMR spectrum showed two resonances at  $\delta$  101.19 and 105.56 ppm due to the acetylenic carbons, and a resonance at  $\delta$  119.03 due to the ethene carbons.<sup>182</sup>

The palladium/copper catalysed cross-coupling of tetrachloroethene to other terminal alkynes proceeded smoothly under similar conditions (**Scheme 19**). The Pd(0)/Cu(I) (5%) catalysed reaction of tetrachloroethene with excess phenylacetylene in refluxing triethylamine afforded 1,6-*bis*(phenyl)-3,4-*bis*(phenylethynyl)-hex-3-ene-1,5-diyne (**22c**) in 60% yield after chromatographic

work-up.<sup>x</sup> This compound has been prepared previously by carbenoid coupling routes, albeit in only 11% yield,<sup>190</sup> and also by the procedure illustrated in **Scheme 15**.<sup>208</sup> Compound **22c** was identified by comparison of the spectroscopic data with that previously reported.<sup>190</sup>



**Scheme 19.** Palladium/copper catalysed cross-coupling of tetrachloroethene to terminal alkynes.

The substituted arylalkyne, 4-ethynylbenzonitrile, also coupled smoothly under analogous conditions to afford 1,6-*bis*(cyanophenyl)-3-4-*bis*((4-cyanophenyl)ethynyl)hex-3-ene-1,5-diyne (**22e**) (42%). The compound **22e** was exceptionally insoluble in all common solvents. However, sufficient material could be dissolved in hot d<sub>6</sub>-DMSO to permit a <sup>1</sup>H NMR spectrum to be obtained. The expected pattern in the aromatic region was observed (δ 7.77, 7.93; 2 × d, *J*<sub>HH</sub> = 8 Hz). The IR spectrum exhibited a weak absorption band for ν(C=C) at 1600 cm<sup>-1</sup>, and another weak absorption band for ν(CN) at 2224 cm<sup>-1</sup>, the absorption band for ν(C≡C) was not observed. The EI-MS spectrum exhibited the molecular ion at *m/z* 528.

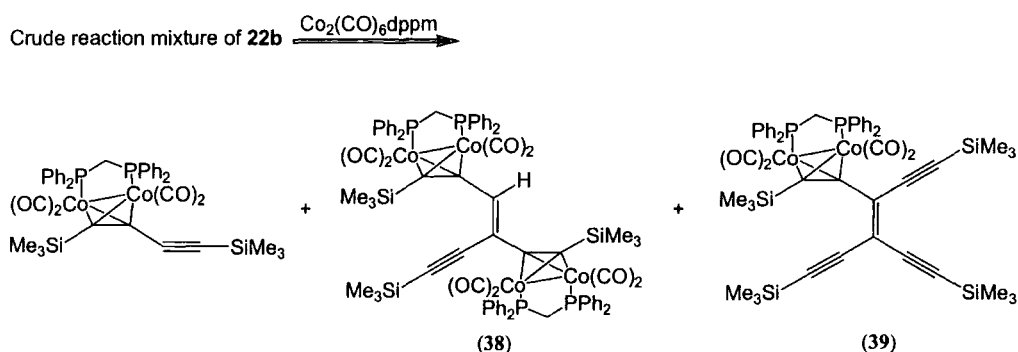
The successful preparation of **22c** and **22e** by Pd/Cu catalysed coupling reactions of tetrachloroethene is in stark contrast to the failed Eglington-type coupling of tetraiodoethene with copper phenylacetylide.<sup>176</sup> However, attempts to cross-couple more electron-rich alkynes, including ferrocenylacetylene, with tetrachlorethylene have not yet been successful.

<sup>x</sup> Synthesis and characterisation courtesy of P. Zuber.

### 3.3. Reaction of Dicobalt Hexacarbonyl

#### *bis*(Diphenylphosphino)methane with 1,6-*bis*(Trimethylsilyl)-3,4-*bis*((trimethylsilyl)ethynyl)hex-3-ene-1,5-diyne

Dicobalt carbonyls  $[\text{Co}_2(\text{CO})_6(\text{L}_2)]$  react readily with alkynes to afford complexes of the general type  $[\text{Co}_2(\mu\text{-}\eta^2\text{-alkyne})(\text{CO})_4(\text{L}_2)]$ .<sup>209</sup> These compounds often crystallise readily, and as such are appealing derivatives for establishing the nature of otherwise difficult to characterise acetylenes.<sup>210</sup> In an effort to obtain further evidence for the products formed in diisopropylamine, the crude product mixture containing **22b** was allowed to react with  $[\text{Co}_2(\text{CO})_6(\mu\text{-dppm})]$  in refluxing benzene. The reaction was followed by TLC and, when judged complete, the solvent was removed and the residue purified by preparative TLC. The dicobalt complexes  $[\text{Co}_2(\text{CO})_4(\mu\text{-dppm})](\mu, \eta^2\text{-Me}_3\text{SiC}_2\text{C}\equiv\text{CSiMe}_3)$  (29%),  $[\{\text{Co}_2(\text{CO})_4(\mu\text{-dppm})\}_2\{\mu, \eta^2\text{-}\mu, \eta^2\text{-(Me}_3\text{SiC}_2\text{C(H)=C(C}_2\text{SiMe}_3)\text{C}\equiv\text{CSiMe}_3)\}]$  (**38**) (9%) and  $[\text{Co}_2(\text{CO})_4(\mu\text{-dppm})\{\mu, \eta^2\text{-Me}_3\text{SiC}_2\text{C(C}\equiv\text{CSiMe}_3)\text{=C(C}\equiv\text{CSiMe}_3)_2\}]$  (**39**) (44%) were obtained (**Scheme 20**).



**Scheme 20.** Products resulting from a reaction between crude **22b** and  $[\text{Co}_2(\text{CO})_6(\mu\text{-dppm})]$ .

The diyne product,  $[\text{Co}_2(\mu, \eta^2\text{-Me}_3\text{SiC}_2\text{C}\equiv\text{CSiMe}_3)(\text{CO})_4(\mu\text{-dppm})]$ , was readily identified by comparison of the spectroscopic data with that previously

reported.<sup>211,212</sup> The IR spectrum of **38** contained strong  $\nu(\text{CO})$  absorption bands at 2021, 1997, and 1970  $\text{cm}^{-1}$ , consistent for a compound of the type  $[\text{Co}_2(\text{alkyne})(\text{CO})_4(\mu\text{-dppm})]$  bearing an electron withdrawing group.<sup>213</sup> The  $^1\text{H}$  NMR spectrum of **38** contained three singlet resonances in the region of  $\delta$  -0.17-0.40 ppm each which are consistent with the presence of three  $\text{SiMe}_3$  groups. The multiplets at  $\delta$  3.43 and 3.67 ppm were attributed to the protons of the  $\text{CH}_2$  moiety, while the multiplet at  $\delta$  3.59 ppm was attributed to the vinyl proton. The aromatic region contained the usual resonances for the phenyl groups associated with the dppm ligands. The  $^{13}\text{C}$  NMR spectrum shows three resonances at  $\delta$  0.00-1.44 ppm corresponding to the three  $\text{SiMe}_3$  groups. The two resonances at  $\delta$  36.00 and 38.62 ppm are attributed to the  $\text{CH}_2$  moiety, while the two resonances at  $\delta$  106.22 and 106.57 ppm are attributed to the acetylenic carbons. There are sixteen resonances that fall in the aromatic region ranging from  $\delta$  125.59 to 139.65 ppm, due to the phenyl groups associated with the dppm ligands. The last four remaining resonances are carbonyl carbons. The FAB-MS spectrum exhibited the molecular ion at  $m/z$  1545 and fragment ions at  $m/z$  1517-1489 showing the consecutive loss of two carbonyls.

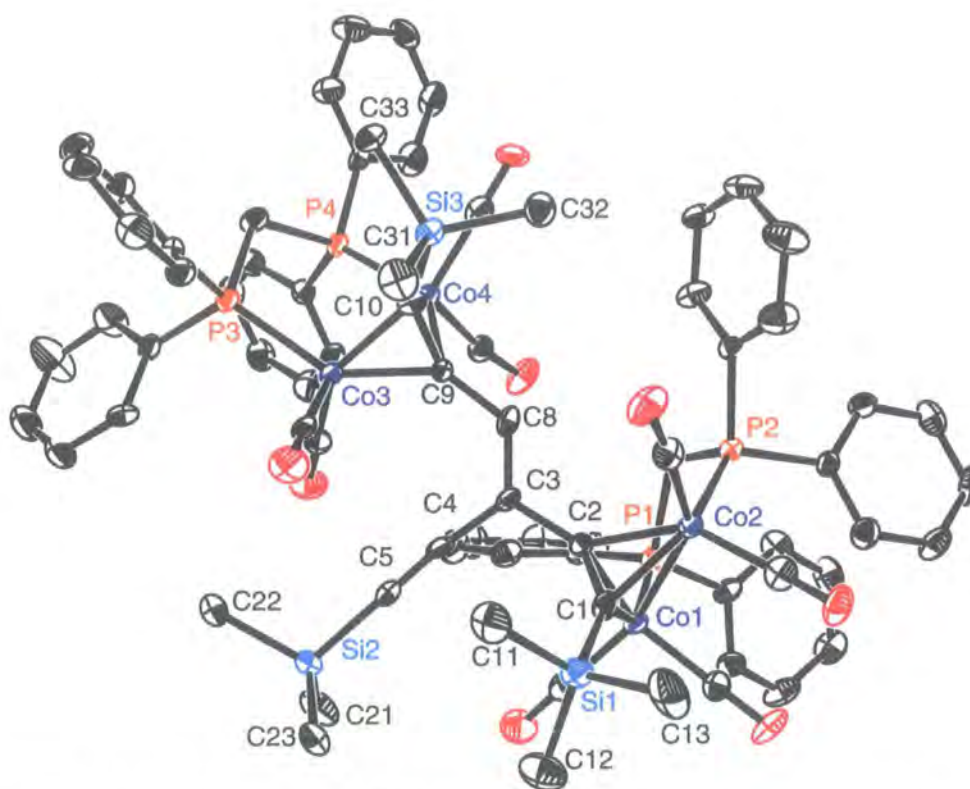
The molecular structure of **38** was confirmed by X-ray crystallography using single crystals grown from  $\text{CH}_2\text{Cl}_2:\text{MeOH}$  and is shown in **Figure 56**, with crystallographic data given in **Table 7**. There was one molecule in the asymmetric unit cell along with two molecules of  $\text{CH}_2\text{Cl}_2$  and half molecule of  $\text{MeOH}$ .

Table 7. Crystal data and structure refinement for 38, 39, and 40.

	38	39	40
Empirical formula	C <sub>78.33</sub> H <sub>78</sub> Cl <sub>7</sub> Co <sub>4</sub> O <sub>8</sub> P <sub>4</sub> Si <sub>3</sub>	C <sub>51</sub> H <sub>58</sub> Co <sub>2</sub> O <sub>4</sub> P <sub>2</sub> Si <sub>4</sub>	C <sub>40</sub> H <sub>40</sub> Co <sub>2</sub> O <sub>4</sub> P <sub>2</sub> Si <sub>2</sub>
Formula weight	1839.39	1027.13	820.70
Temperature	120(2) K	120(2) K	120(2) K
Wavelength	0.71073 Å	0.71073 Å	0.71073 Å
Crystal system	Triclinic	Triclinic	Monoclinic
Space group	P-1	P-1	P2(1)/n
Unit cell dimensions	a = 16.1865(13) Å α = 72.923(3)° b = 16.1599(14) Å β = 89.949(4)° c = 16.9861(15) Å γ = 83.932(4)°	a = 12.846(1) Å α = 109.391(4)° b = 14.881(2) Å β = 95.169(3)° c = 17.221(1) Å γ = 115.508(4)°	a = 11.529(2) Å α = 90° b = 18.967(2) Å β = 104.118(7)° c = 19.026(3) Å γ = 90°
Volume	4221.3(6) Å <sup>3</sup>	2695.5(4) Å <sup>3</sup>	4034.8(10) Å <sup>3</sup>
Z	2	2	4
Density (calculated)	1.447 Mg/m <sup>3</sup>	1.266 Mg/m <sup>3</sup>	1.351 Mg/m <sup>3</sup>
Absorption coefficient	1.164 mm <sup>-1</sup>	0.804 mm <sup>-1</sup>	0.999 mm <sup>-1</sup>
F(000)	1882	1072	1696
Crystal size	0.2 x 0.15 x 0.05 mm <sup>3</sup>	0.40 x 0.19 x 0.17 mm <sup>3</sup>	0.44 x 0.20 x 0.14 mm <sup>3</sup>
Crystal colour		dark violet	
Crystal shape		block	
Theta range for data collection	1.25 to 27.51°	1.30 to 28.28°	1.54 to 28.29°
Index ranges	-21 ≤ h ≤ 21, -20 ≤ k ≤ 21, -22 ≤ l ≤ 22	-15 ≤ h ≤ 17, -19 ≤ k ≤ 19, -20 ≤ l ≤ 22	-15 ≤ h ≤ 15, -25 ≤ k ≤ 25, -25 ≤ l ≤ 25



Reflections collected	46934	22544	45514
Independent reflections	19221 [R(int) = 0.1399]	13117 [R(int) = 0.0190]	10018 [R(int) = 0.0485]
Completeness to theta	99.0 %	98.1 %	99.8 %
Absorption correction	Semi-empirical from equivalents	Integration	Integration
Max. and min. transmission	0.943 and 0.798	0.896 and 0.739	0.877 and 0.698
Refinement method	Full-matrix least-squares on F <sup>2</sup>	Full-matrix least-squares on F <sup>2</sup>	Full-matrix least-squares on F <sup>2</sup>
Data / restraints / parameters	19221 / 0 / 959	13117 / 0 / 568	10018 / 0 / 457
Goodness-of-fit on F <sup>2</sup>	0.977	1.038	1.017
Final R indices [I>2sigma(I)]	R1 = 0.0774, wR2 = 0.1700	R1 = 0.0382, wR2 = 0.0976	R1 = 0.0610, wR2 = 0.1326
R indices (all data)	R1 = 0.1940, wR2 = 0.2288	R1 = 0.0502, wR2 = 0.1055	R1 = 0.0938, wR2 = 0.1542
Largest diff. peak and hole	0.857 and -1.448 e.Å <sup>-3</sup>	0.960 and -0.389 e.Å <sup>-3</sup>	2.363 and -1.658 e.Å <sup>-3</sup>

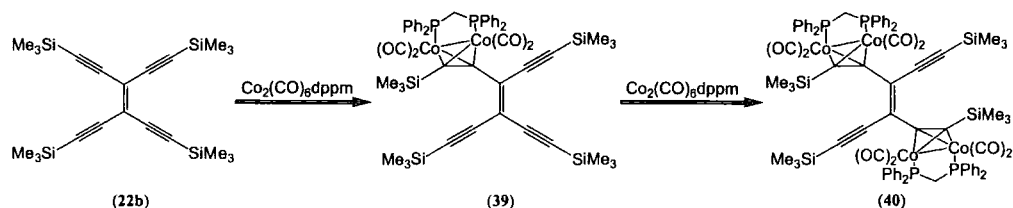


**Figure 56.** Molecular structure of **38** depicted with a 50% ellipsoid probability.  
Hydrogen atoms have been omitted for clarity.

The  $\text{Co}_2(\mu\text{-}\eta^2\text{-alkyne})(\text{CO})_4(\mu\text{-dppm})$  portion of **38** is unremarkable with the Co-Co bond lengths being 2.484(14) (2.517(14) Å), the coordinated C-C bonds are 1.363(10) and 1.369(10) Å, the Co-C(alkyne) bonds span the range 1.932(7)-2.020(7) Å, averaging 1.975 Å. The coordinated C-C bond lengths (1.363(10)-1.369(10) Å) display the usual elongation relative to the uncoordinated  $\text{C}\equiv\text{C}$  alkynyl moieties (1.201(11) Å). The C(3)-C(8) C=C bond length, 1.355(10) Å, is similar to those normally encountered in 1,1,2,2-tetraethynylethene derivatives. The formal C-C single bonds C(2)-C(3) and C(8)-C(9) linking the cluster coordinated alkyne moieties to the central C(3)-C(8) core display a trend towards elongation relative the C(4)-C(3) and C(8)-C(7), which is attributed to the difference in hybridisation at the cluster carbon C(2), and also C(9). The cobalt clusters and pendant ethynyl groups are found positioned around the olefinic core in a manner which reduces the steric interactions between them. The Co-Co

vectors are approximately perpendicular, with the Si(3)Me<sub>3</sub> group occupying a portion of the void space around C(8). The Co(3)-Co(4) cluster moiety would appear to have some influence on the C(4)-C(5) alkynyl group, which bends away from the cluster giving slightly abnormal C(8)-C(3)-C(4) (124.9(6)°) and C(2)-C(3)-C(4) (113.5(6)°) bond angles.

The reaction of pure **22b** and [Co<sub>2</sub>(CO)<sub>6</sub>(μ-dppm)] afforded only [Co<sub>2</sub>(CO)<sub>4</sub>(dppm){μ,η<sup>2</sup>-Me<sub>3</sub>SiC<sub>2</sub>C(C≡CSiMe<sub>3</sub>)=C(C≡CSiMe<sub>3</sub>)<sub>2</sub>}] (**39**) as a single product (**Scheme 21**). Recrystallisation gave red brittle crystals, the colour being characteristic of the attachment of one [Co<sub>2</sub>(CO)<sub>6</sub>(μ-dppm)] moiety in the compound.



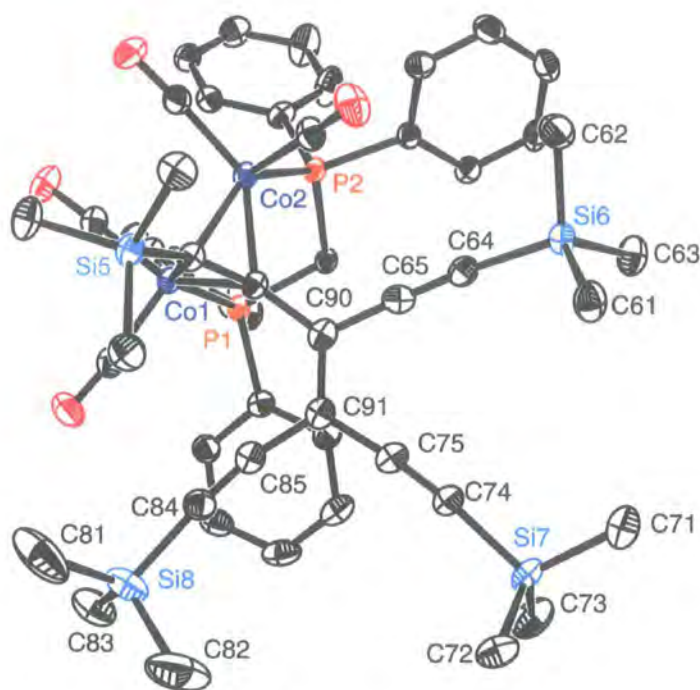
**Scheme 21.** Synthetic protocol for the formation of **39** and **40**.

The <sup>1</sup>H NMR spectrum of **39** contained four singlet peaks in the region of 0.00–0.30 ppm consistent with the presence of four SiMe<sub>3</sub> groups. A set of two unresolved multiplets appears at δ 3.51 and 3.71 ppm attributed to the diastereiotopic protons of the CH<sub>2</sub> moiety. The aromatic region revealed two multiplets at δ 7.18 and 7.35 ppm assigned to the phenyl moieties of the dppm ligand. The <sup>13</sup>C NMR spectrum shows four resonances corresponding to the four SiMe<sub>3</sub> groups at δ 0.00–2.30 ppm. The resonance at δ 36.40 ppm arose from the CH<sub>2</sub> moiety, and only seven of the quarternary carbon resonances were observed, falling in the range δ 98.23–111.14 ppm. Eight out of the ten carbon resonances fall in the aromatic region while the remaining two resonances at δ 204.63 and 206.97 ppm are carbonyl carbons. The FAB-MS spectrum did not exhibit the molecular ion, instead it showed fragment ions at *m/z* 999–915 showing the

consecutive loss of four carbonyls, while the IR spectrum had  $\nu(\text{CO})$  absorption bands at 2023, 1999, and 1973  $\text{cm}^{-1}$ .

The molecular structure of **39** was confirmed by X-ray crystallography using single crystals grown from  $\text{CH}_2\text{Cl}_2:\text{MeOH}$  and is shown in **Figure 57**, with crystallographic data given in **Table 7**. The  $\text{Co}_2(\mu\text{-}\eta^2\text{-alkyne})(\text{CO})_4(\mu\text{-dppm})$  portion of **39** contains Co-Co bond lengths of 2.466(4) Å, the coordinated C-C bonds is 1.350(3) Å, the Co-C(alkyne) bonds span the range 1.973(18)-1.993(18) Å, averaging 1.975 Å. The coordinated C-C bond lengths (1.350(3) Å) display the usual elongation relative to the uncoordinated  $\text{C}\equiv\text{C}$  alkynyl moieties (1.201(11)-1.214(3) Å). The C(90)-C(91) C=C bond lengths, 1.365(3) Å, while the formal C-C single bonds were in the range of 1.427(3)-1.448 (3) Å, these are similar to those normally encountered in 1,1,2,2-tetraethynylethene derivatives.

The *bis*(dicobalt) complex  $[\{\text{Co}_2(\text{CO})_4(\text{dppm})\}_2\{\mu\text{-}\eta^2\text{:}\eta^2\text{-Me}_3\text{SiC}_2\text{C}(\text{C}\equiv\text{CSiMe}_3)\text{C}(\text{C}\equiv\text{CSiMe}_3)\text{C}_2\text{SiMe}_3\}]$  (**40**) could not be obtained directly from reactions of **22b** and  $[\text{Co}_2(\text{CO})_6(\mu\text{-dppm})]$ . After initial formation of **39**, the excess dicobalt,  $[\text{Co}_2(\text{CO})_6(\mu\text{-dppm})]$ , reagent underwent a self condensation reaction to give  $[\text{Co}_4(\text{CO})_8(\mu\text{-dppm})_2]$  rather than forming the desired *bis*(dicobalt) product, probably due to steric reasons. In order to obtain **40**, the precursor, **39**, had to be isolated, then further reacted with excess  $[\text{Co}_2(\text{CO})_6(\mu\text{-dppm})]$  at reflux for a several hours for the second  $[\text{Co}_2(\text{CO})_4(\mu\text{-dppm})]$  moiety to coordinated to the least sterically hindered triple bond (in the *trans* position) of **39** (**Scheme 21**). Upon recrystallisation dark green, fine crystals were obtained suitable for X-ray analysis.

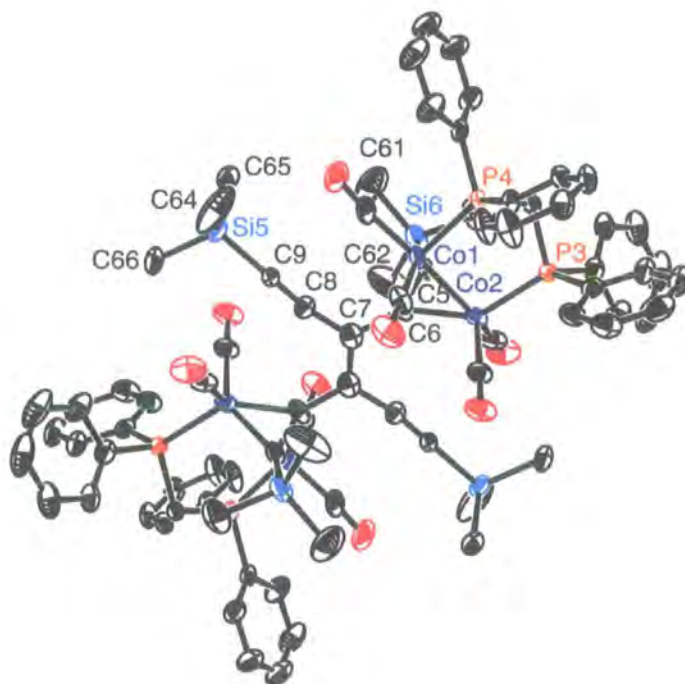


**Figure 57.** Molecular structure of **39** depicted with a 50% ellipsoid probability.  
Hydrogen atoms have been omitted for clarity.

The IR spectrum of **40** contained strong  $\nu(\text{CO})$  absorption bands at 2024, 2001, and 1976  $\text{cm}^{-1}$ , and a weak absorption band for  $\nu(\text{C}\equiv\text{C})$  at 2127  $\text{cm}^{-1}$ . The FAB-MS spectrum exhibited the molecular ion at  $m/z$  1641 and fragment ions at  $m/z$  1612-1360 showing the consecutive loss of two to ten carbonyls. The  $^1\text{H}$  NMR spectrum of showed two singlet resonances at  $\delta$  0.22 and 0.55 ppm attributed to the two symmetrical  $\text{SiMe}_3$  groups. The multiplets at  $\delta$  3.46 and 3.64 ppm were attributed to the protons of the  $\text{CH}_2$  moiety. The aromatic region contained a multiplet at 7.17 ppm and a singlet at  $\delta$  7.86 ppm which as a collective are attributed to the phenyl moieties of the dppm ligand. The  $^{13}\text{C}$  NMR spectrum shows two resonances corresponding to the  $\text{SiMe}_3$  groups at  $\delta$  0.00 and 2.06 ppm. The resonance at  $\delta$  27.42 ppm is attributed to the  $\text{CH}_2$  moiety, and the four resonances between  $\delta$  80.95-88.73 ppm are attributed to the acetylenic carbons. There are eight resonances that fall in the aromatic region ranging from  $\delta$  128.18 to 132.93 ppm exhibiting shifts common to the phenyl of the dppm ligand.

The carbonyl carbons were not observed due to the relatively poor quality of the spectrum, due in part to the presence of paramagnetic cobalt containing impurities in the NMR sample.

The molecular structure of **40** was confirmed by X-ray crystallography using single crystals grown from CH<sub>2</sub>Cl<sub>2</sub>:MeOH and is shown in **Figure 58**, with crystallographic data given in **Table 7**. The Co<sub>2</sub>(μ-η<sup>2</sup>-alkyne)(CO)<sub>4</sub>(μ-dppm) portion of **40** is typical with the Co-Co bond lengths being 2.490(9) Å, the coordinated C-C bonds is 1.354(7) Å, the Co-C(alkyne) bonds span the range 1.909(7)-1.914(6) Å. The coordinated C-C bond lengths (1.354(7) Å) display the usual elongation relative to the uncoordinated C≡C alkynyl moieties (1.223(11)). The C=C bond length is 1.357(9) Å, while the formal C-C single bonds were in the range of 1.441(9)-1.474 (6) Å. These parameters are similar to those normally encountered in 1,1,2,2-tetraethynylethenes derivatives.

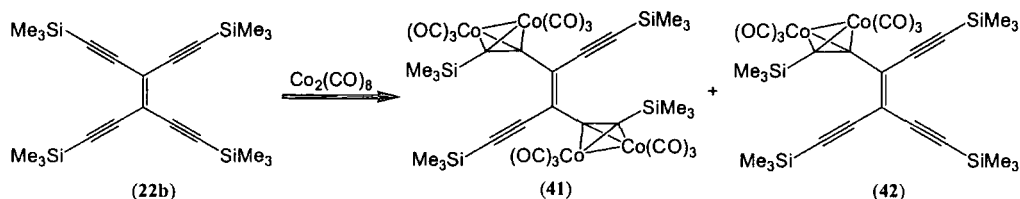


**Figure 58.** Molecular structure of **40** depicted with a 50% ellipsoid probability. Hydrogen atoms have been omitted for clarity.



### 3.4. Reaction of Dicobalt Octacarbonyl with 1,6- bis(Trimethylsilyl)-3,4-bis((trimethylsilyl)ethynyl)hex-3-ene- 1,5-diyne

The reaction of **22b** with an excess of the less sterically demanding reagent  $[\text{Co}_2(\text{CO})_8]$  were also investigated (**Scheme 22**). Two complexes were separated by preparative TLC. The major product formed was the dark green double adduct  $[\{\text{Co}_2(\text{CO})_6\}_2\{\mu,\eta^2\text{-Me}_3\text{SiC}_2\text{C}(\text{C}\equiv\text{CSiMe}_3)=\text{C}(\text{C}\equiv\text{CSiMe}_3)\text{C}_2\text{SiMe}_3\}]$  (**41**) (67%). The minor product  $[\text{Co}_2(\text{CO})_6\{\mu,\eta^2\text{-Me}_3\text{SiC}_2\text{C}(\text{C}\equiv\text{CSiMe}_3)=\text{C}(\text{C}\equiv\text{CSiMe}_3)_2\}]$  (**42**) (17%) was obtained as a red-brown crystalline material.



**Scheme 22.** Synthetic protocol for the formation of **41** and **42**.

The IR spectrum of **41** had strong  $\nu(\text{CO})$  absorption bands at 2088, 2056, and  $2030\text{ cm}^{-1}$ . The FAB-MS spectrum did not exhibit the molecular ion, but did contain fragment ions at  $m/z$  870-648 showing the consecutive loss of four to twelve carbonyls, indicating the presence of two  $[\text{Co}_2(\text{CO})_8]$  moieties. The  $^1\text{H}$  NMR spectrum only showed two singlet resonances at  $\delta$  0.00 and 0.15 ppm attributed to the two symmetrical  $\text{SiMe}_3$  groups. The  $^{13}\text{C}$  NMR spectrum shows two resonances corresponding to the  $\text{SiMe}_3$  groups at  $\delta$  0.00 and 2.08 ppm, while the five quaternary carbon resonances ( $\delta$  83.69, 105.10, 107.10, 113.34 and 127.83) indicate the formation of the *trans* disubstituted material.<sup>33</sup> The remaining resonance in the  $^{13}\text{C}$  NMR spectrum at  $\delta$  200.89 ppm is due to carbonyl carbons.

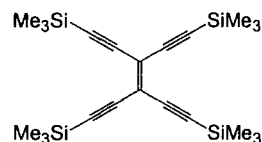
The  $^1\text{H}$  NMR spectrum of **42** displayed only two singlet peaks at  $\delta$  0.00 and 0.16 ppm due to  $\text{SiMe}_3$  groups, while the  $^{13}\text{C}$  NMR spectrum shows four resonances corresponding to the four  $\text{SiMe}_3$  groups between  $\delta$  0.00-1.74 ppm. All ten quaternary carbons ( $\delta$  84.01, 97.47, 100.73, 102.97, 104.39, 104.54, 105.55, 111.67, 112.22, 134.72 ppm) are observed in the  $^{13}\text{C}$  NMR spectrum along with a carbonyl carbon at  $\delta$  200.24 ppm. The FAB-MS spectrum did not exhibit the molecular ion, instead it showing fragment ions at  $m/z$  670-530 indicating the consecutive loss of one to six carbonyls, while the IR spectrum had  $\nu(\text{CO})$  absorption bands at 2089, 2056, and 2030  $\text{cm}^{-1}$ . In no case were the complexes in which three or four of the alkynyl moieties had been coordinated by dicobalt moieties detected.

### 3.5 Conclusion

The  $\text{Pd(0)/Cu(I)}$  catalysed coupling reaction of terminal alkynes with tetrachloroethene in  $\text{NEt}_3$ , but not  $\text{Pr}_2\text{NH}$ , affords the corresponding tetraethynylethenes in good yield. The alkyne moieties are available for coordination by up to two dicobalt fragments, giving the *trans* isomers as expected on steric grounds.

### 3.6. Experimental

#### 3.6.1. 1,6-bis(Trimethylsilyl)-3-4-bis((trimethylsilyl)ethynyl)hex-3-ene-1,5-diyne (**22b**)



Dry  $\text{NEt}_3$  (100 ml) was introduced to an oven-dried Schlenk flask and rigorously degassed by three freeze-pump-thaw sequences. Tetrachloroethylene (1 ml, 9.77 mmol) was added followed by trimethylsilyl acetylene (7 ml, 49.53

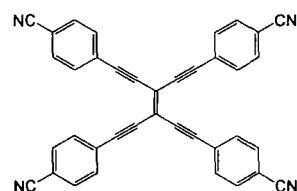


mmol), Pd(PPh<sub>3</sub>)<sub>4</sub> (0.26 g, 0.23 mmol) and CuI (0.05 g, 0.26 mmol). The solution was heated at reflux overnight forming a dark red solution with white precipitate presumed to be alkylammonium salts salt [HNEt<sub>3</sub>]I. The precipitate was removed by filtration, and the filtrate concentrated. The impurities in the filtrate were extracted into acidified MeOH leaving behind the product which was then filtered off. The product was recrystallised from hot EtOH (1.16 g, 2.81 mmol, 29%).

**CAUTIONARY NOTE:** In the presence of a trace amount of the amine reaction solvent, sufficient methoxide is generated during the precipitation step to desilylate the highly ethynylated reaction products, which upon concentration may spontaneously detonate. It is therefore *essential* that the precipitation be carried out with MeOH acidified by addition of several drops of HCl.

IR (nujol):  $\nu(\text{C}\equiv\text{C})$  2166 m, 2147 m ( $\text{C}\equiv\text{C}$ ),  $\nu(\text{C}=\text{C})$  1612 wb  $\text{cm}^{-1}$ . <sup>1</sup>H NMR (499 MHz, CDCl<sub>3</sub>):  $\delta$  0.00 (s, 36H, SiMe<sub>3</sub>). <sup>13</sup>C NMR (125 MHz, CDCl<sub>3</sub>):  $\delta$  0.06 (SiMe<sub>3</sub>), 101.19, 105.56 (2 x  $\text{C}\equiv\text{C}$ ), 119.03 ( $\text{C}=\text{C}$ ). EI<sup>+</sup> - MS ( $m/z$ ): 412 [M]<sup>+</sup>, 397 [M- CH<sub>3</sub>]<sup>+</sup>. Anal. Calc'd for Si<sub>4</sub>C<sub>22</sub>H<sub>36</sub>.2MeOH: C 60.50, H 9.25 %. Found: C 60.99, H 8.73%.

### 3.6.2. 1,6-bis(Cyanophenyl)-3-4-bis((4-cyanophenyl)ethynyl)hex-3-ene-1,5-diyne (22e)

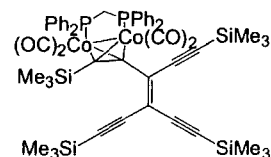


Dry NEt<sub>3</sub> (100 ml) was introduced to an oven-dried Schlenk flask and rigorously degassed by three freeze-pump-thaw sequences. Tetrachloroethylene (0.25 ml, 2.44 mmol) was added followed by ethynylbenzonitrile (1.25 g, 9.84 mmol), Pd(PPh<sub>3</sub>)<sub>4</sub> (0.14 g, 0.12 mmol) and CuI (0.02 g, 0.10 mmol). The solution was heated at reflux overnight forming a dark red solution with brown precipitate. The precipitate was collected by filtration, and the filtrate concentrated to yield a

second crop of the crude product. The precipitate was purified by column chromatography (silica gel, acetone). The product was recrystallised from hot acetonitrile to give the desired product as a yellow solid (0.54 g, 1.02 mmol, 42%).

IR (nujol):  $\nu(\text{CN})$  2224 w,  $\nu(\text{C}=\text{C})$  1600 w  $\text{cm}^{-1}$ .  $^1\text{H}$  NMR (499 MHz, DMSO):  $\delta$  7.78 (d, 8H, Ar,  $J_{\text{HH}}=8.39$ ), 7.95 (d, 8H, Ar,  $J_{\text{HH}}=8.59$ ).  $\text{EI}^+$  - MS ( $m/z$ ): 528  $[\text{M}]^+$ . Anal. Calc'd for  $\text{C}_{38}\text{H}_{16}\text{N}_4 \cdot 3/2\text{CH}_3\text{CN}$ : C 80.40, H 3.48, N 13.06%. Found: C 80.87, H 2.89, N 9.96%.

### 3.6.3. $[\text{Co}_2(\text{CO})_4(\text{dppm})\{\mu,\eta^2\text{-Me}_3\text{SiC}_2\text{C}(\text{C}\equiv\text{CSiMe}_3)=\text{C}(\text{C}\equiv\text{CSiMe}_3)_2\}]$ (39)



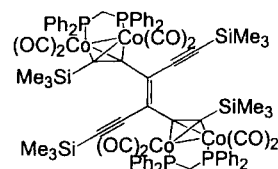
A round bottomed flask was charged with 1,6-bis(trimethylsilyl)-3-4-bis((trimethylsilyl)ethynyl)hex-3-ene-1,5-diyne (0.10 g, 0.24 mmol) and  $\text{Co}_2(\text{CO})_4(\text{dppm})$  (0.05 g, 0.08 mmol) which were dissolved in dry benzene (20 ml). The reaction was heated at reflux for 15 min after which three additional portions of  $\text{Co}_2(\text{CO})_4(\text{dppm})$  (0.05 g, 0.08 mmol) were subsequently added. The reaction was then cooled and the solvent removed *in vacuo*. The product was purified by preparative TLC (20:80  $\text{CH}_2\text{Cl}_2$ :hexane) and the major brown band was recrystallised from  $\text{CH}_2\text{Cl}_2$ :MeOH (0.16 g, 0.15 mmol, 62%).

IR (cyclohexane):  $\nu(\text{CO})$  2023 s, 1999 vs, 1973 s,  $\nu(\text{C}=\text{C})$  1653 m  $\text{cm}^{-1}$ .  $^1\text{H}$  NMR (499 MHz,  $\text{CDCl}_3$ ):  $\delta$  0.00 (s, 9H,  $\text{SiMe}_3$ ), 0.07 (s, 9H,  $\text{SiMe}_3$ ), 0.24 (s, 9H,  $\text{SiMe}_3$ ), 0.30 (s, 9H,  $\text{SiMe}_3$ ), 3.51 (m, 1H,  $\text{CH}_2$ ), 3.71 (m, 1H,  $\text{CH}_2$ ), 7.18 (m, 12H, Ar), 7.35 (m, 8H, Ar).  $^{13}\text{C}$  NMR (125 MHz,  $\text{CDCl}_3$ ):  $\delta$  0.00, 0.29, 0.66, 2.30 (4 x  $\text{SiMe}_3$ ), 36.40 ( $\text{CH}_2$ ), 98.11, 104.42, 105.35, 106.73, 107.04, 110.01, 111.02 (7 x

C≡C, C=C), 128.49, 128.56, 129.63, 129.89, 131.84, 132.52, 137.67, 141.11 (8 x Ar), 204.63, 206.97 (2 x CO). FAB - MS (*m/z*): 999 [M-CO]<sup>+</sup>, 971-915 [M-*n*CO]<sup>+</sup> (*n*=2-4). Anal. Calc'd for Co<sub>2</sub>P<sub>2</sub>O<sub>4</sub>Si<sub>4</sub>C<sub>51</sub>H<sub>58</sub>.1/2CH<sub>2</sub>Cl<sub>2</sub>: C 57.83, H 5.52%. Found: C 57.08, H 5.93%.

### 3.6.4. [ $\{Co_2(CO)_4(dppm)\}_2\{\mu-\eta^2:\eta^2-$

$Me_3SiC_2C(C\equiv CSiMe_3)C(C\equiv CSiMe_3)C_2SiMe_3\}$ ] (40)



A round bottomed flask was charged with [ $Co_2(CO)_4(dppm)\{\mu,\eta^2-$   $Me_3SiC_2C(C\equiv CSiMe_3)=C(C\equiv CSiMe_3)_2\}$ ] (0.18 g, 0.17 mmol) and  $Co_2(CO)_4(dppm)$  (0.40 g, 0.6 mmol) which were dissolved in dry benzene (20 ml). The reaction was heated at reflux for 3 h turning the solution brown which was then cooled and the solvent removed *in vacuo*. The product was purified by preparative TLC (1:1 CH<sub>2</sub>Cl<sub>2</sub>:hexane) and the low riding major brown band recrystallised from CH<sub>2</sub>Cl<sub>2</sub>:MeOH (0.03 g, 0.018 mmol, 10%).

IR (cyclohexane):  $\nu(C\equiv C)$  2127 w,  $\nu(CO)$  2024 m, 2001 s, 1976 m cm<sup>-1</sup>. <sup>1</sup>H NMR (499 MHz, CDCl<sub>3</sub>):  $\delta$  0.22 (s, 18H, SiMe<sub>3</sub>), 0.55 (s, 18H, SiMe<sub>3</sub>), 3.46 (m, 2H, CH<sub>2</sub>), 3.64 (m, 2H, CH<sub>2</sub>), 7.17 (m, 38H, Ar), 7.86 (s, 2H, Ar). <sup>13</sup>C NMR (125 MHz, CDCl<sub>3</sub>):  $\delta$  0.00, 2.06 (2 x SiMe<sub>3</sub>), 27.42 (CH<sub>2</sub>), 80.95, 84.49, 86.61, 88.73 (4 x C≡C, C=C), 128.18, 128.38, 128.73, 129.80, 129.99, 131.49, 131.92, 132.93 (8 x Ar). FAB - MS (*m/z*): 1641 [M+H]<sup>+</sup>, 1612-1360 [M-*n*CO]<sup>+</sup> (*n*=2-10). Anal. Calc'd for Co<sub>4</sub>P<sub>4</sub>O<sub>8</sub>Si<sub>4</sub>C<sub>80</sub>H<sub>80</sub>.2.5CH<sub>2</sub>Cl<sub>2</sub>: C 53.51, H 4.59%. Found: C 53.79, H 5.13%.

### 3.6.5. Reaction of crude 1,6-bis(trimethylsilyl)-3-4-

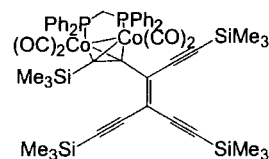
#### *bis*((trimethylsilyl)ethynyl)hex-3-ene-1,5-diyne with [Co<sub>2</sub>(CO)<sub>6</sub>(dppm)]

A round bottomed flask was charged with a crude reaction mixture of 1,6-bis(trimethylsilyl)-3-4-bis((trimethylsilyl)ethynyl)hex-3-ene-1,5-diyne (0.10 g, 0.24 mmol) and Co<sub>2</sub>(CO)<sub>4</sub>(dppm) (0.14 g, 0.23 mmol) which were dissolved in dry benzene (20 ml). The reaction was heated at reflux for 15 min after which an additional portion of Co<sub>2</sub>(CO)<sub>4</sub>(dppm) (0.12 g, 0.19 mmol) was added and the reaction continued for a further 15 min. The reaction was then cooled and the solvent removed *in vacuo*. The products were purified by preparative TLC (20:80 CH<sub>2</sub>Cl<sub>2</sub>:hexane) which gave red, yellow-brown and green bands. These were identified as Co<sub>2</sub>(CO)<sub>4</sub>(dppm)( $\mu,\eta^2$ -Me<sub>3</sub>SiC<sub>2</sub>C $\equiv$ CSiMe<sub>3</sub>) (29%), [Co<sub>2</sub>(CO)<sub>4</sub>(dppm){ $\mu,\eta^2$ -Me<sub>3</sub>SiC<sub>2</sub>C(C $\equiv$ CSiMe<sub>3</sub>)=C(C $\equiv$ CSiMe<sub>3</sub>)<sub>2</sub>}] (44%), and [{Co<sub>2</sub>(CO)<sub>4</sub>(dppm)}<sub>2</sub>{ $\mu,\eta^2$ -(Me<sub>3</sub>SiC<sub>2</sub>C(H)=C(C $\equiv$ CSiMe<sub>3</sub>)<sub>2</sub>)}] (9%) respectively. All the products were recrystallised from CH<sub>2</sub>Cl<sub>2</sub>:MeOH.

#### 3.6.5.1. [Co<sub>2</sub>(CO)<sub>4</sub>(dppm)( $\mu,\eta^2$ -Me<sub>3</sub>SiC<sub>2</sub>C $\equiv$ CSiMe<sub>3</sub>)]

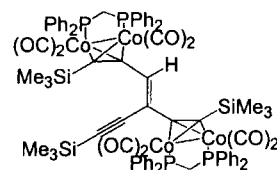
IR (cyclohexane):  $\nu(\text{CO})$  2028 s, 2006 vs, 1979 s cm<sup>-1</sup>. <sup>1</sup>H NMR (499 MHz, CDCl<sub>3</sub>):  $\delta$  0.21 (s, 9H, SiMe<sub>3</sub>), 0.33 (s, 9H, SiMe<sub>3</sub>), 3.29 (m, 1H, CH<sub>2</sub>), 3.37 (m, 1H, CH<sub>2</sub>), 7.02 (s, 6H, Ar), 7.15 (s, 2H, Ar), 7.23 (s, 6H, Ar), 7.43 (s, 6H, Ar). <sup>13</sup>C NMR (399 MHz, CDCl<sub>3</sub>):  $\delta$  0.00 (SiMe<sub>3</sub>), 35.44 (CH<sub>2</sub>), 99.67, 107.87 (2 x C $\equiv$ C), 127.58, 127.68, 127.94, 128.77, 129.49, 130.31, 132.56, 133.31, 138.39 (9 x Ar), 201.17, 206.95 (2 x CO).

3.6.5.2.  $[\text{Co}_2(\text{CO})_4(\text{dppm})\{\mu, \eta^2\text{-Me}_3\text{SiC}_2\text{C}(\text{C}\equiv\text{CSiMe}_3)=\text{C}(\text{C}\equiv\text{CSiMe}_3)_2\}]$   
(39)



IR (cyclohexane):  $\nu(\text{CO})$  2023 s, 1999 vs, 1973 s  $\text{cm}^{-1}$ .  $^1\text{H}$  NMR (499 MHz,  $\text{CDCl}_3$ ):  $\delta$  0.00 (s, 9H,  $\text{SiMe}_3$ ), 0.07 (s, 9H,  $\text{SiMe}_3$ ), 0.24 (s, 9H  $\text{SiMe}_3$ ), 0.30 (s, 9H,  $\text{SiMe}_3$ ), 3.51 (m, 1H,  $\text{CH}_2$ ), 3.71 (m, 1H,  $\text{CH}_2$ ), 7.18 (m, 12H, Ar), 7.35 (m, 8H, Ar).  $^{13}\text{C}$  NMR (125 MHz,  $\text{CDCl}_3$ ):  $\delta$  0.00, 0.29, 0.66, 2.30 (4 x  $\text{SiMe}_3$ ), 36.40 ( $\text{CH}_2$ ), 98.11, 104.42, 105.35, 106.73, 107.04, 110.01, 111.02 (7 x  $\text{C}\equiv\text{C}$ ), 128.49, 128.56, 129.63, 129.89, 131.84, 132.52, 137.67, 141.11 (8 x Ar), 204.63, 206.97 (2 x CO). FAB - MS ( $m/z$ ): 999-915  $[\text{M}-n\text{CO}]^+$  ( $n=1-4$ ). Anal. Calc'd for  $\text{Co}_2\text{P}_2\text{O}_4\text{Si}_4\text{C}_{51}\text{H}_{58} \cdot 1/2\text{CH}_2\text{Cl}_2$ : C 57.83, H 5.52%. Found: C 57.08, H 5.93%.

3.6.5.3.  $[\{\text{Co}_2(\text{CO})_4(\text{dppm})\}_2\{\mu, \eta^2\text{-(Me}_3\text{SiC}_2\text{C}(\text{H})=\text{C}(\text{C}\equiv\text{CSiMe}_3)_2)\}]$  (38)



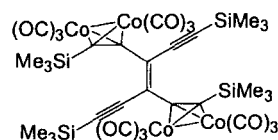
IR (cyclohexane):  $\nu(\text{CO})$  2021 s, 1997 vs, 1970 vs  $\text{cm}^{-1}$ .  $^1\text{H}$  NMR (499 MHz,  $\text{CDCl}_3$ ):  $\delta$  -0.17 (s, 9H,  $\text{SiMe}_3$ ), 0.13 (s, 9H,  $\text{SiMe}_3$ ), 0.40 (s, 9H,  $\text{SiMe}_3$ ), 3.43 (m, 2H,  $\text{CH}_2$ ), 3.59 (m, 1H, CH), 3.67 (m, 2H,  $\text{CH}_2$ ), 7.02 (m, 10H, Ar), 7.19 (m, 8H, Ar), 7.30 (m, 16H, Ar), 7.46 (s, 8H, Ar).  $^{13}\text{C}$  NMR (399 MHz,  $\text{CDCl}_3$ ):  $\delta$  0.00, 1.16, 1.44 (3 x  $\text{SiMe}_3$ ), 36.00, 38.62 (2 x  $\text{CH}_2$ ), 106.22, 106.57 (2 x  $\text{C}\equiv\text{C}$ ), 125.59, 127.78, 127.85, 128.03, 128.46, 128.53, 128.83, 129.14, 129.37, 129.56, 131.01, 131.18, 132.59, 132.78, 136.00, 139.65 (16 x Ar), 203.22, 204.56, 207.24, 207.79

(4 x CO). FAB - MS ( $m/z$ ): 1545  $[M]^+$ , 1517-1489  $[M-nCO]^+$  ( $n=1-2$ ). Anal. Calc'd for  $Co_4P_4O_8Si_3C_{75}H_{72} \cdot 1/3CH_2Cl_2$ : C 57.45, H 4.62%. Found: C 57.79, H 4.70%.

### 3.6.6. Reaction of 1,6-*bis*(trimethylsilyl)-3-4-*bis*((trimethylsilyl)ethynyl)hex-3-ene-1,5-diyne with $[Co_2(CO)_8]$

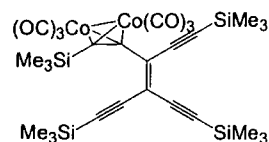
A round bottomed flask was charged with 1,6-*bis*(trimethylsilyl)-3-4-*bis*((trimethylsilyl)ethynyl)hex-3-ene-1,5-diyne (0.05 g, 0.12 mmol) and  $Co_2(CO)_8$  (0.11 g, 0.32 mmol) which were dissolved in dry benzene (10 ml). The reaction was stirred for 2 h then the solvent removed *in vacuo*. The product was purified by preparative TLC (20:80  $CH_2Cl_2$ :hexane) yielding a green and a brown band, identified as  $[ \{Co_2(CO)_6\}_2 \{ \mu-\eta^2:\eta^2-Me_3SiC_2C(C \equiv C SiMe_3)C(C \equiv C SiMe_3)C_2SiMe_3 \} ]$  (0.082 g, 0.08 mmol, 67%) and  $[Co_2(CO)_6 \{ \mu,\eta^2-Me_3SiC_2C(C \equiv C SiMe_3)=C(C \equiv C SiMe_3)_2 \} ]$  (0.011 g, 0.02 mmol, 17%) respectively.

#### 3.6.6.1. $[ \{Co_2(CO)_6\}_2 \{ \mu-\eta^2:\eta^2-Me_3SiC_2C(C \equiv C SiMe_3)C(C \equiv C SiMe_3)C_2SiMe_3 \} ]$ (41)



IR (cyclohexane):  $\nu$  (CO) 2088 s, 2056 vs, 2030 vs  $cm^{-1}$ .  $^1H$  NMR (399 MHz,  $CDCl_3$ ):  $\delta$  0.00 (s, 18H,  $SiMe_3$ ), 0.15 (s, 18H,  $SiMe_3$ ).  $^{13}C$  NMR (399 MHz,  $CDCl_3$ ):  $\delta$  0.00, 2.08 (2 x  $SiMe_3$ ), 84.08, 105.49, 107.49, 113.73, 128.22 (5 x  $C \equiv C$ ,  $C=C$ ), 200.89 (CO). FAB - MS ( $m/z$ ): 872-648  $[M-nCO]^+$  ( $n=4-12$ ). Anal. Calc'd for  $Co_4O_{12}Si_4C_{34}H_{36}$ : C 41.46, H 3.65%. Found: C 42.65, H 4.15%.

3.6.6.2.  $[\text{Co}_2(\text{CO})_6\{\mu, \eta^2\text{-Me}_3\text{SiC}_2\text{C}(\text{C}\equiv\text{CSiMe}_3)=\text{C}(\text{C}\equiv\text{CSiMe}_3)_2\}]$  (42)



IR (cyclohexane):  $\nu$  (CO) 2089 s, 2056 vs, 2030 vs  $\text{cm}^{-1}$ .  $^1\text{H}$  NMR (499 MHz,  $\text{CDCl}_3$ ), ( $\delta$ ): 0.00 (s, 9H,  $\text{SiMe}_3$ ), 0.16 (s, 27H,  $\text{SiMe}_3$ ).  $^{13}\text{C}$  NMR (125 MHz,  $\text{CDCl}_3$ ):  $\delta$  0.00, 0.26, 0.44, 1.74 (4 x  $\text{SiMe}_3$ ), 84.63, 98.09, 101.35, 103.59, 105.02, 105.16, 106.17, 112.29, 112.84, 135.34 (10 x  $\text{C}\equiv\text{C}$ ,  $\text{C}=\text{C}$ ), 200.24 (CO). FAB - MS ( $m/z$ ): 670-530 $[\text{M} - n\text{CO}]^+$  ( $n=1-6$ ). Anal. Calc'd for  $\text{Co}_2\text{O}_6\text{Si}_4\text{C}_{28}\text{H}_{36}$ .  $2\text{CH}_2\text{Cl}_2$ : C 44.44, H 4.85%. Found: C 45.22, H 5.32%.

## Chapter 4. Studies Utilising Density Functional Theory

### 4.1. The Relationship between Molecular Modelling and Chemistry

The Schrödinger equation and statistical mechanics can provide a mathematical model of chemistry, and in principle can be used to help answer problems in chemistry for which the answers are not readily available or apparent from experimental methods. If the Schrödinger equation could be solved for a molecule, a complete set of information, consistent with the postulates of quantum mechanics, could be derived for the molecule. However, the Schrödinger equation can only be solved exactly for the H atom. In order to obtain a workable result, it is necessary to make several approximations, which can take forms such as the Hartree-Fock formalism. It is prudent to remember that molecular modelling is not without limitations and caution must be taken not to over interpret the results. Molecular modelling can comfortably answer questions regarding energy differences between different systems, geometries, and electronic distribution of the molecule, although significantly larger errors are associated with bond energies, ionisation potentials and activation energies.

In general molecular modelling does not reproduce experimental results exactly, especially since molecular modelling (usually) assumes a gas phase environment in order to simplify calculations by neglecting environmental effects. Therefore it is more pertinent to compare property trends than the comparison of absolute values. It is not the purpose of this discussion to quantitatively explain the different methods in molecular modelling and the different algorithms associated with them. However, those related to the work presented here will be explained qualitatively in the discussion which follows.



## 4.2. Electronic Structure Calculation Methods

Since the Schrödinger equation cannot be solved directly for any system other than the H-atom, a number of approximations need to be invoked. The Born-Oppenheimer approximation is based on the idea that electrons move much faster than atomic nuclei and hence the movement of electrons can be considered independently to the movement of the nuclei. It is also assumed that in multi-electron systems, the electrons experience a static potential due to the nuclei, while the nuclei are subjected to the average potential field from the electrons. Hence, the Schrödinger equation for molecular systems may be divided into two expressions, one describing nuclear motion and one describing the motion of electrons.<sup>214</sup>

The determination of an accurate approximation of the electronic wavefunction for a molecule is a non-trivial task, and either *ab initio* or semi-empirical methods may be employed. The following discussion will concentrate on the *ab initio* method since the standard computer packages used in this work, Gaussian 98,<sup>201</sup> employs these methods. The approximation in *ab initio* methods lies in the choice of the model used to solve the wavefunction, which in turn affects the accuracy of the computational results.<sup>214</sup> Furthermore, all the integral expressions which must be solved for the chosen method of describing the electronic structure and the chosen method of constructing the wavefunction are evaluated without further approximations or input from experimental data. This is the reason the *ab initio* method is called the exact method.<sup>215</sup>

In most *ab initio* methods the wavefunctions are calculated by a self-consistent field (SCF) method which can employ either the Hartree-Fock (HF) or Density Functional Theory (DFT) formalism. In an SCF method each electron of a molecule moves in an average potential field caused by all of the (other) electrons in the molecule. Since electrons are not static points, the orbitals which contain them must be described mathematically using a set of basis functions as

building blocks. Together, these basis functions are known as basis sets and a wide variety have been developed.<sup>214</sup>

Two forms of basis functions have been widely used, namely the Slater-type orbital (STO) and Gaussian type orbitals. The STO, are rather difficult to manipulate mathematically and have largely been superseded by Gaussian type orbitals. While a single Gaussian function does not provide a good representation of an atomic orbital, the functions are easily manipulated since the product of two Gaussian functions is another Gaussian function. The combinations of Gaussians can be used to make good approximations to atomic orbitals.<sup>216</sup> The variation principle states that as basis sets are approximations of the true wavefunction, and the energies derived from them will always be too high. Better basis sets comprising a larger number of Gaussians, results in lower energies for the system. The simplest type of basis set, a minimal basis set, is comprised of one atomic orbital function for each filled atomic electron configuration. An improvement in accuracy of the approximation can be obtained by doubling the number of functions used, and this is specified by listing the exponents for each type of orbital used, e.g. doubling the number of a minimal basis set leads to a double *zeta* quality basis set.<sup>217</sup>

A convenient short-hand notation has been developed to describe the basis sets. The number before a G in a basis set title indicates the number of Gaussians used with a larger number giving an increased precision in the basis set, e.g. STO-3G indicates that three Gaussian functions have been used to form each Slater-type orbital. A split valence basis set uses two different models and is denoted with a hyphen, with the number on either side of the hyphen corresponding to the number of Gaussian functions used in either part of the model. An example of a split valence basis set is the 3-21G basis set, which is the smallest basis set in common use.<sup>216</sup> In this particular basis set, the core orbitals are described using three Gaussian functions, while the valence orbitals are described by two sets of

functions which arise from a linear combination of two Gaussian functions and an additional single Gaussian function.<sup>214</sup>

The assumptions implemented so far in the basis sets ignore the distortion by one atom of the atomic orbitals on adjacent atoms. This can be taken into account by including orbitals with higher values of the quantum number  $l$ . Such basis sets are known as polarisation functions and are capable of giving a reasonable description of a molecule in the ground or low lying excited state. Polarisation functions are denoted by asterisks after the basis set, and additional diffuse functions indicated by a + sign, e.g. the 6-31+G\*. A single asterisk indicates polarisation functions on non-hydrogen atoms, while a double asterisk, as in 6-31G\*\*, indicates polarisation functions on all atoms.<sup>216</sup>

#### 4.2.1. Density Functional Theory

Density Functional Theory (DFT) is a method used to calculate the electronic structure of molecules based on the electron density through a molecule rather than molecular orbitals,<sup>218</sup> and enables the calculation of the electronic properties of larger systems. In DFT the procedure begins with an expression for the total energy of the system written as a function of the total electron density for a given position of the atomic nuclei. The total energy may be derived, in a formally exact way, from three terms, a kinetic energy term, an electrostatic or Coulombic energy term, and a many body term, which contains all exchange and correlation effects. This derivation is constructed in such a way that the kinetic energy term corresponds to the kinetic energy of a system of non-interacting particles that yield the same density associated with the original electron system. The exact form of the universal energy density functional is unknown, and the strategy employed is to approximate it by various methods. Widely used formulas such as SVWN, BLYP, B3LYP, B3PW91, are examples of these models. These formulas are named based on either the Slater (S) or the Becke (B) gradient corrected functionals, the people who discovered these functionals such as Lee-

Yang-Parr (LYP), and the year it was discovered. DFT methods require a certain degree of "trial and error" in order to find the most appropriate basis set for any particular given system.<sup>219</sup>

The elementary algorithm for solution of electronic structures using DFT based methods is relatively simple. For a given molecular geometry (i.e. set of nuclear positions) the DFT equations are solved by expanding the one-electron wavefunctions (molecular orbitals) into a basis set. Following the Aufbau principle, the orbitals are occupied and a new density function is formed, completing one cycle in the SCF procedure. Convergence acceleration schemes are used to create a new input density from the previous input and output density. Once self-consistency is achieved, the total energy for this geometry with corresponding molecular properties can be calculated. If the goal is geometry optimisation, the energy gradients are evaluated and used in the choice of a new geometry. A new SCF cycle is then started from the new geometry and the cycle repeated until convergence is achieved.<sup>219</sup>

The agreement of calculated DFT geometries and electronic properties are comparable with traditional correlated methods. However, the applicability of DFT to all atoms of the periodic table and to various types of bonding with consistent accuracy, and the fact that scaling of computational effort with molecular size is equal or less than a third power, which is in contrast to traditional molecular orbital methods, all make DFT methods extremely appealing.<sup>216, 217</sup> However, one of the major drawbacks of DFT is that it only applies to the ground state, modelling of the excited state is still a major problem for DFT.<sup>217</sup>

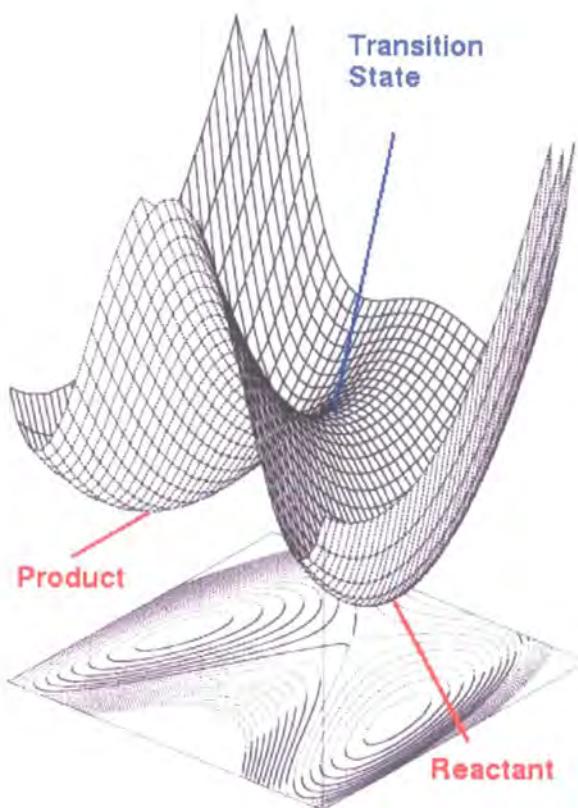
#### **4.2.2. Applicability of Density Functional Theory to Transition Metal Systems**

Due to the importance of transition metals in chemistry as key components in catalysts, as well as structural, electronic and photoactive molecular elements, it has become increasingly important that computational chemistry can predict the behaviour of such systems accurately. Transition metals range from electronically saturated, closed shell complexes to species with many unpaired electrons. Closed shell transition metal complexes can be handled using the closed shell methods, which approximate the core electrons using a static core potential. However, real problems arise when trying to deal with open shell complexes where there is a mixing of a large number of low-lying atomic electronic states to achieve optimal bonding. Fortunately the approximations used in DFT methods deal with this problem fairly well giving good qualitative descriptions. One of the drawbacks of DFT is that large errors for total energy are usually obtained. However, since the energy difference between two distinct states are most often of interest, these errors cancel out and give remarkable accuracy in DFT based modelling. Transition metal chemistry is a particular field where DFT has good accuracy for larger systems and has been used as a standard tool for the prediction of molecular structures.<sup>220</sup>

#### **4.3. Geometry Optimisation**

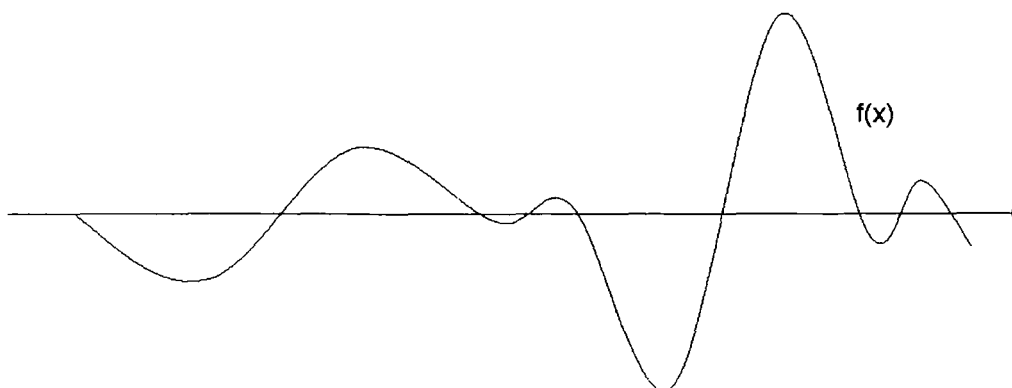
One of the most important tasks of computational chemistry is the reliable prediction of molecular structures. Due to improvements in the Kohn-Sham density functional theory algorithms for geometry optimisation, these methods can give geometry optimised structure results with an expected accuracy of  $\pm 0.02$  Å or better for bond lengths in molecules.<sup>220</sup> Geometry optimisation is the process of finding minima and saddle points on a potential energy surface. A potential energy surface describes the energy of a molecule as a function of its geometry; a

simple two dimensional potential energy surface can be seen in **Figure 59**. The equilibrium geometry of a molecule corresponds to the structure of the molecule at the global minimum of the potential energy surface, while the transition state structure corresponds to the structure at the first order saddle point.<sup>217</sup>



**Figure 59.** A generalised view of a potential energy surface.<sup>217</sup>

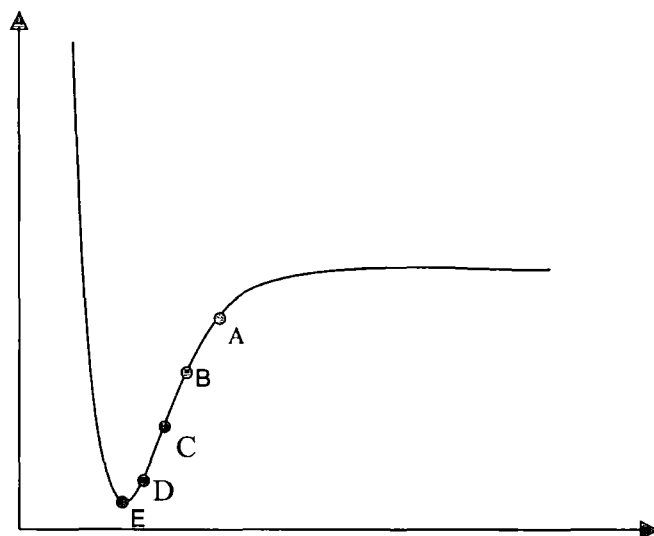
On a potential energy surface there might be several minima representing different conformers and isomers of the molecule, as illustrated in **Figure 60**. If the valley leading to the minimum is steep, then the molecule is fairly rigid and well defined, while if the valley is shallow and broad the molecule is flexible or reactive and its structure less well defined.



**Figure 60.** A one dimensional function containing several minima.

Finding the optimised geometry of a molecule involves an unconstrained optimisation in all directions on the potential energy surface. There are many different algorithms for finding minima, which have led to a host of different routines and computer programs to accomplish this task with relative ease. It is not intended in this discussion to explain the structure of optimisation algorithms, but rather to explain in general terms the important factors required by user to obtain the desired information.<sup>217</sup>

Energy minimisation as a function of geometry for a diatomic molecule is illustrated in **Figure 61**. The initial geometry A can be moved to a lower energy by making small changes to the geometry. This is then repeated from B to E in subsequent energy lowering steps, until all possible small changes to the structure increase the energy of the structure. This point (E) is called the minimum energy point.<sup>216</sup> To find the minimum energy point in a one dimensional system is quite easy; however, when a molecule has  $3N-6$  ( $N$ = number of atoms) degrees of freedom a large number of energy steps are needed, and the process becomes rather complicated. In real systems a large number of small steps need to be taken to avoid by-passing the minimum energy point altogether.<sup>216</sup>



**Figure 61.** Energy minimisation as a function of geometry for a diatomic molecule.

Once geometry optimisation is achieved, then other properties of the system of interest can be obtained; for example, population analysis, transition states, and vibrational frequencies. The text below illustrates finding a transition state. An analysis of the first derivative of a given point on the potential energy surface can give information of whether the potential energy surface is flat, i.e. a zero derivative; while the second derivative can be used to distinguish between minima, maxima, and saddle points.<sup>216</sup> The transition state is the highest point on a reaction path that requires the least amount of energy to get from reactants to products. A reaction path is described as the steepest descent path connecting a transition state to a minimum. A requirement of a transition state is that its first derivative to be zero and the energy must be a maximum along the reaction path. The transition state must also be a minimum for all directions perpendicular to the path. If this is not the case, then there is a nearby path with a lower barrier and a lower energy transition structure.<sup>217</sup> For a point on the potential energy surface to be a minimum it must satisfy two conditions. First of all, the first derivative must be zero and secondly, that the second derivative matrix (Hessian) must be positive



definite, or in other words, all the vibrational frequencies must be real, i.e., no imaginary frequencies.<sup>217</sup>

#### 4.4. Polyynyl Complexes as Potential Molecular Wires

Organometallic complexes of polyynyl  $[(C\equiv C)_nR]$ , polyynediyl  $[(C\equiv C)_n]$ , polyenyliene  $[(=C)_nR_2]$  and polyenyliene  $[(=C)_n=]$  ligands, which are highly unsaturated analogues of well-known acetylide and carbene ligands, have been extensively investigated in recent times. While several recent reviews,<sup>221-224</sup> and a notable piece of theoretical work,<sup>225-227</sup> have summarised the properties associated with the cumulated (i.e.  $\{C=C\}_n$ ) carbon ligands, the electronic structures of polyynyl complexes are less well defined. Given the significant interest in polyynyl complexes as potential components for molecular scale wires<sup>15, 43, 228</sup> and NLO active materials<sup>229-232</sup> a detailed description of these complexes is obviously desirable.<sup>233</sup> An electronic structure investigation of polyynyl complexes can answer the questions associated with the nature of bonding within the  $M-(C\equiv C)_n-R$   $\sigma$  and  $\pi$  framework, the electron distribution within the  $C\equiv C$  bonds and the degree to which it is attenuated by the attachment of the  $ML_n$  fragment which in return is associated with the relative electro- and nucleophilicity of the carbon chain.<sup>234-237</sup> The answers to these questions are crucial to the understanding of the properties of bulk material derived from metal-alkynyl building blocks, because significant  $\pi$ -electron delocalisation within the  $M-(C\equiv C)_n-R/M$  fragment is a prerequisite for the presence of large optical non-linearities and intramolecular electrical conductivities.

A number of studies have attempted to probe the electronic effects of  $\sigma$ -bonded polyynyl ligands,  $(C\equiv C)_nR$ , on certain metal centres by examination of the  $\nu(CO)$  and  $\nu(NO)$  stretching frequencies of the supporting ligands, the values of which were found to increase with increasing values of  $n$ .<sup>65, 67, 68, 73, 238</sup> A detailed, complementary IR and Raman study of polymers with  $[-Pt(PR_3)_2(C\equiv C)-]_n$  units

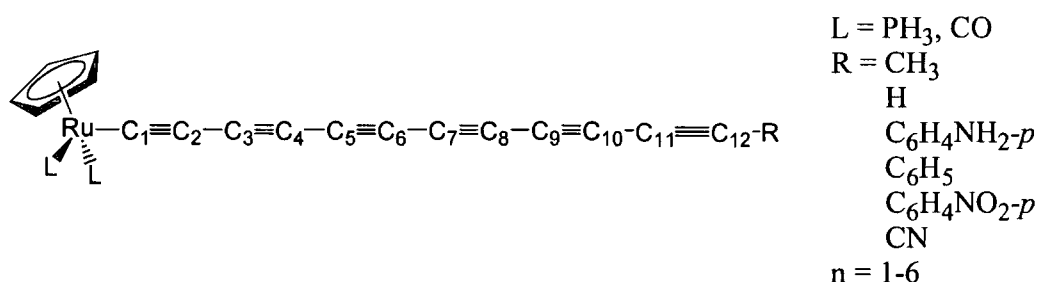
has also been reported.<sup>239</sup> However, the IR data alone cannot distinguish a progressive increase in metal  $\rightarrow \pi$ -ligand back-bonding interactions, due to the lower ligand  $\pi^*$  levels, from a progressively weaker  $\sigma$  donating effect, which is in keeping with acidity measurements of the free poly-ynes,<sup>240</sup> as the vibrational data reflects the *net* electronic effect of the polyynyl ligand.

Molecular orbital calculations of  $[\text{Fe}(\text{C}\equiv\text{CH})(\text{PH}_3)_2\text{Cp}]$  and  $[\text{Fe}(\text{C}\equiv\text{CH})(\text{CO})_2\text{Cp}]$  revealed that the M-CCH bonds in these complexes were nearly purely  $\sigma$  in character, and there is a large energy gap between the occupied metal orbitals and  $\pi^*(\text{C}\equiv\text{CH})$  levels. The filled  $\pi(\text{C}\equiv\text{CH})$  orbital mixes extensively with the higher lying filled metal orbitals.<sup>241</sup> The electronic structure of  $[\text{Fe}(\text{C}\equiv\text{CC}\equiv\text{CH})(\text{CO})_2\text{Cp}]$  has also been probed using He(I) and He(II) photoelectron spectroscopy (PES), which allows for ligand  $\pi$ -bonding effects to be distinguished from  $\sigma$ -bonding and charge potential effects.<sup>242</sup> This study also described the orbital interaction diagram for the  $[\text{Fe}(\text{CO})_2\text{Cp}]^+$  and  $[\text{C}\equiv\text{CC}\equiv\text{CH}]^-$  fragments.<sup>242</sup> The Fe-C  $\sigma$  bond was found to be formed by donation from the diynyl  $\sigma_{\text{sp}}$  orbital into empty metal  $d_{z^2}$  orbitals, while the most significant  $\pi$ -type interactions occur between occupied diynyl  $\pi$  electron set of levels and occupied metal  $d\pi$  orbitals. The diynyl ligand was found to be a relatively good  $\pi$ -donor, and as a result of the filled-filled (or four-electron, two orbital)  $\pi$ -interactions of the ligand with the metal, the HOMO contained considerable diynyl  $\pi$  character. Conversely, the  $\pi$ -acceptor character of the  $[\text{C}\equiv\text{CC}\equiv\text{CH}]$  ligand is negligible, with the empty  $\pi^*$  orbitals of the  $[\text{C}\equiv\text{CC}\equiv\text{CH}]^-$  fragment lying 13.9 eV above the occupied orbitals of similar symmetry.<sup>242</sup>

Attempts to derive electronic structure information from molecular structural data have not been conclusive, since the length of a  $\text{C}\equiv\text{C}$  bond is an unreliable measure of bond order (due to crystal packing forces) and the X-ray data generally available is often of poor quality.<sup>68, 165, 238, 243-256, 257 60, 258</sup> However,

it may be said that in all cases studied to date, the polyynyl ligand displays appreciable  $\text{C}\equiv\text{C}-\text{C}\equiv\text{C}$  character, with an alternating pattern of short and long C-C bond lengths. Often, the polycarbon ligands are not strictly linear but rather exhibit a degree of curvature, which has been attributed to crystal packing effects.<sup>62, 67, 68, 70, 259</sup>

The inconsistencies in the conclusions reached by the IR (which may suggest that the diynyl ligand is a good  $\pi$ -acceptor) and PES studies (which indicate the diynyl ligand to be a good  $\pi$ -donor) may be due to different evaluation methods. The  $\nu(\text{CO})$  parameters reflect the net electronic effects of the ligand while the PES results are based on metal band splitting of the  $\pi$ -type orbitals. In light of these ambiguities, an examination of the electronic structure of a series of complexes  $[\text{Ru}\{(\text{C}\equiv\text{C})_n\text{R}\}(\text{L})_2\text{Cp}]$  ( $n = 1-6$ ;  $\text{L} = \text{CO}, \text{PH}_3$ ) featuring end-capping groups R with a range of electronic properties ( $\text{R} = \text{CH}_3, \text{H}, \text{C}_6\text{H}_4\text{NH}_2\text{-}p, \text{C}_6\text{H}_5, \text{C}_6\text{H}_4\text{NO}_2\text{-}p, \text{CN}$ ) was undertaken (**Figure 62**). Organic groups were chosen as end-caps since the degree of charge separation between metal fragments in these types of compounds are comparable to the one between a metal donor fragment and a classic organic acceptor.<sup>260</sup> The chosen end-caps vary from those having electron donating properties to electron withdrawing end-caps.



**Figure 62.** Series of complexes  $[\text{Ru}\{(\text{C}\equiv\text{C})_n\text{R}\}(\text{L})_2\text{Cp}]$  ( $n = 1-6$ ;  $\text{L} = \text{CO}, \text{PH}_3$ ) featuring end-capping groups R ( $\text{R} = \text{CH}_3, \text{H}, \text{C}_6\text{H}_4\text{NH}_2\text{-}p, \text{C}_6\text{H}_5, \text{C}_6\text{H}_4\text{NO}_2\text{-}p, \text{CN}$ ) used in the study.

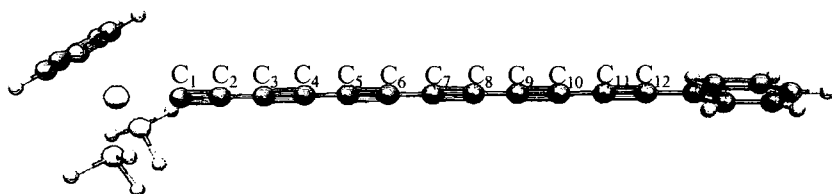
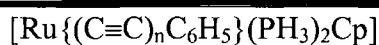
Cyanide is different to the other electron withdrawing end-caps but was chosen since cyanoacetylene has been shown to act as bridging ligands which has the capability of promoting electronic interactions between metal centres,<sup>261</sup> as well as the suggestion that  $(C\equiv C)_nCN$  ligands may act as building blocks in nanoelectronic digital circuits.<sup>262</sup> It has also been demonstrated that the use of a cyanide contact between organic molecular scale wire and a palladium probe would allow an increase in the conductivity of the molecular scale wires.<sup>86</sup> Due to the properties of cyanide described above, the behavior of CN and the  $M-(C\equiv C)_nCN$  series will be highlighted in the discussion as appropriate.

## 4.5. Electronic Structure of Polyynyl Complexes

### 4.5.1. Geometry Optimisation

The geometries calculated for  $[Ru\{(C\equiv C)_nR\}(PH_3)_2Cp]$  ( $R = C_6H_5, CN$ ) ( $n = 1, 2$ ) are in good agreement with the experimental structures of the  $PPh_3$  analogues (**Table 8 and 9**).<sup>60, 261, 273</sup> Complete agreement in the metrical parameters of the optimised and experimental structures should not be expected given the differences in supporting ligands ( $PH_3$  vs.  $PPh_3$ ), the gas-phase nature of the computation, the relatively small basis set employed and errors inherent within the functional. Nevertheless, the structural deviations such as they are fall well within 0.03 Å giving confidence in the accuracy and relevance of the computed geometries for the phenylbutadiynyl complex, and the other compounds described herein.

**Table 8.** Bond lengths associated with the metal-polyynyl portion of the molecules  $[\text{Ru}\{(\text{C}\equiv\text{C})_n\text{C}_6\text{H}_5\}(\text{PH}_3)_2\text{Cp}]$ . Experimental values are given in *italics*.



Bond (Å)	n					
	1 <sup>273</sup>	2 <sup>60</sup>	3	4	5	6
Ru-C(1)	2.008 <i>2.016(3)</i>	1.988 <i>1.994(4)</i>	1.980	1.974	1.970	1.968
C(1)-C(2)	1.227 <i>1.215(4)</i>	1.233 <i>1.206(5)</i>	1.235	1.236	1.238	1.238
C(2)-C(3)		1.359 <i>1.389(6)</i>	1.350	1.347	1.344	1.342
C(3)-C(4)		1.223 <i>1.200(6)</i>	1.231	1.233	1.235	1.236
C(4)-C(5)			1.351	1.343	1.338	1.336
C(5)-C(6)			1.225	1.233	1.237	1.238
C(6)-C(7)				1.349	1.340	1.337
C(7)-C(8)				1.226	1.233	1.237
C(8)-C(9)					1.349	1.339
C(9)-C(10)					1.226	1.234
C(10)-C(11)						1.348
C(11)-C(12)						1.225
C(2n)-C <sub>6</sub> H <sub>5</sub>	1.427 <i>1.456(4)</i>	1.421 <i>1.416(6)</i>	1.420	1.419	1.419	1.420

**Table 9.** Bond lengths associated with the metal-polyynyl portion of the molecules  $[\text{Ru}\{(\text{C}\equiv\text{C})_n\text{CN}\}(\text{PH}_3)_2\text{Cp}]$ . Experimental values are given in *italics*.

[Ru{(C≡C) <sub>n</sub> CN}(PH <sub>3</sub> ) <sub>2</sub> Cp]						
n						
Bond (Å)	1	2 <sup>261</sup>	3	4	5	6
Ru-C(1)	1.984	1.970 <i>1.9605(19)</i>	1.964	1.962	1.960	1.957
C(1)-C(2)	1.231	1.236 <i>1.221(3)</i>	1.238	1.239	1.240	1.241
C(2)-C(3)		1.348	1.342	1.340	1.339	1.332
C(3)-C(4)		1.227	1.234	1.236	1.238	1.236
C(4)-C(5)			1.341	1.336	1.333	1.326
C(5)-C(6)			1.229	1.236	1.239	1.236
C(6)-C(7)				1.340	1.335	1.325
C(7)-C(8)				1.229	1.236	1.235
C(8)-C(9)					1.341	1.328
C(9)-C(10)					1.229	1.232
C(10)-C(11)						1.335
C(11)-C(12)						1.226
C(2n)-C	1.365	1.360 <i>1.366(3)</i>	1.359	1.359	1.359	1.351
C-N	1.172	1.172 <i>1.153(3)</i>	1.172	1.171	1.172	1.174

For each of the complexes  $[\text{Ru}\{(\text{C}\equiv\text{C})_n\text{C}_6\text{H}_5\}(\text{PH}_3)_2\text{Cp}]$  examined ( $n = 1-6$ ), the  $\text{C}\equiv\text{C}$  bond length of the alkyne moiety directly attached to the phenyl group was remarkably invariant (1.226 -1.223 Å) as were the  $\text{C}-\text{C}_6\text{H}_5$  bond lengths (1.421 – 1.419 Å). The most striking feature of the computed structures of the  $[\text{Ru}\{(\text{C}\equiv\text{C})_n\text{C}_6\text{H}_5\}(\text{PH}_3)_2\text{Cp}]$  series lies in the steady decrease in the  $\text{Ru}-\text{C}(1)$  bond length with increasing values of  $n$  (**Table 8**). Further comment on this point is deferred to the discussion of charge distribution in these complexes below. Similar trends in bond lengths were observed for the cyano(poly)ynyl series  $[\text{Ru}\{(\text{C}\equiv\text{C})_n\text{CN}\}(\text{PH}_3)_2\text{Cp}]$  (**Table 9**), and thus discussion is concentrated around bond lengths of  $[\text{Ru}\{(\text{C}\equiv\text{C})_n\text{C}_6\text{H}_5\}(\text{PH}_3)_2\text{Cp}]$ .

As the polyyne ligand is allowed to lengthen, a strict  $\text{C}\equiv\text{C}/\text{C}-\text{C}$  bond alternation pattern along the carbon chain emerges, with  $\text{C}\equiv\text{C}$  bond lengths falling in the range 1.223–1.238 Å, and  $\text{C}-\text{C}$  between 1.337–1.359 Å (**Table 8**). As the chain length increases, a trend towards slightly longer  $\text{C}\equiv\text{C}$  groups and shorter  $\text{C}-\text{C}$  single bonds was observed, particularly for the interior alkyne moieties of the longer chain complexes. An examination of the parent polyynes  $[\text{H}(\text{C}\equiv\text{C})_n\text{H}]$ , using the same computational methods to ensure internal consistency in the data, showed similar trends in the  $\text{C}\equiv\text{C}$  and  $\text{C}-\text{C}$  bond lengths, with the parameters of the interior  $\text{C}\equiv\text{C}/\text{C}-\text{C}$  bonds approaching a limit of 1.234 /1.340 Å with increasing  $n$  (**Table 10**). Various computational studies have been performed of the  $\text{H}(\text{C}\equiv\text{C})_n\text{H}$  series, and the data collected here is in good general agreement.<sup>274, 275</sup> Therefore, it would appear that the metal centre plays little role in determining the bond lengths of the remote acetylenic moieties, and the small variations in structure are more an inherent property of the conjugated chain than a function of the metal centre.

**Table 10.** Computed bond lengths associated with the polyynes  $[H(C\equiv C)_nH]$ .

H-(C $\equiv$ C) <sub>n</sub> -H						
Bond (Å)	n					
	1	2	3	4	5	6
C(1)-C(2)	1.205	1.212	1.215	1.216	1.216	1.216
C(2)-C(3)		1.369	1.360	1.357	1.355	1.354
C(3)-C(4)		1.212	1.223	1.227	1.228	1.229
C(4)-C(5)			1.360	1.348	1.345	1.343
C(5)-C(6)			1.215	1.227	1.232	1.232
C(6)-C(7)				1.357	1.345	1.341
C(7)-C(8)				1.216	1.228	1.233
C(8)-C(9)					1.355	1.343
C(9)-C(10)					1.216	1.229
C(10)-C(11)						1.354
C(11)-C(12)						1.216

#### 4.5.2. Electronic Structure and Bonding

The bonding of an acetylide ligand to a transition metal fragment may be described in terms of overlap of the sp hybridised  $\sigma$  orbital of the  $C\equiv CR$  fragment with a metal fragment orbital of similar symmetry, usually composed of a large metal d-orbital component. In the case of  $[Ru(C\equiv CR)L_x]$  [ $L_x = (PH_3)_2Cp$ , *trans*-( $PH_3$ )<sub>4</sub>Cl], a small metal-to-ligand back-bonding contribution was identified, which increased in the order  $R = H < C_6H_5 < C_6H_4NO_2-p$ . However, the most significant  $\pi$ -orbital mixing arises from filled-filled interactions between the metal  $d\pi$  orbitals and the occupied ligand  $\pi$ -orbitals.<sup>241, 276-279</sup> Similar four-electron-two-



orbital interactions have been found in the iron diyne complex  $\text{Fe}(\text{C}\equiv\text{CC}\equiv\text{CH})(\text{CO})_2\text{Cp}^{242}$  and various diyndiyl complexes.<sup>55, 57, 58 280, 281</sup>

To help understand how the metal centre interacts with the polyyne ligand a simplified representation of the fragment orbital interaction diagram for  $[\text{Ru}(\text{PH}_3)_2\text{Cp}]^+$  and  $[(\text{C}\equiv\text{C})_n\text{R}]^-$  ( $\text{R} = \text{C}_6\text{H}_5$ ,  $n = 2$  and  $6$ ) was obtained from DFT calculations (**Figure 63**). To begin the discussion, the frontier orbitals of the  $[\text{Ru}(\text{PH}_3)_2\text{Cp}]^+$  fragment are considered. The lowest energy orbital is the  $d_{x^2-y^2}$  (**Figure 63**) which is the d-orbital least destabilised by the interactions with the Cp ring and phosphine ligands. Locally, this orbital does not have the correct symmetry to interact with the polyyne chain orbitals and remains essentially non-bonding and destabilised only slightly by Coulombic repulsion from the anionic ligand. The next highest metal fragment orbitals are the quasi-degenerate  $d_{xz}$  and  $d_{yx}$  pair which are of correct symmetry to interact with a similar pair of quasi-degenerate orbitals on the  $[(\text{C}\equiv\text{C})_n\text{R}]^-$  fragment. For all  $[(\text{C}\equiv\text{C})_n\text{R}]^-$  species considered in this work these later orbitals invariably consist of  $\text{C}_{p\pi}$  interactions which are bonding across bonds formally considered  $\text{C}\equiv\text{C}$  triple bonds and anti-bonding between those formally considered C-C single bonds. This pair is denoted as  $\pi_x$  and  $\pi_y$  for brevity. These orbitals form a filled bonding and anti-bonding set with the  $d_{xz}$  and  $d_{yz}$  orbitals the latter combination of which becomes the pair of quasi-degenerate HOMOs of the combined molecule. These HOMOs are only slightly stabilised by minor mixing (1-5%) with the next highest set of  $\pi$  orbitals (denoted  $\pi_x^*$  and  $\pi_y^*$  for simplicity) on the  $[(\text{C}\equiv\text{C})_n\text{R}]^-$  fragment, and are somewhat removed from the rest of the occupied orbitals. Thus to a first order approximation, the  $d_{xz}-\pi_x$  and  $d_{yz}-\pi_y$  pairs may both be considered to be derived from 4-electron 2-orbital interactions. By far the strongest interaction occurs between the HOMO of the  $[(\text{C}\equiv\text{C})_n\text{R}]^-$  fragment, which is a  $\sigma$ -type lone pair (LP) orbital located on the terminal carbon and the  $d_{z^2}$  on Ru. This pair forms a strong bonding and anti-bonding pair of which only the bonding combination is occupied. Finally, the highest metal d-orbital is the  $d_{xy}$  which, like the  $d_{x^2-y^2}$ , does

not have the correct local symmetry to interact with the  $[(\text{C}\equiv\text{C})_n\text{R}]^-$  fragment orbitals and is thus non-bonding and only destabilised by Coulombic interactions with the carbon chain. Therefore, a simple description of the bonding between the  $[\text{Ru}(\text{PH}_3)_2\text{Cp}]^+$  and  $[(\text{C}\equiv\text{C})_n\text{R}]^-$  fragments involves a net Ru-C single bond, and that the metal orbitals do not have a significant net interaction with the  $\pi$  orbitals of the polyynyl ligand. The presence of the metal fragment only introduces a weak perturbation effect on the polyyne fragment by inducing a minor mixing within the  $[(\text{C}\equiv\text{C})_n\text{R}]^-$   $\pi$  orbitals.

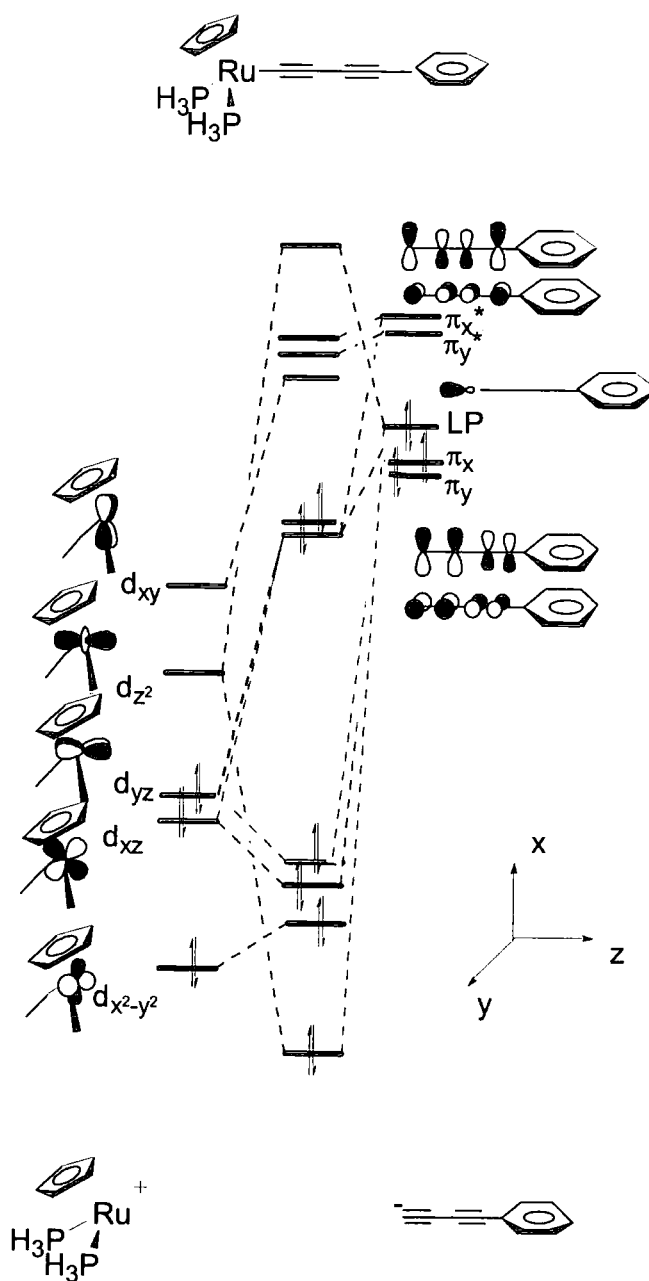
It is interesting to compare the effect of increasing polyynyl ligand chain length on the fragment orbital interaction diagram (**Figure 63a and b**) and the composition of the frontier orbitals (**Figure 64**).<sup>xi</sup> Overall, the general features of the orbital interaction diagrams are similar, save for a steady decrease in the energies of the frontier orbitals of the  $[(\text{C}\equiv\text{C})_n\text{R}]^-$  fragment, by about 2.5 eV between  $n = 2$  and  $n = 6$ , due to the greater capacity of the longer polyynyl fragments to stabilise the negative charge. This steady decrease in isolobal frontier orbital energy occurs for both  $\sigma$  and  $\pi$  states and is largely attenuated beyond  $n = 4$  for the  $\text{C}_6\text{H}_5$  end cap: the  $n = 6$  orbital energies are only 0.5 eV lower in energy than those for  $n = 4$  (**Figure 65**). This effect is strongly correlated with the nature of the end group where, in general, the more powerful electron withdrawing groups stabilise the negative charge. For example, the frontier orbitals of the  $(\text{C}\equiv\text{C})_2\text{CN}^-$  fragment which are isolobal with those of the  $\text{C}_5\text{H}_6$  series, and roughly equivalent in energy to those of  $[(\text{C}\equiv\text{C})_6\text{C}_6\text{H}_5]^-$ , are stabilised with respect to those of  $[(\text{C}\equiv\text{C})_6\text{C}_6\text{H}_5]^-$ . Likewise, there is a stabilisation of about 1.5 eV for the orbitals of  $[(\text{C}\equiv\text{C})_6\text{CN}]^-$  relative to those of  $(\text{C}\equiv\text{C})_2\text{CN}^-$ . Hence, the frontier orbitals of the fragment can be stabilised by CN or  $\text{C}_6\text{H}_4\text{NO}_2$  groups to a greater extent than H or  $\text{C}_6\text{H}_5$  end-caps, but the general trend of more stable fragment orbitals with increasing chain length is preserved. The stabilisation of the frontier orbitals has two major consequences upon bonding to the

---

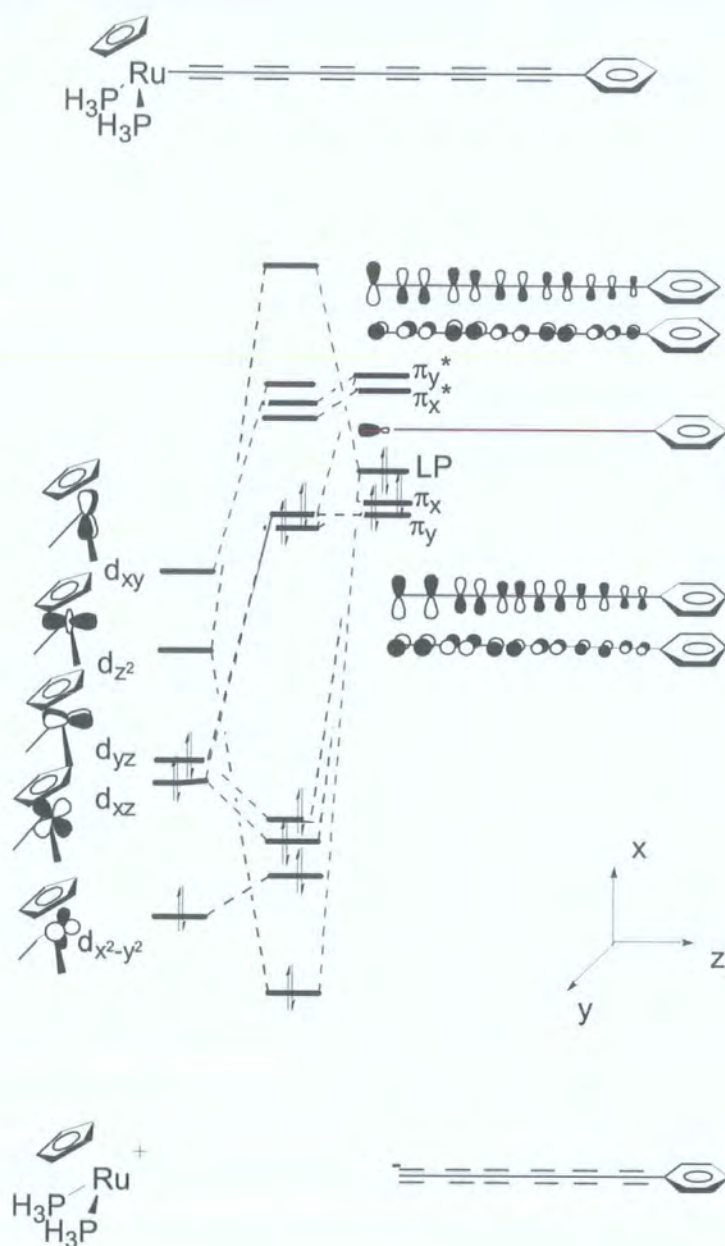
<sup>xi</sup> Interaction diagram courtesy of R. Rousseau.

$[\text{Ru}(\text{PH}_3)_2\text{Cp}]^+$  fragment. First, the  $\sigma$ -donation of the lone pair orbital is less effective in transferring charge to the metal centre. Second, the net contribution from the metal centre to the HOMOs of the combined molecule is reduced for the longer polyynyl complexes (**Figure 64**).

(a)



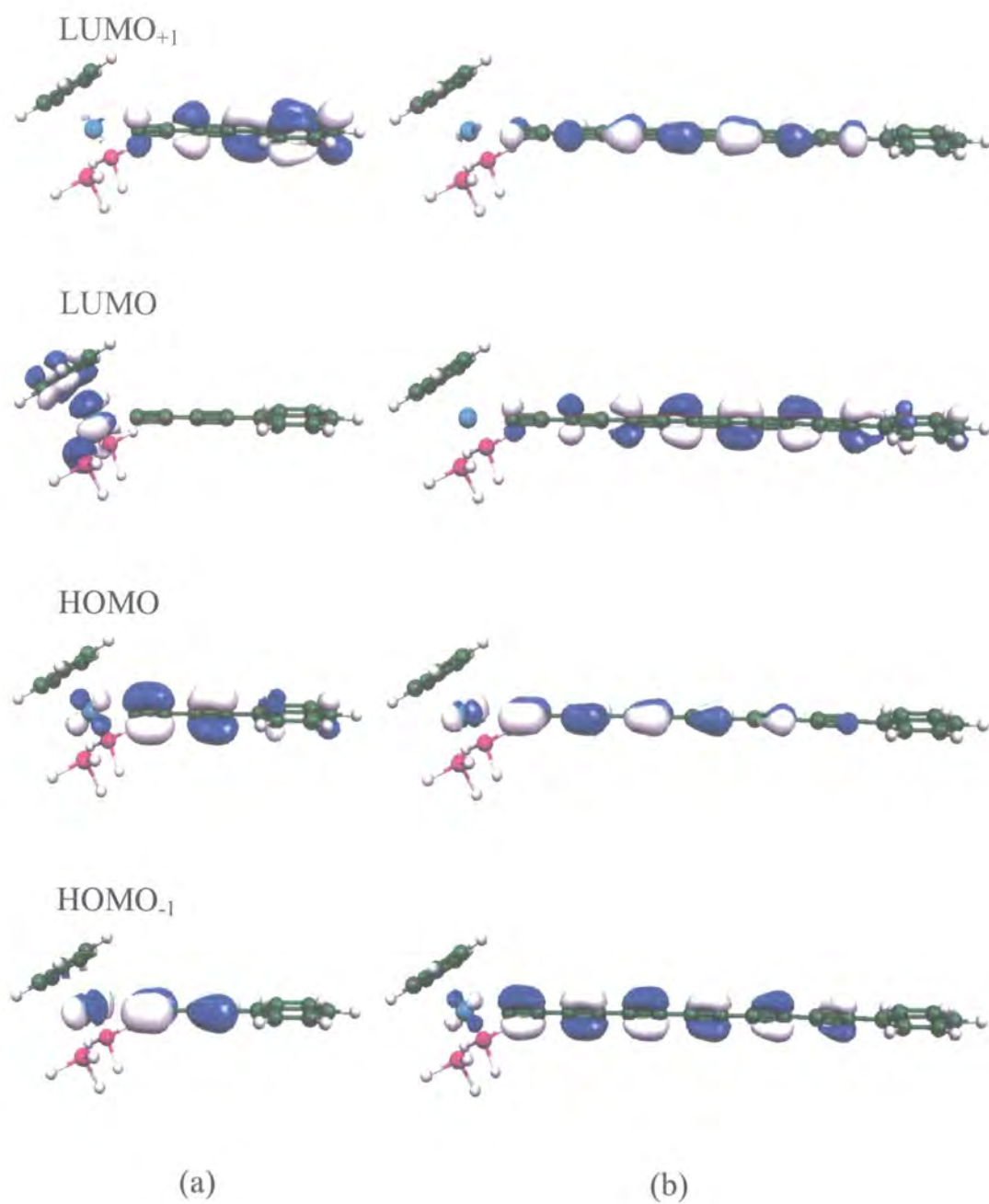
(b)



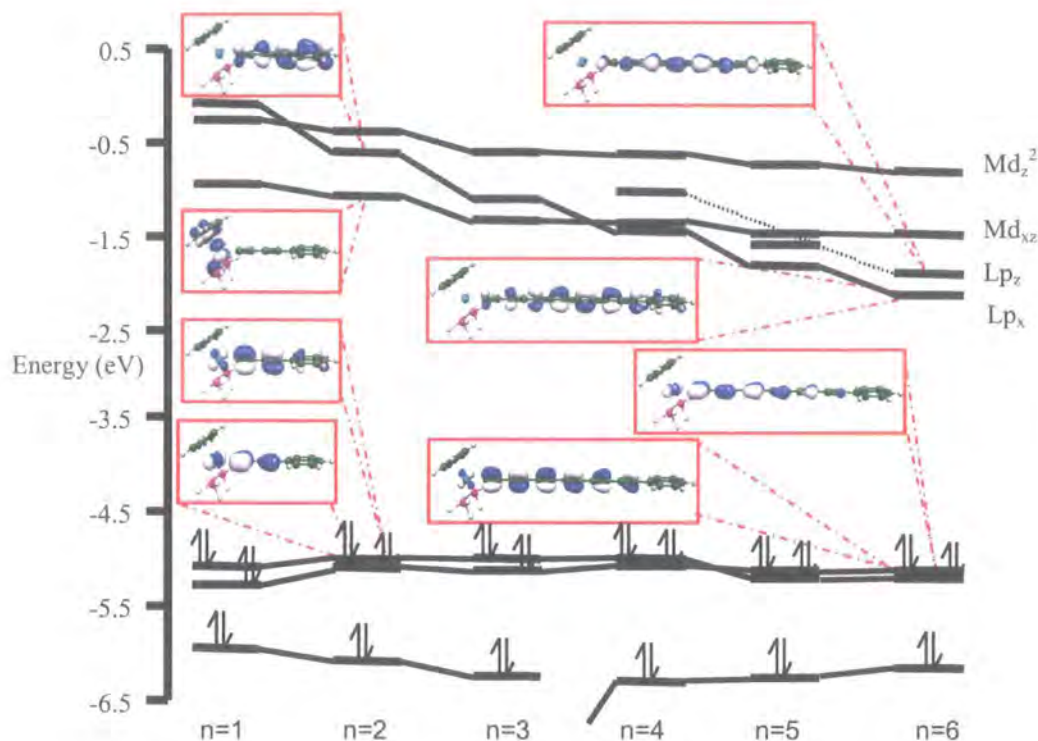
**Figure 63.** Schematic molecular orbital diagram for the complexes

(a)  $[\text{Ru}\{(\text{C}\equiv\text{C})_2\text{C}_6\text{H}_5\}(\text{PH}_3)_2\text{Cp}]$  and (b)  $[\text{Ru}\{(\text{C}\equiv\text{C})_6\text{Ph}\}(\text{PH}_3)_2\text{Cp}]$

depicting the interactions between the frontier orbitals of  $[\text{Ru}(\text{PH}_3)_2\text{Cp}]^+$  and  $[(\text{C}\equiv\text{C})_n\text{C}_6\text{H}_5]^-$ .



**Figure 64.** Orbital contour iso-surface (0.005 a.u.) plots of the frontier orbitals of (a) [Ru{(C≡C)<sub>2</sub>C<sub>6</sub>H<sub>5</sub>}(PH<sub>3</sub>)<sub>2</sub>Cp] and (b) [Ru{(C≡C)<sub>6</sub>C<sub>6</sub>H<sub>5</sub>}(PH<sub>3</sub>)<sub>2</sub>Cp].



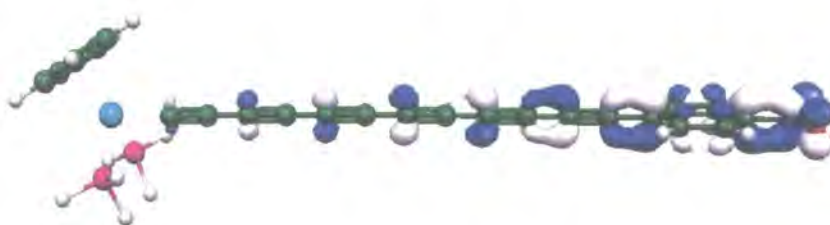
**Figure 65.** HOMO - LUMO gap decrease for  $[\text{Ru}\{(\text{C}\equiv\text{C})_n\text{C}_6\text{H}_5\}(\text{PH}_3)_2\text{Cp}]$ .

The HOMO and  $\text{HOMO}_{-1}$  of each member of the  $[\text{Ru}\{(\text{C}\equiv\text{C})_n\text{C}_6\text{H}_5\}(\text{PH}_3)_2\text{Cp}]$  series are  $\pi$ -type in character and are delocalised over the metal and polyynyl chain. They exhibit bonding character between the carbons of the  $\text{C}\equiv\text{C}$  moieties and antibonding interactions between the metal centre and  $\text{C}(1)$ , and also the carbons of the  $\text{C}-\text{C}$  single bonds within the polyynyl chain. In each case, one of these components is of the correct symmetry to interact with the phenyl  $\pi$ -system, but only in the case of the shorter chain complexes is the HOMO significantly delocalised over the phenyl ring (**Figure 64**). There is a substantial stabilisation of the LUMO with increasing values of  $n$  due to the decreasing energy of the ligand  $\pi$ -type orbitals (**Figure 63 and 65**). Consequently, the large energy gap that separates the occupied and unoccupied orbital sets in the diyne complex decreases with increasing chain length and the composition of the LUMO shifts from being predominantly metal  $d_{xy}$  in character to almost exclusively polyynyl ( $\pi^*_x$  and  $\pi^*_y$ ) centred (**Figure 64**). Therefore, as the



polyynyl ligand becomes longer, the complexes begin to exhibit qualitatively similar frontier orbitals regardless of the nature of the end-cap R.

In polyynyl complexes  $[\text{Ru}\{(\text{C}\equiv\text{C})_n\text{R}\}(\text{PH}_3)_2\text{Cp}]$  containing the electron donating end-caps ( $\text{R} = \text{H}$ ,  $\text{CH}_3$  and  $\text{C}_6\text{H}_4\text{NO}_2\text{-}p$ ) the HOMO-LUMO gap decreases by approximately 1 eV as the chain is lengthened from one alkynyl moiety to six, while for the CN-capped series the gap decreases by as much as 1.5 eV (**Table 11**). A much smaller decrease in HOMO-LUMO gap (0.5 eV) was found for the  $\text{C}_6\text{H}_4\text{NO}_2\text{-}p$  series, which is somewhat surprising given the similar electron withdrawing power of the CN and  $\text{C}_6\text{H}_4\text{NO}_2\text{-}p$  groups, but may be attributed to the significant contribution of the  $\text{NO}_2$  group to the LUMO in this case (**Figure 66**). Therefore it would appear that while the end-cap has a role in tuning the orbital energies, the electronic structure and orbital composition is largely the same for all complexes examined in this study.



**Figure 66.** Orbital contour iso-surface (0.005 a.u.) plot of the LUMO of the nitrophenyl substituted complex  $[\text{Ru}\{(\text{C}\equiv\text{C})_6\text{C}_6\text{H}_4\text{NO}_2\text{-}p\}(\text{PH}_3)_2\text{Cp}]$ : compare with **Figure 64a**.

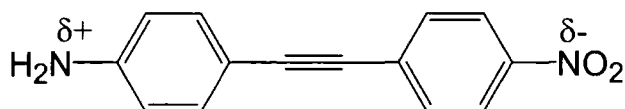
**Table 11.** HOMO-LUMO energies of  $[\text{Ru}\{(\text{C}\equiv\text{C})_n\text{R}\}(\text{PH}_3)_2\text{Cp}]$  ( $\text{R} = \text{C}_6\text{H}_4\text{NH}_2\text{-}p$ ,  $\text{CH}_3$ ,  $\text{H}$ ,  $\text{C}_6\text{H}_5$ ,  $\text{C}_6\text{H}_4\text{NO}_2\text{-}p$ ,  $\text{CN}$ ).

$[\text{Ru}\{(\text{C}\equiv\text{C})_n\text{R}\}(\text{PH}_3)_2\text{Cp}]$		E	HOMO	E	LUMO	E	HOMO-
R	n	(eV)	(eV)	(eV)	(eV)	LUMO	LUMO (eV)
$\text{C}_6\text{H}_4\text{NH}_2\text{-}p$	2		-4.332		-0.918		3.413
	3		-4.412		-1.058		3.353
	4		-4.503		-1.130		3.372
	5		-4.712		-1.147		3.225
	6		-4.649		-1.736		2.914
$\text{CH}_3$	2		-4.617		-0.868		3.749
	3		-4.645		-1.053		3.591
	4		-4.694		-1.205		3.489
	5		-4.799		-1.686		3.114
	6		-4.803		-1.694		3.109
$\text{H}$	2		-4.828		-0.967		3.861
	3		-4.832		-1.157		3.674
	4		-4.874		-1.269		3.604
	5		-4.900		-1.481		3.418
	6		-4.939		-1.860		3.079
$\text{C}_6\text{H}_5$	2		-4.732		-1.001		3.731
	3		-4.755		-1.164		3.591
	4		-4.788		-1.337		3.452
	5		-4.830		-1.675		3.155
	6		-4.866		-1.964		2.902
$\text{C}_6\text{H}_4\text{NO}_2\text{-}p$	2		-5.214		-2.133		3.053
	3		-5.124		-2.318		3.081
	4		-5.085		-2.481		2.604
	5		-5.088		-2.625		2.463
	6		-5.231		-2.700		2.531
$\text{CN}$	2		-5.395		-1.513		3.882
	3		-5.355		-1.571		3.783
	4		-5.317		-1.976		3.341
	5		-5.305		-2.317		2.988
	6		-5.287		-2.567		2.720



### 4.5.3. Charge Distribution

To complement the orbital analysis outlined above, the charge distribution within the  $[\text{Ru}\{(\text{C}\equiv\text{C})_n\text{C}_6\text{H}_5\}(\text{PH}_3)_2\text{Cp}]$  series was examined. Summation of the natural charge on each of the fragments  $[\text{Ru}(\text{PH}_3)_2\text{Cp}]$ ,  $[(\text{C}\equiv\text{C})_n]$  and  $[\text{C}_6\text{H}_5]$  indicated a substantial amount of negative charge residing on the polyyne chain, the majority of which resides on the alkyne moiety adjacent to the metal centre due to the involvement of this moiety in the strong, polar covalent  $\sigma$ -bond with the metal centre (**Table 12**). The amount of charge distributed along the carbon chain is significantly larger than was found for the *p*-amino-*p*'-nitrodiphenyl ethyne systems (0.14 electron) due to the presence of the metal centre in the present work (**Figure 67**).<sup>282</sup> In agreement with the fragment orbital analysis, the larger *n* chains bear a greater negative charge, resulting in larger positive charge on both the  $[\text{Ru}(\text{PH}_3)_2\text{Cp}]$  and  $[\text{C}_6\text{H}_5]$  fragments (**Table 12**). The resulting increased Coulombic attraction between the metal and carbon fragments with increasing *n* is speculated to be responsible for the decreased Ru-C(1) bond length computed for the longer chain polyyne complexes (**Table 8**).



**Figure 67.** The compounds *p*-amino-*p*'-nitrodiphenyl ethyne.

**Table 12.** Fragment charges and total charge distribution for  
 $[\text{Ru}\{(\text{C}\equiv\text{C})_n\text{C}_6\text{H}_5\}(\text{PH}_3)_2\text{Cp}]$ .

n	q Ru(PH <sub>3</sub> ) <sub>2</sub> Cp (e <sup>-</sup> )	q (C≡C) <sub>n</sub> (e <sup>-</sup> )	q C <sub>6</sub> H <sub>5</sub> (e <sup>-</sup> )	qC <sub>(1+2)</sub> (e <sup>-</sup> )	qC <sub>(3-n)</sub> (e <sup>-</sup> )	% qC <sub>(1+2)</sub>	% qC <sub>(3-n)</sub>
1	0.498	-0.427	-0.071				
2	0.537	-0.491	-0.046	-0.446	-0.045	90.808	9.191
3	0.558	-0.532	-0.026	-0.434	-0.098	81.615	18.385
4	0.574	-0.562	-0.011	-0.426	-0.136	75.726	24.273
5	0.585	-0.582	-0.002	-0.417	-0.164	71.769	28.231
6	0.602	-0.597	-0.005	-0.412	-0.185	68.989	31.010

The total amount of charge deposited on the polyynyl chain is related not only to the length of the polyynyl ligand, but also to the electronic nature of the non-metal end-cap. This is illustrated for the diyynyl series ( $n = 2$ ) in (Table 13). As the non-metal end-cap becomes more electron-withdrawing there is a decrease of up to 0.1 electron in the amount of charge residing on the diyynyl fragment, and an increase in the fractional electronic charge on the end-cap (Table 13). Again, the majority of the charge on the polyynyl fragment is contained on the alkyne moiety adjacent to the metal centre in all cases examined. However, within the most structurally similar set of complexes considered (i.e.  $\text{R} = \text{C}_6\text{H}_5$ ,  $\text{C}_6\text{H}_4\text{NH}_2$ -*p*,  $\text{C}_6\text{H}_4\text{NO}_2$ -*p*) it is noticed that as the R group becomes more electron withdrawing the percentage of charge located on the  $\text{C}(1)\equiv\text{C}(2)$  acetylene moiety with respect to the total charge on the carbon fragment increases significantly [ $\text{R} = \text{C}_6\text{H}_4\text{NH}_2$ -*p* (70.77%) <  $\text{C}_6\text{H}_5$  (90.81 %) <  $\text{C}_6\text{H}_4\text{NO}_2$ -*p* (94.80 %)]. This observation is in agreement with the trends in frontier orbital energies of the  $[(\text{C}\equiv\text{C})_n\text{R}]^-$  fragments, as the greater the electron accepting ability of the non-metal end-cap, the more the

Ru-C(1) bond is polarised towards the polyynyl ligand, and hence the more the charge on the metal bonded alkyne moiety increases.

**Table 13.** Fragment charges and total charge distribution for the substituted diynyl complexes  $[\text{Ru}\{(\text{C}\equiv\text{C})_2\text{R}\}(\text{PH}_3)_2\text{Cp}]$ .

R	q Ru(PH <sub>3</sub> ) <sub>2</sub> Cp (e <sup>-</sup> )	q (C≡C) <sub>2</sub> (e <sup>-</sup> )	q R (e <sup>-</sup> )	qC <sub>(1+2)</sub> (e <sup>-</sup> )	qC <sub>(3+4)</sub> (e <sup>-</sup> )
C <sub>6</sub> H <sub>4</sub> NH <sub>2</sub> - <i>p</i>	0.660	-0.640	-0.020	-0.453	-0.187
H	0.533	-0.767	0.235	-0.452	-0.315
CH <sub>3</sub>	0.557	-0.572	0.015	-0.458	-0.114
C <sub>6</sub> H <sub>5</sub>	0.537	-0.491	-0.046	-0.446	-0.045
C <sub>6</sub> H <sub>4</sub> NO <sub>2</sub> - <i>p</i>	0.565	-0.451	-0.113	-0.427	-0.023
CN	0.593	-0.508	-0.085	-0.421	-0.087

The gross charge distribution model is one way to rationalise the properties of the polyynyl complexes. However, it is impossible to probe structure and reactivity questions deeply without acknowledging the individual contributions made by  $\sigma$  and  $\pi$  components. As demonstrated by the fragment orbital analysis presented above, and by similar work reported elsewhere,<sup>241-244, 276-279</sup> the dominant  $\sigma$ -type contribution arises from the interaction of the metal  $d_{z^2}$  type fragment orbital with the orbital of same symmetry on the polyynyl ligand and thus the C(1) atom has the greatest net negative charge. However, an examination of the charge residing within the  $\pi$ -orbitals (denoted  $\pi$ -charge,  $q_\pi$ ) on each acetylenic carbon centre of the polyynyl ligand reveals a trend towards charge alternation in the  $\pi$  cloud along the polyynyl chain with positive charge residing on the odd-positioned carbon atoms [C(1, 3, 5, ...)] and negative charge on the even atoms [C(2, 4, 6, ...)] (**Table 14**). Some distortions to this pattern are

found for the carbon centres of the alkyne moieties adjacent to the phenyl group, presumably arising from the  $\text{C}\equiv\text{C}-\text{C}_6\text{H}_5$  interactions (Table 14). The  $\pi$ -charge alternation is more pronounced for the systems with electron-withdrawing groups, and this is clearly illustrated by the  $n = 6$  series (Table 15). In keeping with the polarisation argument given above for the gross charge distribution there is a slight increase (0.02 e) in the  $\pi$ -charge on C(1) and C(2) as the R group is varied from  $\text{C}_6\text{H}_5$  to  $\text{C}_6\text{H}_4\text{NO}_2\text{-}p$  (Table 15).

**Table 14.** Distribution of  $\pi$ -charge throughout the polyynyl ligand in the complexes  $[\text{Ru}\{(\text{C}\equiv\text{C})_n\text{C}_6\text{H}_5\}(\text{PH}_3)_2\text{Cp}]$ .

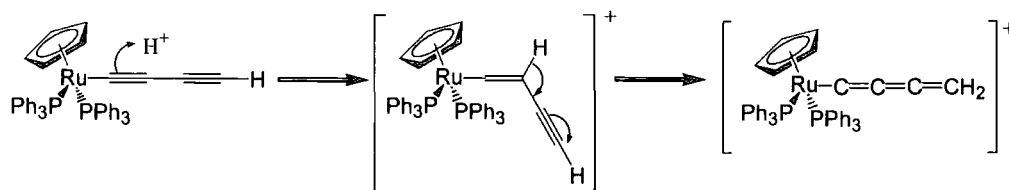
$[\text{Ru}\{(\text{C}\equiv\text{C})_n\text{C}_6\text{H}_5\}(\text{PH}_3)_2\text{Cp}]$						
	n					
Charge (e <sup>-</sup> )	1	2	3	4	5	6
$q\pi_1$	0.087	0.119	0.138	0.150	0.163	0.169
$q\pi_2$	-0.152	-0.183	-0.187	-0.188	-0.192	-0.193
$q\pi_3$		-0.005	0.021	0.035	0.046	0.053
$q\pi_4$		-0.040	-0.084	-0.090	-0.094	-0.096
$q\pi_5$			-0.034	-0.003	0.012	0.021
$q\pi_6$			0.002	-0.048	-0.058	-0.043
$q\pi_7$				-0.042	-0.010	0.003
$q\pi_8$				0.024	-0.031	-0.041
$q\pi_9$					-0.047	-0.006
$q\pi_{10}$					0.038	-0.017
$q\pi_{11}$						-0.052
$q\pi_{12}$						0.051
Total	-0.065	-0.109	-0.144	-0.162	-0.173	-0.151

**Table 15.** Distribution of  $\pi$ -charge throughout the hexynyl ligand in the complexes  $[\text{Ru}\{(\text{C}\equiv\text{C})_6\text{R}\}(\text{PH}_3)_2\text{Cp}]$  ( $\text{R} = \text{C}_6\text{H}_4\text{NH}_2\text{-}p$ ,  $\text{CH}_3$ ,  $\text{H}$ ,  $\text{C}_6\text{H}_5$ ,  $\text{C}_6\text{H}_4\text{NO}_2\text{-}p$ ,  $\text{CN}$ ).

$[\text{Ru}\{(\text{C}\equiv\text{C})_6\text{R}\}(\text{PH}_3)_2\text{Cp}]$						
Charge ( $e^-$ )	R					
	$\text{C}_6\text{H}_4\text{NH}_2\text{-}p$	$\text{CH}_3$	$\text{H}$	$\text{C}_6\text{H}_5$	$\text{C}_6\text{H}_4\text{NO}_2\text{-}p$	$\text{CN}$
$q\pi_1$	0.161	0.168	0.176	0.169	0.191	0.198
$q\pi_2$	-0.177	-0.193	-0.196	-0.193	-0.202	-0.200
$q\pi_3$	0.044	0.049	0.056	0.053	0.062	0.076
$q\pi_4$	0.081	-0.095	-0.098	-0.096	-0.107	-0.105
$q\pi_5$	0.009	0.016	0.025	0.021	0.028	0.048
$q\pi_6$	-0.056	-0.060	-0.065	-0.043	-0.071	-0.074
$q\pi_7$	-0.008	-0.002	0.011	0.003	0.015	0.040
$q\pi_8$	-0.032	-0.037	-0.045	-0.041	-0.052	-0.060
$q\pi_9$	-0.011	-0.024	-0.003	-0.006	0.000	0.040
$q\pi_{10}$	-0.010	-0.012	-0.025	-0.018	-0.034	-0.055
$q\pi_{11}$	-0.070	-0.082	-0.059	-0.052	-0.031	0.047
$q\pi_{12}$	0.056	0.072	0.048	0.051	0.025	-0.070
Total	-0.013	-0.201	-0.175	-0.152	-0.176	-0.115

Several reactions of polyynyl species with electrophilic reagents have been reported, with addition of the electrophile to C(2) or C(4) being found.<sup>237, 249</sup> The computational results reported here are entirely consistent with these works, and taken together suggest that the addition of electrophiles to polyynyl complexes occur under charge control. Given the significantly larger charge on C(2), protonation of  $[\text{Ru}(\text{C}\equiv\text{CC}\equiv\text{CH})(\text{PPh}_3)_2\text{Cp}]$  at C(4) is somewhat surprising.<sup>237</sup> The

steric bulk of the metal fragment may therefore also play a role in determining the site of attack, and the possibility that this latter reaction occurs with preliminary protonation at C(2) giving the alkynylvinylidene cation  $[\text{Ru}\{\text{C}=\text{C}(\text{H})\text{C}\equiv\text{CH}\}(\text{PPh}_3)_2\text{Cp}]^+$  being followed by subsequent rearrangement to the suspected butatrienylidene product  $[\text{Ru}(\text{C}=\text{C}=\text{C}=\text{CH}_2)(\text{PPh}_3)_2\text{Cp}]^+$  cannot be discounted (Scheme 23).<sup>236</sup>



**Scheme 23.** Addition of electrophiles to polyynyl complexes.

#### 4.5.4. C-C Bond Order

As alluded to above and based on the qualitative orbital diagrams of **Figure 63**, to a first approximation metal-alkyne  $\pi$  interactions may be considered to have a limited effect on the bonding framework. However, d- $\pi$  interactions do cause remixing of the frontier  $\pi$ -orbitals on the  $[(\text{C}\equiv\text{C})_n\text{R}]^-$  fragment. To quantify this contribution to the electronic structure of the  $[\text{Ru}\{(\text{C}\equiv\text{C})_n\text{R}\}(\text{PPh}_3)_2\text{Cp}]$  species, it is necessary to assess it in terms of the overall bond order of the C-C bonds. This simple parameter may be used as a qualitative descriptor to avoid unduly complicated descriptions that would undoubtedly arise for the larger species where an analysis of mixing effects within many orbitals would be required to unravel the underlying mechanism. Here, the bond order is determined by half the difference of the bonding and anti-bonding electron population, as determined by Natural Bond Order (NBO) analysis,<sup>263</sup> for each of the C-C bonds.

The computed C-C bond orders for the acetylide series  $[\text{Ru}(\text{C}\equiv\text{CR})(\text{PH}_3)_2\text{Cp}]$  ( $\text{R} = \text{H}, \text{CH}_3, \text{C}_6\text{H}_5, \text{C}_6\text{H}_4\text{NO}_2\text{-}p, \text{C}_6\text{H}_4\text{NH}_2\text{-}p, \text{CN}$ ) are given in **Table 16**. This data shows that electron withdrawing end-caps induce the lowest C(1)-C(2) bond orders, which results in part from a decrease in the total bonding density almost all of which comes from the carbon centred  $\pi$ -bonding orbitals. Moreover, there is an almost equivalent increase in the population in the carbon centred anti-bonding orbitals, the majority of which are  $\pi$ -type. Thus, in addition to the small increase in the electron density on the C-C backbone, which is induced by the electron-withdrawing R groups and deposited in C-C  $\pi^*$  orbitals, there is also a significant contribution from promotion of electrons in C-C  $\pi$ -bonding orbitals to C-C  $\pi$ -anti-bonding orbitals. This polarisation, or remixing, of the  $\pi$ -electrons is the underlying reason for the increase of  $\text{C}\equiv\text{C}$  bond lengths observed in these molecules relative to acetylene. Overall, the observed trends in C(1) $\equiv$ C(2) bond length may be rationalised in terms of a secondary remixing of the backbone  $\pi$ -orbitals induced either by the metal fragment or by the non-metal end group.

**Table 16.** Computed bond order associated with the  $\text{C}\equiv\text{C}$  triple bond of the acetylide ligand in the substituted complexes  $[\text{Ru}(\text{C}\equiv\text{CR})(\text{PH}_3)_2\text{Cp}]$  ( $\text{R} = \text{C}_6\text{H}_4\text{NH}_2\text{-}p, \text{CH}_3, \text{H}, \text{C}_6\text{H}_5, \text{C}_6\text{H}_4\text{NO}_2\text{-}p, \text{CN}$ ).

$[\text{Ru}\{(\text{C}\equiv\text{C})\text{R}\}(\text{PH}_3)_2\text{Cp}]$			
R	$\rho$ Bonding	$\rho$ Antibonding	BO
$\text{C}_6\text{H}_4\text{NH}_2\text{-}p$	5.860	0.221	2.820
H	5.966	0.137	2.914
$\text{CH}_3$	5.917	0.189	2.864
$\text{C}_6\text{H}_5$	5.848	0.215	2.816
$\text{C}_6\text{H}_4\text{NO}_2\text{-}p$	5.795	0.226	2.785
CN	5.778	0.273	2.753

As the polyyne ligand chain length is increased from  $n = 1$  to  $n = 6$ , there is a corresponding decrease in the  $C(1)\equiv C(2)$  bond order (Table 17). Again, the diminished bond order of the  $C(1)\equiv C(2)$  moiety may be attributed to a combination of the decreased bonding density and a corresponding increase in the anti-bonding density (Table 17). A similar process of orbital mixing and electron redistribution is also evident within the parent molecule  $H(C\equiv C)_6H$ . For the remaining  $C\equiv C$  bonds in the carbon backbone the order of this polarisation is similar to that of the  $H(C\equiv C)_6H$  species indicating that the end groups strongly perturb only the  $C\equiv C$  unit to which they are directly attached. These observations are in agreement with, and extend, the bonding model proposed in previous studies,<sup>260</sup> despite the difference in the methodologies used.

#### 4.5.5. Variation of the Supporting Ligand on the Metal

To explore the effect of ligand substitution on the structural and electronic properties of these species, the carbonyl diynyl complexes  $[Ru\{(C\equiv C)_nR\}(CO)_2Cp]$  ( $n = 1, 2$ ) were investigated and comparative fragment orbital interaction diagrams for  $[Ru(PH_3)_2Cp]^+$  and  $[Ru(CO)_2Cp]^+$  with the acetylide anion  $[C\equiv CH]^-$  are given in Figure 68.<sup>xii</sup> As expected, the frontier orbitals of the  $[Ru(CO)_2Cp]^+$  fragment are similar to those of the phosphine analogue, although the electron withdrawing nature of the carbonyl ligands lowers the energy of the d-orbitals by about 1 eV, and thus the interaction diagram with the  $[C\equiv CH]^-$  is qualitatively similar to that shown in Figure 63. Substitution of CO for  $PH_3$  can be seen to have a similar (but opposite) effect to including an electron withdrawing group as a non-metal end cap or to lengthening the carbon backbone.

<sup>xii</sup> Interaction diagram courtesy of R. Rousseau.



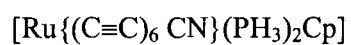
**Table 17.** Computed bond order associated with the hexatriynyl ligand C-C and C≡C bonds in the substituted complexes [Ru{(C≡C)<sub>6</sub>R}(PH<sub>3</sub>)<sub>2</sub>Cp] (R = C<sub>6</sub>H<sub>4</sub>NH<sub>2</sub>-*p*, CH<sub>3</sub>, H, C<sub>6</sub>H<sub>5</sub>, C<sub>6</sub>H<sub>4</sub>NO<sub>2</sub>-*p*, CN) and [H(C≡C)<sub>6</sub>H].

[Ru{(C≡C) <sub>6</sub> C <sub>6</sub> H <sub>5</sub> } (PH <sub>3</sub> ) <sub>2</sub> Cp]			
	ρ Bonding	ρ Antibonding	BO
C(1)-C(2)	5.688	0.334	2.677
C(2)-C(3)	1.970	0.031	0.969
C(3)-C(4)	5.614	0.424	2.595
C(4)-C(5)	1.973	0.026	0.974
C(5)-C(6)	5.600	0.044	2.778
C(6)-C(7)	1.974	0.025	0.974
C(7)-C(8)	5.605	0.432	2.586
C(8)-C(9)	1.974	0.025	0.974
C(9)-C(10)	5.631	0.402	2.615
C(10)-C(11)	1.974	0.025	0.974
C(11)-C(12)	5.708	0.402	2.653

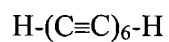
  

[Ru{(C≡C) <sub>6</sub> C <sub>6</sub> H <sub>4</sub> NO <sub>2</sub> - <i>p</i> } (PH <sub>3</sub> ) <sub>2</sub> Cp]			
	ρ Bonding	ρ Antibonding	BO
C(1)-C(2)	5.667	0.336	2.665
C(2)-C(3)	1.959	0.037	0.961
C(3)-C(4)	5.597	0.442	2.577
C(4)-C(5)	1.961	0.033	0.964
C(5)-C(6)	5.584	0.452	2.566
C(6)-C(7)	1.961	0.032	0.964
C(7)-C(8)	5.589	0.442	2.574
C(8)-C(9)	1.961	0.032	0.964
C(9)-C(10)	5.617	0.411	2.603

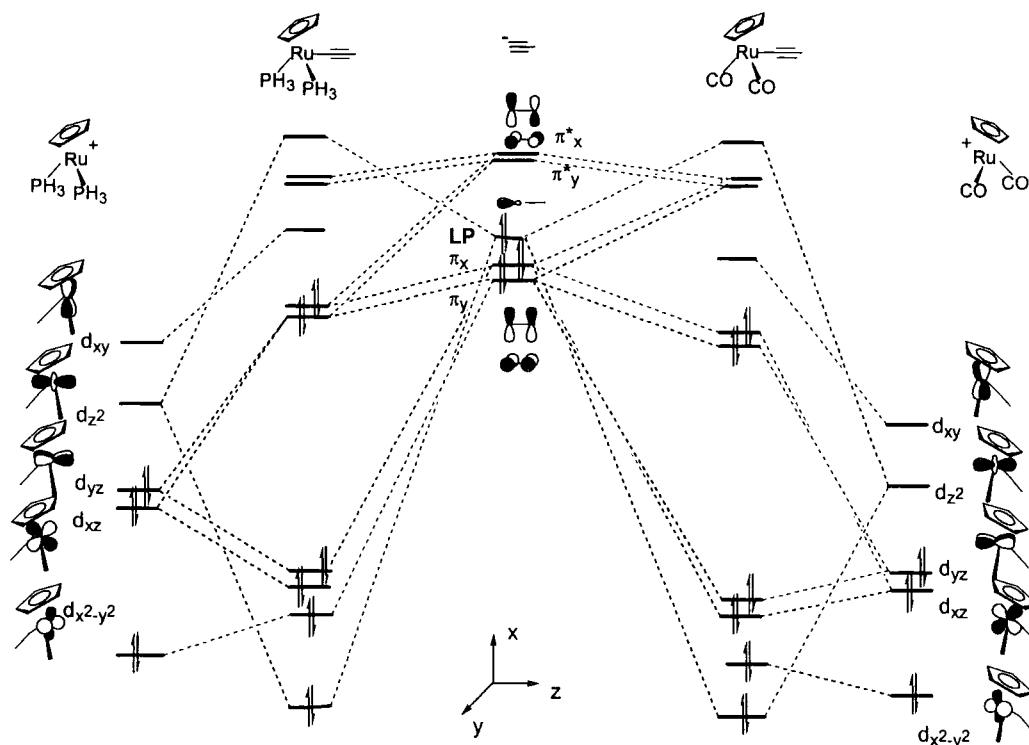
C(10)-C(11)	1.961	0.033	0.964
C(11)-C(12)	5.696	0.306	2.694



	ρ Bonding	ρ Antibonding	BO
C(1)-C(2)	5.661	0.340	2.660
C(2)-C(3)	1.970	0.031	0.969
C(3)-C(4)	5.588	0.440	2.575
C(4)-C(5)	1.973	0.026	0.974
C(5)-C(6)	5.573	0.452	2.560
C(6)-C(7)	1.974	0.025	0.974
C(7)-C(8)	5.575	0.443	2.566
C(8)-C(9)	1.974	0.025	0.974
C(9)-C(10)	5.595	0.418	2.588
C(10)-C(11)	1.974	0.025	0.974
C(11)-C(12)	5.660	0.362	2.649



	ρ Bonding	ρ Antibonding	BO
C(1)-C(2)	5.800	0.177	2.812
C(3)-C(4)	5.646	0.351	2.647
C(5)-C(6)	5.614	0.386	2.614
C(7)-C(8)	5.614	0.386	2.614
C(9)-C(10)	5.646	0.351	2.647
C(11)-C(12)	5.800	0.177	2.812



**Figure 68.** Schematic molecular orbital diagram for the complexes

a)  $[\text{Ru}(\text{C}\equiv\text{CH})(\text{PH}_3)_2\text{Cp}]$  and (b)  $[\text{Ru}(\text{C}\equiv\text{CH})(\text{CO})_2\text{Cp}]$  depicting the interactions between the frontier orbitals of  $[\text{Ru}(\text{PH}_3)_2\text{Cp}]^+$  and  $[\text{Ru}(\text{CO})_2\text{Cp}]^+$  with  $[\text{C}\equiv\text{CH}]^-$ .

In keeping with the strongly electron withdrawing nature of the carbonyl supporting ligands, analysis of the charge distribution within the carbonyl series reveals considerably less electron density residing on the diyne ligand and the non-metal end-cap (**Table 18**). In essence, the CO ligands withdraw the excess negative charge from the acetylide ligand onto the metal fragment. This leads to a lengthening of the Ru-C(1) bond by about 0.01 Å and a decrease in the C(1)≡C(2) bond length by the same amount relative to the phosphine substituted analogue. It follows that the alternation of the  $\pi$ -charge along the carbon backbone will be attenuated, and while in almost all cases similar trends in  $\pi$ -charge are found

between the CO and PH<sub>3</sub> species the net  $\pi$ -charge is decreased by about 30% (Table 19).

**Table 18.** Total charge distribution in the diynyl carbonyl complexes

[Ru{(C≡C)<sub>2</sub>R}(CO)<sub>2</sub>Cp] (R = C<sub>6</sub>H<sub>4</sub>NH<sub>2</sub>-*p*, CH<sub>3</sub>, H, C<sub>6</sub>H<sub>5</sub>, C<sub>6</sub>H<sub>4</sub>NO<sub>2</sub>-*p*, CN).

[Ru{(C≡C) <sub>2</sub> R}(CO) <sub>2</sub> Cp]						
R	q Ru(CO) <sub>2</sub> Cp (e <sup>-</sup> )	q (C≡C) <sub>2</sub> (e <sup>-</sup> )	q R (e <sup>-</sup> )	qC <sub>(1+2)</sub> (e <sup>-</sup> )	qC <sub>(3+4)</sub> (e <sup>-</sup> )	
C <sub>6</sub> H <sub>4</sub> NH <sub>2</sub> - <i>p</i>	0.413	-0.422	0.008	-0.617	0.142	
H	0.427	-0.666	0.238	-0.404	-0.197	
CH <sub>3</sub>	0.414	-0.438	0.024	-0.540	0.114	
C <sub>6</sub> H <sub>5</sub>	0.427	-0.400	-0.026	-0.606	0.153	
C <sub>6</sub> H <sub>4</sub> NO <sub>2</sub> - <i>p</i>	0.463	-0.376	-0.086	-0.607	0.177	
CN	0.505	0.059	-0.565	-0.635	0.695	

As noted previously, electronic properties such as redox potential and the energy of electronic transitions largely depend upon the relative electron withdrawing/donating strength of the various metal and non-metal end groups.<sup>260</sup> In many respects, replacement of the phosphine supporting ligands by CO has a similar effect of opposite polarity to including an electron withdrawing R group, or increasing the length of the polyyne ligand. Thus rational ligand substitution about the metal may also serve as a route by which to modify the electronic structure and hence the reactivity and redox properties of these compounds.

**Table 19.** Distribution of  $\pi$ -charge throughout the diyndyl ligand in the complexes  $[\text{Ru}\{(\text{C}\equiv\text{C})_6\text{R}\}(\text{L})_2\text{Cp}]$  ( $\text{L} = \text{CO}, \text{PH}_3$ ;  $\text{R} = \text{C}_6\text{H}_4\text{NH}_2\text{-}p$ ,  $\text{CH}_3$ ,  $\text{H}$ ,  $\text{C}_6\text{H}_5$ ,  $\text{C}_6\text{H}_4\text{NO}_2\text{-}p$ ,  $\text{CN}$ ).

R	[Ru{(C≡C) <sub>2</sub> R}(CO) <sub>2</sub> Cp]				[Ru{(C≡C) <sub>2</sub> R}(PH <sub>3</sub> ) <sub>2</sub> Cp]			
	q $\pi_1$	q $\pi_2$	q $\pi_3$	q $\pi_4$	q $\pi_1$	q $\pi_2$	q $\pi_3$	q $\pi_4$
C <sub>6</sub> H <sub>4</sub> NH <sub>2</sub> - <i>p</i>	0.080	-0.142	-0.045	-0.001	0.104	-0.175	-0.030	-0.035
H	0.106	-0.152	-0.036	-0.018	0.120	-0.187	-0.029	-0.045
CH <sub>3</sub>	0.075	-0.137	-0.059	0.009	0.097	-0.177	-0.050	-0.021
C <sub>6</sub> H <sub>5</sub>	0.097	-0.145	-0.021	-0.012	0.119	-0.183	-0.005	-0.040
C <sub>6</sub> H <sub>4</sub> NO <sub>2</sub> - <i>p</i>	0.149	-0.166	0.020	-0.045	0.064	-0.193	0.029	-0.062
CN	0.178	-0.174	0.134	-0.113	0.175	-0.204	0.078	-0.136

#### 4.5.6. Effects of Oxidation

The oxidation chemistry of diyndyl complexes has been investigated thoroughly using a combination of synthetic, electrochemical, structural and spectro-electrochemical techniques.<sup>55, 57, 58, 280</sup> Similar studies of polyynyl complexes are much less advanced and primarily limited to electrochemical measurements.<sup>73, 227, 283-285</sup> To provide more detailed insight into the effects of oxidation on polyynyl species, the electronic structure of the  $[\text{Ru}\{(\text{C}\equiv\text{C})_n\text{C}_6\text{H}_5\}(\text{PH}_3)_2\text{Cp}]^+$  cations was analysed.

For a *qualitative* understanding of the changes induced by removal of a single electron from these species it is useful to refer the molecular orbital diagrams in **Figure 63**. First, removal of an electron from the HOMO of these species should lead to a reduction in the net repulsive interaction between the metal  $d_{xz}$  and  $d_{yz}$  orbitals and the  $\pi_x$  and  $\pi_y$  orbitals of the polyynyl ligand. Since this orbital is largely centred on the polycarbon chain, oxidation should be

expected to give rise to a corresponding change in the C-C bonding interactions. The optimised geometries calculated for each of the complexes  $[\text{Ru}\{(\text{C}\equiv\text{C})_n\text{C}_6\text{H}_5\}(\text{PH}_3)_2\text{Cp}]^+$  ( $n = 1-6$ ) reveal a significant decrease in the Ru-C(1) bond length from *ca.* 2.00 Å in the neutral species to *ca.* 1.900 Å in the oxidised form, an increase of 0.01-0.02 Å in the C≡C bond lengths and a 0.02-0.03 Å decrease in the length of the C-C single bonds (**Table 20**). These structural differences correlate well with the HOMO structure depicted in **Figure 64** in that bond lengths increase where the orbital interactions are bonding and conversely decrease where they are anti-bonding.

**Table 20.** Bond lengths associated with the metal-polyynyl portion of the radical cations  $[\text{Ru}\{(\text{C}\equiv\text{C})_n\text{C}_6\text{H}_5\}(\text{PH}_3)_2\text{Cp}]^+$ .

$[\text{Ru}\{(\text{C}\equiv\text{C})_n\text{C}_6\text{H}_5\}(\text{PH}_3)_2\text{Cp}]^+$						
	n					
Bond (Å)	1	2	3	4	5	6
Ru-C(1)	1.929	1.909	1.904	1.903	1.904	1.905
C(1)-C(2)	1.249	1.257	1.259	1.258	1.259	1.258
C(2)-C(3)		1.326	1.317	1.314	1.313	1.313
C(3)-C(4)		1.240	1.249	1.254	1.254	1.255
C(4)-C(5)			1.326	1.314	1.311	1.309
C(5)-C(6)			1.238	1.248	1.253	1.255
C(6)-C(7)				1.328	1.316	1.312
C(7)-C(8)				1.236	1.246	1.252
C(8)-C(9)					1.33	1.318
C(9)-C(10)					1.285	1.245
C(10)-C(11)						1.331
C(11)-C(12)						1.233
C(2n)-C <sub>6</sub> H <sub>5</sub>	1.400	1.399	1.399	1.404	1.405	1.406

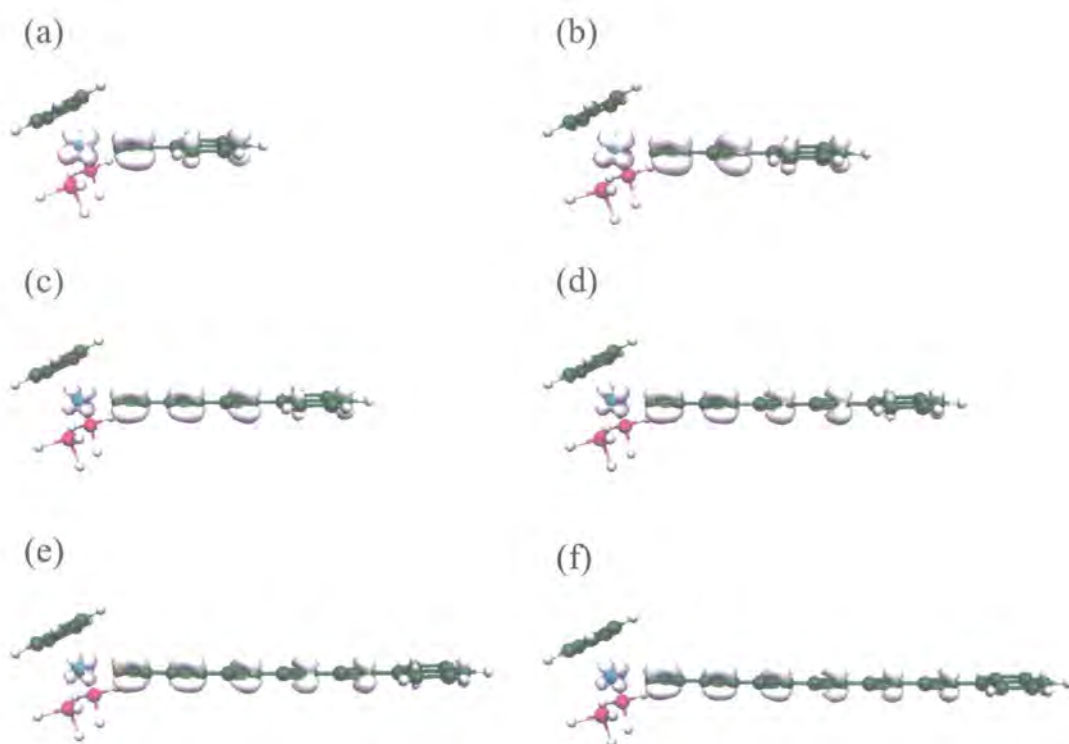
For complexes with a value of  $n$  less than three a comparison of the charge distribution in the oxidised (**Table 21**) and neutral (**Table 12**) forms indicates that approximately half of the electron lost originates from the metal fragment with the remainder originating from the polyynyl ligand and the phenyl group (**Table 21**). As the length of the polyynyl ligand increases the carbon ligand becomes the dominant source of the oxidised electron, which is in complete accord with the nature of the HOMO in the neutral species (**Table 21, Figure 64**). Thus for small  $n$  there is a significant effect on the Ru-C bond length upon oxidation as a large part of the electron removed originates from the metal centre, and this effect becomes less as the chain is lengthened. The carbon-carbon bond lengths are much less sensitive to the change since the fraction of electron lost is divided over all the carbon centres of the polyynyl ligand.

As a complementary measure of the origin of the oxidised electron, distribution of unpaired electron spin density in the oxidised species is calculated. This corresponds to the probability distribution of the radical electron that would be generated following oxidation of the neutral species. Graphical displays of the spin density in the cationic species show a significant amount of spin density between the  $C\equiv C$  triple bonded carbon centres (**Figure 69**). The spin density for all these species is in good qualitative agreement with the shape of the orbital generated by the anti-bonding combination of  $d_{xz}$  and  $\pi_x$  (**Figures 63 and 64**) indicating that the remaining unpaired electron is strongly delocalised. It is important to note that despite the fact that the molecule is fully able to rearrange its structure and thus localise the unpaired electron this is in fact not observed and the radical prefers to be delocalised over the entire molecule. In passing, in all cases the unpaired spin density corresponds to the  $d_{xz}$  and  $\pi_x$  anti-bonding pair despite the fact that it is not the HOMO for species with  $n \leq 2$ . This is related to the relaxation of the orbitals upon oxidation and the fact that in the neutral species the two highest occupied orbitals are quasi-degenerate.

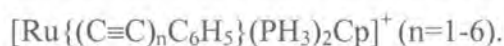
**Table 21.** Fragment charges for  $[\text{Ru}\{(\text{C}\equiv\text{C})_n\text{C}_6\text{H}_5\}(\text{PH}_3)_2\text{Cp}]^+$ .

$[\text{Ru}\{(\text{C}\equiv\text{C})_n\text{C}_6\text{H}_5\}(\text{PH}_3)_2\text{Cp}]^+$			
n	q Ru(PH <sub>3</sub> ) <sub>2</sub> Cp (e <sup>-</sup> )	q (C≡C) <sub>n</sub> (e <sup>-</sup> )	q C <sub>6</sub> H <sub>5</sub> (e <sup>-</sup> )
1	0.943	-0.186	0.243
2	0.924	-0.121	0.196
3	0.876	-0.073	0.197
4	0.866	-0.045	0.178
5	0.770	0.065	0.165
6	0.844	0.002	0.154
<hr/>			
Δq (neutral-oxidised)			
n	Δq Ru(PH <sub>3</sub> ) <sub>2</sub> Cp (e <sup>-</sup> )	Δq (C≡C) <sub>n</sub> (e <sup>-</sup> )	Δq C <sub>6</sub> H <sub>5</sub> (e <sup>-</sup> )
1	0.445	0.241	0.314
2	0.387	0.370	0.242
3	0.318	0.459	0.223
4	0.292	0.517	0.189
5	0.239	0.594	0.167
6	0.242	0.599	0.158

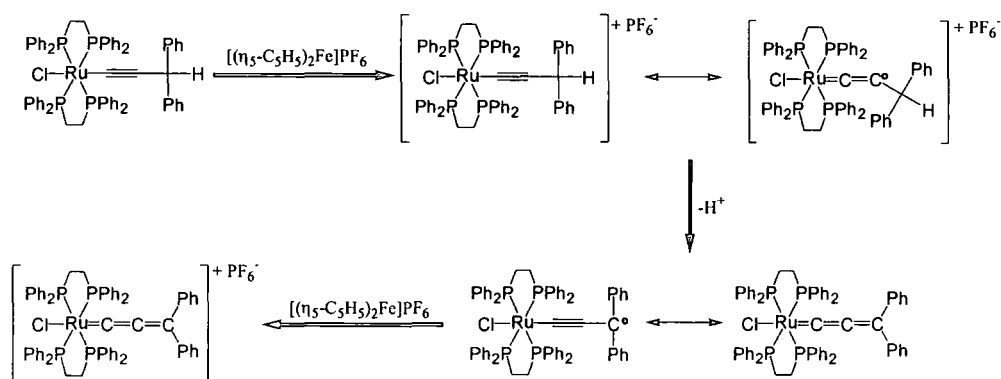




**Figure 69.** Orbital contour iso-surface (0.005 a.u.) plot of the computed spin density distribution in the radical cation

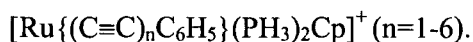


Experimental evidence for the claim that half of the odd-electron in species of the type  $[\text{Ru}\{(\text{C}\equiv\text{C})_n\text{R}\}\text{L}]^+$  ( $n \leq 3$ ) (**Table 12**) is lost from the metal fragment and the remainder originating from the ligand and R group is found in a study which performed oxidation (ferrocenium) of *trans*- $[\text{Cl}(\text{dppe})_2\text{Ru}-\text{C}\equiv\text{C}-\text{CHR}_2]$  ( $\text{R} = \text{H}, \text{CH}_3, \text{C}_6\text{H}_5$ ).<sup>286</sup> The study found that ruthenium(II) acetylides are easily oxidised, and that the stability of the metal centre cationic radical depends on the nature of substituents. If the radical cation is thermally stable ( $\text{R} = \text{H}, \text{CH}_3$ ), subsequent reactions can only occur on C(2). In contrast, when the neutral radical can be stabilised at the termini of the chain ( $\text{R} = \text{C}_6\text{H}_5$ ), i.e. at C(3), proton elimination occurs, and further oxidation leads to the formation of a cumulenenic structure (**Scheme 24**).<sup>286</sup>



**Scheme 24.** Rearrangement of *trans*-[Cl(dppe)<sub>2</sub>Ru-C≡C-CH(C<sub>6</sub>H<sub>5</sub>)<sub>2</sub>] radical cation.

These observations raise the issue of the degree to which oxidation induces structural reorganisation within the polyynyl chain and thus increasing the net amount of cumulenenic (=C=C=) character in the molecule. To address this point, the net bond order associated with the carbon centres of the carbon-rich ligand is considered again. In almost all the species examined, oxidation leads to decrease in the C≡C bonding density and thus reduction of the C≡C bond order. However, only for the  $n = 4$  species is any appreciable cumulenenic character observed and even then the effect is localised along the first four carbons (**Table 22**). Moreover, the net bond order of C(2)-C(3) and C(4)-C(5) bonds increases only slightly (*ca.* 0.3) indicating a minor contribution from the cumulenenic form to these bonds at best. These small changes are easily rationalised in terms of the fact that the oxidation removes an essentially delocalised electron which only has a minor effect upon any particular C-C bond within the acetylenic backbone.

**Table 22.** Net bond order along the carbon chain in the radical cations

$[\text{Ru}\{(\text{C}\equiv\text{C})_6\text{C}_6\text{H}_5\}(\text{PH}_3)_2\text{Cp}]^+$						
	n					
Bond Order	1	2	3	4	5	6
C(1)-C(2)	2.35	2.26	2.23	2.21	2.49	2.51
C(2)-C(3)		0.97	0.97	1.32	0.97	0.97
C(3)-C(4)		2.29	2.18	2.16	2.43	2.43
C(4)-C(5)			0.97	1.32	0.97	0.97
C(5)-C(6)			1.43	2.18	2.44	2.43
C(6)-C(7)				0.91	0.97	0.97
C(7)-C(8)				2.62	2.50	2.46
C(8)-C(9)					0.97	0.97
C(9)-C(10)					2.63	2.51
C(10)-C(11)						0.97
C(11)-C(12)						2.64
C(2n)-C <sub>6</sub> H <sub>5</sub>	0.97	0.97	0.97	0.97	0.97	0.97

This property is extremely beneficial for the ultimate realisation of the goal of employing these types of compounds as molecular scale wires.<sup>15, 43, 228</sup> If a resonant conductance mechanism, which will generate a transient ionic species, acts across a polyyne wire the associated conversion of electrical energy to vibrational energy will ultimately cause the wire to fragment. This effect has been found to lead to the molecular desorption from Si substrates in STM experiments with organic adsorbates on silicon surfaces.<sup>287</sup> This restriction may be surmounted by employing species which show little geometric rearrangement upon change in oxidation state, such as the polyyne species described in this work.

## 4.6. Conclusion

The DFT calculations indicate that the electronic structure of polyynyl complexes is best described in terms of a strong metal-carbon  $\sigma$ -bond complimented by a series of filled orbital-filled orbital antibonding  $\pi$  interactions. This supports and extends the conclusions reached for the electronic structure of acetylide complexes and the diyne complex  $\text{Fe}(\text{C}\equiv\text{CC}\equiv\text{CH})(\text{CO})_2\text{Cp}$  described previously.<sup>242, 241, 276-279</sup> The increase in IR frequencies observed for CO and NO supporting ligands with increasing polyynyl ligand chain length is therefore better attributed to decreased  $\sigma$ -donation from the ligand to the metal centre, and not to increased metal-ligand  $\pi$ -back-bonding. Since the energy of the frontier orbitals of these complexes are related to the degree of  $\sigma$ -donating properties, and hence the length, of the polyynyl ligand in addition to the nature of the supporting ligands (phosphine vs. carbonyl) and the non-metal end-cap it should prove possible to tune the redox potentials of these species in a rational manner. This has been demonstrated using the  $[(\eta^2\text{-dppe})(\eta^5\text{-C}_5\text{Me}_5)\text{Fe}(\text{C}\equiv\text{CC}_6\text{H}_4\text{X})]$  series for which electrochemical<sup>288</sup> as well as Raman and IR spectra is available.<sup>289</sup> This ability to choose oxidation potential has further implications towards energy matching of these wire-like materials to the Fermi level of metallic conductors. The charge distribution along the carbon chain is also susceptible to the nature of the supporting ligands and the electronic properties of the non-metal end-cap. Since the charge distribution along the carbon ligand suggests a measure of charge control in the reactions of these species and as the range of polyynyl complexes available for reactivity studies increases, subtle differences in reactivity patterns correlated to these factors may become evident. The odd-electron in the oxidised species is fully delocalised over the metal and polyynyl ligand, becoming more carbon centred as the length of the polyynyl ligand increases, although the ligand itself retains considerable polyynyl character.

## 4.7. Experimental

### 4.7.1. Computational Method

Geometry optimisation and orbital calculations were performed using the B3LYP function<sup>200</sup> as implemented within the Gaussian 98 software package,<sup>201</sup> with a 3-21G\* basis set for ruthenium and a 6-31G\*\* basis set for all other atoms. These conclusions were tested against the LanL2DZ basis set used in previous work and consistent trends in bond distances and charge distributions with only small variations in the absolute values of these parameters (0.03 Å in bond length and 0.05 e in charge) were found.<sup>260</sup> Default criteria within the software were employed for geometry optimisation, which places an uncertainty of less than  $\pm 0.005$  Å on bond lengths.  $C_s$  symmetry is imposed on both electronic and nuclear degrees of freedom during optimisation and no stationary point analysis was performed. Population analysis was performed within the formalisation of natural orbitals.<sup>263</sup> Although this charge analysis is not in any way unique it does allow us to report relative charges which are not sensitive to basis set, as is the case for Mulliken population, and thus the results are consistent whether a minimal or extended basis set is used. For the case of oxidised species the structures were fully optimised using the unrestricted open shell formalism. The deviation of the electronic state from a pure doublet was minimal as measured by values of the spin operator  $S$  where the maximum deviation from  $S^2 = 0.75$  (pure doublet) was found to be at most 0.01 indicating negligible spin contamination. As a complementary approach a fragment orbital analysis was performed with the Amsterdam Density Functional Program (ADF) and the double zeta basis set included with the package was employed for all atoms.<sup>264, 265-268</sup> The Becke Perdew-86 functional combination was employed which provide Kohn-Sham orbitals in excellent agreement with the B3LYP orbitals obtained from Gaussian 98.<sup>269-271</sup> Finally, the results of the orbital calculations were displayed graphically using Molekel.<sup>272</sup>

## Chapter 5. Synthetic and Computational Study of $\text{Ru}_4\text{C}_4$ Clusters

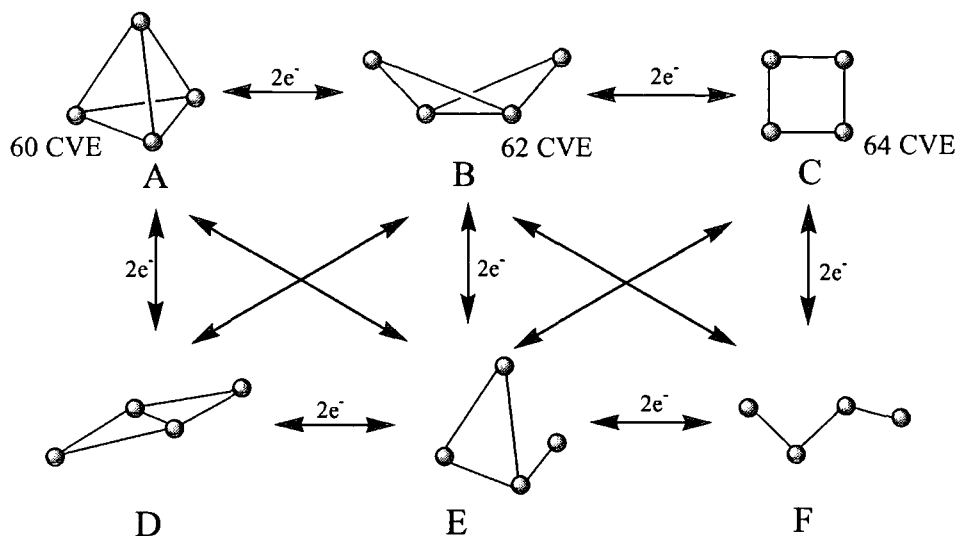
### 5.1. Transition Metal Cluster as Potential Molecular Switches

Metal clusters are the source of a remarkably diverse range of chemistry, exhibiting a seemingly endless array of structural variations. Metal clusters have the ability to undergo an incredible variety of chemical transformations as a result of fragmentation and/or condensation of the metal core, ligand substitution reactions, and the unusual electronic and steric properties of small molecules, such as hydrocarbons trapped within the coordination environment of these multi-metallic frameworks.<sup>290</sup>

Transition metal clusters can undergo both skeletal rearrangement as well as skeletal isomerism. Skeletal rearrangement is often characterised either by the presence of weak metal-metal interactions within the cluster core or a low energy pathway between two polyhedra with similar relative energies. Moreover, these types of rearrangements are often quite subtle; examples of this type of isomerisation are the wing flapping motion of a butterfly cluster, cluster core isomerism from planar to tetrahedral, and cluster breathing motion which enables metals to interchange position, as well as exchange of ligand position.<sup>291</sup> Skeletal isomerism is defined as existing between compounds with similar stoichiometry characterised by similar ligands but with different skeletal geometry. The different bonding modes of ligands to a metal core, usually accompanied by a change in the electron contribution to the cluster electron count, seem to be one of the major causes of skeletal isomerism.<sup>291</sup>

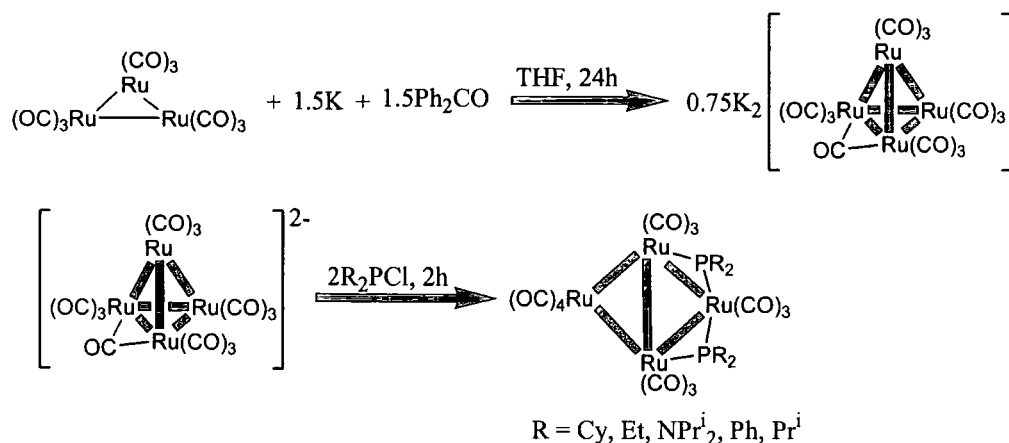
Of particular interest are the various skeletal isomers associated with tetranuclear metal cluster complexes (**Scheme 25**). The initial tetrahedral structure (**A**) has a Cluster Valence Electron (CVE) count of 60, and in undergoing

rearrangement, two electrons are added for every metal-metal bond lost. Thus, the butterfly structure (**B**) will have 62 electrons, while a square planar structure (**C**) has 64 electrons.<sup>291</sup>



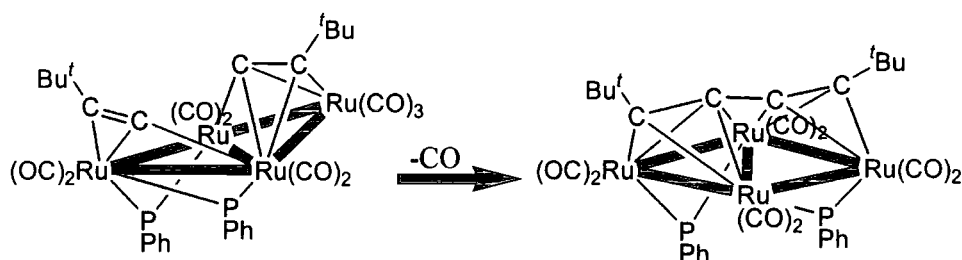
**Scheme 25.** Skeletal rearrangement in tetranuclear clusters.

An example of a skeletal transformation (**A**→**D**) can be seen when the 60 electron tetrahedral  $\text{K}_2[\text{Ru}_4(\text{CO})_{13}]$  is reacted with  $\text{R}_2\text{PCl}$  ( $\text{R} = \text{Cy}, \text{Et}, \text{NPr}^i_2, \text{Ph}, \text{Pr}^i$ ) resulting in a partial opening of the  $\text{Ru}_4$  frameworks and results in the formation of a 64 electron  $[\text{Ru}_4(\text{CO})_{13}(\mu\text{-PR}_2)_2]$  cluster with a planar butterfly polyhedron possessing coplanar phosphido bridges. The ruthenium core consists of two normal Ru-Ru bonds and three elongated ones (**Scheme 26**).<sup>292</sup>



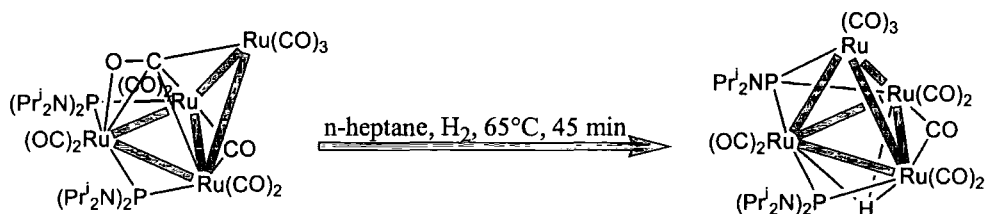
**Scheme 26.** Skeletal transformation from a tetrahedral to a flattened butterfly core structure.

Upon thermolysis the 64 electron butterfly complex  $[\text{Ru}_4(\mu\text{-PPh}_2)_2(\text{C}_2\text{Bu}^t)_2(\text{CO})_9]$  underwent C-C bond coupling through carbon monoxide elimination to form  $[\text{Ru}_4(\mu\text{-PPh}_2)_2(\text{C}_2\text{Bu}^t)_2(\text{CO})_8]$  with a flattened butterfly core structure which is an example of skeletal rearrangement (**B**→**D**) (**Scheme 27**).<sup>293</sup> Transformation of a 62 electron butterfly cluster (**B**) to 60 electron tetrahedral one (**A**) can be accomplished by heating of  $[\text{Ru}_4\{\mu\text{-P}(\text{NPr}^i)_2\}_2(\text{CO})_{11}]$  under a purge of hydrogen resulting in a smooth conversion to  $[\text{Ru}_4(\mu_3\text{-H})\{\mu\text{-P}(\text{NPr}^i)_2\}\{\mu_3\text{-P}(\text{NPr}^i)_2\}(\text{CO})_{10}]$  via hydrogenolysis of a phosphido bridge (**Scheme 28**).<sup>294</sup>



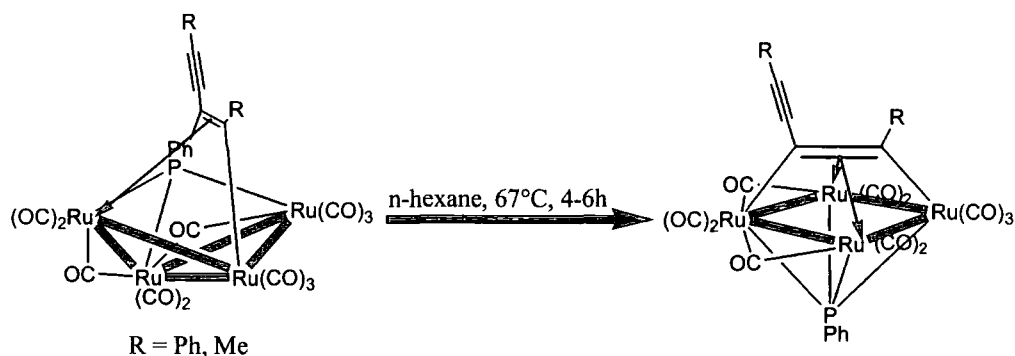
**Scheme 27.** Skeletal transformation from a puckered to a flattened butterfly core structure.





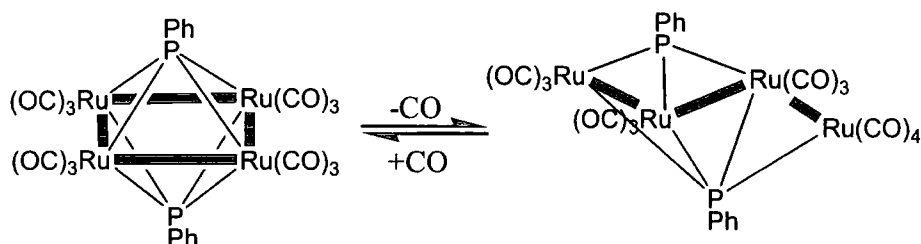
**Scheme 28.** Skeletal transformation from a butterfly to a tetrahedral core structure.

Skeletal transformation (**B**→**C**) can be seen when the 62 electron butterfly cluster  $[\text{Ru}_4\{\mu_4\text{-P(Ph)C(C}\equiv\text{CR)CR}\}(\text{CO})_{12}]$  ( $\text{R} = \text{Ph, Me}$ ) is heated at reflux resulting in a loss of one carbon monoxide ligand to afford the 64 electron cluster  $[\text{Ru}_4\{\mu_4\text{-P(Ph)C(C}\equiv\text{CR)CR}\}(\text{CO})_{11}]$  ( $\text{R} = \text{Ph, Me}$ ) with a distorted square planar core arrangement (**Scheme 29**). This skeletal rearrangement involves P-C bond cleavage and transfer of the originally basal  $\mu_3\text{-PPh}$  vertex to an apical position, adopting the form as a  $\mu_4\text{-cluster}$  stabilising fragment.<sup>295</sup> A similar rearrangement can be seen for the complex  $[\text{Ru}_4\{\text{PhPC(Ph)C(Ph)}\}(\text{CO})_{12}]$  which affords  $[\text{Ru}_4\{\text{PhPC(Ph)C(Ph)}\}(\text{CO})_{11}]$  again with the loss of a carbonyl.<sup>296</sup>



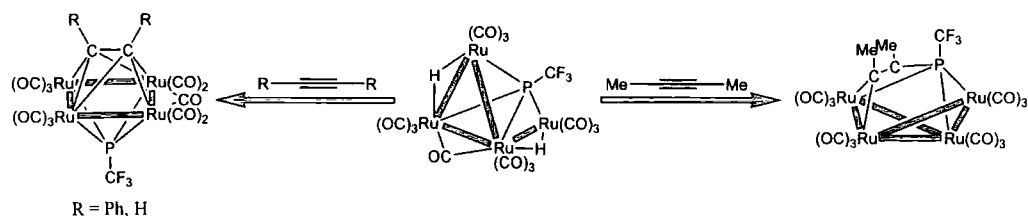
**Scheme 29.** Skeletal transformation from a puckered butterfly to square planar core structure.

Tetranuclear cluster skeletal transformation ( $C \rightarrow F$ ) can be seen when  $[Ru_4(\mu_4-PPh)_2(CO)_{12}]$  (64 CVE) is reacted with an equivalent of carbon monoxide to afford  $[Ru_4(\mu_3-PPh)_2(CO)_{13}]$  (66 CVE). The initial rectangular cluster has undergone a Ru–Ru scission and the PPh groups both cap three metal atoms rather than four (**Scheme 30**).<sup>297</sup> A similar rearrangement can be observed when the square cluster  $[Os_4(\mu_4-S)(\mu_4-HC_2CO_2Me)(CO)_{11}]$  reacts with carbon monoxide to form  $[Os_4(\mu_3-S)(\mu_4-HC_2CO_2Me)(CO)_{12}]$  which consists of a chain of four atoms connected by three metal-metal bonds. These processes are reversible which can be achieved by the thermal elimination of the carbon monoxide ligands.<sup>298</sup>



**Scheme 30.** Skeletal transformation from a square planar to a linear chain core structure.

Reaction of a spiked triangle cluster such as  $[Ru_4(\mu-H)_2(\mu_4-PCF_3)(CO)_{13}]$  (64 CVE) with  $MeC \equiv CMe$  gives, as a result of metal skeletal rearrangement and P–C bond formation, the butterfly cluster  $[Ru_4(C_4Me_4)(\mu_4-PCF_3)(CO)_{12}]$  (62 CVE).<sup>299</sup> This gives an example of skeletal transformation ( $E \rightarrow B$ ) (**Scheme 31**). In a similar reaction, the spiked triangle cluster,  $[Ru_4(\mu-H)_2(\mu_4-PCF_3)(CO)_{13}]$ , can be reacted with an alkyne under mild conditions to give square planar cluster  $[Ru_4(RC_2R)(\mu_4-PCF_3)(CO)_{11}]$  ( $R = Ph, H$ ) with the same electron count of 64 electrons. The acetylene ligands are attached to the metal square planar planes *via*  $2\sigma + 4\pi$  bonds, which is an example of skeletal isomerism ( $E \rightarrow C$ ).<sup>299</sup>



**Scheme 31.** Skeletal transformation from a spiked triangle to a square planar and a spiked triangle to a butterfly core structure.

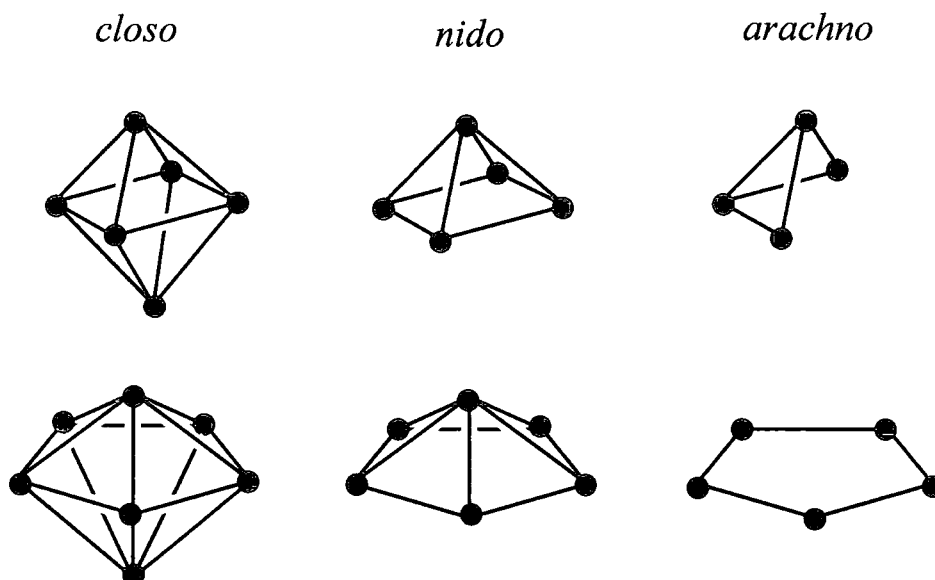
The ability of the  $M_4C_4$  cluster core to adopt stable structures related by a two electron step, one which would appear to be suitable for allowing delocalisation of electronic charge through the cluster core, suggests that similar cluster architectures may be suitable for use as molecular junctions with an integrated capacity for molecular switching. Metal clusters offer face, edge and vertex sites for the attachment of ligands and delocalised frontier orbitals derived from the bonding, non-bonding and anti-bonding combinations of metallic orbitals from the fragments which comprise the vertices of the polyhedron.<sup>300</sup> The electronic flexibility associated with the polyhedral metal cluster core, together with ethynyl based “molecular-wires” will be exploited to prepare molecular junctions or switches which are compatible with the molecular components being developed as part of molecular electronics.<sup>13, 15, 17</sup>

## 5.2. Theoretical and Structural Analysis

The bonding in polynuclear metal clusters is commonly accounted for by the polyhedral skeletal electron pair (PSEP) theory.<sup>301, 302</sup> This theory has been particularly useful in predicting or rationalising the geometrical structures in organometallic cluster compounds that do not conform to the effective atomic number (EAN) formalism. The rule predicts the stability of organometallic compounds and simply states that stability is attained or gained when all of the bonding and non bonding orbitals are occupied. The EAN is counted by summing the number of electrons from the metal atom plus the total number of electrons

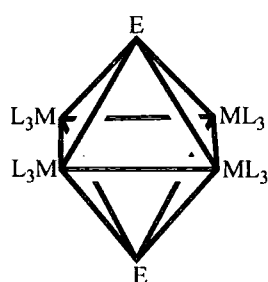
donated by the ligands and this number should equal the number of electrons of the next highest noble gas.<sup>302</sup> The conformity between the two schemes within metal clusters of low metal-metal connectivity is due to the fact that the nine  $nd$ ,  $(n+1)s$ , and  $(n+1)p$  orbitals are valence orbitals, in which all their bonding capacity is used when the EAN is reached.

The PSEP theory relates the structural arrangement of a cluster with the number of CVEs and in particular the number of electron pairs involved in skeletal bonding. *Closo* metallic arrangements based upon  $n$  vertex deltahedra are expected to possess  $(14n+2)$  CVEs or  $(n+1)$  skeletal electron pairs (SEP) (**Figure 70**). The removal of one or two cluster vertices, for example by addition of electron pairs, leads to more open geometries, the *nido* and *arachno* structures (**Figure 70**). The *nido* form has  $(14n+4)$  CVEs or  $(n+2)$  SEP, while *arachno* form has  $(14n+6)$  CVEs or  $(n+3)$  SEP. The large HOMO-LUMO gap between the bonding/nonbonding and antibonding molecular orbitals for main group clusters and their transition metal carbonyl analogues explains partly the success of the PSEP theory. The introduction of additional electrons over and above the number required to populate the bonding and non-bonding molecular orbitals therefore leads to either a general expansion of the metallic cluster core, or the elongation or cleavage of a specific M-M bond. Despite the success of the PSEP theory in understanding a large variety of organometallic clusters, it presents limitations in application to mixed main group-transition metal systems. The theory fails to account for skeletal isomerism, isomer interconversion or unexpected geometries.<sup>215</sup>



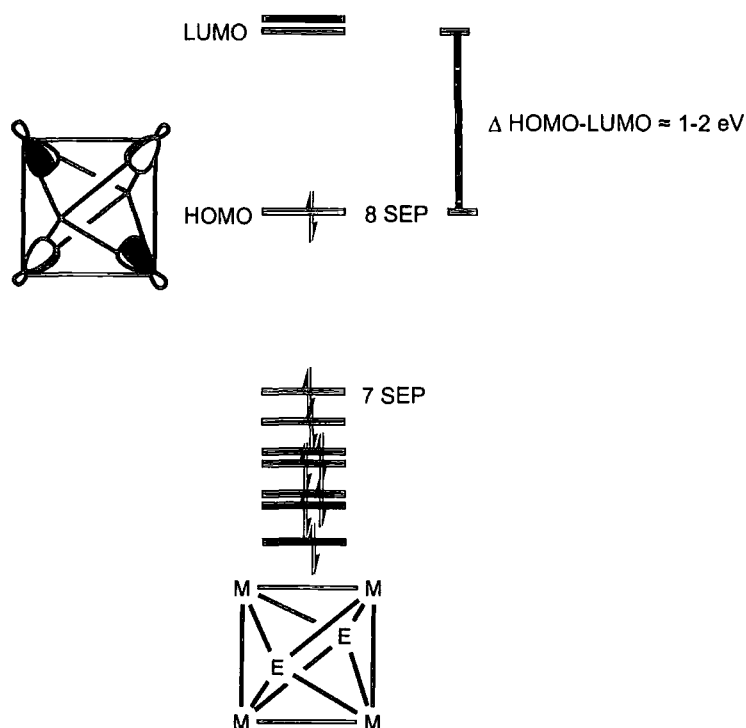
**Figure 70.** Example of a *closo*, *nido*, and *arachno* structures and their relationship to each other.

Detailed theoretical studies have been performed on the *closo*-octahedral  $M_4E_2$  organometallic cluster where M is a transition metal, and E is a second, third or fourth row main group atom of a conical fragment (discussed below) (**Figure 71**). These compounds do not conform to the PSEP theory and can have two possible electron counts, either seven or eight skeletal electron pairs.



**Figure 71.**  $M_4E_2$  compound, where M is a transition metal, and E is a second, third or fourth row main group atom of a conical fragment.

Another feature of these compounds is that they have a short E...E non bonded interatomic distance which is only 15-20% longer than a normal E-E bond. The frontier orbitals of  $M_4E_2$  show an unperturbed non-bonding orbital lying approximately in the middle of the energy gap separating a cluster of seven bonding skeletal  $\pi$ -type molecular orbitals levels from the antibonding molecular orbitals (Figure 72).<sup>303</sup> The presence of this nonbonding orbital allows the possibility of two electron counts for this kind of  $M_4E_2$  octahedral cluster, namely seven or eight SEPs depending on whether this orbital is populated or not.



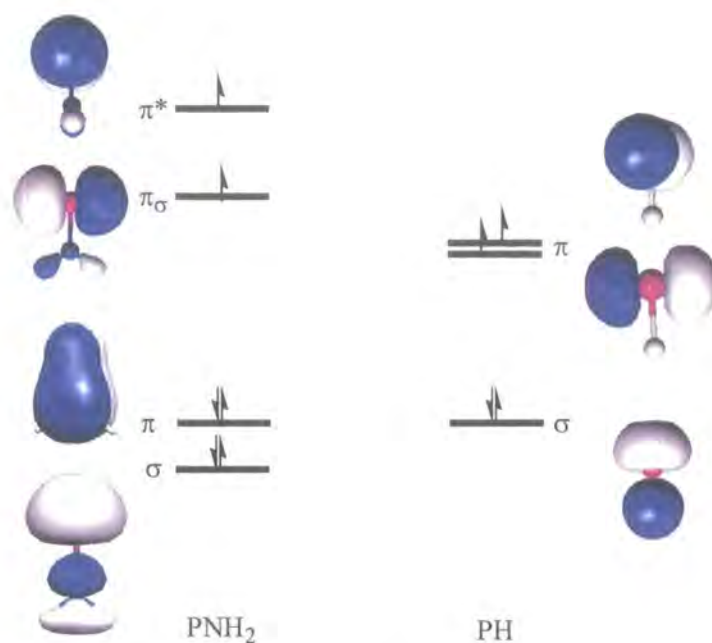
**Figure 72.** Qualitative molecular orbital diagram of  $M_4L_n(\mu_4-E)_2$  cluster exhibiting pseudo  $D_{4h}$  symmetry.

The presence of this non-bonding orbital is due to the approximate  $D_{4h}$  symmetry for the cluster core, which does not allow mixing into the LUMO, and the weak M-M antibonding character.<sup>304</sup> The non-bonding orbital is mainly metal in character and as such strongly dependant on the electronegativity of the metal

atoms, with more electronegative metals lowering the energy of the orbital, thus favouring the eight SEP count. This is why most ruthenium clusters of this type have seven SEP, while iron can have both seven and eight SEPs and cobalt has eight SEPs.<sup>305</sup>

The presence of a conical fragment such as alkyl phosphinidene (PR) on a  $M_4E_2$  compounds renders the core of the cluster square planar with a  $D_{4h}$  symmetry. A conical fragment possesses one  $\sigma$ -type frontier orbital and two  $\pi$ -type frontier orbitals that are degenerate and have the same shape (**Figure 73**).<sup>304</sup> Examples of these can be seen in compounds such as  $[Fe_4(CO)_{12}(\mu_4-PR)_2]$  ( $R = Ph$ ),<sup>306</sup>  $[Fe_4(CO)_{11}(\mu_4-PR)_2]$  ( $R = Me, t-Bu, Ph, Tol$ ),<sup>306-308</sup> and  $[Ru_4(CO)_{11}(\mu_4-PR)_2]$  ( $R = Ph, t-Bu$ ).<sup>306, 309</sup>

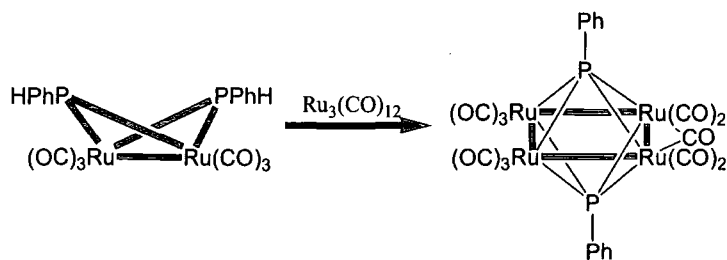
Ruthenium clusters can be induced to possess eight SEP, for example by the presence of a non-conical fragment. A non-conical fragment is basically the same as a conical fragment, the only difference is that the orbitals lie in two different perpendicular planes (**Figure 73**).<sup>304</sup> The presence of this fragment leads to a puckered square core structure for the  $Ru_4P_2$  skeleton which gives rise to a  $D_{2d}$  symmetry. Consequently, the HOMO of the molecule is stabilised favouring the eight SEP count such as in  $[Ru_4(CO)_{12}(\mu_4-PNR_2)_2]$  ( $R = Et, Pr^i$ ).<sup>304, 310</sup> Another cluster exhibiting pseudo  $D_{2d}$  symmetry,  $[Fe_4(CO)_{11}\{P(OMe)_3\}P-p-Tol)_2]$ , also has an eight SEP cluster.<sup>308</sup>



**Figure 73.** Orbitals of a non-conical fragment ( $\text{PNH}_2$ ) and a conical fragment ( $\text{PH}$ ).

Compounds of the type  $\text{Fe}_4\text{P}_2$  and  $\text{Ru}_4\text{P}_2$  exist both in their unsaturated  $[\text{Ru}_4(\text{CO})_{11}(\mu_4\text{-PR})_2]$  form as well as in the saturated  $[\text{Ru}_4(\text{CO})_{12}(\mu_4\text{-PR})_2]$  form. These unsaturated compounds can be synthesised by a reaction of  $\text{M}_3(\text{CO})_{12}$  and  $\text{PRH}_2$  which gives a variety of tri-, tetra-, penta- and hexa-nuclear phosphinidene capped products.<sup>309</sup> Alternatively a reaction of  $[\text{M}_2(\mu_2\text{-PRH})_2(\text{CO})_6]$  with  $\text{M}_3(\text{CO})_{12}$  also gives the desired product of  $[\text{Ru}_4(\text{CO})_{11}(\mu_4\text{-PR})_2]$  (**Scheme 32**).<sup>307</sup> The four metal atoms of  $[\text{Ru}_4(\text{CO})_{11}(\mu_4\text{-PR})_2]$  are perfectly square planar with each metal atom bonded to one terminal carbonyl above and below the plane. The remaining carbonyls are co-planar with the metal-metal edge, with one carbonyl symmetrically bridging the shortest metal-metal edge.<sup>309</sup> Addition of CO gives the saturated compound with the metal atoms still square planar and all the twelve carbonyls being terminal. This process is reversible, and elimination of CO by heating under vacuum reverts the saturated compound back to the unsaturated compound.<sup>297, 307</sup>



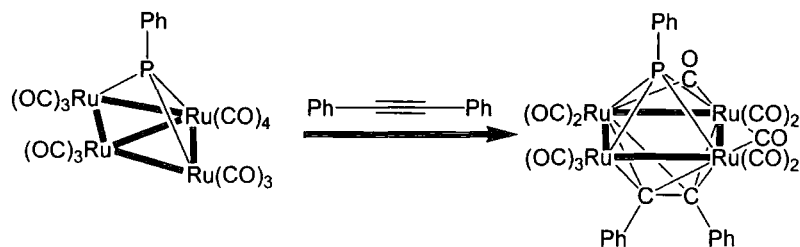


**Scheme 32.** Example of a synthetic route to produce  $[\text{Ru}_4(\text{CO})_{11}(\mu_4\text{-PPh})_2]$ .

The molecular orbital scheme described above for  $\text{M}_4\text{E}_2$  compounds predicts that the seven SEP clusters should be reducible, and the eight SEP clusters oxidisable. As predicted, the unsaturated  $[\text{M}_4(\text{CO})_{11}(\mu_4\text{-PR})_2]$  ( $\text{M} = \text{Ru}, \text{Fe}, \text{R} = \text{Ph}$ ) compounds cannot be oxidised, but can easily be reduced. Two electrochemically reversible one-electron reductions were observed for the iron compound, while an additional one-electron reduction is observable for the ruthenium cluster as well as similar reduction peaks observed for the iron cluster.<sup>306</sup> The eight SEP situation is unstable for the ruthenium cluster resulting in it taking up more than two electrons by being reduced beyond the dianionic state or by addition of two CO ligands.<sup>306</sup>

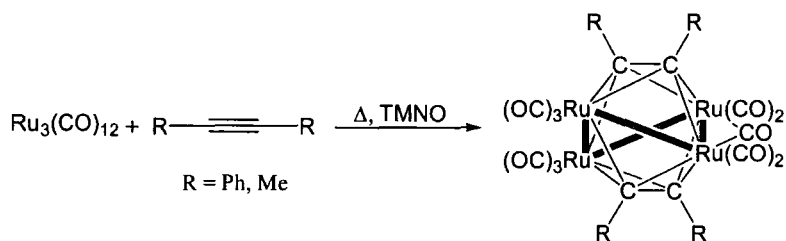
Reaction of the butterfly phosphinidene cluster complex  $[\text{Ru}_4(\text{CO})_{13}(\mu_3\text{-PPh})]$  with diphenylacetylene affords, as one of the products, the *clos*o-square planar  $[\text{Ru}_4(\text{CO})_{11}(\mu_3\text{-PPh})(\mu_4\text{-PhC}_2\text{Ph})]$ , with seven vertices, and possessing eight SEP as expected (**Scheme 33**).<sup>296</sup> A similar reaction resulted in the conversion of  $[\text{Fe}_4(\text{CO})_{10}(\mu_3\text{-PR})]$  to  $[\text{Fe}_4(\text{CO})_9(\mu_4\text{-PR})(\mu_4\text{-R}'\text{C}_2\text{R}'')]$  ( $\text{R} = \text{C}_6\text{H}_5$ ).<sup>311</sup> Other compounds of this type that have been synthesised include  $[\text{Ru}_4(\text{CO})_{11}(\text{RC}_2\text{R})(\mu_4\text{-PCF}_3)]$  ( $\text{R} = \text{H}, \text{Ph}$ )<sup>299</sup> and  $[\text{Ru}_4(\text{CO})_{11}(\text{RC}\equiv\text{CC}\equiv\text{CR})(\mu_4\text{-PPh})]$  ( $\text{R} = \text{Ph}, \text{Me}$ ).<sup>295</sup> The latter series of compounds have a distorted square planar core capped on one side by a PR group and on the other side by  $\text{RC}\equiv\text{CR}$ , with molecules containing two bridging carbonyls. These compounds contain only 62 electrons so are formally electron deficient by two electrons. However,

$[\text{Ru}_4(\text{CO})_{11}(\text{RC}\equiv\text{CC}\equiv\text{CR})(\mu_4\text{-PPh})]$  ( $\text{R} = \text{Ph}, \text{Me}$ ) can also be classified as a *closo*-pentagonal bipyramid arrangement of  $\text{Ru}_4\text{PC}_2$ , which is consistent with PSEP theory having seven vertices, and possessing eight SEP as expected.<sup>295</sup>



**Scheme 33.** Conversion of  $[\text{Ru}_4(\text{CO})_{13}(\mu_3\text{-PPh})]$  to  $[\text{Ru}_4(\text{CO})_{11}(\mu_3\text{-PPh})(\mu_4\text{-PhC}_2\text{Ph})]$ .

Reaction of  $\text{M}_3(\text{CO})_{12}$  with an alkyne under reflux conditions or with treatment of trimethyl N-oxide ( $\text{Me}_3\text{NO}$ , TMNO) results in clusters of the type  $[\text{M}_4(\mu_4\text{-RC}_2\text{R})_2(\text{CO})_{11}]$  ( $\text{M} = \text{Fe}, \text{Ru}$ ,  $\text{R} = \text{Ph}, \text{Me}$ ) (**Scheme 34**).<sup>170, 312, 313</sup> The compound  $[\text{Ru}_4(\mu_4\text{-HC}_2\text{H})_2(\text{CO})_{11}]$  has been synthesised *via* a different method using a reaction of  $\text{Ru}_3(\text{CO})_{12}$  and  $\text{CaC}_2$ .<sup>314</sup> Compounds of this type that have been synthesised include  $[\text{Fe}_4(\mu_4\text{-HC}_2\text{Et})_2(\text{CO})_{11}]$ ,<sup>312</sup>  $[\text{Ru}_4(\mu_4\text{-PhC}_2\text{Ph})_2(\text{CO})_{11}]$ <sup>170</sup> and  $[\text{Ru}_4(\mu_4\text{-MeC}_2\text{Ph})_2(\text{CO})_{11}]$ .<sup>313</sup> The four metal atoms in these clusters form a distorted square with the two acetylenic bonds almost perpendicular to each other.



**Scheme 34.** Synthesis of  $[\text{Ru}_4(\mu_4\text{-RC}_2\text{R})_2(\text{CO})_{11}]$  ( $\text{R} = \text{Ph}, \text{Me}$ ).

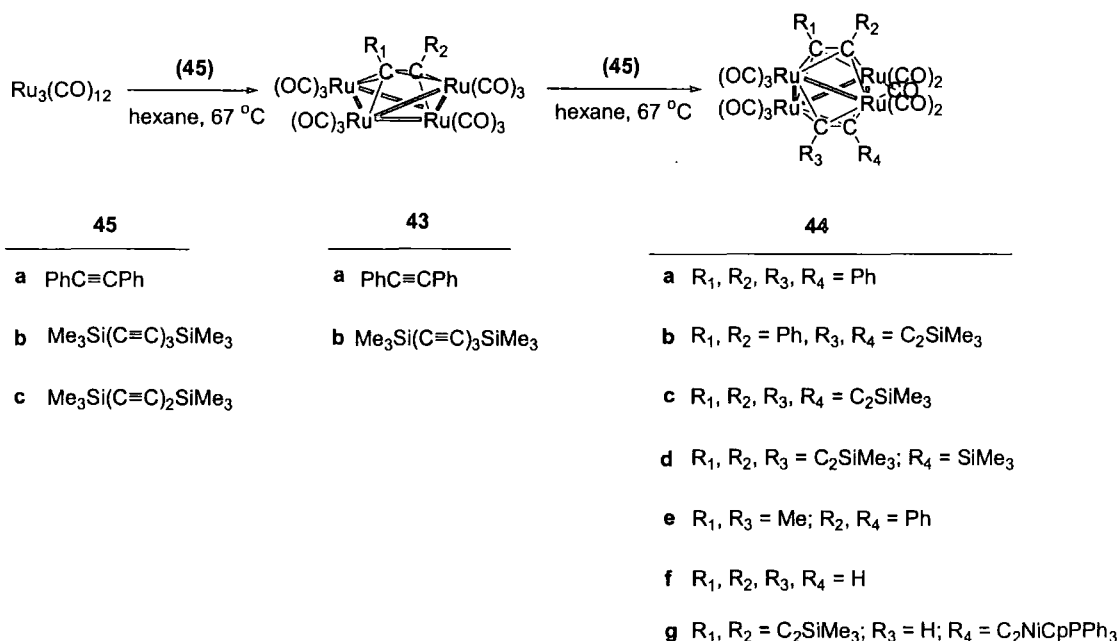
If the alkyne is considered as a four electron donor (one electron for each  $\sigma$ -bond, and two electrons for the  $\pi$ -bonds to the metal), then the cluster is lacking two electrons with respect to the EAN rule which requires it to have 64 CVE. Therefore it is better to rationalise the structure and bonding in terms of PSEP theory where the  $M_4C_4$  skeleton can be described as a *closo*-dodecahedron which has eight skeletal atoms and offering the expected nine SEP count.

Other compounds that possess similar core structure geometry to those described above are that of  $[Cp'_4Fe_4(HC_2H)_2]$  ( $Cp' = C_5H_5, C_5H_4Me$ ).<sup>315, 316</sup> Electrochemical oxidation of these compounds afforded two-electron oxidation waves. These compounds have been chemically oxidised giving the monocationic cluster product which possessed structures very similar to that of the neutral with slightly shorter Fe-Fe bonds.

### 5.3. Synthesis and Characterisation of $Ru_4C_4$ Clusters

The thermal reactions of alkynes and polyynes with  $Ru_3(CO)_{12}$  are sensitive to both the nature of the alkyne and the precise reaction conditions employed.<sup>290, 53</sup> The clusters of the type  $[Ru_4(\mu-R_2C_2R)(CO)_{12}]$  (**43**) were readily prepared in moderate yield from the thermal reaction of  $[Ru_3(CO)_{12}]$  with the alkynes  $PhC\equiv CPh$  (**45a**) or  $Me_3Si(C\equiv C)_3SiMe_3$  (**45b**) to give  $[Ru_4(\mu-PhC_2Ph)(CO)_{12}]$  (**43a**),<sup>169, 317</sup> and  $[Ru_4(\mu-SiMe_3C\equiv CC_2C\equiv CSiMe_3)(CO)_{12}]$  (**43b**)<sup>168</sup> respectively in refluxing hexane (**Scheme 35**). The reaction was readily followed by IR spectroscopy [ $\nu(CO)$ ]. Unreacted  $Ru_3(CO)_{12}$  was recovered from the cooled reaction mixtures as a crystalline precipitate of high purity, which may be recycled in subsequent reactions, adding to the appeal of this method. The product clusters, which are most likely formed by condensation of  $[Ru_3(\mu_3-R_2C_2R')(CO)_{10}]$  with an  $Ru(CO)_n$  fragment generated *in situ*,<sup>168, 318</sup> were easily separated from the other products by column chromatography or preparative TLC. An analogous two-step reaction describes the reaction of  $[Ru_3(CO)_{10}(MeCN)_2]$  with 1,6-bis(trimethylsilyl)-1,3,5-hexatriyne to afford  $[Ru_3(\mu-Me_3$ .

$\text{SiC}\equiv\text{CC}_2\text{C}\equiv\text{CSiMe}_3)(\text{CO})_{10}]$  and subsequent reaction with  $\text{Ru}(\text{CO})_5$  to afford **43b**.<sup>318</sup>



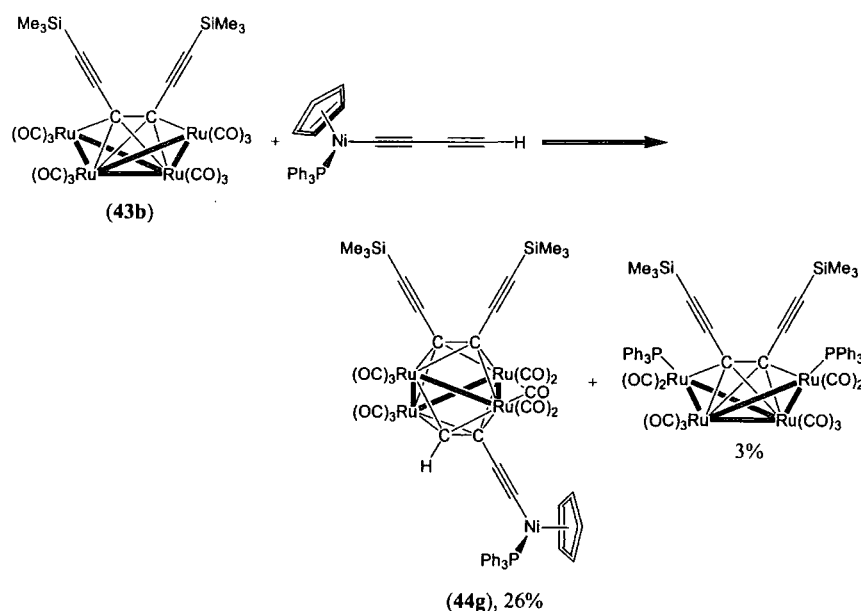
**Scheme 35.** Formation of  $[\text{Ru}_4(\mu_4\text{-RC}_2\text{R})(\mu_4\text{-R}'\text{C}_2\text{R}')(\text{CO})_{11}]$  type clusters.

Further reaction of **43a** with an equivalent of the alkynes **45a** or **45b**, again in refluxing hexane, gave  $[\text{Ru}_4(\mu_4\text{-PhC}_2\text{Ph})_2(\text{CO})_{11}]$  (**44a**)<sup>170</sup> and  $[\text{Ru}_4(\mu_4\text{-PhC}_2\text{Ph})(\mu_4\text{-Me}_3\text{SiC}\equiv\text{CC}_2\text{C}\equiv\text{CSiMe}_3)(\text{CO})_{11}]$  (**44b**), respectively, by insertion of the alkyne into one of the Ru-Ru bonds in the octahedral cluster core and loss of CO. The metal and carbon atoms of the  $\text{Ru}_4\text{C}_4$  core of these  $\text{Ru}_4(\mu\text{-alkyne})_2(\text{CO})_{11}$  clusters define a triangulated dodecahedron. Cluster **44a** has also been obtained (18%) from the low temperature TMNO assisted reaction of  $\text{Ru}_3(\text{CO})_{12}$  and diphenyl acetylene.<sup>170</sup> Complex **44b** was obtained in higher yield (23%) from a reaction between **43b** and **45a**. Reaction of **43b** with **45b** or  $\text{Me}_3\text{Si}(\text{C}\equiv\text{C})_2\text{SiMe}_3$  (**45c**) gave  $[\text{Ru}_4(\mu_4\text{-Me}_3\text{SiC}\equiv\text{CC}_2\text{C}\equiv\text{CSiMe}_3)_2(\text{CO})_{11}]$  (**44c**) and  $[\text{Ru}_4(\mu_4\text{-Me}_3\text{SiC}\equiv\text{CC}_2\text{C}\equiv\text{CSiMe}_3)(\mu_4\text{-Me}_3\text{SiC}_2\text{C}\equiv\text{CSiMe}_3)(\text{CO})_{11}]$  (**44d**)<sup>xiii</sup> respectively

<sup>xiii</sup> Compound courtesy of P.J.Low.

(Scheme 35). The clusters **44a-d** were all readily characterised by standard spectroscopic methods, and also single crystal X-ray diffraction in the case of **44b**, and **44d** (Table 23). Analogous clusters, such as  $[\text{Ru}_4(\mu\text{-MeC}_2\text{Ph})_2(\text{CO})_{11}]$  (**44e**),<sup>313</sup> were prepared *via* similar techniques, while the parent cluster  $[\text{Ru}_4(\mu\text{-HC}_2\text{H})_2(\text{CO})_{11}]$  (**44f**)<sup>314</sup> was prepared by thermolysis of smaller ruthenium cluster carbides.

The synthetic method employed to yield **44a-d** has the advantage of being able to form a range of substituted clusters possessing a triangulated dodecahedron core through the sequential reaction with two different alkynes, diynes or polyynes. This method was utilised in the synthesis of  $[\text{Ru}_4(\mu_4\text{-Me}_3\text{SiC}\equiv\text{CC}_2\text{C}\equiv\text{CSiMe}_3)(\mu_4\text{-(HC}_2\text{C}\equiv\text{C)Ni(PPh}_3\text{)Cp})(\text{CO})_{11}]$  (**44g**) which arose as a major product from a reaction of **43b** and  $[\text{Ni}(\text{C}\equiv\text{C}\equiv\text{CH})(\text{PPh}_3)\text{Cp}]$  (Scheme 36).<sup>165</sup> A minor product,  $[\text{Ru}_4(\mu_4\text{-}\eta^2\text{-(Me}_3\text{SiC}\equiv\text{CC}_2\text{C}\equiv\text{CSiMe}_3)(\text{CO})_{10}(\text{PPh}_3)_2]$ , was also obtained which resulted from a substitution of two of the CO ligands at the wingtips of the  $\text{Ru}(\text{CO})_3$  centres on **43b** by  $\text{PPh}_3$  (Scheme 36).



**Scheme 36.** Products obtained from a reaction between **43b** and  $\text{Ni}(\text{C}\equiv\text{C}\equiv\text{CH})(\text{PPh}_3)\text{Cp}$ .

**Table 23.** X-ray crystal structure data of compounds **44b** and **44d**.

	<b>44b</b>	<b>44d</b>
Empirical formula	C <sub>37</sub> H <sub>28</sub> O <sub>11</sub> Ru <sub>4</sub> Si <sub>2</sub>	C <sub>33</sub> H <sub>36</sub> O <sub>11</sub> Ru <sub>4</sub> Si <sub>4</sub>
Formula weight	1109.05	1125.26
Temperature	120(2) K	173(2) K
Wavelength	0.71073 Å	0.71073 Å
Crystal system	Monoclinic	Monoclinic
Space group	P2 <sub>1</sub> /c	Cm
Unit cell dimensions	a = 27.2520(9) Å α = 90° b = 9.5309(3) Å β = 108.51(1)° c = 33.374(1) Å γ = 90°	a = 13.5503(8) Å α = 90° b = 13.7423(9) Å β = 101.0900(10)° c = 12.3319(7) Å γ = 90°
Volume	8219.9(4) Å <sup>3</sup>	2253.5(2) Å <sup>3</sup>
Z	8	2
Density (calculated)	1.792 Mg/m <sup>3</sup>	1.658 Mg/m <sup>3</sup>
Absorption coefficient	1.555 mm <sup>-1</sup>	1.470 mm <sup>-1</sup>
F(000)	4336	1108
Crystal size	0.60 x 0.08 x 0.06 mm <sup>3</sup>	0.3 x 0.25 x 0.2 mm <sup>3</sup>
Theta range for data collection	1.28 to 27.50°	1.68 to 28.75°
Index ranges	-35 ≤ h ≤ 35, -12 ≤ k ≤ 12, -43 ≤ l ≤ 43	-18 ≤ h ≤ 18, -18 ≤ k ≤ 18, -16 ≤ l ≤ 16
Reflections collected	65769	13383
Independent reflections	18870 [R(int) = 0.0657]	6019 [R(int) = 0.0503]
Completeness to theta	99.9 %	99.8 %
Absorption correction	Semi-empirical from equivalents	Empirical
Max. and min. transmission	0.9125 and 0.4555	
Refinement method	Full-matrix least-squares on F <sup>2</sup>	Full-matrix least-squares on F <sup>2</sup>
Data / restraints / parameters	18870 / 0 / 973	6019 / 44 / 403
Goodness-of-fit on F <sup>2</sup>	1.037	0.943
Final R indices[I > 2σ(I)]	R1 = 0.0469, wR2 = 0.1031	R1 = 0.0359, wR2 = 0.0612
R indices (all data)	R1 = 0.0787, wR2 = 0.1123	R1 = 0.0487, wR2 = 0.0645
Extinction coefficient		0.000005(12)
Largest diff. peak and hole	2.154 and -0.915 e.Å <sup>-3</sup>	0.673 and -0.460 e.Å <sup>-3</sup>

The IR spectrum of **44c** was characterised by a series of strong absorptions for terminal  $\nu(\text{CO})$  at 2088, 2064, 2040, 2027 and 2008  $\text{cm}^{-1}$ , and an additional broad absorption at 1854  $\text{cm}^{-1}$  characteristic of bridging carbonyl ligands. The free alkyne moieties gave rise to weak  $\nu(\text{C}\equiv\text{C})$  absorption bands at 2158 and 2131  $\text{cm}^{-1}$ . The  $^1\text{H}$  NMR spectrum contained a singlet at  $\delta$  0.03 ppm due to the  $\text{SiMe}_3$  groups. The  $^{13}\text{C}$  NMR spectrum revealed a single broad resonance at  $\delta$  197.91 ppm from carbonyl ligands, which are rendered equivalent on the NMR timescale by rapid intramolecular exchange processes involving the migration of all the carbonyl groups around the tetra-ruthenium plane in a merry-go-round process.<sup>313</sup> The variety of possible matches between carbonyl and metal orbitals are most likely due to a smooth continuum of possible conformations.<sup>319</sup> The reaction pathway for terminal-bridging-terminal carbonyl exchange between metal atoms has been demonstrated *via* structural correlation methods to show that CO exchange is a facile process with a broad low-energy maximum separating the more stable terminal and fully-bridging carbonyls.<sup>320</sup>

The  $^{13}\text{C}$  NMR spectrum for **44c** also contained a resonance at  $\delta$  0.03 ppm due to the four  $\text{SiMe}_3$  groups, which were rendered magnetically equivalent on the NMR timescale by the various fluxional processes within the molecule, and two resonances at  $\delta$  97.83 and 109.61 ppm arising from the pendant acetylenic groups. The carbon nuclei of the  $\text{Ru}_4\text{C}_4$  core were detected as one sharp singlet at  $\delta$  113.00 ppm. The FAB-MS spectrum exhibited a molecular ion at  $m/z$  1149, followed by fragment ions derived from the sequential loss of up to nine carbonyl ligands.

The IR spectrum of **44b** was characterised by a series strong absorptions for terminal  $\nu(\text{CO})$  at 2088, 2074, 2063, 2050, 2043, 2026, 2009, 1998, 1981  $\text{cm}^{-1}$ , while the absorptions characteristic of bridging carbonyl ligands was not observed. The free alkyne moieties gave rise to a weak  $\nu(\text{C}\equiv\text{C})$  absorption band at

2130  $\text{cm}^{-1}$ . The FAB-MS spectrum did not exhibit the molecular ion; however, a fragment ion at  $m/z$  1052 arising to the loss of two carbonyls, followed by fragment ions derived from the sequential loss of up to eleven carbonyl ligands were observed. Attempts to obtain NMR spectra were hampered by the apparent instability of the compound in solution. Decomposition was observed at the end of even a short  $^1\text{H}$  NMR data collection.

The IR spectrum of **44d** was characterised by a series of absorptions for terminal  $\nu(\text{CO})$  at 2092, 2067, 2060, 2027, 1989 and 1975  $\text{cm}^{-1}$ , with an additional absorption at 1850  $\text{cm}^{-1}$  characteristic of bridging carbonyl ligands. The free alkyne moieties gave rise to weak  $\nu(\text{C}\equiv\text{C})$  absorption bands at 2130  $\text{cm}^{-1}$ . The FAB-MS spectrum exhibited a molecular ion at  $m/z$  1125, followed by fragment ions derived from the sequential loss of up to eleven carbonyl ligands. The  $^1\text{H}$  NMR spectrum contained three singlets at  $\delta$  0.04, 0.07 and 0.18 ppm due to the  $\text{SiMe}_3$  groups. The  $^{13}\text{C}$  NMR spectrum revealed a single resonance at  $\delta$  198.85 ppm for the carbonyl ligands, as well as three resonances at  $\delta$  -1.05, -0.39 and 5.91 ppm due to the  $\text{SiMe}_3$  groups. The four resonances at  $\delta$  96.57, 104.50, 109.71 and 110.43 ppm were attributed to the acetylenic moieties, while the carbon nuclei of the  $\text{Ru}_4\text{C}_4$  core were detected as three singlets at  $\delta$  112.26, 114.68 and 141.14 ppm.

The IR spectrum of **44g** was characterised by a series of absorptions for terminal  $\nu(\text{CO})$  at 2095, 2070, 2038, 2032, 2010 and 1977  $\text{cm}^{-1}$ , with an additional broad absorption at 1819  $\text{cm}^{-1}$  characteristic of bridging carbonyl ligands. The free alkyne moieties gave rise to a weak  $\nu(\text{C}\equiv\text{C})$  absorption band at 2130  $\text{cm}^{-1}$ . The FAB-MS spectrum exhibited a molecular ion at  $m/z$  1365, followed by fragment ions derived from the sequential loss of up to eight carbonyl ligands. The  $^1\text{H}$  NMR spectrum contained a singlet at  $\delta$  0.07 ppm due to the  $\text{SiMe}_3$  groups, and another singlet at  $\delta$  2.35 ppm arising from the terminal proton attached to the  $\text{C}_2$  portion of the cluster. The Cp moiety gave rise to a singlet



resonance at  $\delta$  5.05 ppm, while the aromatic region contained characteristic peaks due to the PPh<sub>3</sub> moiety. The <sup>13</sup>C NMR spectra revealed a single resonance at  $\delta$  198.82 ppm for the carbonyl ligands, as well a resonance at  $\delta$  1.26 ppm due to the SiMe<sub>3</sub> groups. The Cp group gave rise to a peak at  $\delta$  89.54 ppm, while the acetylenic moieties gave rise to four resonances ( $\delta$  91.54, 94.42, 106.25, 106.62 ppm). The carbon nuclei of the Ru<sub>4</sub>C<sub>4</sub> core were detected as three singlets at  $\delta$  109.04, 111.86 and 155.98 ppm. The aromatic region showed an envelope of ten aromatic peaks between  $\delta$  126.96 and 132.82 ppm. The remaining resonances expected for the aromatic carbons were not observed, due in part to the long relaxation time associated with these quaternary carbon centres.

The minor product (3%) obtained from the reaction of **43b** and [Ni(C $\equiv$ C $\equiv$ CH)(PPh<sub>3</sub>)Cp] was [Ru<sub>4</sub>( $\mu_4$ - $\eta^2$ -(Me<sub>3</sub>SiC $\equiv$ CC<sub>2</sub>C $\equiv$ CSiMe<sub>3</sub>)(CO)<sub>10</sub>(PPh<sub>3</sub>)<sub>2</sub>] (**Scheme 36**). This compound resulted from the substitution of two carbonyl groups by PPh<sub>3</sub> moieties, since it is not possible for an electronically saturated M<sub>4</sub>C<sub>2</sub> octahedral cluster to add the new ligand without loss of an equal number of two electron donor ligands. In contrast, the unsaturated iron cluster [Fe<sub>4</sub>(CO)<sub>11</sub>( $\mu_4$ -PR)<sub>2</sub>] (R = <sup>t</sup>Bu, Ph, Tol) readily adds nucleophiles resulting in [Fe<sub>4</sub>(CO)<sub>11</sub>(L)( $\mu_4$ -PR)<sub>2</sub>] (L = CO, <sup>t</sup>BuN, P(OMe)<sub>3</sub>).<sup>307, 309, 321</sup>

The PPh<sub>3</sub> moieties of [Ru<sub>4</sub>( $\mu_4$ - $\eta^2$ -(Me<sub>3</sub>SiC $\equiv$ CC<sub>2</sub>C $\equiv$ CSiMe<sub>3</sub>)(CO)<sub>10</sub>(PPh<sub>3</sub>)<sub>2</sub>] are positioned on the butterflies wing tips. This positioning was confirmed *via* X-ray crystallography connectivity studies, although the full structure was not solved. A study on [Ru<sub>4</sub>(CO)<sub>9</sub>( $\mu_4$ - $\eta^2$ -(C<sub>6</sub>H<sub>8</sub>)( $\eta^6$ -C<sub>6</sub>H<sub>6</sub>))] has shown that the wingtip isomer of this compound is preferentially formed from the reaction of [Ru<sub>4</sub>(CO)<sub>12</sub>( $\mu_4$ - $\eta^2$ -(C<sub>6</sub>H<sub>8</sub>))] and with TMNO in the presence of C<sub>6</sub>H<sub>8</sub>.<sup>322</sup> Alternatively heating of [Ru<sub>4</sub>(CO)<sub>12</sub>( $\mu_4$ - $\eta^2$ -(C<sub>6</sub>H<sub>8</sub>))] with C<sub>6</sub>H<sub>8</sub> produces the hinge isomer, which upon standing at ambient temperature converts to the wingtip isomer. The mechanism proposed involves a low energy slippage of the benzene

moiety over the cluster framework, possibly *via* the an edge bridged arene molecule as an intermediate.<sup>322</sup>

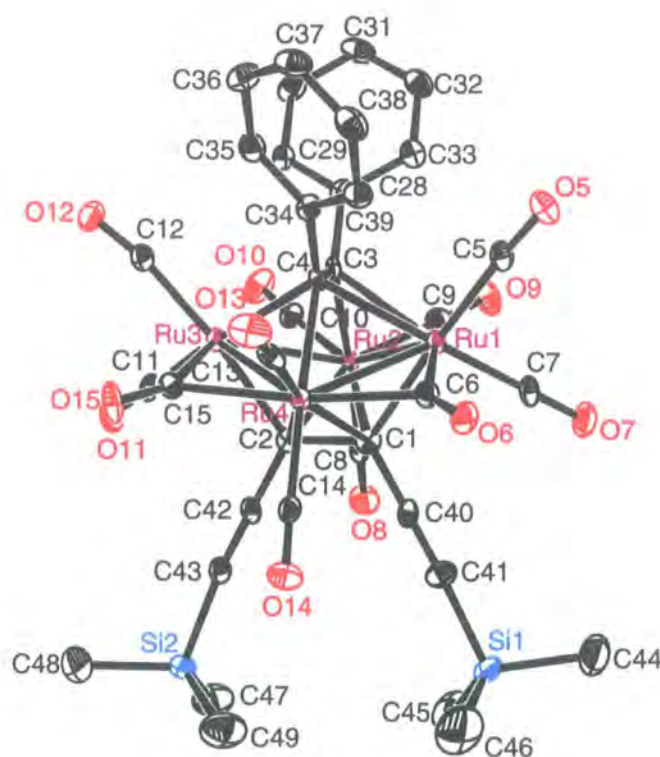
The IR spectrum of  $[\text{Ru}_4(\mu_4\text{-}\eta^2\text{-(Me}_3\text{SiC}\equiv\text{CC}_2\text{C}\equiv\text{CSiMe}_3\text{)})(\text{CO})_{10}(\text{PPh}_3)_2]$  was characterised by a series of absorptions for terminal  $\nu(\text{CO})$  at 2054, 2025, 2005, 2032, 1990 and 1978  $\text{cm}^{-1}$ . The free alkyne moieties gave rise to weak  $\nu(\text{C}\equiv\text{C})$  absorption bands at 2097  $\text{cm}^{-1}$ . The FAB-MS spectrum exhibited a molecular ion at  $m/z$  1428, followed by fragment ions derived from the sequential loss of up to nine carbonyl ligands. The  $^1\text{H}$  NMR spectra contained a singlet at  $\delta$  -0.26 ppm due to the  $\text{SiMe}_3$  groups, as well as resonances between  $\delta$  7.28 and 7.95 ppm arising from aromatic protons of the  $\text{PPh}_3$  moiety. The  $^{13}\text{C}$  NMR spectra revealed a single resonance at  $\delta$  199.85 ppm for the carbonyl ligands, as well as a resonance at  $\delta$  -0.00 due to the  $\text{SiMe}_3$  groups. The carbon nuclei of the  $\text{Ru}_4\text{C}_4$  core were detected as a single resonance at  $\delta$  113.13 ppm, while the acetylenic carbons gave rise resonances at  $\delta$  95.95 and 128.67 ppm. The aromatic region exhibited four resonances between  $\delta$  130.03 and 136.64 ppm.

## 5.4. Molecular Structures

The structure of **44a** has previously been reported<sup>170</sup> but in contrast attempts to obtain a sensible structure solution for **44c** were hampered by severe disorder in the crystal lattice. Crystal structures for similar clusters, such as **44e**<sup>313</sup> and the parent cluster **44f**<sup>314</sup> have also been obtained.

The structure of **44b** (Figure 74) has been determined (Table 23), and may be compared with the structures of **44a**,<sup>170</sup> **44e**,<sup>313</sup> and the parent complex **44f** (Table 24).<sup>314</sup> The clusters **44** feature nine SEP, or 62 CVE, which supports a description of the polyhedral cluster core in terms of a triangulated *closo*-dodecahedral  $\text{Ru}_4\text{C}_4$  cluster core. The gross structural features across the series are similar, and in all cases the metal centers sit  $\pm 0.31\text{-}0.34$  Å from the mean least

square plane that passes through them. In the solid state, **44f** carries two  $\mu$ -CO ligands located on adjacent Ru-Ru edges, while **44a** and **44e** each feature ten terminal and one bridging carbonyl ligand. The Ru-Ru bond lengths in these previously characterised examples fall in the range 2.73 – 2.83 Å, with the shorter bonds being associated with the  $\mu$ -CO ligands. In terms of the Ru<sub>4</sub> framework, the two alkyne ligands lie on opposite faces, with each being attached by two  $\sigma$  [Ru-C( $\sigma$ ) 2.15-2.19 Å] and two  $\pi$  [Ru-C( $\pi$ ) 2.30-2.38 Å] bonds. The C-C bond lengths reflect the interactions with the metals, and are considerably longer than the C $\equiv$ C bonds in free alkynes, falling in the range 1.406(8)-1.509(8)Å.



**Figure 74.** Molecular Structure of **44b** showing the atom labelling scheme depicted with a 50% ellipsoid probability. Hydrogen atoms have been omitted for clarity.

Table 24. Bond length comparison of 44a-44f.

	44a <sup>170†</sup>		44b		44d	44f <sup>314†</sup>	44f (theory)	44f <sup>2-</sup> (theory)	44f <sup>2-</sup> (theory)
	molecule 1	molecule 2	molecule 1	molecule 2					
Ru(1)-Ru(4)	2.8716(7)	2.8658(7)	2.7567(6)	2.8339(6)	2.8521(3)	2.7732(14)	2.824	2.858	2.752
Ru(1)-Ru(2)	2.7618 (7)	2.7628(7)	2.8815(6)	2.8530(7)	2.7948(2)	2.8338(14)	2.865	2.866	3.144
Ru(2)-Ru(3)	2.8649 (7)	2.8692(7)	2.8462(6)	2.7452(6)	2.8386(2)	2.8338(14)	2.871	3.001	2.736
Ru(3)-Ru(4)	2.7656(7)	2.7668(7)	2.7448(5)	2.8123(7)	2.7583(2)	2.7732(14)	2.829	2.866	3.014
Ru(1)-C(1)	2.221(6)	2.198(6)	2.161(5)	2.122(6)	2.0432(10)	2.143(12)	2.159	2.209	2.187
Ru(1)-C(4)	2.339(6)	2.278(6)	2.303(5)	2.353(5)	2.221	2.72(10)	2.333	2.177	3.093
Ru(1)-C(3)	2.273(6)	2.365(6)	2.419(5)	2.350(6)	2.262	2.312(12)	2.402	2.995	2.215
Ru(2)-C(3)	2.210(6)	2.207(6)	2.147(5)	2.208(6)	2.180	2.11(2)	2.121	2.183	3.010
Ru(2)-C(1)	2.365(5)	2.329(6)	2.273(5)	2.318(6)	2.2961(10)	2.310(15)	2.360	2.184	2.956
Ru(2)-C(2)	2.275(6)	2.288(6)	2.290(5)	2.267(5)	2.2961(10)	2.310(15)	2.351	2.995	3.308
Ru(3)-C(2)	2.192(6)	2.189(6)	2.150(5)	2.170(6)	2.2783(10)	2.143(12)	2.163	2.184	2.237
Ru(3)-C(4)	2.498(6)	2.484(6)	2.351(5)	2.430(6)	2.416	2.272(10)	2.340	2.952	2.175
Ru(3)-C(3)	2.311(5)	2.320(6)	2.397(5)	2.344(6)	2.329	2.312(12)	2.394	2.185	3.022
Ru(4)-C(4)	2.180(6)	2.195(6)	2.220(5)	2.171(5)	2.222	2.138(16)	2.163	2.177	2.988
Ru(4)-C(2)	2.514(6)	2.478(6)	2.310(5)	2.273(6)	2.2161(10)	2.283(12)	2.365	2.209	2.942
Ru(4)-C(1)	2.306(6)	2.334(5)	2.328(5)	2.358(6)	2.4123(11)	2.283(12)	2.369	2.981	2.229
C(1)-C(2)	1.406(8)	1.420(8)	1.428(7)	1.428(8)	1.426(2)	1.366(17)	1.389	1.401	1.397
C(3)-C(4)	1.407(8)	1.425(8)	1.422(7)	1.509(8)	1.416(2)	1.39(3)	1.395	1.428	1.403
O(5)-C(5)	1.146(7)	1.136(7)	1.135(6)	1.138(7)	1.1344(14)	1.118(17)	1.149	1.162	1.171
O(6)-C(6)	1.158(7)	1.156(7)	1.153(6)	1.146(7)	1.165(3)	1.14(3)	1.165	1.176	1.179
O(7)-C(7)	1.179(7)	1.180(7)	1.131(6)	1.147(7)	1.170(3)	1.13(3)	1.152	1.162	1.172

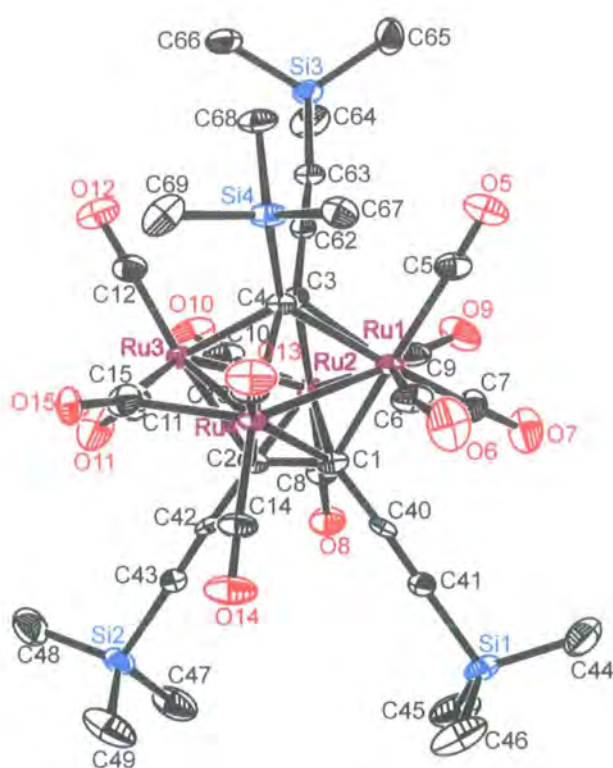
O(8)-C(8)	1.136(7)	1.155(7)	1.137(6)	1.138(7)	1.1349(18)	1.06(3)	1.145	1.166	1.171
O(9)-C(9)	1.145(7)	1.144(8)	1.127(7)	1.138(7)	1.142(4)	1.13(3)	1.150	1.180	1.171
O(10)-C(10)	1.129(7)	1.132(7)	1.146(6)	1.159(7)	1.136(3)	1.13(3)	1.150	1.165	1.181
O(11)-C(11)	1.147(7)	1.144(7)	1.138(6)	1.137(7)	1.135(3)	1.13(3)	1.152	1.166	1.170
O(12)-C(12)	1.125(7)	1.152(8)	1.135(6)	1.147(7)	1.1344(14)	1.118(17)	1.149	1.165	1.172
O(13)-C(13)	1.128(7)	1.142(7)	1.133(6)	1.141(7)	1.145(2)	1.10(3)	1.148	1.162	1.172
O(14)-C(14)	1.130(7)	1.123(7)	1.127(6)	1.139(7)	1.150(2)	1.19(3)	1.147	1.162	1.170
O(15)-C(15)	1.118(7)	1.153(7)	1.149(6)	1.135(7)	1.087(3)	1.14(3)	1.166	1.180	1.187
Diff from mean plane									
Ru(1)	+0.3350	-0.3293	+0.3409	-0.3312			+0.3124	0	+0.0332
Ru(2)	-0.3345	+0.3287	-0.3280	+0.3433			-0.3066	0	-0.0331
Ru(3)	+0.3340	-0.3296	+0.3473	-0.3486			+0.3112	0	+0.0334
Ru(4)	0.3345	+0.3301	-0.3602	+0.3364			-0.3170	0	-0.0332

† using atom labelling as depicted in Figures 74 and 75

The solid state structure of **44b** contains two independent molecules which differ in the arrangement of the carbonyl ligands around the Ru<sub>4</sub>C<sub>4</sub> core and the pattern of metal-metal bond lengths. Molecule 1 of **44b** contains a single bridging carbonyl ligand [Ru(3)-C(15) 2.053(6); Ru(4)-C(15) 2.090(6) Å; Ru(3)-C(15)-Ru(4) 83.0(2)°] spanning the shortest Ru-Ru bond [Ru(3)-Ru(4) 2.7453(6) Å, Ru(4)-Ru(1) 2.8124(7), Ru(2)-Ru(1) 2.8339(6), Ru(2)-Ru(3) 2.8530 Å]. The Ru-C(alkyne) bond lengths cover a slightly greater range than displayed in the previous examples, with Ru-C(σ) bonds in the range 2.122(6)-2.208(6) Å, and Ru-C(π) between 2.267(5)-2.430(6) Å. The tetrahedral distortion in the Ru<sub>4</sub> core is approximately ±0.33-0.36 Å from the mean least squares plane that passes through them, which is a larger deviation than that found for **44a** and **44e** (Table 24).

Molecule 2 of **44b** contains two semi-bridging carbonyl groups [Ru(3)-C(15) 2.010(5); Ru(4)-C(15) 2.218(5) Å; Ru(3)-C(15)-Ru(4) 80.8(2)°; Ru(4)-C(6) 2.184(5); Ru(1)-C(6) 2.024(5) Å; Ru(4)-C(6)-Ru(1) 81.8(2)°] spanning the adjacent edges Ru(3)-Ru(4) [2.7448(5) Å] and Ru(4)-Ru(1) [2.7567(6) Å]. The other Ru-Ru bond lengths are considerably longer [Ru(3)-Ru(2) 2.8462(6), Ru(2)-Ru(1) 2.8815(6) Å]. The Ru-C(σ) bond lengths fall within the range 2.147(5)-2.221(5) Å, while Ru-C(π) span 2.273(5)-2.418(5) Å. The tetrahedral distortion in the Ru<sub>4</sub> core is approximately ±0.33-0.34 Å from the mean least squares plane that passes through them. Most compounds of the type **44** exhibit structures possessing only one bridging carbonyl with the exception of the structure described above and one found for **44d** and **44f**.<sup>314</sup> In both molecules, there is a correlation between the Ru-C(alkyne) bond lengths, with the carbon centers that form the shorter σ-bonds also being involved in the longer Ru-C(π) bonds. The tetrahedral distortion associated with each molecule, as defined by a shift of the metal centers from the mean least squares plane that passes through them, is ca. ±0.34 Å (Molecule 1/2).

The structural study of **44d** (Figure 75) was complicated to some extent by disorder in the carbonyl ligands, the molecular parameters associated with the Ru<sub>4</sub>C<sub>4</sub> cluster core are similar to those of the other examples in the series, with Ru-Ru bond lengths spanning the range 2.7583(2) – 2.8521(3) Å, and Ru-C bond lengths between 2.216(1) - 2.296(1) Å. Of the eleven carbonyl ligands, two adopt a bridging mode. The C-C bond lengths within the cluster core are 1.426(2) [(C(1)-C(2))] Å and 1.416(2) [(C(3)-C(4))] Å.



**Figure 75.** Molecular Structure of **44d** showing the atom labelling scheme depicted with a 30% ellipsoid probability. Hydrogen atoms have been omitted for clarity.

Treatment of the triangulated cluster core in **44** using the EAN formalisation results in the same problems as encountered in the phosphinidene clusters [M<sub>4</sub>(CO)<sub>11</sub>(PR)<sub>2</sub>] (M = Fe, Ru). In each case, if the phosphinidene (PR)

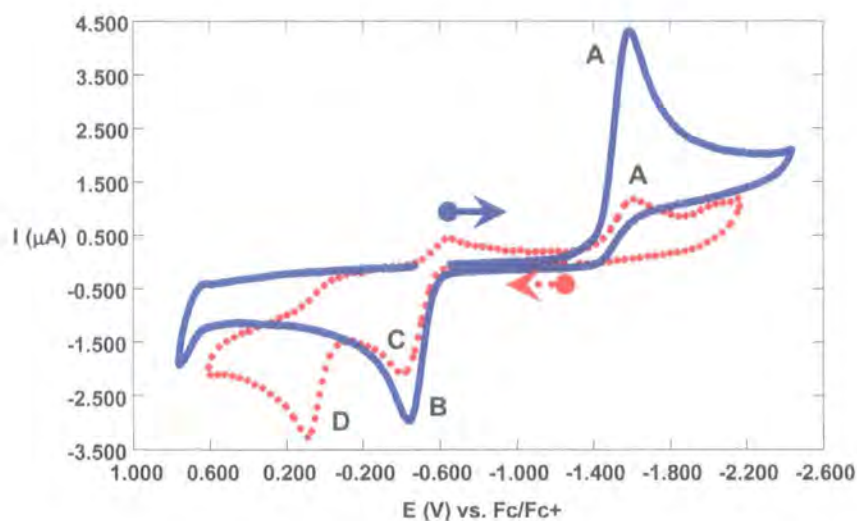
or alkyne ligands are treated as four electron donors in the usual manner, electron counts of 62 CVE are obtained, which are two electrons short of the 64 CVE's demanded by  $M_4$  square frameworks. Similar inconsistencies are encountered with the octahedral triangulated cluster core in **43** which has 60 CVE's, two short of the 62 CVE required. The failings of two-centre two-electron bonding models in descriptions of cluster systems are well-documented,<sup>215, 323</sup> and electronically, the clusters of the type  $[M_4(CO)_{11}(L)_2]$  are well described in terms of PSEP concepts, containing either seven or nine skeletal pairs, as required for six and eight vertex polyhedra respectively. While electron counting rules facilitate structural correlation, they do not necessarily provide insight into chemical properties, which depend on the finer details of electronic structure, which can be provided by theoretical calculations. The electronic flexibility displayed by square-based  $M_4$  frameworks which have been described above prompted us to examine the electrochemical and chemical response of **44**.

## 5.5. Electrochemistry and IR Spectroelectrochemistry

The CV response of dichloromethane solutions of **44a** or **44c** (Figure 76) were characterised by a single, chemically irreversible reduction process (A) in each case [ $E_p(A)$ : **2a** -1.528 V; **2c** -1.580 V vs.  $Fc/Fc^+$ ] with the oxidation peak B appearing only as a consequence of the reduction A.<sup>xiv</sup> Polarography of the same solution showed only one reduction wave [ $E_{1/2}$ : **2a** -1.418 V; **2c** -1.387 V], and in each case logarithmic analysis gave a linear plot with a slope of 47 mV. This value is between that expected for a  $1e^-$  (59 mV) and  $2e^-$  reduction processes (29.5 mV). However, bulk electrolysis performed at a mercury-pool electrode at -1.60 V consumed exactly 2 F/mol, while the initial red-orange solution turned yellow. Bulk re-oxidation at +0.30 V also consumed 2 F/mol and restored the initial red-orange colour to the solution. Curiously, the cyclic voltammogram of the yellow electrolysis solution was characterised by two, one-electron oxidation waves, which were only partially chemically reversible.

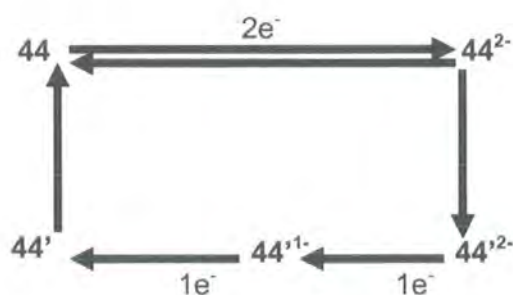
<sup>xiv</sup> Cyclic voltammetry data courtesy of C. Nervi.





**Figure 76.** Cyclic voltammetry trace of **44c** at 100 mV/s.

The electrochemical data is consistent with the following cycle (**Figure 77**): the clusters **44** are reduced in a single two electron event to give a dianion **44<sup>2-</sup>**, which can be re-oxidised in a single two electron process on the CV timescale. On longer timescales, **44<sup>2-</sup>** is unstable, converting to a second species **44',<sup>2-</sup>** via a non-electrochemical process. Compound **44',<sup>2-</sup>** is re-oxidised in two sequential one-electron steps back to **44**.



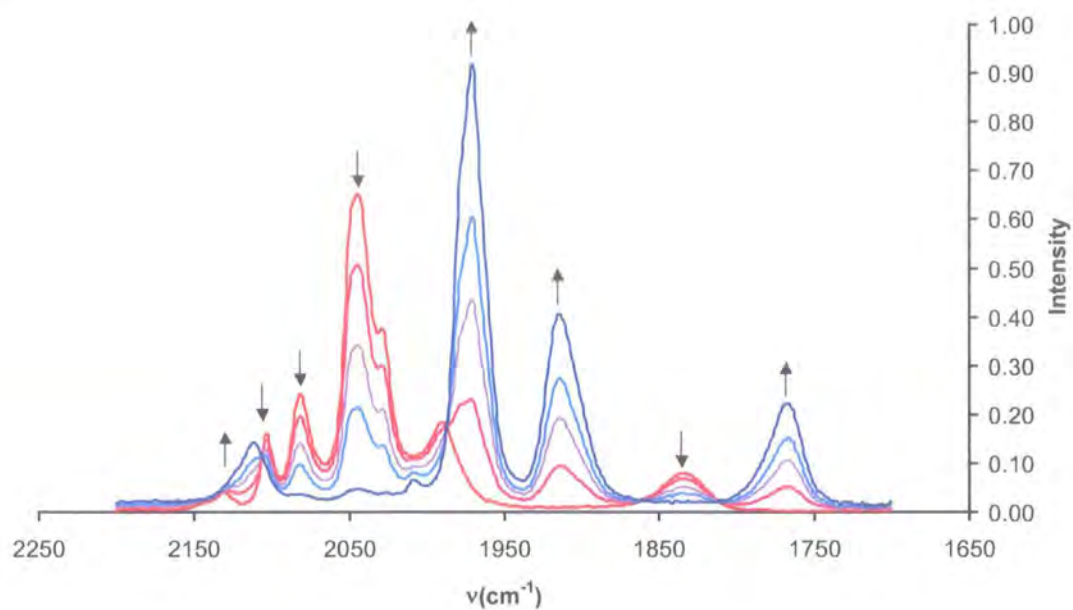
**Figure 77.** Electrochemical cycle of **44**.

Infra-red spectroelectrochemical studies were carried out to gain some insight into the chemical processes occurring during the electrochemical cycle (**Figure 78**).<sup>xv</sup> The  $\nu(\text{CO})$  patterns of **44a** and **44c** in 1,2-dichloroethane containing 0.1 M  $\text{NBu}_4\text{PF}_6$  supporting electrolyte were similar to the spectra in cyclohexane. Four terminal carbonyl bands were observed at 1988, 2044 and 2027(sh), 2080, and 2132  $\text{cm}^{-1}$ . The bridging carbonyl gave rise to a weaker, broad band at 1831  $\text{cm}^{-1}$  while the  $\nu(\text{C}\equiv\text{C})$  band from the pendant alkynyl moieties was observed at 2132  $\text{cm}^{-1}$  (**Figure 78a**). *In situ* reduction caused these characteristic absorption bands to collapse giving way to a new set of bands associated with the electrochemically generated dianion **44a**<sup>2-</sup>  $\nu(\text{CO})$  1953 vs, 1897 m, 1749 w  $\text{cm}^{-1}$ ; **44c**<sup>2-</sup>  $\nu(\text{C}\equiv\text{C})$  2107 w,  $\nu(\text{CO})$  1962 vs, 1903 m, 1751 w  $\text{cm}^{-1}$  (**Figure 78b**). The decrease in carbonyl stretching frequencies is consistent with the greater electron density associated with **44c**<sup>2-</sup>, and the chemical reversibility of the electrochemical event was verified by the almost clean regeneration of **44c** upon re-oxidation. The conversion of **44** to a new compound upon reduction, with three isosbestic points at 2102, 1979, 1850 and 1795  $\text{cm}^{-1}$  indicate a quantitative conversion (**Figure 78b**). There was no change in the spectroelectrochemical behaviour of **44c** under atmospheres of  $\text{N}_2$  or  $\text{CO}$ , which suggests that carbonyl dissociation processes are not involved with the electrochemical reduction and subsequent transformations.

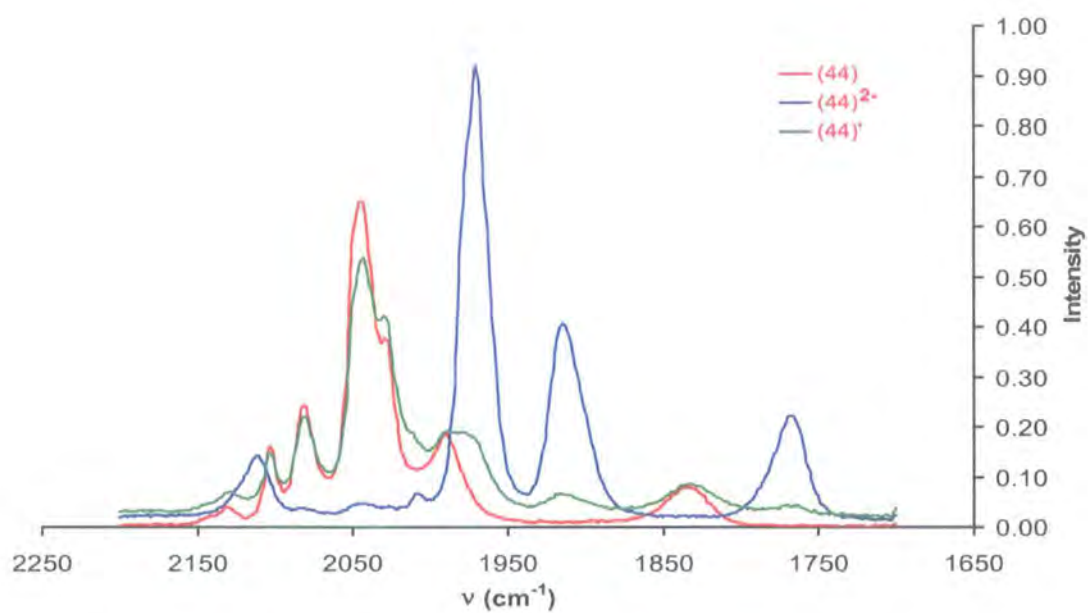
---

<sup>xv</sup> IR spectroelectrochemistry data courtesy of C. Nervi.

a)



b)

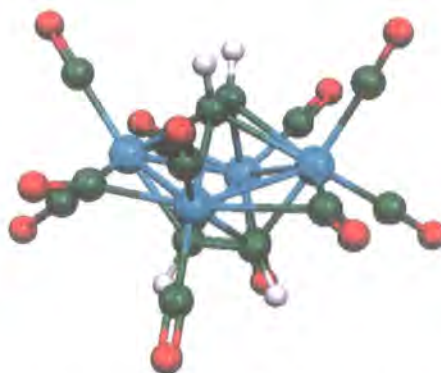


**Figure 78.** a) IR spectroelectrochemical spectra obtained following the reduction of **44c** in 1,2-dichloroethane solution. b) IR spectra comparison of the starting solution, after full reduction at  $-1.80$  V, and after re-oxidation at  $+0.30$  V.

The spectroelectrochemical experiments clearly supported the voltammetry data, and confirmed the chemical stability of the redox generated products and chemical reversibility of the cycle. However, only limited structural information could be derived from the IR spectroscopic data. In order to probe the redox products in more detail, a computational analysis of the cycle was undertaken.

## 5.6. Computational Analysis

To facilitate theoretical analysis, a simplified model complex,  $[\text{Ru}_4(\text{CO})_{11}(\mu_4\text{-HC}_2\text{H})_2]$  (**44f**), with 62-electrons has been adopted (**Figure 79**). Geometry optimisation, orbital calculations and transition state calculations were performed using the B3LYP functional<sup>200</sup> with a 3-21G\* basis set for ruthenium and a 6-31G\*\* basis set for carbon, hydrogen, and oxygen. At the time this study was undertaken, the structure of **44f** had not been reported, and the coordinates from the crystal structure of **44a** were used as a starting geometry. Default criteria within the software were employed for geometry optimisation, which places an uncertainty of less than  $\pm 0.005 \text{ \AA}$  on bond lengths. The dependence of the calculation upon basis set was tested using the TZVP basis set. After optimisation in  $C_1$ , the coordinates were symmetrised, re-optimisation in the required point group was performed, even though the symmetrised structures had very low gradients, and frequency analysis carried out. All reported structures had (3N-6) positive vibrational eigenvalues and the transition state was found to have one imaginary vibrational eigenvalue.



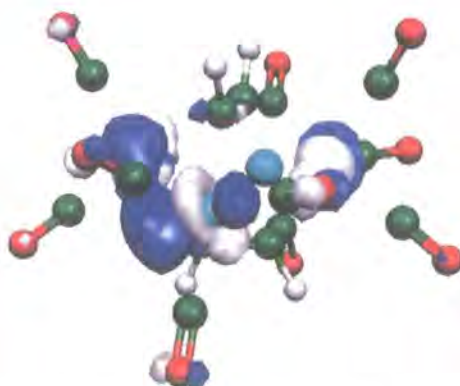
**Figure 79.** Geometry optimised structure of **44f** calculated using Gaussian98 at a B3LYP/6-31G\*\* level.

Selected bond lengths and angles for **44f** are summarised in **Table 24**, along with the data relating to the crystallographically determined structures of **44a-f**. While quantitative agreement between the observed and calculated data is not expected due the nature of the calculations and structural approximations involved, the optimised geometry of **44f** is in good agreement with the general trends observed for **44a-f**, which allows a degree of confidence in the accuracy of the computations, and the conclusions drawn from them.

The geometry optimised model structure of **44f** (**Figure 79**) shows the same gross structure as the experimental complexes, with the four metal centres forming a puckerred square arrangement with the alkyne moieties oriented diagonally across opposite corners giving the anticipated trigonal dodecahedron structure. Each metal centre carries two terminal carbonyl ligands, and in addition, one symmetrical bridging and two semi-bridging carbonyl ligands can be identified. The Ru-Ru bond lengths fall in the range 2.824-2.879 Å, the longest bond being that which is not bridged. The tetrahedral distortion in the Ru<sub>4</sub> core is approximately  $\pm 0.31\text{Å}$  from the mean least squares plane that passes through them, similar to those found for **44a-f**.

An analysis of the orbital structure of the cluster reveals the expected nest of low lying occupied orbitals derived from various combinations of the metal,

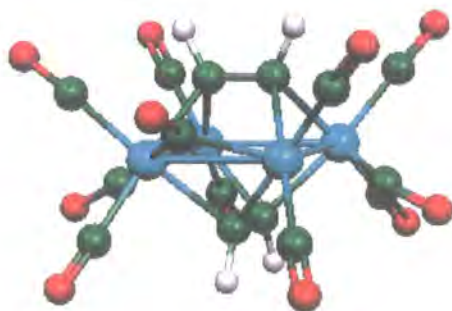
carbonyl and alkyne fragments. The HOMO and HOMO<sub>-1</sub> are somewhat removed from the remainder of the occupied orbitals and are comprised mainly of anti-bonding combinations of the  $d_{z^2}$  orbitals (**Figure 80**). The LUMO consists largely of Ru-Ru and Ru-C(alkyne) anti-bonding interactions. The HOMO-LUMO gap of 3.9 eV is large and the structure is expected to be stable with an eight SEP count.



**Figure 80.** HOMO of **44f** calculated using Gaussian98 at a B3LYP/6-31G\*\* level.

In order to simulate the events occurring following reduction in the CV cell, the number of electrons in the structurally optimised model **44f** was increased by two to give the 10-SEP/64-CVE dianion **44f**<sup>2-</sup>, and the structure re-optimised (**Figure 81**). The four ruthenium centres in **44f**<sup>2-</sup> define a planar rectangular structure, with the alkyne vectors, which are mutually orthogonal, located above and below this plane and in contrast to **44f** are parallel to two of the metal edges. The Ru<sub>4</sub>C<sub>4</sub> core can therefore be described as two trigonal prisms fused orthogonally through the M<sub>4</sub> face. Predictions based on electron counting rules would suggest that the 64-CVE dianion could be described as a Ru<sub>4</sub> square cluster, a suggestion which is entirely in agreement with the optimised geometry.



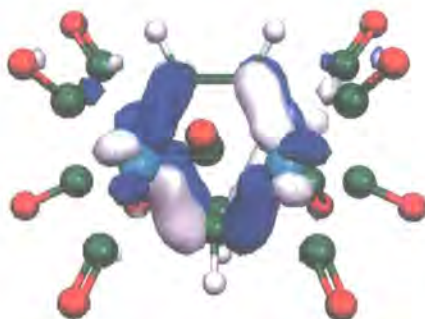


**Figure 81.** Geometry optimised structure of  $44f^{2-}$  calculated using Gaussian98 at a B3LYP/6-31G\*\* level.

In the strictest sense, the static isomers of  $44f$  and  $44f^{2-}$  obtained from the optimisation process have low symmetry ( $C_2$  and  $C_s$ , respectively), with the carbonyl ligands being distributed in response to the overall shape change in the  $Ru_4C_4$  cluster core. However, the carbonyl ligands are fluxional on the NMR time scale in the real systems  $44$ , and likely to also be fluxional in the corresponding dianions. If the location of the carbonyl ligands are factored out, the  $Ru_4C_4$  cores have pseudo  $C_{2v}$  ( $44f$ ) and  $D_{2d}$  ( $44f^{2-}$ ) symmetry. The higher symmetry of the dianion would account for the reduction in the number of bands observed following reduction in the experimental IR spectra (**Figure 78**).

The  $Ru_4C_4$  core of the  $44f^{2-}$  has three “normal” Ru-Ru bonds (2.858, 2.866, 2.866 Å) and one long one (3.001 Å), with the three bridging carbonyls spanning the shorter Ru-Ru bonds (**Figure 81**, **Table 24**). Each metal centre also carries two terminal carbonyl ligands. The bridging form of the carbonyl ligand is more basic at the oxygen and more electron withdrawing with respect to the cluster than the terminal form.<sup>320</sup> The increased number of bridging carbonyls is therefore not surprising, as this provides an avenue to delocalise the excess charge in the dianion. Based upon Mulliken population analysis, the additional electron density in  $44f^{2-}$  is distributed over the  $Ru_4$  centres (0.406e<sup>-</sup>), the alkyne carbons (0.235e<sup>-</sup>) and the carbonyl ligands (1.548e<sup>-</sup>). The average metal-metal bond length

in the dianion  $44f^{2-}$  (2.89 Å) is only slightly longer than the average in the calculated structure of the neutral species (2.84 Å), while the Ru-C(alkyne) bond lengths fall in the range 2.177 – 2.209 Å (avg. 2.18 Å), consistent with the description of each in terms of a Ru-C  $\sigma$ -bond. The C(1,3)-C(2,4) bond lengths increase following reduction of the cluster from 1.389/1.395 Å in the optimised structure  $44f$  to 1.401/1.428 Å in the dianion  $44f^{2-}$ . The HOMO of  $44f^{2-}$ , which is removed from the remaining occupied orbitals, is essentially formed by mixing of a set of metal d-orbitals with the alkyne  $\pi^*$  orbitals, giving a molecular orbital which is strongly Ru-C bonding, and C-C anti-bonding and accounting for the observed structural trends (**Figure 82**).

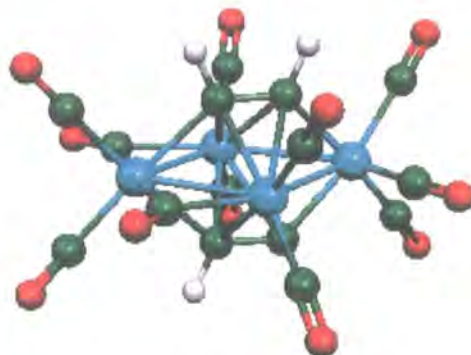


**Figure 82.** HOMO of  $44f^{2-}$  calculated using Gaussian98 at a B3LYP/6-31G\*\* level.

To mimic the re-oxidation event observed in the initial CV sweep (**Figure 76**), two electrons were removed from  $44f^{2-}$  and the geometry re-optimised, affording a new structure  $Ru_4(CO)_{11}(\mu_4-HC_2H)_2$  ( $44f^\dagger$ ), (**Figure 83**) which resides in a local minimum along the reaction pathway between  $44f^{2-}$  and  $44f$ . In this intermediate structure, the alkyne vectors are parallel to each other and lie diagonally across the  $Ru_4$  plane. The reaction pathway between  $44f^{2-}$ ,  $44f^\dagger$  and  $44f$  was examined in some detail to clarify the relationship between these species. A transition state structure calculation was performed, during which the transient species  $44f^\ddagger$  was identified. The core geometry in  $44f^\ddagger$  is characterised by a puckered arrangement of the metal atoms, with the metal atoms lying



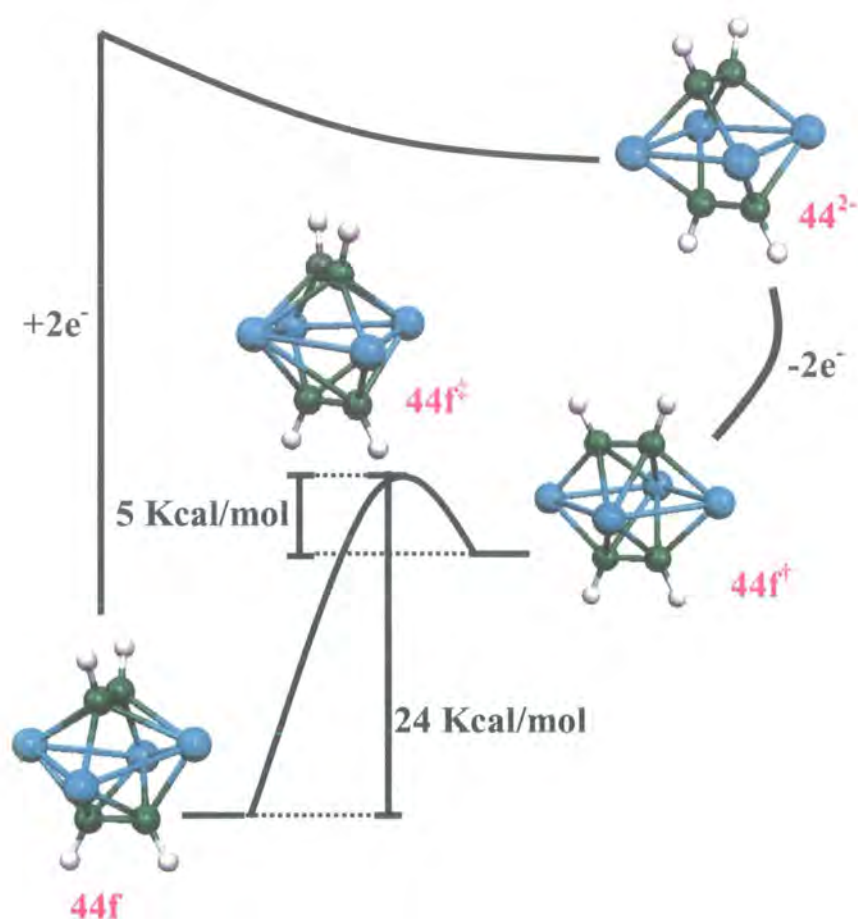
approximately  $\pm 0.12\text{--}0.13$  Å from the mean least squares plane that passes through them. The alkyne vectors are twisted from the parallel arrangement in  $44f^\dagger$  but not yet at positions required by  $44f$ . An energy barrier of 5 Kcal/mol was calculated for the forward reaction  $44f^\dagger \rightarrow 44f$ . The barrier to the back reaction was calculated to be 24 Kcal/mol. The changes in the metal atom framework that accompany the overall transformation  $44f \rightarrow 44f^{2-} \rightarrow 44f^\dagger \rightarrow 44f^\ddagger \rightarrow 44f$  are shown schematically in **Scheme 37**. Initial reduction of **44** (**Figure 76**, wave A) results in the consumption of two electrons per molecule, and the formation of the square cluster  $44^{2-}$ . This dianion is itself redox active, being re-oxidised (**Figure 76**, wave B) to give an intermediate,  $44f^\dagger$ , which is thermodynamically unstable with respect to **44**. Thus, while the electrochemical events are chemically reversible, the process is not diffusion controlled, and the cycle is electrochemically irreversible.



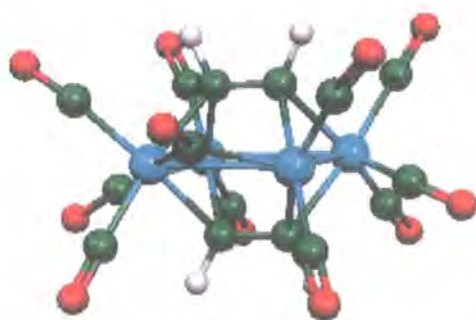
**Figure 83.** Geometry optimised structure of  $44f^\dagger$  calculated using Gaussian98 at a B3LYP/6-31G\*\* level.

The different voltammograms observed on the CV and bulk electrolysis timescales, but in the absence of any further electrochemical event, strongly suggests the presence of a second, structurally related dianion,  $44f^{2-}$ . Using the calculated geometry of  $44f^{2-}$  as a starting point, one of the alkyne vectors was rotated by  $90^\circ$  and the structure re-optimised, resulting in a second 64-CVE dianion structure,  $44f^{2-}$  (**Figure 84**), some 4 Kcal/mol more stable than  $44f^{2-}$ . The

structure of  $44f^{2-}$  can also be obtained by taking the structure of  $44f^{2-}$ , and using molecular dynamics, each atom is given approximately 400 K of kinetic energy. Then the structure is allowed to equilibrate for about 1 ps simulation time at the specified temperature. By applying the specified amount of kinetic energy to the nuclei, this effectively acts as heating of the system, allowing it to overcome the energy barrier. Then the structure is cooled over a period of one second, and the new structure of  $44f^{2-}$  obtained.

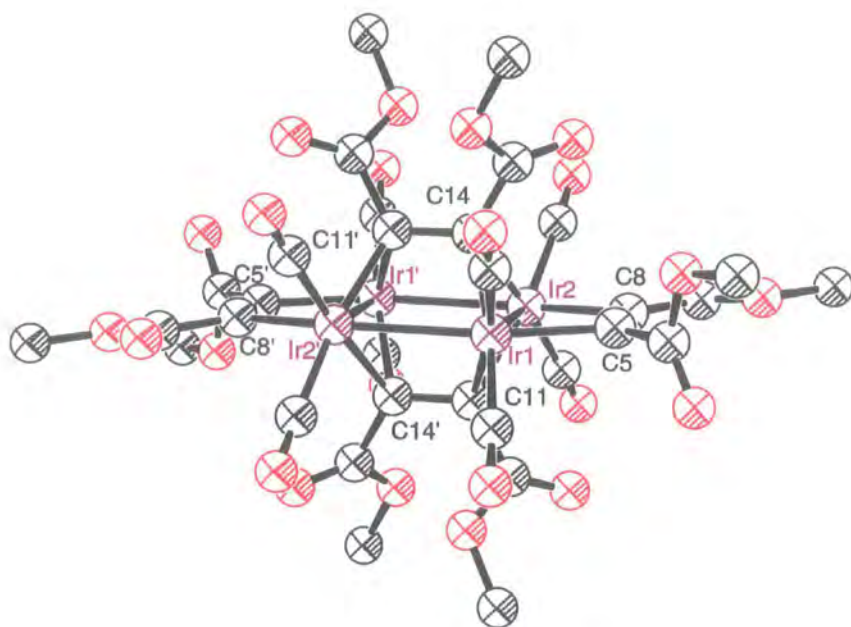


**Scheme 37.** Changes in the metal atom framework that accompany the overall transformation  $44f \rightarrow 44f^{2-} \rightarrow 44f^{+} \rightarrow 44f^{2+} \rightarrow 44f$ .



**Figure 84.** Geometry optimised structure of  $44f^{2-}$  calculated using Gaussian98 at a B3LYP/6-31G\*\* level.

The structure of  $44f^{2-}$  is simply related to that of  $44f^{2-}$  by the re-orientation of one of the alkyne vectors, such that they lie parallel to each other and directed at the mid-point of a Ru-Ru bond. This core geometry is identical to that found in the molecular structure of  $[\text{Ir}_4(\text{CO})_8\{\text{MeCO}_2\text{C}_2\text{MeCO}_2\}_4]$  (**Figure 85**), the only 64-CVE  $\text{M}_4(\text{alkyne})_2$  cluster to have been crystallographically characterised to date.<sup>324</sup> The tetrairidium complex is centrosymmetric with the four iridium atoms defining the rectangle, each iridium is bonded to two terminal carbonyls with the short Ir-Ir edge bridged by the two substituted acetylenes ligands. The other acetylene ligands lie above and below the metal plane capping the rectangular face with the acetylenic C-C vector lying approximately parallel to the longer Ir-Ir edge. The edge bridging acetylenes donate two electrons each to the complex, and the face capping ligand donates four electrons making  $[\text{Ir}_4(\text{CO})_8\{\text{MeCO}_2\text{C}_2\text{MeCO}_2\}_4]$  a 64-electron complex.<sup>324</sup>

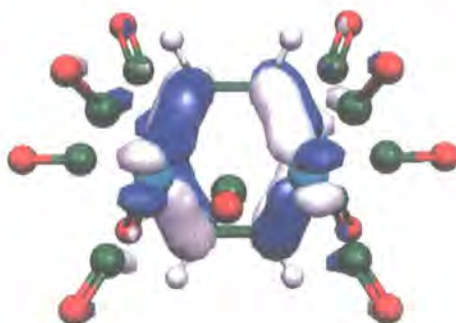


**Figure 85.** Molecular structure of  $[\text{Ir}_4(\text{CO})_8\{\text{MeCO}_2\text{C}_2\text{MeCO}_2\}_4]$  depicted with a 50% ellipsoid probability. Hydrogen atoms have been omitted for clarity.<sup>324</sup>

The optimised geometry of  $44\text{f}^{2-}$  has three short Ru-Ru bonds (2.752, 2.736 Å) and two long bonds (3.144, 3.014 Å), with the three bridging carbonyls spanning all but the longest Ru-Ru bond (**Figure 84, Table 24**); each metal centre also carries two terminal carbonyl ligands. Based upon Mulliken population analysis, the additional electron density in  $44\text{f}^{2-}$  is distributed over the  $\text{Ru}_4$  centres ( $0.288e^-$ ), the alkyne carbons ( $0.512e^-$ ) and the carbonyl ligands ( $1.200e^-$ ). The average metal-metal bond length in the dianion  $44\text{f}^{2-}$  (2.90 Å) is only slightly longer than the average in  $[\text{Ir}_4(\text{CO})_8\{\text{MeCO}_2\text{C}_2\text{MeCO}_2\}_4]$  (2.76 Å), while the Ru-C(alkyne) bond lengths fall in the range 2.175 – 3.308 Å (avg. 2.69 Å), which is also slightly longer to that found in the iridium complex (2.13(3) Å). The C(1,3)-C(2,4) bond lengths increase following reduction of the cluster from 1.389/1.395 Å in the optimised structure **44f** to 1.397/1.403 Å in the dianion  $44\text{f}^{2-}$ , consistent with the value found for the alkyne unit in the iridium complex (1.446 Å). The HOMO of  $44\text{f}^{2-}$  is essentially the same as that of **44f**, which is strongly Ru-C

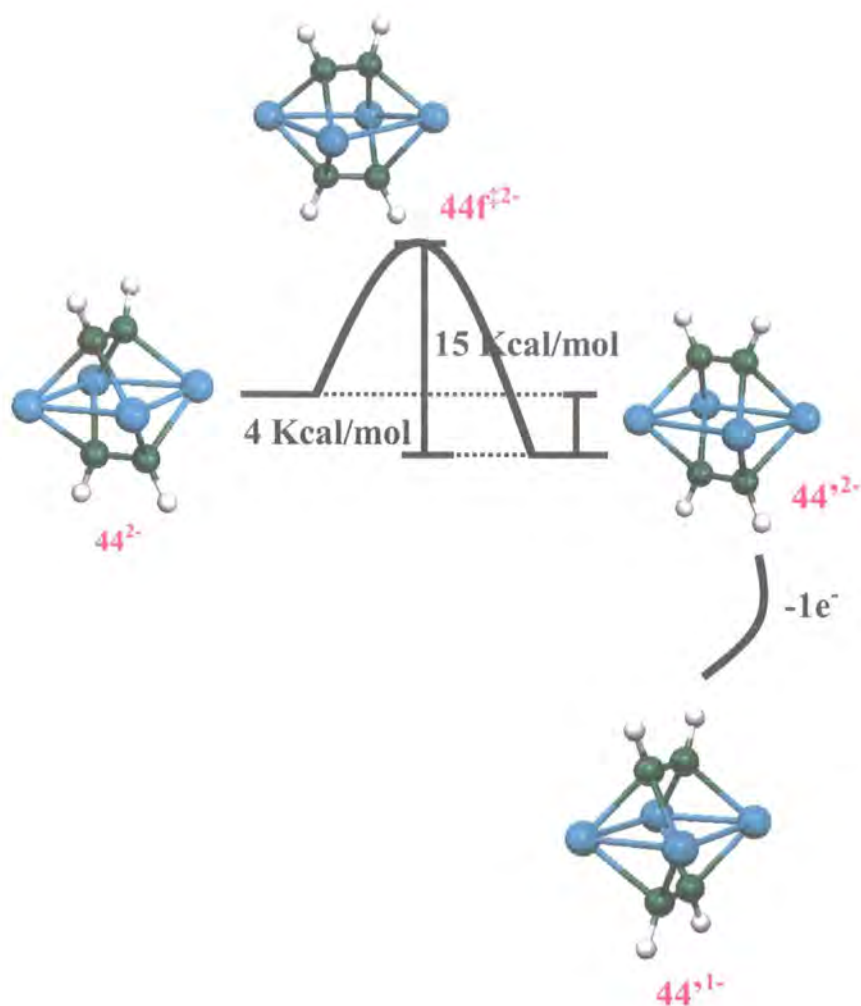


bonding, and C-C anti-bonding and accounts for the observed structural trends (**Figure 86**). This structure of  $44f^{2-}$  is lower in energy than that of  $44f^{2-}$  by approximately 4 Kcal/mol making it thermodynamically favoured. The reaction pathway between  $44f^{2-}$ ,  $44f^{2-}$  and  $44f$  was examined in some detail to clarify the relationship between these species. A transition state structure calculation was carried out, during which the transient species  $44f^{2-}$  was identified which has an energy barrier of 15 Kcal/mol (**Scheme 28**).



**Figure 86.** HOMO of  $44f^{2-}$  calculated using Gaussian98 at a B3LYP/6-31G\*\* level: compare with **Figure 82**.

To mimic the chemical reversibility of the bulk electrolysis experiment performed in the IR spectrochemical cell two electrons were removed from  $44f^{2-}$  and the geometry re-optimised, affording  $44f$  again (**Figure 77**). Convergence problems were encountered on route to  $44f$ , resulting in a series of almost iso-energetic structures, which have similar core structures to  $44f$ , and differ only in minor arrangements of the carbonyl ligands and precise orientations of the alkyne vectors. The convergence problems encountered during this geometry optimisation process suggest that this species resides on a fairly flat portion of the potential energy surface.



**Scheme 38.** Changes in the metal atom framework that accompany the overall transformation  $44f^{2-} \rightarrow 44f^{2-}$ .

The remaining point to address lies in the observation of a stable 63-CVE species ( $44^{1-}$ ) during the re-oxidation of the dianions  $44'^{2-}$ , but not from re-oxidation of  $44^{2-}$  (Scheme 38) as was observed in the CV trace. Unfortunately, computational restrictions have prevented us from further analysing this portion of the reaction scheme. It is obvious that the global minimum for each potential surface for the different redox pathways (Scheme 37 and 38) will be the same, and rather the stability of the odd-electron form derived from  $44'^{2-}$  must lie in the subtlety of the reaction profile, and contain a somewhat deeper local minimum.

Nevertheless, the experimental result is clear, and the distinct behaviour of the two dianions upon re-oxidation clearly indicates the relative stability of the mono-anion derived from **44f**<sup>2-</sup>.

## 5.7. Molecular Switching Behaviour

**Scheme 37** illustrates a cycle broadly similar to that proposed for a mechanochemical switching device based upon redox active [2]-catenanes (**Figure 16**).<sup>102</sup> In the case of the Ru<sub>4</sub>C<sub>4</sub> cluster core, the dodecahedral geometry observed in **44** and calculated in **44f** represents the “open” position of the switch. The HOMO is more or less localised around the metal “belt” and in the absence of a delocalised orbital linking the cluster core carbon centres these sites, and any pendant groups upon them, are effectively “insulated”.

Reduction of **44** ( $E_{1/2}$  ca.  $-1.5$  V), which consumes two electrons, gives the thermodynamically and kinetically stable dianion **44**<sup>2-</sup>. The excess electron density is relieved by adoption of the open M<sub>4</sub> framework and re-orientation of the alkyne moieties to permit M(d)-C( $\pi^*$ ) back-bonding. This back-bonding interaction results in a HOMO which is delocalised over not just the metal centres, but also the carbon centres of both alkyne moieties. This delocalised orbital therefore offers a route for “through-bond” electronic interactions between the alkyne carbons, and any groups pendant to them with appropriate orbital symmetry, through the Ru<sub>4</sub> core. The cluster switch can therefore be regarded as “open” in the reduced form. A similar orbital structure is also observed for the thermodynamically more stable isomer **44'**<sup>2-</sup>. On rapid time-scales, the dianion **44**<sup>2-</sup> is cleanly re-oxidised to the neutral state, *via* the pathway shown in **Scheme 37**, at potentials of ca.  $-0.5$  V, giving a switching potential of ca.  $1$  V. On longer time scales, the dianion isomerises to the more thermodynamically stable **44'**<sup>2-</sup> which is itself re-oxidised in two steps, also starting at potentials near  $-0.5$  V.

The ability of the  $M_4C_4$  cluster core to adopt stable structures related by a two electron step, one of which would appear to be suitable for permitting delocalisation of electronic charge through the cluster core, suggests that similar cluster architectures may be suitable for use as molecular junctions with an integrated capacity for molecular switching. These are obviously long term aspirations, but the potential for metal clusters in this area is an appealing avenue for investigation alongside more established organic frameworks.

## 5.8. Experimental

### 5.8.1. Spectroelectrochemistry

Tetrabutylammonium hexafluorophosphate was re-crystallised three times from 95% ethanol and dried in vacuum oven at 110°C overnight. Electrochemistry was performed with an EG&G PAR 273 electrochemical analyser connected to a PC, employing the software M270. A standard three-electrode cell was designed to allow the tip of the reference electrode to closely approach the working electrode. The reference electrode was Standard Calomel Electrode (SCE). The working electrode for CV was a glassy carbon (GC) electrode; for polarography a dropping mercury electrode (DME) with flow rate of 1.22 mg s<sup>-1</sup> at a reservoir height of 0.5 m was employed. Drop time (typically 1 s) was controlled by an electromechanical hammer. The auxiliary electrode was a platinum wire. Positive feedback *iR* compensation was applied routinely. Measurements were carried out under Ar in freshly distilled anhydrous deoxygenated solvents. Solutions were 5 × 10<sup>-4</sup> M with respect to the compounds under study and 1 × 10<sup>-1</sup> M with respect to the supporting electrolyte, [Bu<sub>4</sub>N][PF<sub>6</sub>]. Potentials (versus SCE) are referred to the ferrocene (0/+1) couple. Under our experimental conditions the Fc/Fc<sup>+</sup> couple was evaluated to be +0.46 V vs. SCE in dichloromethane. Each experiment was carried out in duplicate. Spectroelectrochemistry was performed in an optically transparent thin-layer electrochemical (OTTLE) cell assembled as previously described;<sup>325</sup> spectra were recorded on a Bruker Equinox 55 FT-IR spectrometer.

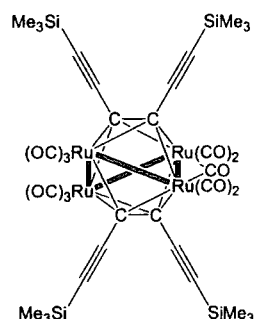


### 5.8.2. Computational Method

Geometry optimisation, orbital calculations and transition state calculations were performed using the B3LYP functional<sup>200</sup> as implemented within the Gaussian 98 software package,<sup>201</sup> with a 3-21G\* basis set for ruthenium and a 6-31G\*\* basis set for all other atoms. Default criteria within the software were employed for geometry optimisation, which places an uncertainty of less than  $\pm 0.005$  Å on bond lengths. The dependence of the calculation upon basis set was tested using the TZVP basis set and stationary point analysis were performed. Results of these calculations were in qualitative agreement with those reported here, thus giving confidence that the qualitative picture of the chemistry is converged with respect to this parameter. After optimisation in C1 coordinates were symmetrised, reoptimisation in the required point group was performed, even though the symmetrised structures had very low gradients, and frequency analysis carried out. All reposted structures had (3n-6) positive vibrational eigenvalues and the transition state was found to have one imaginary vibrational eigenvalue. Finally, the results of the orbital calculations were displayed graphically using Molekel.<sup>272</sup>

### 5.8.3. Experimental

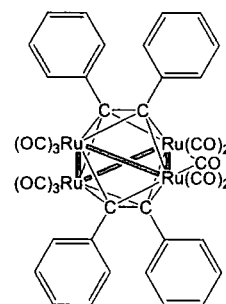
#### 5.8.3.1. $[\text{Ru}_4(\mu_4\text{-}\eta^2\text{-Me}_3\text{SiC}\equiv\text{CC}_2\text{C}\equiv\text{CSiMe}_3)_2(\text{CO})_{11}]$ (44c)



A solution of  $\text{Ru}_4(\mu_4\text{-}\eta^2\text{-Me}_3\text{SiC}\equiv\text{CC}_2\text{C}\equiv\text{CSiMe}_3)(\text{CO})_{12}$  (0.14 g, 0.13 mmol) in hexane (20 ml) was treated with  $\text{Me}_3\text{SiC}\equiv\text{CC}\equiv\text{CC}\equiv\text{CSiMe}_3$  (0.13 g, 0.46 mmol) and the solution heated at reflux for 8 h, cooled and the solvent removed. The crude product was purified by preparative TLC (hexane). The orange band contained the desired product and was recrystallised from  $\text{CH}_2\text{Cl}_2$ :hexane (0.04 g, 0.03 mmol, 23%).

IR (cyclohexane):  $\nu(\text{C}\equiv\text{C})$  2158 w, 2131 m,  $\nu(\text{CO})$  2088 s, 2064 s, 2040 s, 2027 s, 2008 s, 1854 m  $\text{cm}^{-1}$ .  $^1\text{H}$  NMR (499 MHz,  $\text{CDCl}_3$ ):  $\delta$  0.03 (s, 36H,  $\text{SiMe}_3$ ).  $^{13}\text{C}$  NMR (125 MHz,  $\text{CDCl}_3$ ):  $\delta$  0.03 ( $\text{SiMe}_3$ ), 113.00 ( $\text{C}_2$ ), 97.83, 109.61, (2 x  $\text{C}\equiv\text{C}$ ), 197.91 (CO). FAB - MS ( $m/z$ ): 1149  $[\text{M}]^+$ , 1121-897  $[\text{M}-n\text{CO}]^+$   $n=2-9$ . Anal. Calc'd for  $\text{Ru}_4\text{Si}_4\text{O}_{11}\text{C}_{35}\text{H}_{36}$ : C 36.58, H 3.13%. Found: C 37.47, H: 3.70%.

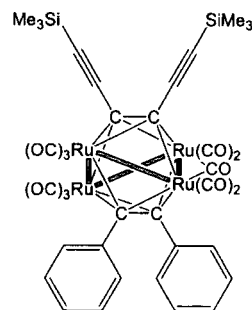
### 5.8.3.2. $[\text{Ru}_4(\mu_4\text{-}\eta^2\text{-PhC}_2\text{Ph})_2(\text{CO})_{11}]$ (44a)



A solution of  $\text{Ru}_4(\text{CO})_{12}(\mu_4\text{-}\eta^2\text{-PhC}_2\text{Ph})$  (0.07 g, 0.06 mmol) in hexane (20 ml) was treated with diphenylacetylene (0.02 g, 0.11 mmol) and heated at reflux for 6 h. The solution was cooled and red precipitate collected by filtration. The filtrate was heated at reflux overnight with additional diphenylacetylene (0.02 g, 0.11 mmol) to give a second crop of product. The combined precipitate (0.05 g, 0.05 mmol, 51%) was recrystallised from  $\text{CH}_2\text{Cl}_2\text{:MeOH}$  (51%).

IR (cyclohexane):  $\nu(\text{C}_2)$  2085m, 2055 ms,  $\nu(\text{CO})$  2040 s, 2023 s, 1981 ms, 1835 m  $\text{cm}^{-1}$ .  $^1\text{H}$  NMR (499 MHz,  $\text{CDCl}_3$ ):  $\delta$  6.71 (m, 8H, Ar), 6.93 (q, 12H, Ar).  $^{13}\text{C}$  NMR (125 MHz,  $\text{CDCl}_3$ ):  $\delta$  126.67 ( $\text{C}_2$ ), 127.23, 128.56, 144.81, 148.08 (4 x Ar), 199.09 (CO). FAB - MS ( $m/z$ ): 1014  $[\text{M}-2\text{CO}]^+$ , 986-762  $[\text{M}-n\text{CO}]^+$   $n=3-9$ . Anal. Calc'd for  $\text{Ru}_4\text{C}_{39}\text{O}_{11}\text{H}_{20} \cdot 1/3\text{CH}_2\text{Cl}_2$ : C 42.98, H 1.85%. Found: C 42.75, H 1.86%.

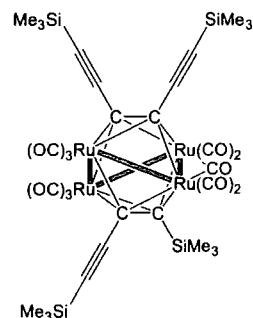
### 5.8.3.3. $[\text{Ru}_4(\mu_4\text{-}\eta^2\text{-Me}_3\text{SiC}\equiv\text{CC}_2\text{C}\equiv\text{CSiMe}_3)(\mu_4\text{-}\eta^2\text{-PhC}_2\text{Ph})(\text{CO})_{11}]$ (44b)



A solution of  $\text{Ru}_4(\mu_4\text{-}\eta^2\text{-Me}_3\text{SiC}\equiv\text{CC}_2\text{C}\equiv\text{CSiMe}_3)(\text{CO})_{12}$  (0.56 g, 0.55 mmol) in hexane (20 ml) was treated with diphenylacetylene (0.58 g, 2.07 mmol) and the solution heated at reflux for 8 h, cooled and the solvent removed. The crude product was purified by preparative TLC (hexane). The orange band contained the desired product and was recrystallised from  $\text{CH}_2\text{Cl}_2$ :hexane (0.32 g, 0.27 mmol, 49%).

IR (cyclohexane):  $\nu(\text{C}\equiv\text{C})$  2130 w,  $\nu(\text{CO})$  2088 w, 2074 w, 2063 s, 2050 s, 2043 m, 2026 s, 2009 m, 1998 m, 1981 m  $\text{cm}^{-1}$ . FAB - MS ( $m/z$ ): 1052 $[\text{M} - 2\text{CO}]^+$ , 1024-800  $[\text{M}-n\text{CO}]^+$   $n=3-11$ . Anal. Calc'd for  $\text{Ru}_4\text{C}_{37}\text{O}_{11}\text{H}_{28}\text{Si}_2\cdot 2.5\text{C}_6\text{H}_{14}$ : C 46.17, H 4.76%. Found: C 46.17, H 3.17%.

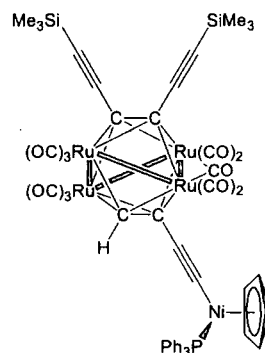
#### 5.8.3.4. $[\text{Ru}_4(\mu_4\text{-Me}_3\text{SiC}\equiv\text{CC}_2\text{C}\equiv\text{CSiMe}_3)(\mu_4\text{-Me}_3\text{SiC}_2\text{C}\equiv\text{CSiMe}_3)(\text{CO})_{11}]$ (44d)



A solution of  $\text{Ru}_4(\mu_4\text{-}\eta^2\text{-Me}_3\text{SiC}\equiv\text{CC}_2\text{C}\equiv\text{CSiMe}_3)(\text{CO})_{12}$  (0.05 g, 0.056 mmol) in hexane (10 ml) was treated with  $\text{Me}_3\text{SiC}\equiv\text{CC}\equiv\text{CSiMe}_3$  (0.03 g, 0.162 mmol) and the solution heated at reflux for 6 h, cooled and the solvent removed. The crude product was purified by preparative TLC (5% $\text{CH}_2\text{Cl}_2$ :hexane). The major yellow band contained the desired product and was recrystallised from  $\text{CHCl}_3$ :hexane (0.03 g, 0.02 mmol, 45%) to afford orange block shaped crystals.

IR (cyclohexane):  $\nu(\text{C}\equiv\text{C})$  2130 w,  $\nu(\text{CO})$  2092 s, 2067 s, 2060 s, 2027 s, 1989 s, 1975 s, 1850  $\text{s cm}^{-1}$ .  $^1\text{H NMR}$  (499 MHz,  $\text{CDCl}_3$ ):  $\delta$  0.04 (s, 18H,  $\text{SiMe}_3$ ), 0.07 (s, 9H,  $\text{SiMe}_3$ ), 0.18 (s, 9H,  $\text{SiMe}_3$ ).  $^{13}\text{C NMR}$  (125 MHz,  $\text{CDCl}_3$ ):  $\delta$  -1.05, -0.39, 5.91 (3 x  $\text{SiMe}_3$ ), 112.26, 114.68, 141.14 (3 x  $\text{C}_2$ ), 96.57, 104.50, 109.71, 110.43, (4 x  $\text{C}\equiv\text{C}$ ), 198.85 (CO). FAB - MS ( $m/z$ ): 1125  $[\text{M}]^+$ , 1097-817  $[\text{M}-n\text{CO}]^+$   $n=1-11$ . Anal. Calc'd for  $\text{Ru}_4\text{Si}_4\text{O}_{11}\text{C}_{33}\text{H}_{36}$ : C 35.23, H 3.20%. Found: C 34.86, H: 3.26%.

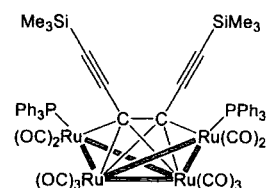
5.8.3.5.  $[\text{Ru}_4(\mu_4\text{-}\eta^2\text{-Me}_3\text{SiC}\equiv\text{CC}_2\text{C}\equiv\text{CSiMe}_3)(\mu_4\text{-}\eta^2\text{-(HC}_2\text{C}\equiv\text{C)Ni(PPh}_3\text{)Cp(CO)}_{11})]$  (44g)



A solution of  $\text{Ru}_4(\text{CO})_{12}(\mu_4\text{-Me}_3\text{SiC}\equiv\text{CC}_2\text{C}\equiv\text{CSiMe}_3)$  (0.2 g, 0.21 mmol) in hexane (20 ml) was treated with  $\text{Ni}(\text{C}\equiv\text{C}\equiv\text{CH})(\text{PPh}_3)\text{Cp}$  (0.1 g, 0.23 mmol) and the solution was heated at reflux for 6 h after which another equivalent  $\text{Ni}(\text{C}\equiv\text{CC}\equiv\text{CH})(\text{PPh}_3)\text{Cp}$  (0.1 g, 0.23 mmol) was added and the reaction mixture was heated at reflux overnight. The solution was filtered, the solvent removed and the crude product purified by preparative TLC (60:40 hexane: $\text{CH}_2\text{Cl}_2$ ). The first band (red) was identified as  $\text{Ru}_4(\mu_4\text{-}\eta^2\text{-(Me}_3\text{SiC}\equiv\text{CC}_2\text{C}\equiv\text{CSiMe}_3)(\text{CO})_{10}(\text{PPh}_3)_2$  (0.01 g, 0.007 mmol, 3%). The major band (orange) contained the desired product (0.08 g, 0.06 mmol, 26%).

IR ( $\text{CH}_2\text{Cl}_2$ ):  $\nu(\text{C}\equiv\text{C})$  2130 w,  $\nu(\text{CO})$  2095 m, 2070 m, 2038 m, 2032 m, 2010 w, 1977 m, 1819 w  $\text{cm}^{-1}$ .  $^1\text{H}$  NMR (499 MHz,  $\text{CDCl}_3$ ):  $\delta$  0.07 (s, 18H,  $\text{SiMe}_3$ ), 2.35 (s, 1H,  $\text{C}_2\text{H}$ ), 5.05 (s, 5H, Cp), 7.32 (t, 5H, Ar), 7.40 (t, 3H, Ar), 7.48 (t, 6H, Ar), 7.67 (t, 1H, Ar).  $^{13}\text{C}$  NMR (125 MHz,  $\text{CDCl}_3$ ):  $\delta$  1.26 ( $\text{SiMe}_3$ ), 89.54 (Cp), 109.04, 111.86, 155.98 (2 x  $\text{C}_2$ ), 91.54, 94.42, 106.25, 106.62 (4 x  $\text{C}\equiv\text{C}$ ), 126.96, 127.04, 127.48, 129.13, 129.27, 131.06, 131.89, 132.33, 132.72, 132.82 (10 x Ar), 198.82 (CO).  $^{31}\text{P}$  NMR (203 MHz,  $\text{CDCl}_3$ ):  $\delta$  44.0 ( $\text{PPh}_3$ ). FAB - MS ( $m/z$ ): 1365  $[\text{M}]^+$ , 1337-1141  $[\text{M}-n\text{CO}]^+$   $n=2-8$ .

5.8.3.6.  $[\text{Ru}_4(\mu_4-\eta^2-(\text{Me}_3\text{SiC}\equiv\text{CC}_2\text{C}\equiv\text{CSiMe}_3)(\text{CO})_{10}(\text{PPh}_3)_2]$



IR ( $\text{CH}_2\text{Cl}_2$ ):  $\nu(\text{C}\equiv\text{C})$  2097 w,  $\nu(\text{CO})$  2054 m, 2025 m, 2005 w, 1990 w, 1978 w  $\text{cm}^{-1}$ .  $^1\text{H}$  NMR (499 MHz,  $\text{CDCl}_3$ ):  $\delta$  -0.26 (s, 18H,  $\text{SiMe}_3$ ), 7.28 (m, 4H, Ar), 7.45 (m, 18H, Ar), 7.95 (m, 8H, Ar).  $^{13}\text{C}$  NMR (125 MHz,  $\text{CDCl}_3$ ):  $\delta$  -0.00 ( $\text{SiMe}_3$ ), 113.13 ( $\text{C}_2$ ), 95.95, 128.67 ( $\text{C}\equiv\text{C}$ ), 130.03, 131.27, 131.96, 136.64 (4 x Ar), 199.85 (CO).  $^{31}\text{P}$  NMR (200 MHz,  $\text{CDCl}_3$ ):  $\delta$  34.80 ( $\text{PPh}_3$ ). FAB - MS ( $m/z$ ): 1428  $[\text{M}]^+$ , 1400-1176  $[\text{M}-n\text{CO}]^+$   $n=2-9$ .

## Bibliography

1. G. E. Moore, *Electronics*, **38**, 114, 1965.
2. R. L. Carroll and C. B. Gorman, *Angew. Chem. Int. Ed. Engl.*, **41**, 4378, 2002.
3. G. D. Wilk, R. M. Wallace, and J. M. Anthony, *J. Appl. Phys.*, **89**, 5243, 2001.
4. J. A. Gupta, D. Landheer, J. P. McCaffery, and G. I. Sprule, *Appl. Phys. Lett.*, **78**, 17818, 2001.
5. J. M. Tour, M. Kozaki, and J. M. Seminario, *J. Am. Chem. Soc.*, **120**, 8486, 1998.
6. R. Wu, J. S. Schumm, D. L. Pearson, and J. M. Tour, *J. Org. Chem.*, **61**, 6906, 2003.
7. A. R. Pease, J. O. Jeppesen, J. F. Stoddart, Y. Luo, C. P. Collier, and J. R. Heath, *Acc. Chem. Res.*, **34**, 433, 2001.
8. A. Aviram and M. A. Ratner, *Chem. Phys. Lett.*, **29**, 277, 1974.
9. R. M. Metzger, *Synth. Met.*, **124**, 107, 2001.
10. R. M. Metzger, B. Chen, U. Höpfner, M. V. Lakshmikantham, D. Vuillaume, T. Kawai, X. Wu, H. Tachibana, T. V. Hughes, H. Sakurai, J. W. Baldwin, C. Hosch, M. P. Cava, L. Brehmer, and G. J. Ashwell, *J. Am. Chem. Soc.*, **119**, 10455, 1997.
11. M. A. Ratner, *Materials Today*, **20**, 2002.
12. Y. Wada, M. Tsukada, M. Fujihira, K. Matsushige, T. Ogawa, M. Haga, and S. Tanaka, *Jpn. J. Appl. Phys.*, **39**, 3835, 2000.
13. *Electron Transfer in Chemistry*, Vol. 5, Wiley-VCH, London, 2000.
14. V. Balzani, A. Credi, F. M. Raymo, and J. F. Stoddart, *Angew. Chem. Int. Ed. Engl.*, **39**, 3348, 2000.
15. M. D. Ward, *J. Chem. Educ.*, **78**, 321, 2001.
16. D. Goldhaber-Gordon, M. S. Montemerlo, J. C. Love, G. J. Opiteck, and J. C. Ellenbogen, *Proc. of the IEEE*, **85**, 521, 1997.
17. J. M. Tour, *Acc. Res. Chem.*, **33**, 791, 2000.
18. R. M. Metzger, *Chem. Rev.*, **103**, 3803, 2003.
19. L. A. Bumm, J. J. Arnold, M. T. Cygan, T. D. Dunbar, T. P. Burgin, L. Jones II, D. L. Allara, J. M. Tour, and P. S. Weiss, *Science*, **271**, 1705, 1996.
20. J. M. Seminario, A. G. Zacarias, and J. M. Tour, *J. Am. Chem. Soc.*, **120**, 3970, 1998.
21. K. Stokbro, J. Taylor, and M. Brandybyge, *J. Am. Chem. Soc.*, **125**, 3674, 2003.
22. G. K. Ramachandran, T. J. Hopson, A. M. Rawlett, L. A. Nagahara, A. Primak, and S. M. Lindsay, *Science*, **300**, 1413, 2003.
23. J. M. Seminario, P. A. Derosa, and J. L. Bastos, *J. Am. Chem. Soc.*, **124**, 10266, 2002.
24. L. Jones II, J. S. Schumm, and J. M. Tour, *J. Org. Chem.*, **62**, 1388, 1997.
25. D. L. Pearson and J. M. Tour, *J. Org. Chem.*, **62**, 1376, 1997.



26. F.-R. F. Fan, J. Yang, L. Cai, D. W. Price, S. M. Dirk, D. V. Kosynkin, Y. Yao, A. M. Rawlett, J. M. Tour, and A. J. Bard, *J. Am. Chem. Soc.*, **124**, 5550, 2002.
27. J. Chen, W. Wang, M. A. Reed, A. M. Rawlett, D. W. Price, and J. M. Tour, *Appl. Phys. Chem.*, **77**, 1224, 2000.
28. H. Shirakawa, *Angew. Chem. Int. Ed. Engl.*, **40**, 2574, 2001.
29. W. J. Feast, J. Tsibouklis, K. L. Pouwer, L. Groenendaal, and E. W. Meijer, *Polymer*, **37**, 5017, 1996.
30. M. Sarkar, S. Okada, H. Matsuzawa, H. Matsuda, and H. Nakanishi, *J. Mater. Chem.*, **10**, 819, 2000.
31. *Metal Catalysed Cross Coupling Reactions*, Wiley-VCH Verlag GmbH, Weinheim, 1998.
32. M. Schreiber, J. Anthony, F. Diederich, M. E. Spahr, R. Nesper, M. Hubrich, F. Bommeli, L. Degiorgi, P. Wachter, P. Kaatz, C. Bosshar, P. Günter, M. Colussi, U. W. Suter, C. Boudon, J.-P. Gisselbrecht, and M. Gross, *Adv. Mater.*, **6**, 786, 1994.
33. J. Anthony, A. M. Boldi, Y. Rubin, M. Hobi, V. Gramlich, C. B. Knobler, P. Seiler, and F. Diederich, *Helv. Chim. Acta*, **78**, 13, 1995.
34. R. E. Martin, U. Gubler, J. Cornil, M. Balakina, C. Boudon, C. Bosshard, J.-P. Gisselbrecht, F. Deiderich, P. Günter, M. Gross, and J.-L. Brédas, *Chem. Eur. J.*, **6**, 3622, 2000.
35. R. E. Martin, U. Gubler, C. Boudon, C. Bosshard, J.-P. Gisselbrecht, P. Günter, M. Gross, and F. Deiderich, *Chem. Eur. J.*, **6**, 4400, 2000.
36. M. J. Edelmann, M. A. Estermann, V. Gramlich, and F. Diederich, *Helv. Chim. Acta*, **84**, 473, 2001.
37. A. P. H. J. Schenning, J.-D. Arndt, M. Ito, A. Stoddart, M. Schreiber, P. Siensen, R. E. Martin, C. Boudon, J.-P. Gisselbrecht, M. Gross, V. Gramlich, and F. Deiderich, *Helv. Chim. Acta*, **84**, 296, 2001.
38. R. E. Martin and F. Diederich, *Angew. Chem. Int. Ed. Engl.*, **38**, 1350, 1999.
39. P. Avouris, *Acc. Chem. Res.*, **35**, 1026, 2002.
40. N. Robertson and C. A. McGowan, *Chem. Soc. Rev.*, **32**, 96, 2003.
41. S. J. Tans, A. R. M. Verschueren, and C. Dekker, *Nature*, **393**, 49, 1998.
42. R. Martel, T. Schmidt, H. R. Shea, T. Hertel, and P. Avouris, *Appl. Phys. Lett.*, **73**, 2447, 1998.
43. M. D. Ward, *Chem. Ind.*, 640, 1997.
44. M. Bruce and P. J. Low, *Adv. Organomet. Chem.*, **50**, 231, 2004.
45. N. S. Hush, *Prog. Inorg. Chem.*, **8**, 391, 1967.
46. M. B. Robin and P. Day, *Adv. Inorg. Chem. Radiochem.*, **10**, 247, 1967.
47. C. Cruetz, *Prog. Inorg. Chem.*, **30**, 1, 1983.
48. B. S. Braunschwig, C. Cruetz, and N. Sutin, *Chem. Soc. Rev.*, **31**, 168, 2002.
49. S. F. Nelson and H. Q. Tran, *J. Phys. Chem. A*, **103**, 8139, 1999.
50. D. E. Richardson and H. Taube, *Inorg. Chem.*, **21**, 1278, 1981.
51. C. Creutz, *Prog. Inorg. Chem.*, **30**, 1, 1983.
52. T. J. Meyer, *Acc. Chem. Res.*, **11**, 94, 1978.

53. P. J. Low and M. I. Bruce, *Adv. Organomet. Chem.*, R. West and A. F. Hill, Eds., Academic Press, London, 2002.
54. F. Coat and C. Lapinte, *Coord. Chem. Rev.*, **178–180**, 431, 1998.
55. N. Le Narvor, L. Toupet, and C. Lapinte, *J. Am. Chem. Soc.*, **117**, 7129, 1995.
56. M. Guillemot, L. Toupet, and C. Lapinte, *Organometallics*, **1710**, 1998.
57. M. Brady, W. Weng, Y. Zhou, J. W. Seyler, A. J. Amoroso, A. Arif, M. Böhme, G. Frenking, and J. A. Gladysz, *J. Am. Chem. Soc.*, **119**, 775, 1997.
58. M. I. Bruce, P. J. Low, K. Costuas, J.-F. Halet, S. P. Best, and G. A. Heath, *J. Am. Chem. Soc.*, **122**, 1949, 2000.
59. S. Szafert and J. A. Gladysz, *Chem. Rev.*, **103**, 4175, 2003.
60. M. I. Bruce, B. C. Hall, B. D. Kelly, P. J. Low, B. W. Skelton, and A. H. White, *J. Chem. Soc. Dalton Trans.*, 3719, 1999.
61. M. I. Bruce, B. G. Ellis, P. J. Low, B. W. Skelton, and A. H. White, *Organometallics*, **22**, 3184, 2003.
62. W. Mohr, J. Stahl, F. Hampel, and J. A. Gladysz, *Inorg. Chem.*, **40**, 3263, 2001.
63. Y. Zhou, J. W. Seyler, W. Weng, A. M. Arif, and J. A. Gladysz, *J. Am. Chem. Soc.*, **115**, 8509, 1993.
64. W. E. Meyer, A. J. Amoroso, C. R. Horn, M. Jaeger, and J. A. Gladysz, *Organometallics*, **20**, 1115, 2001.
65. R. Dembinski, T. Bartik, B. Bartik, M. Jaeger, and J. A. Gladysz, *J. Am. Chem. Soc.*, **122**, 810, 2000.
66. F. Coat and C. Lapinte, *Organometallics*, **15**, 477, 1996.
67. A. Wong, P. C. W. Kang, C. D. Tagge, and D. R. Leon, *Organometallics*, **9**, 1992, 1990.
68. Y. Sun, N. J. Taylor, and A. J. Carty, *Organometallics*, **11**, 4293, 1992.
69. S. Le Stang, F. Paul, and C. Lapinte, *Organometallics*, **19**, 1035, 2000.
70. T. B. Peters, J. C. Bohling, A. M. Arif, and J. A. Gladysz, *Organometallics*, **18**, 3261, 1999.
71. C. N. Horn, J. M. Martin-Alvarez, and J. A. Gladysz, *Organometallics*, **21**, 5386, 2002.
72. C. N. Horn and J. A. Gladysz, *Eur. J. Inorg. Chem.*, 2211, 2003.
73. F. Coat, M.-A. Guillevic, L. Toupet, F. Paul, and C. Lapinte, *Organometallics*, **16**, 5988, 1997.
74. R. M. Metzger, *J. Mater. Chem.*, **9**, 2027, 1999.
75. P. F. H. Schwab, B. C. Noll, and J. Michl, *J. Org. Chem.*, **67**, 5476, 2002.
76. N. J. Long, A. J. Martin, F. F. de Biani, and P. Zanello, *J. Chem. Soc. Dalton Trans.*, 2017, 1998.
77. M. P. Cifuentes, C. E. Powell, M. G. Humphrey, G. A. Heath, M. Samoc, and B. Luther-Davies, *J. Phys. Chem. A*, **105**, 9625, 2001.
78. T. Weyland, C. Lapinte, G. Frapper, M. J. Calhorda, J.-F. Halet, and L. Toupet, *Organometallics*, **16**, 2024, 1997.
79. H. Fink, N. J. Long, A. J. Martin, G. Opromolla, A. J. P. White, D. J. Williams, and P. Zanello, *Organometallics*, **16**, 2646, 1997.

80. T. Weyland, K. Costuas, L. Toupet, J.-F. Halet, and C. Lapinte, *Organometallics*, **19**, 4228, 2000.
81. C. Patoux, C. Coudret, J.-P. Launay, C. Joachim, and A. Gourdon, *Inorg. Chem.*, **36**, 5037, 1997.
82. P. Karafiloglou and J.-P. Launay, *Chem. Phys.*, **250**, 1, 1999.
83. M. Uno and P. H. Dixneuf, *Angew. Chem. Int. Ed. Engl.*, **37**, 1714, 1998.
84. M. J. Irwin, L. Manojlovic - Muir, K. W. Muir, R. J. Puddephatt, and D. S. Yufit, *Chem. Commun.*, 219, 1997.
85. T. Weyland, K. Costuas, A. Mari, J.-F. Halet, and C. Lapinte, *Organometallics*, **17**, 5569, 1998.
86. J. M. Tour, A. M. Rawlett, M. Kozaki, Y. Yao, R. C. Jagessar, S. M. Dirk, D. W. Price, M. A. Reed, C.-W. Zhou, J. Chen, W. Wang, and I. Campbell, *Chem. Eur. J.*, **7**, 5118, 2001.
87. J. M. Tour, M. Kozaki, and J. M. Seminario, *J. Am. Chem. Soc.*, **120**, 8486, 1998.
88. C. Eikmeier, H. Junga, A. J. Matzger, F. Scherlag, M. Shim, and K. P. C. Vollhardt, *Angew. Chem. Int. Ed. Engl.*, **36**, 2103, 1997.
89. M. B. Goldfinger, B. C. Khusrav, and T. M. Swager, *J. Am. Chem. Soc.*, **119**, 4578, 1997.
90. M. B. Goldfinger, B. C. Khusrav, and T. M. Swager, *J. Org. Chem.*, **63**, 1676, 1998.
91. K. Honda, T. Maruyama, and T. Yamamoto, *Synth. Met.*, **90**, 153, 1997.
92. H. Li, D. R. Powell, K. Hayashi, and R. West, *Macromolecules*, **31**, 52, 1998.
93. K. M. Jones and T. M. Keller, *Polymer*, **36**, 187, 1995.
94. C. Bosshard, R. Spreiter, P. Günter, R. R. Tykwinski, M. Schreiber, and F. Diederich, *Adv. Mater.*, **8**, 231, 1996.
95. R. R. Tykwinski, M. Schreiber, V. Gramlich, P. Seiler, and F. Diederich, *Adv. Mater.*, **8**, 226, 1996.
96. L. Gobbi, P. Seiler, F. Diederich, and V. Gramlich, *Helv. Chim. Acta*, **83**, 1711, 2000.
97. G. M. Tsivgoulis and J.-M. Lehn, *Chem. Eur. J.*, **2**, 1399, 1996.
98. T. Kawai, T. Sasaki, and M. Irie, *Chem. Commun.*, 711, 2001.
99. S. Kobatake, K. Uchida, E. Tsuchida, and M. Irie, *Chem. Commun.*, 2804, 2002.
100. H. Cho and E. Kim, *Macromolecules*, **35**, 8684, 2002.
101. S. Fraysse, C. Coudret, and J.-P. Launay, *Eur. J. Inorg. Chem.*, 1581, 2000.
102. C. P. Collier, J. O. Jeppesen, Y. Luo, J. Perkins, E. W. Wong, J. R. Heath, and J. F. Stoddart, *J. Am. Chem. Soc.*, **123**, 12632, 2001.
103. J. O. Jeppesen, J. Becher, and J. F. Stoddart, *Org. Lett.*, **4**, 557, 2002.
104. A. M. Elizarov, S.-H. Chiu, and J. F. Stoddart, *J. Org. Chem.*, **67**, 9175, 2002.
105. D. I. Gittins, D. Bethell, D. J. Schiffrin, and R. J. Nichols, *Nature*, **408**, 67, 2000.
106. D. Feldheim, *Nature*, **408**, 45, 2000.

107. L.-F. Joulie, E. Schatz, M. D. Ward, F. Weber, and L. J. Yellowlees, *J. Chem. Soc., Dalton Trans.*, 799, 1994.
108. F. M. Raymo, *Adv. Mater.*, **14**, 401, 2002.
109. L. Gobbi, P. Seiler, F. Deiderich, V. Gramlich, C. Boudon, J.-P. Gisselbrecht, and M. Gross, *Helv. Chim. Acta*, **84**, 743, 2001.
110. V. De Waele, U. Schmidhammer, T. Mrozek, J. Daub, and E. Riedle, *J. Am. Chem. Soc.*, **124**, 2438, 2002.
111. F. M. Raymo and S. Giordani, *J. Am. Chem. Soc.*, **124**, 2004, 2002.
112. F. M. Raymo, S. Giordani, A. J. P. White, and D. J. Williams, *J. Org. Chem.*, **68**, 4158, 2003.
113. M. A. Reed, J. Chen, A. M. Rawlett, D. W. Price, and J. M. Tour, *App. Phys. Lett.*, **78**, 3735, 2001.
114. J. Chen, M. A. Reed, A. M. Rawlett, and J. M. Tour, *Science*, **286**, 1550, 1999.
115. P. F. H. Schwab, M. D. Levin, and J. Michl, *Chem. Rev.*, **99**, 1863, 1999.
116. P. N. W. Baxter, *J. Org. Chem.*, **66**, 4170, 2001.
117. K. Sonogashira, Y. Tohada, and N. Hagihara, *Tetrahedron Lett.*, **50**, 4467, 1975.
118. K. Sonogashira, *J. Organomet. Chem.*, **653**, 46, 2002.
119. S. Takahashi, Y. Kuroyama, K. Sonogashira, and N. Hagihara, *Synthesis*, 627, 1980.
120. D. Mesnard, F. Bernadou, and L. Migniac, *J. Chem. Res. (S)*, 270, 1981.
121. P. Siemsen, R. C. Livingston, and F. Diederich, *Angew. Chem. Int. Ed. Engl.*, **39**, 2632, 2000.
122. Y. Tobe, N. Utsumi, K. Kawabata, A. Nagano, K. Adachi, S. Araki, M. Sonoda, K. Hirose, and K. Naemura, *J. Am. Chem. Soc.*, **124**, 5350, 2002.
123. J. M. Tour, *Chem. Rev.*, **96**, 537, 1996.
124. U. H. F. Bunz, *Chem. Rev.*, **100**, 1605, 2000.
125. D. Zhao and J. S. Moore, *Chem. Commun.*, 807, 2003.
126. J. M. Tour, L. Cheng, D. P. Nackashi, Y. Yao, A. K. Flatt, S. K. St. Angelo, T. E. Mallouk, and P. D. Franzon, *J. Am. Chem. Soc.*, **125**, 13279, 2003.
127. Z. J. Donhauser, B. A. Mantooth, K. F. Kelly, L. A. Bumm, J. D. Monnell, J. J. Stapleton, D. W. J. Price, A. M. Rawlett, D. L. Allara, J. M. Tour, and P. S. Weiss, *Science*, **292**, 2303, 2001.
128. J. Cornil, Y. Karzazi, and J. L. Bredas, *J. Am. Chem. Soc.*, **124**, 3516, 2002.
129. U. H. F. Bunz, *Acc. Chem. Res.*, **34**, 998, 2001.
130. J. Kim, I. A. Levitsky, D. T. McQuade, and T. M. Swager, *J. Am. Chem. Soc.*, **124**, 7710, 2002.
131. W. A. Reinerth, L. Jones II, T. P. Burgin, C. Zhou, C. J. Muller, M. R. Deshpande, M. A. Reed, and J. M. Tour, *Nanotechnology*, **9**, 246, 1998.
132. J. Kim and T. M. Swager, *Nature*, **411**, 1030, 2001.
133. M. Levitus, K. Schmieder, H. Ricks, K. D. Shimizu, U. H. F. Bunz, and M. A. Garcia-Garibay, *J. Am. Chem. Soc.*, **123**, 4259, 2001.

134. A. Beeby, K. Findlay, P. J. Low, and T. B. Marder, *J. Am. Chem. Soc.*, **124**, 8280, 2002.
135. P. Nguyen, S. Todd, D. V. D. B iggelaar, N. J. Taylor, T. B. Marder, F. Wittmann, and R. Friend, *Synlett*, 299, 1994.
136. M. I. Sluch, G. Godt, U. H. F. Bunz, and M. A. Berg, *J. Am. Chem. Soc.*, **123**, 6447, 2001.
137. A. Beeby, K. Findlay, P. J. Low, T. B. Marder, P. Matousek, A. W. Parker, S. R. Rutter, and M. Towrie, *Chem. Commun.*, 2406, 2003.
138. Z. Chenia, T. Livneh, I. Pro-Bar, and J. E. Koresch, *Vibr. Spectrosc.*, **25**, 119, 2001.
139. T. Ishibashi and H. Hamaguchi, *J. Phys. Chem. A*, **102**, 2263, 1998.
140. M. Kijima, I. Kinohita, and H. Shirakawa, *Synth. Metals*, **101**, 145, 1999.
141. H. Suzuki, *Org. Synth.*, **51**, 94, 1971.
142. E. B. Merkushev, N. D. Simakhina, and G. M. Koveshnikova, *Synthesis*, 486, 1980.
143. E. Negishi, M. Kitora, and C. Xu, *J. Org. Chem.*, **62**, 8957, 1997.
144. S. R. Rutter and A. Beeby, *Unpublished results*, 2003.
145. M. Weigelt, D. Becher, E. Poetsch, C. Bruhn, and D. Steinborn, *Z. Anorg. Allg. Chem.*, **625**, 1542, 1999.
146. T. Debaerdemaeker, A. Kutoglu, G. Schmid, and L. Weber, *Acta Crystallogr. B*, **29**, 1283, 1973.
147. E. Negishi and L. Anastasia, *Chem. Rev.*, **103**, 1979, 2003.
148. J. K. Surette, M.-A. MacDonald, M. J. Zaworotko, and R. D. Singer, *J. Chem. Cryst.*, **24**, 715, 1994.
149. J. G. Rodriguez, S. S. Ramos, R. Martin-Villamil, I. Fonseca, and A. Albert, *J. Chem. Soc., Perkin Trans. I*, **541**, 1996.
150. J. J. Mayerle, T. C. Clarke, and K. Bredfeldt, *Acta Crystallogr.*, **35**, 1519, 1979.
151. K. Kondo, S. Yasuda, T. Sakaguchi, and M. Miya, *J. Chem. Soc. Chem. Commun.*, 55, 1995.
152. H. Hart and K. Harada, *Tetrahedron Lett.*, **26**, 29, 1985.
153. S. Stavber, P. Kralj, and M. Zupan, *Synthesis*, **11**, 1513, 2002.
154. H. Hart, K. Harada, and C.-J. Du, *J. Org. Chem.*, **50**, 3104, 1985.
155. R. C. Evers and G. J. Moore, *J. Polym. Sci. A, Polym. Chem.*, **26**, 3213, 1988.
156. T. Yamamoto, K. Honda, N. Ooba, and S. Tomaru, *Macromolecules*, **31**, 7, 1998.
157. D. D. Perrin and W. L. F. Amarego, *Purification of Organic Chemicals*, Pergamon, Oxford, 1988.
158. A. B. Holmes and C. N. Sporikou, *Org. Synth. Coll. VIII*, 606, 1993.
159. P. Nguyen, Z. Yuan, L. Agocs, G. Lesley, and T. B. Marder, *Inorg. Chim. Acta*, **220**, 289, 1994.
160. D. R. Coulson, *Inorg. Synth.*, **28**, 107, 1990.
161. H. C. Clark and K. R. Dixon, *J. Am. Chem. Soc.*, **91**, 596, 1969.
162. L. S. Chia and W. R. Cullen, *Inorg. Chem.*, **14**, 482, 1975.
163. S. Luo, Y. Liu, Y. Liang, and Y. Ma, *Synth. Commun.*, **30**, 1569, 2000.

164. P. J. Low, *Ph.D. Thesis*, Adelaide University, Adelaide, 1996.
165. J. F. Gallagher, P. Butler, and A. R. Manning, *Acta Crystallogr.*, **C54**, 342, 1998.
166. Y. Rubin, S. S. Lin, C. B. Knobler, J. Anthony, A. M. Boldi, and F. Diederich, *J. Am. Chem. Soc.*, **113**, 6943, 1991.
167. M. I. Bruce, C. Hameister, G. Swincer, and R. C. Wallis, *Inorg. Synth.*, **28**, 270, 1990.
168. P. J. Low, K. A. Udachin, G. D. Enright, and A. J. Carty, *J. Organomet. Chem.*, **578**, 103, 1999.
169. B. F. G. Johnson, J. Lewis, and K. T. Schorpp, *J. Organomet. Chem.*, **91**, C13, 1975.
170. J. E. Davies, B. F. G. Johnson, C. M. Martin, R. H. H. Pearson, and P. J. Dyson, *J. Organomet. Chem.*, **550**, 431, 1998.
171. U. H. F. Bunz, Y. Rubin, and Y. Tobe, *Chem. Soc. Rev.*, **28**, 107, 1999.
172. F. Diederich, *Chem. Commun.*, 219, 2001.
173. F. Diederich, *Pure Appl. Chem.*, **71**, 265, 1999.
174. M. B. Nielsen and F. Deiderich, *Synlett*, **4**, 544, 2002.
175. R. R. Tykwinski and Y. Zhao, *Synlett*, **12**, 1939, 2002.
176. Y. Hori, K. Noda, S. Kobayashi, and H. Taniguchi, *Tetrahedron Lett.*, 3563, 1969.
177. H. Houbtman, *Angew. Chem. Int. Ed. Engl.*, **14**, 498, 1975.
178. H. Houbtman, *Tetrahedron*, **32**, 1293, 1976.
179. G. Hynd, G. B. Jones, G. Plourde II, and J. M. Wright, *Tetrahedron Lett.*, **40**, 4481, 1999.
180. G. B. Jones, J. M. Wright, G. W. Plourde II, G. Hynd, R. S. Huber, and J. E. Mathews, *J. Am. Chem. Soc.*, **122**, 1937, 2000.
181. R. R. Tykwinski, F. Diederich, V. Gramlich, and P. Seiler, *Helv. Chim. Acta*, **79**, 634, 1996.
182. Y. Rubin, C. B. Knobler, and F. Diederich, *Angew. Chem. Int. Ed. Engl.*, **31**, 698, 1991.
183. R. R. Tykwinski and F. Diederich, *Liebigs Ann. Recueil*, 649, 1997.
184. A. H. Alberts and H. J. Wynberg, *J. Chem. Soc., Chem. Commun.*, 1988.
185. R. R. Tykwinski, M. Schreiber, R. P. Carlon, F. Diederich, and V. Gramlich, *Helv. Chim. Acta.*, **79**, 2249, 1996.
186. C. Boudon, J.-P. Gisselbrecht, M. Gross, A. M. Boldi, R. Faust, T. Lange, D. Philp, J.-D. Van Loon, and F. Deiderich, *J. Electroanal. Chem.*, **394**, 187, 1995.
187. T. Lange, J.-D. van Loon, R. R. Tykwinski, M. Schreiber, and F. Deiderich, *Synthesis*, 537, 1996.
188. R. E. Martin, J. Bartek, F. Deiderich, R. R. Tywinski, E. C. Meister, A. Hilger, and H. P. Lüthi, *J. Chem. Soc. Perkin Trans. II*, 233, 1998.
189. R. R. Tykwinski, A. Hilger, F. Deiderich, H. P. Lüthi, P. Seiler, V. Gramlich, J.-P. Gisselbrecht, C. Boudon, and M. Gross, *Helv. Chim. Acta*, **83**, 1484, 2000.
190. H. Hopf, M. Kreutzer, and P. G. Jobes, *Chem. Ber.*, **124**, 1471, 1991.

191. F. Diederich, D. Philp, and P. Seiler, *J. Chem. Soc., Chem. Commun.*, 205, 1994.
192. F. Diederich, R. Faust, V. Gramlich, and P. Seiler, *J. Chem. Soc., Chem. Commun.*, 2045, 1994.
193. R. Faust, F. Diederich, V. Gramlich, and P. Seiler, *Chem. Eur. J.*, **1**, 111, 1995.
194. P. Siemsen, U. Gubler, C. Bosshard, P. Günter, and F. Deiderich, *Chem. Eur. J.*, **7**, 1333, 2001.
195. M. S. Khan, A. K. Kakkar, N. J. Long, J. Lewis, P. Raithby, P. Nguyen, T. B. Marder, F. Wittmann, and R. H. Friend, *J. Mater. Chem.*, **4**, 1227, 1992.
196. S. Takahashi, H. Morimoto, E. Murata, S. Kataoka, K. Sonogashira, and N. Hagihara, *Polym. Sci., Polym. Chem. Ed.*, **20**, 565, 1982.
197. P. L. Porter, S. Guha, K. Kang, and C. C. Frazier, *Polymer*, **32**, 1756, 1991.
198. W. Lu, N. Zhu, and C.-M. Che, *J. Organomet. Chem.*, **670**, 11, 2003.
199. M. Bruschi, M. G. Giuffreda, and H. P. Lüthi, *Chem. Eur. J.*, **8**, 4216, 2002.
200. A. D. Becke, *J. Chem. Phys.*, **98**, 5648, 1993.
201. M. J. Frisch, G. W. Trucks, H. B. Schlegel, G. E. Scuseria, M. A. Robb, J. R. Cheeseman, V. G. Zakrzewski, J. Montgomery, J. A. R. E. Stratmann, J. C. Burant, S. Dapprich, J. M. Millam, A. D. Daniels, K. N. Kudin, M. C. Strain, O. Farkas, J. Tomasi, V. Barone, M. Cossi, R. Cammi, B. Mennucci, C. Pomelli, C. Adamo, S. Clifford, J. Ochterski, G. A. Petersson, P. Y. Ayala, Q. Cui, K. Morokuma, D. K. Malick, A. D. Rabuck, K. Raghavachari, J. B. Foresman, J. Cioslowski, J. V. Ortiz, B. B. Stefanov, G. Liu, A. Liashenko, P. Piskorz, I. Komaromi, R. Gomperts, R. L. Martin, D. J. Fox, T. Keith, M. A. Al-Laham, C. Y. Peng, A. Nanayakkara, C. Gonzalez, M. Challacombe, P. M. W. Gill, B. Johnson, W. Chen, M. W. Wong, J. L. Andres, C. Gonzalez, M. Head-Gordon, E. S. Replogle, and J. A. Pople, *Gaussian 98, Revision A.3*, Gaussian, Inc., Pittsburgh PA, 1998.
202. *Handbook of Organopalladium Chemistry for Organic Synthesis*, Vol. 1, John Wiley & Sons, Inc., New York, 2002.
203. A. Köllhofer, T. Pullmann, and H. Plenio, *Angew. Chem. Int. Ed. Engl.*, **42**, 1056, 2003.
204. A. F. Littke and G. C. Fu, *J. Org. Chem.*, **64**, 10, 1999.
205. M. E. Eberhard, Z. Wang, and C. M. Jensen, *Chem. Commun.*, **8**, 818, 2002.
206. A. G. Fallis, *Can. J. Chem.*, **77**, 159, 1999.
207. C. Amatore and A. Jutand, *Acc. Chem. Res.*, **33**, 314, 2000.
208. D. Philp, V. Gramlich, P. Seiler, and F. Diederich, *J. Chem. Soc. Perkin Trans. II*, 875, 1995.
209. R. S. Dickson and P. J. Fraser, *Adv. Organomet. Chem.*, **12**, 323, 1974.
210. M. I. Bruce, B. D. Kelly, B. W. Skelton, and A. H. White, *J. Chem. Soc., Dalton Trans.*, 847, 1999.

211. F. Diederich, Y. Rubin, O. L. Chapman, and N. S. Goroff, *Helv. Chim. Acta*, **77**, 1441, 1994.
212. M. I. Bruce, P. J. Low, A. Werth, B. W. Skelton, and A. H. White, *J. Chem. Soc., Dalton Trans.*, 1551, 1996.
213. T. J. Snaith, P. J. Low, R. Rousseau, H. Puschmann, and J. A. K. Howard, *J. Chem. Soc., Dalton Trans.*, 292, 2001.
214. D. M. Hirst, *A Computational Approach to Chemistry*, Blackwell Scientific Publications, Oxford, 1990.
215. J.-F. Halet, *Coord. Chem. Rev.*, **635**, 637, 1995.
216. J. M. Goodman, *Chemical Applications of Molecular Modelling*, Royal Society of Chemistry, Cambridge, 1998.
217. *Encyclopedia of Computational Chemistry*, Wiley-VCH Verlag GmbH, Weinheim, 1998.
218. R. G. Parr and W. Yang, *Annu. Rev. Phys. Chem.*, **46**, 701, 1995.
219. *Density Functional Methods in Chemistry*, Springer-Verlag, London, 1991.
220. W. Koch and M. C. Holthausen, *A Chemist's Guide to Density Functional Theory*, Wiley-VCH Verlag GmbH, Weinheim, 2001.
221. M. I. Bruce and A. G. Swincer, *Adv. Organomet. Chem.*, **22**, 59, 1983.
222. M. I. Bruce, *Chem. Rev.*, **91**, 197, 1991.
223. M. I. Bruce, *Chem. Rev.*, **98**, 2797, 1998.
224. D. Touchard and P. H. Dixneuf, *Coord. Chem. Rev.*, **178-180**, 409, 1999.
225. F. De Angelis, A. Sgamellotti, and N. Re, *Organometallics*, **21**, 5944, 2002.
226. N. Re, A. Sgamellotti, and C. Floriani, *Organometallics*, **19**, 1115, 2002.
227. N. Auger, D. Touchard, S. Rigaut, J.-F. Halet, and J.-Y. Saillard, *Organometallics*, **22**, 1638, 2003.
228. M. D. Ward, *Chem. Ind.*, 568, 1996.
229. H. B. Fyfe, M. Mlekuz, G. Stringer, N. J. Taylor, and T. B. Marder, *NATO, ASI Series, Series E*, **206**, 331, 1992.
230. I.-Y. Wu, J. T. Lin, J. Luo, C.-S. Li, C. Tsai, Y. S. Wen, C.-C. Hsu, F.-F. Yeh, and S. Liou, *Organometallics*, **17**, 2188, 1998.
231. M. H. Garcia, M. P. Robalo, A. R. Dias, M. T. Duarte, W. Wensellers, G. Aerts, E. Goovaerts, M. P. Cifuentes, S. Hurst, M. G. Humphrey, M. Samoc, and B. Luther-Davies, *Organometallics*, **21**, 2107, 2002.
232. C. E. Powell, M. P. Cifuentes, J. P. Morrall, R. Stranger, M. G. Humphrey, M. Samoc, B. Luther-Davies, and G. A. Heath, *J. Am. Chem. Soc.*, **125**, 602, 2003.
233. N. J. Long and C. K. Williams, *Angew. Chem. Int. Ed.*, **42**, 2586, 2003.
234. D. Touchard, P. Haquette, A. Daridor, L. Toupet, and P. H. Dixneuf, *J. Am. Chem. Soc.*, **116**, 11157, 1994.
235. D. Touchard, P. Haquette, A. Romero, and P. H. Dixneuf, *Organometallics*, **17**, 3844, 1998.
236. S. Rigaut, L. Le Pichon, J.-C. Daran, D. Touchard, and P. H. Dixneuf, *Chem. Commun.*, 1206, 2001.



237. M. I. Bruce, P. Hinterding, E. R. T. Tiekink, B. W. Skelton, and A. H. White, *J. Organomet. Chem.*, **450**, 209, 1993.
238. M. Akita, M.-C. Chung, A. Sakurai, S. Sugimoto, M. Terada, M. Tanaka, and Y. Moro-oka, *Organometallics*, **16**, 4882, 1997.
239. R. D. Markwell, I. S. Butler, A. K. Kakkar, M. S. Khan, Z. H. Al-Zakwani, and J. Lewis, *Organometallics*, **15**, 2331, 1996.
240. R. Eastmond, T. R. Johnson, and D. R. M. Walton, *J. Organomet. Chem.*, **50**, 87, 1973.
241. N. M. Kostic and R. F. Fenske, *Organometallics*, **1**, 974, 1982.
242. D. L. Lichtenberger, S. K. Renshaw, A. Wong, and C. D. Tagge, *Organometallics*, **12**, 3522, 1993.
243. J. Manna, T. C. Stoner, and M. D. Hopkins, *Adv. Organomet. Chem.*, **38**, 79, 1995.
244. P. J. Low and M. I. Bruce, *Adv. Organomet. Chem.*, **48**, 71, 2001.
245. Y. Hayashi, M. Osawa, K. Kobayashi, and Y. Wakatsuki, *Chem. Commun.*, 1617, 1996.
246. Y. Hayashi, M. Osawa, and Y. Wakatsuki, *J. Organomet. Chem.*, **542**, 241, 1997.
247. M. Oberthur, G. Hillebrand, P. Arndt, and R. Kempe, *Chem. Ber. Recueil*, **130**, 789, 1997.
248. M. I. Bruce, M. Ke, P. J. Low, B. W. Skelton, and A. H. White, *Organometallics*, **17**, 3539, 1998.
249. R. Dembinski, T. Lis, S. Szafert, C. L. Mayne, T. Bartik, and J. A. Gladysz, *J. Organomet. Chem.*, **578**, 229, 1999.
250. B. Bartik, R. Dembinski, T. Bartik, A. M. Arif, and J. A. Gladysz, *New. J. Chem.*, **21**, 739, 1997.
251. V. W.-W. Yam, S. H.-F. Chong, and K.-K. Cheung, *Chem. Commun.*, 2121, 1998.
252. V. W.-W. Yam, S. H. F. Chong, and C. C. Ko, *Organometallics*, **19**, 5092, 2000.
253. A. Romero, D. Peron, and P. H. Dixneuf, *J. Chem. Soc., Chem. Commun.*, 1410, 1990.
254. H. Werner, R. Flugel, and B. Windmuller, *Chem. Ber. Recueil*, **130**, 493, 1997.
255. T. B. Marder, G. Lesley, Z. Yuan, H. B. Fyfe, P. Chow, G. Stringer, I. R. Jobe, N. J. Taylor, I. D. Williams, and S. K. Kurtz, *Materials for Nonlinear Optics: Chemical Perspectives, ACS Symp. Ser.*, **455**, Ch 40, 1991.
256. S. M. Al Quaisi, K. J. Galat, M. Chai, D. G. I. Ray, P. L. Rinaldi, C. A. Tessier, and W. J. Youngs, *J. Am. Chem. Soc.*, **120**, 12149, 1998.
257. M. Krieger, R. O. Gould, B. Neumueller, K. Harms, and K. Dehnicke, *Z. Anorg. Allg. Chem.*, **624**, 1434, 1998.
258. F. J. Fernandez, O. Blacque, M. Alfonso, and H. Berke, *Chem. Commun.*, 1266, 2001.
259. R. L. Roberts, H. Pushmann, J. A. K. Howard, J. H. Yamamoto, A. J. Carty, and P. J. Low, *J. Chem. Soc., Dalton Trans.*, 1099, 2003.

260. P. J. Low, R. Rousseau, P. Lam, K. A. Udachin, G. Enright, J. D. Tse, D. D. M. Wayner, and A. J. Carty, *Organometallics*, **18**, 3885, 1999.
261. R. L. Cordiner, D. Corcoran, D. S. Yufit, A. E. Goeta, J. A. K. Howard, and P. J. Low, *J. Chem. Soc., Dalton Trans.*, 3541, 2003.
262. G. A. Stark, A. M. Arif, and J. A. Gladysz, *Organometallics*, **16**, 2909, 1997.
263. A. E. Reed, L. A. Curtiss, and F. Weinhold, *Chem. Rev.*, **88**, 899, 1988.
264. Scientific Computing and Modelling NV, *ADF Program System, Release 2000.02*, Vrije Universiteit; Theoretical Chemistry, De Boelelaan 1083, 1081 HV, Amsterdam, The Netherlands, 2000.
265. E. J. Baerends, D. E. Ellis, and P. Ros, *Chem. Phys.*, **2**, 41, 1973.
266. L. Versluis and T. Zeigler, *J. Chem. Phys.*, **88**, 322, 1988.
267. G. te Velde and E. J. Baerends, *J. Comput. Phys.*, **99**, 84, 1992.
268. C. Fonseca Guerra, J. G. Snijders, G. te Velde, and E. J. Baerends, *Theor. Chem. Acc.*, **99**, 391, 1998.
269. A. D. Becke, *Phys. Rev. A*, **38**, 2398, 1988.
270. J. P. Perdew, *Phys. Rev. B*, **33**, 8822, 1986.
271. J. P. Perdew, *Phys. Rev. B*, **B34**, 7046, 1996.
272. P. Flükiger, H. P. Lüthi, and J. Weber, *Molekel, Revision 4.0*, Swiss Center for Scientific Computing, Manno (Switzerland), 2000.
273. J. M. Wisner, T. J. Bartczak, and J. A. Ibers, *Inorg. Chim. Acta*, **100**, 115, 1985.
274. R. Hoffmann, *Tetrahedron*, **22**, 521, 1966.
275. Q. Fan and G. V. Pfeiffer, *Chem. Phys. Lett.*, **162**, 472, 1989.
276. J. E. McGrady, T. Lovell, R. Stranger, and M. G. Humphrey, *Organometallics*, **16**, 4004, 1997.
277. K. D. John, T. C. Stoner, and M. D. Hopkins, *Organometallics*, **16**, 4948, 1997.
278. R. L. Beddoes, C. Bitcon, and M. W. Whiteley, *J. Organomet. Chem.*, **402**, 85, 1991.
279. M. I. Bruce, M. G. Humphrey, M. R. Snow, and E. R. T. Tiekink, *J. Organomet. Chem.*, **314**, 213, 1986.
280. S. Kheradmandan, K. Heinze, H. W. Schmalle, and H. Berke, *Angew. Chem. Int. Ed. Engl.*, **38**, 2270, 1999.
281. K. Venkatesan, F. J. Fernandez, O. Blacque, T. Fox, M. Alfonso, H. W. Schmalle, and H. Berke, *Chem. Commun.*, 2006, 2003.
282. C. Dehu, F. Meyers, and J. L. Brédas, *J. Am. Chem. Soc.*, **115**, 6198, 1993.
283. W. Wang, T. Bartik, M. Brady, B. Bartik, J. A. Ramsden, A. M. Arif, and J. A. Gladysz, *J. Am. Chem. Soc.*, **117**, 11922, 1995.
284. C. Lebreton, D. Touchard, L. Le Pichon, A. Daridor, L. Toupet, and P. H. Dixneuf, *Inorg. Chim. Acta*, **272**, 188, 1998.
285. S. Rigaut, J. Massue, D. Touchard, J.-L. Fillaut, S. Golhen, and P. H. Dixneuf, *Angew. Chem. Int. Ed. Engl.*, **41**, 4513, 2002.
286. S. Rigaut, F. Monnier, F. Mousset, D. Touchard, and P. H. Dixneuf, *Organometallics*, **21**, 2654, 2002.

287. S. Alavi, R. Rousseau, G. P. Lopinski, W. R. A. and T. Seideman, *Faraday Discuss.*, **117**, 213, 2000.
288. R. Denis, L. Toupet, F. Paul, and C. Lapinte, *Organometallics*, **19**, 4240, 2002.
289. F. Paul, J.-Y. Mevellec, and C. Lapinte, *J. Chem. Soc., Dalton Trans.*, 1783, 2002.
290. *Comprehensive Organometallic Chemistry II*, Vol. 7, Elsevier Science Ltd., Oxford, 1995.
291. *Catalysis and Dynamics and Physical Properties of Metal Clusters*, Vol. 2, Wiley-VCH, Weinheim, 1999.
292. J. F. Corrigan, M. Dinardo, S. Doherty, G. Hogarth, Y. Sun, N. J. Taylor, and A. J. Carty, *Organometallics*, **13**, 3572, 1994.
293. Y. Chi, A. J. Carty, P. Blenkiron, E. Delgado, G. D. Enright, W. Wang, S.-M. Peng, and G.-H. Lee, *Organometallics*, **15**, 5269, 1996.
294. J. F. Corrigan, S. Doherty, N. J. Taylor, and A. J. Carty, *Organometallics*, **12**, 993, 1993.
295. J. F. Corrigan, S. Doherty, N. J. Taylor, and A. J. Carty, *Organometallics*, **12**, 1365, 1993.
296. J. Lunniss, S. A. MacLaughlin, N. Taylor, A. J. Carty, and E. Sappa, *Organometallics*, **4**, 2066, 1985.
297. J. S. Field, R. J. Haines, and D. N. Smit, *J. Organomet. Chem.*, **240**, C23, 1982.
298. R. D. Adams and S. Wang, *J. Am. Chem. Soc.*, **109**, 924, 1987.
299. H. G. Ang, S. G. Ang, and S. Du, *J. Chem. Soc., Dalton Trans.*, 2963, 1999.
300. *Chains, Clusters, Inclusion Compounds, Paramagnetic Labels, and Organic Rings*, Vol. 5, Elsevier Science BV, Amsterdam, 1994.
301. K. Wade, *Adv. Inorg. Chem. Radiochem.*, **18**, 1, 1976.
302. D. M. P. Mingos and D. J. Wales, *Introduction to Cluster Chemistry*, Vol. 35, Prentice-Hall, New Jersey, 1990.
303. J.-F. Halet, R. Hoffmann, and J.-Y. Saillard, *Inorg. Chem.*, **24**, 1695, 1985.
304. S. Kahlal, K. A. Udachin, L. Scoles, A. J. Carty, and Y.-V. Saillard, *Organometallics*, **19**, 2251, 2000.
305. J.-F. Halet and J.-Y. Saillard, *J. Organomet. Chem.*, **327**, 365, 1987.
306. J. T. Jaeger, J. S. Field, D. Collinson, G. P. Speck, B. M. Peake, J. Hähnle, and H. Vahrenkamp, *Organometallics*, **7**, 1753, 1988.
307. J. T. Jaeger, S. Aime, and H. Vahrenkamp, *Organometallics*, **5**, 245, 1986.
308. H. Vahrenkamp and D. Wolters, *J. Organomet. Chem.*, **224**, C17, 1982.
309. J. S. Field, R. J. Haines, and D. N. Smit, *J. Chem. Soc., Dalton Trans.*, 1315, 1988.
310. W. Wang, J. F. Corrigan, G. D. Enright, N. J. Taylor, and A. J. Carty, *Organometallics*, **17**, 427, 1998.
311. K. Knoll, A. Orama, and G. Huttner, *Angew. Chem. Int. Ed. Engl.*, **23**, 976, 1984.
312. G. E. Sappa, A. Tirtipicchio, and M. T. Camellini, *J. Chem. Soc., Dalton Trans.*, 419, 1978.

313. S. Aime, G. Nicola, D. Osella, A. M. M. Lanfredi, and A. Tirtipicchio, *Inorg. Chim. Acta*, **85**, 161, 1984.
314. M. I. Bruce, N. N. Zaitseva, B. W. Skelton, and A. H. White, *J. Chem. Soc., Dalton Trans.*, 3879, 2002.
315. M. Okazaki, T. Ohtani, S. Inomata, N. Tagaki, and H. Ogino, *J. Am. Chem. Soc.*, **120**, 9135, 1998.
316. M. Okazaki, T. Ohtani, M. Takano, and H. Ogino, *Inorg. Chem.*, **41**, 6726, 2002.
317. B. Johnson, J. Lewis, B. E. Reichert, K. T. Schorpp, and G. M. Sheldrick, *J. Chem. Soc., Dalton Trans.*, 1417, 1977.
318. R. D. Adams, U. H. F. Bunz, W. Fu, and G. Roidl, *J. Organomet. Chem.*, **578**, 55, 1999.
319. F. A. Cotton, *Prog. Inorg. Chem.*, **21**, 1, 1976.
320. R. H. Crabtree and M. Lavin, *Inorg. Chem.*, **25**, 805, 1986.
321. H. Vahrenkamp and D. Wolters, *Organometallics*, **1**, 874, 1982.
322. D. Braga, F. Grepioni, J. J. Byrne, C. M. Martin, B. F. G. Johnson, and A. J. Blake, *J. Chem. Soc., Dalton Trans.*, 1555, 1995.
323. H. E. Housecroft, *Structure and Bonding*, Springer Verlag, Berlin Heidelberg, 1997.
324. P. F. Heveldt, B. F. G. Johnson, J. Lewis, P. R. Raithby, and G. M. Sheldrick, *J. Chem. Soc., Chem. Commun.*, 340, 1978.
325. M. Krejčík, M. Danek, and F. Hartl, *J. Electroanal. Chem.*, **317**, 179, 1991.

